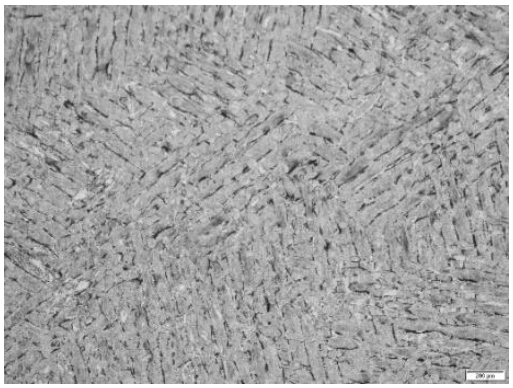
U.PORTO
FEUP FACULDADE DE ENGENHARIA
UNIVERSIDADE DO PORTO

Industrial Applications and Mechanical Characterization of Nickel - Titanium Alloys Manufactured through Laser - Powder Bed Fusion

José Miguel Oliveira Vieira

Master's Thesis



Advisors

Professor Jorge Lino Alves

Engineer Afonso Nogueira

Defendant

Filipe Chaves

Faculty of Engineering of the University of Porto

Mechanical Engineering Master's Degree

Manufacturing Specialization

SEPTEMBER 2024

Agradecimentos

Antes de mais, agradeço à minha família, que me apoiou nas decisões e nas voltas da minha vida. Esta tese é, acima de tudo, para vocês. O meu Pai, a minha Mãe, e os meus dois fantásticos irmãos!

Agradeço ao Senhor Professor Jorge Lino Alves, este, com a sua vasta experiência e conhecimento, tornou-se imprescindível para a realização da tese e guiou-me durante os problemas encontrados durante a sua execução.

Agradeço ao Senhor Engenheiro Afonso Nogueira, e ao pessoal da Hypermetal Lda., a experiência, o conhecimento empresarial e o ambiente de trabalho profissional que foram certamente extremamente desenvolvedores para a dissertação e para o meu conhecimento profissional.

Agradeço aos membros do LET, do LTM, e das oficinas do DEMEC, respetivamente, o Senhor Engenheiro Miguel Figueiredo, o Senhor Professor Ricardo Carbas, e o Senhor Engenheiro José Fecheira pelo auxílio prestado. Adicionalmente, agradeço à Senhora Engenheira Cláudia Lopes, à Senhora Engenheira Diana Paiva, e à Senhora Emília Soares pela ajuda imprescindível em certas dificuldades com as quais me deparei.

Agradeço à Faculdade de Engenharia da Universidade do Porto, a todos os Professores e colegas que me desenvolveram como pessoa, tanto em termos profissionais como pessoais, às senhoras da secretaria, às noites a claro e aos dias a frio, e a todas as lutas que um estudante desenvolve na vida universitária e num curso de caráter industrial-tecnológico.

De notar também o apoio, numa vertente mais material e financeira, das seguintes instituições, cujo auxílio revelou-se imprescindível para a realização da tese:

- Faculdade de Engenharia da Universidade do Porto.
- Hypermetal Lda.
- CATEC – Centro Avanzado de Tecnologías Aeroespaciales.
- Laboratório Associado de Energia, Transportes e Aeronáutica (**UIDB/50022/2020).**
- INEGI - Instituto de Ciência e Inovação em Engenharia Mecânica e Engenharia Industrial.



Abstract

Metal Additive Manufacturing has been experiencing an exponential growth in the Western industrial apparatus, being increasingly adopted in a myriad of high-tech and critical industries, such as aerospace, biomedical, energy and defense. At the same time, Shape Memory Alloys have the capacity to be immensely impacted by such technologies, due to the disruptive manufacturing practises that the conjunction between these two sectors can achieve together. This report explores such possibilities, with the synergetic term of 4D printing.

This Master Thesis was carried out as an internship for the conclusion of the Master's degree in Mechanical Engineering, of the Faculty of Engineering of the University of Porto. This work was developed in a corporate environment, in Hypermetal Lda., with the main objective of developing and producing Ni-Ti pieces and components through L-PBF manufacturing, with focus on modern industrial applications and in its mechanical characterization.

In the initial stages of the thesis, there is a bibliographic review divided between Metal Additive Manufacturing processes, with key focus on Laser-Powder Bed Fusion, and Shape Memory Alloys, with focus on Nickel-Titanium alloys. It addresses the definition, classification, mechanisms, process parameters, defects, post-processing, practical applications, and market and economic considerations and projections.

The main objective is the experimental study of the manufacturing process and viability of Ni-Ti components for modern industries, produced through the Laser – Powder Bed Fusion process, with subsequent evaluation of its properties and the influence of manufacturing parameters. Various specimens were also manufactured and tested, so as to evaluate its mechanical properties, through metallic, metallurgical and application tests, with discussion of the results achieved, regarding various properties (tensile, compressive, hardness, transformation temperature, fracture toughness) and its microstructure.

Keywords: Metal Additive Manufacturing, L-PBF, Ni-Ti, Nitinol, SMAs, 3D printing, 4D printing, Hypermetal, SME, mechanical engineering, manufacturing engineering.

Contents

List of Figures viii
List of Tables xiv
Acronyms xv
1. Introduction 1
1.1. Objectives 1
1.2. Hypermetal - Metal Additive Manufacturing 1
1.3. Master Thesis application 2
1.4. Structure and organization 2
2. Bibliographic Review 3
2.1. Metal Additive Manufacturing 3
2.1.1. Phases of Production 4
2.1.2. Classification and Technologies 5
2.1.3. Laser – Powder Bed Fusion 6
2.1.3.1. Process Steps 8
2.1.3.2. Subprocesses & variations 10
i) SLM vs DMLS vs LaserCUSING vs LMF 10
ii) L-PBF vs EB-PBF 11
iii) Hybrid possibilities of L-PBF 13
iv) Low-cost alternatives 15
2.1.3.3. Laser-Powder Mechanisms 15
2.1.3.4. Laser Types 16
2.1.3.5. Processing parameters 17
2.1.3.6. Thermal relations 18
2.1.3.7. Advantages of L-PBF 19
2.1.3.8. Limitations of L-PBF 21
2.1.3.9. Post-processing 23
i) Support material removal 24
ii) Surface texture improvements 25
iii) Accuracy improvements 26
iv) Aesthetics 27
v) Surface treatment technologies 27
2.1.3.10. Materials 28
2.1.3.11. Applications 30

i) Aerospace 30
ii) Biomedical 32
iii) Automotive 34
iv) Mould industries 36
v) Energy sector 36
vi) Defense and Military technology 38
2.1.3.12. Market & Economical Considerations 40
2.2. Shape Memory Alloys 42
2.2.1. Ni-Ti alloys 43
2.2.2. Ni-Ti phase diagram 45
2.2.3. Mechanism classification 47
2.2.3.1. R-phase 47
2.2.3.2. Shape memory effect (pseudoplasticity) 48
2.2.3.3. Superelasticity (pseudoelasticity) 50
2.2.3.4. Two-way SME 51
2.2.3.5. Full-way SME 53
2.2.4. Applications 53
i) Couplings 54
ii) Aerospace 56
iii) Blast protection 57
iv) Actuators 59
v) Automotive 60
vi) Biomedical 61
2.2.5. Market & Economical Considerations 63
2.3. 4D printing 65
2.3.1. Modern and near-future applications 67
2.3.2. Research developed 69
2.3.3. Market & Economical Considerations 70
2.4. Expected Properties 72
3. Experimental part 77
3.1. Materials and Methods 77
3.1.1. General overview 78
3.1.2. Material composition 78
3.1.3. Additive manufacturing 79
3.1.4. Post-processing 82
3.1.5. Clamp creation 83

3.1.6. Annealing 84
3.1.7. Development, modelling and testing 88
3.1.7.1. Tensile Testing 88
3.1.7.2. Compressive testing 90
3.1.7.3. Fracture toughness testing 91
3.1.7.4. Transformation temperature testing 93
3.1.7.5. Hardness testing 95
i) First procedure 95
ii) Second procedure 96
3.1.7.6. Shape memory recovery testing 97
3.1.7.7. Microstructure testing 98
3.1.7.8. Porosity testing 99
3.2. Results and discussion 99
3.2.1. Tensile properties 99
3.2.2. Compressive properties 103
3.2.3. Toughness properties 106
3.2.4. Transformation temperature properties 108
3.2.5. Hardness properties 111
3.2.6. Microstructure 116
3.2.6.1. Compression microstructure 116
3.2.6.2. Traction microstructure 116
3.2.6.3. Charpy microstructure 117
3.2.7. Porosity 118
3.2.7.1. Non-annealed sample 118
3.2.7.2. Annealed sample 119
3.2.8. Shape memory recovery 121
3.2.9. SEM analysis 123
3.2.9.1. Microstructural 123
i) Non-annealed sample 124
ii) Annealed sample 125
3.2.9.2. Composition analysis 126
i) First image – non-annealed sample 126
ii) Second image – non-annealed sample 127
iii) Third image – annealed sample 128
4. Conclusion 131
4.1. Future works 133

References 134
Annexes. 147
Annex A – Different types of MAM technologies 148
a) Direct Energy Deposition 148
b) Material / Binder Jetting 149
c) Material Extrusion 151
d) Hybrid possibilities 151
Annex B – Laser - Powder Mechanisms 153
a) Solid-state sintering 153
b) Chemical-induced sintering 155
c) Liquid-phase sintering 156
I. Distinct Binder and Structural Materials 156
II. Indistinct Binder and Structural Materials 158
d) Full Melting 158
Annex C – Processing Parameters 159
Annex D – Thermal Interactions 162
Annex E – Accuracy Improvements 167
i) Sources of error 167
ii) Model pre-processing 168
iii) Machining strategy 169
Annex F – Surface Finishing Technologies 169
a) Mechanical 169
b) Chemical 172
c) Thermal 173
Annex G – Tension calculus 175
Annex H – Compression calculus 177
Annex I – SME calculus 180

List of Figures

Figure 1 - Different types of manufacturing processes. 3
Figure 2 - Unit costs curves based on production volume. 4
Figure 3 - Main steps of AM and production phase. 4
Figure 4 - AM categories. 5
Figure 5 - Metal AM market. 6
Figure 6 - Renishaw RenAM 500Q. 7
Figure 7 - Various international corporations serving the L-PBF market. 8
Figure 8 - L-PBF process schematic. 8
Figure 9 - Alternative L-PBF process schematic. 9
Figure 10 - Classification of AM-processes regarding DIN EN ISO/ASTM 52900 and VDI 3405. 10
Figure 11 - L-PBF vs EB-PBF. 12
Figure 12 - Typical machining operation of hybrid L-PBF. 13
Figure 13 - Matsuura LUMEX Avance-25 hybrid L-PBF and its effects. 14
Figure 14 - LMI Alpha 140 unit and inert gas and axis system. 15
Figure 15 - Primary binding mechanisms in PBF processes. 15
Figure 16 - Best practices for dfAM. 20
Figure 17 - Topological optimization process. 20
Figure 18 - High value aerospace bracketry. 21
Figure 19 - Automated powder removal system in a Solukon SFM-AT800. 24
Figure 20 - Dental frame before and after post-processing support removal. 25
Figure 21 - Stair-stepping effect. 26
Figure 22 - Materials mentioned in publications regarding L-PBF. 28
Figure 23 - Materials in studies regarding Nickel super alloys. 29
Figure 24 – L-PBF produced metallic bracket 31
Figure 25 - AlSi10 mirror demonstrator for ESA. 31
Figure 26 - T901 turboshaft. 32
Figure 27 - Biomedical parts produced by L-PBF in the human body. 33
Figure 28 – Design, manufacturing, deployment and regeneration of 3D-printed scaffolds. 33
Figure 29 - Orthopedic implants of Renishaw. 34
Figure 30 - Bugatti brake Titanium calliper & Ford Performance Aluminium Manifold Inlet. 35
Figure 31 - BMWs components produced through L-PBF. 35
Figure 32 - Supply chain for fabrication of tooling for injection molding. 36
Figure 33 - Siemens 60MW V64.3 turbine and redesigned turbine vane. 37
Figure 34 - Siemens SGT-400 industrial gas turbine: cut section and core engine. 37
Figure 35 - 3D Gas burner from Siemens for the SGT-700 gas turbine in Philippsthal. 38
Figure 36 – L-PBF techniques used in Rheinmetall manufacturing units. 38

Figure 37 - GDLS and GE Additive representatives discussing integration for combat systems. 39
Figure 38 - Submarine components for ThyssenKrupp and engineers of the corporation. 39
Figure 39 - Metal AM solutions total sales for the last 20 years. 40
Figure 40 - Global AM market projections. 40
Figure 41 - MAM market share, by region, in 2022. 41
Figure 42 - Operational temperature of some examples of SMAs and their applications. 42
Figure 43 - Ni-Ti alloys (various compositions). 43
Figure 44 - Main properties of Ni-TI alloys. 44
Figure 45 - Ni-Ti phase diagram 1. 46
Figure 46 – Ni-Ti phase diagram 2. 46
Figure 47 - Example of a single-stage transformation (without R-phase). 48
Figure 48 - Example of a two-stage transformation (with R-phase). 48
Figure 49 - Microstructural state in SME. 49
Figure 50 – Shear modulus–temperature graph of Ni-Ti. 50
Figure 51 – one-way shape memory effect (left) and superelasticity (right). 51
Figure 52 – Superelasticity phenomena. 51
Figure 53 - SMA phases & crystals structure. 52
Figure 54 – OWSMA (a) vs TWSMA (b). 52
Figure 55 - Comparison of different SMA materials in actuation strain and temperature. 53
Figure 56 - Wide range of applications of SMAs. 54
Figure 57 - Cryofit coupling system. 54
Figure 58 – SMA coupling mechanism. 55
Figure 59 - Ni-Ti pipe coupler of a Y12F hydraulic system. 55
Figure 60 - SMA coupler in offshore applications. 55
Figure 61 - Overview of the DARPA Smart Wing program. 56
Figure 62 - Variable Geometry Chevron demonstration. 56
Figure 63 - Example of the blast protection mechanism in the patent. 57
Figure 64 - Energy absorbed by a SMA rod under adiabatic conditions. 58
Figure 65 - Energy absorbed by a SMA rod under twinning conditions. 58
Figure 66 – “Memory Metal” technology. 59
Figure 67 - Various examples of actuators used with Ni-Ti. 60
Figure 68 - Various uses of SMAs in automotive industry. 61
Figure 69 - NiTi self-expandable neurosurgical stent and bone-implant. 62
Figure 70 - Applications of Ni-Ti in biomedical. 62
Figure 71 - SMA market, from 2018 to 2030. 63
Figure 72 - Global SMA market share, by end use, in 2018. 64
Figure 73 - SMA publications by subject areas, from 1990 to 2013. 64
Figure 74 - 4D-printed octahedron with “transformation over time” effect. 65

Figure 75 - Difference between 3D and 4D printing. 65
Figure 76 - Current and near-future applications of 4D printing. 67
Figure 77 - Gartner hype cycle of the year 2018. 69
Figure 78 - Methods for manufacture Ni-Ti alloys and corresponding number of publications 69
Figure 79 - Number of articles from 2012 to 2020 regarding 3D and 4D printing. 70
Figure 80 - 4D printing market size, in billion USD (2022-2032). 71
Figure 81 - Statistics of publications on 4D printing, from Web of Science. 72
Figure 82 – Example of an actuator of CSEM with Ni-Ti SMA alloy usage. 76
Figure 83 - Work order plan fluxgram. 78
Figure 84 - Renishaw AM 250 of CATEC. 80
Figure 85 - Strategy used for manufacturing. 80
Figure 86 - F2516/E8 specimens and E9 specimens. 81
Figure 87 - E23 specimens. 81
Figure 88 – Container with 2 grams of Ni-Ti powder and F 2004 specimens. 81
Figure 89 - HAAS ST10 machine, located at DEMEC machine shop. 82
Figure 90 - GE Fanuc OT machine, located at DEMEC machine shop. 82
Figure 91 - Clamps for both bases of the F2516 specimens. 83
Figure 92 - Clamp in the open positions and locked position. 83
Figure 93 - Specimen in the clamp system before locking and after locking. 83
Figure 94 - Nabertherm N41/H industrial furnace. 84
Figure 95 - Assembly of the thermocouple unto a personal computer for data recovery. 84
Figure 96 – Main annealing groups. 85
Figure 97 – Main annealing chart: temperature vs time. 85
Figure 98 – Group 3 specimens post-annealing. 86
Figure 99 - Secondary annealing groups. 86
Figure 100 - Secondary annealing chart: temperature vs time. 87
Figure 101 – Modelling of the cylindrical test specimen for F 2516. 89
Figure 102 - MTS 810 testing machine. 89
Figure 103 - Instron 3367 testing machine. 90
Figure 104 – Modelling of the short-length specimen for E 9. 90
Figure 105 – Modelling of Charpy V-Notch specimen for E 23. 91
Figure 106 - E23 charpy specimens with improved smoothing. 92
Figure 107 - E23 Charpy test machine (in ready position with the weight), located at LET. 92
Figure 108 – Modelling of the specimen for F 2004. 93
Figure 109 - Netzch DSC 214 Polyma machine. 94
Figure 110 - Wolpert Dia Testor 2Rc hardness tester. 95
Figure 111 - Resin used for hardness testing support. 96
Figure 112 – Samples in resin moulds and the designation of the specimens. 96

Figure 113 - Non-annealed and annealed samples used for the second hardness procedure. 97
Figure 114 - Fluxgram of the SME testing plan. 97
Figure 115 - Microstructure analysis fluxgram. 98
Figure 116 – Graphical result of the three traction specimens. 99
Figure 117 - Theoretical (expected) progression when with adequate manufacture. 101
Figure 118 - Fractured non-annealed specimens. 101
Figure 119 - Bulk vs border CT scan (courtesy of CATEC). 102
Figure 120 – Total results of the three compression specimens. 103
Figure 121 - Nitinol stiffness and relation with phases 105
Figure 122 - Group 1, group 2 and group 3 specimens after impact. 106
Figure 123 - Group 1 Charpy specimen: lateral view (left) and top view (right). 107
Figure 124 - Group 2 Charpy specimen: lateral view (left) and top view (right). 107
Figure 125 - Group 3 Charpy specimen: lateral view (left) and top view (right). 107
Figure 126 - NI-Ti powder DSC graph. 108
Figure 127 – Non-annealed DSC graph. 109
Figure 128 - Annealed at 800ºC DSC graph. 109
Figure 129 - Annealed at 800ºC and 500ºC DSC graph. 109
Figure 130 - Comparison between non-powder samples. 110
Figure 131 – Martensite and austenite curve comparison between the non-powder samples. 111
Figure 132 - Graphical average results of the first hardness procedure. 112
Figure 133 – First procedure non-annealed graphical results. 113
Figure 134 – First procedure annealed graphical results. 113
Figure 135 - Second procedure graphical results. 114
Figure 136 - Graphical average results of global hardness results. 115
Figure 137 - CR1 and CR2 non-annealed microstructure (HF + H2O2). 116
Figure 138 - CR1 and CR2 annealed microstructure (HF + H2O2). 116
Figure 139 - TR1 and TR2 non-annealed microstructure (HF + H2O2). 116
Figure 140 - TR1 and TR2 annealed microstructure (HF + H2O2). 117
Figure 141 - CH1 and CH2 non-annealed microstructure (HF + H2O2). 117
Figure 142 - CH1 and CH2 annealed microstructure (HF + H2O2). 117
Figure 143 - Non-annealed samples with colour threshold input. 118
Figure 144 - Annealed samples with colour threshold input. 119
Figure 145 - Graphical results of the SME test. 121
Figure 146 - Stress-strain curves of the compression across several deformation cycles. 122
Figure 147 – Start and finish of the stress-strain curves across the deformation cycles. 122
Figure 148 - Stress-strain curve and its relation to detwinned martensite. 123
Figure 149 - Base interface images. 124
Figure 150 - Neck interface images. 124

Figure 151 - Base interface images. 125
Figure 152 - Image of non-annealed specimen (first image). 126
Figure 153 - Composition results of the various samples in the first image. 127
Figure 154 - Image of non-annealed specimen (second image). 128
Figure 155 - Composition results of the various samples in the second image. 128
Figure 156 - Image of annealed specimen (third image). 129
Figure 157 - Composition results of the various samples in the third image. 129
Figure 158 – Another example of an actuator of CSEM with Ni-Ti SMA alloy usage. 130
Figure 159 - DED schematic 1. 148
Figure 160 - DED schematic 2. 149
Figure 161 - Binder Jetting schematic. 149
Figure 162 - Schematic of the metal AM processes: (A) material jetting and (B) binder jetting. 150
Figure 163 - Hewlett-Packard Metal Jet S100 process workflow. 150
Figure 164 - Material Extrusion schematic. 151
Figure 165 - Turbine casing manufactured with Lasertec 65. 151
Figure 166 - Hybrid manufacturing for rotors. 152
Figure 167 - Joint Hull Program. 153
Figure 168 - Solid-State Sintering. 154
Figure 169 - Variations of the liquid-phase sintering process. 156
Figure 170 - Different possible scanning patterns. 159
Figure 171 - Scan strategies in L-PBF. 160
Figure 172 - CW vs PW. 161
Figure 173 - Laser process parameters. 161
Figure 174 - Example of scan pattern. 162
Figure 175 - Types of tracks. 163
Figure 176 - Process parameters of track types. 164
Figure 177 - Gaussian distribution of laser beam. 167
Figure 178 – Schematic diagram of the vibratory tumbling process in a free abrasive. 169
Figure 179 - Abrasive blasting processes. 170
Figure 180 - Shot peening mechanism. 171
Figure 181 - Schematic diagram of Abrasive flow machining mechanism. 171
Figure 182 - Chemical polishing operations. 172
Figure 183 - Electrochemical polishing operation. 173
Figure 184 - Laser polishing process: schematic and application example. 174
Figure 185 – Thermal deburring process: schematic and application example. 174
Figure 186 - HIP schematic of the equipment and process. 175
Figure 187 - Group 1 0.2% offset. 175
Figure 188 - Group 2 0.2% offset. 176

Figure 189 - Group 3 0.2% offset. 176
Figure 190 - Group 1 (tensile) elastic region 176
Figure 191 - Group 2 (tensile) elastic region. 177
Figure 192 - Group 3 (tensile) elastic region. 177
Figure 193 - Group 1 compressive yield strength at 0.2% elongation visualization. 178
Figure 194 - Group 2 compressive yield strength at 0.2% elongation visualization. 178
Figure 195 - Group 3 compressive yield strength at 0.2% elongation visualization. 178
Figure 196 - Group 1 (compressive) elastic region. 179
Figure 197 - Group 2 (compressive) elastic region. 179
Figure 198 - Group 3 (compressive) elastic region. 179
Figure 199 – 1st cycle compressive yield strength at 0.2% elongation visualization. 180
Figure 200 - 2nd cycle compressive yield strength at 0.2% elongation visualization. 180
Figure 201 – 3rd cycle compressive yield strength at 0.2% elongation visualization. 181
Figure 202 - 4th cycle compressive yield strength at 0.2% elongation visualization. 181
Figure 203 - 1st cycle (compressive) elastic region. 181
Figure 204 - 2nd cycle (compressive) elastic region. 182
Figure 205 - 3rd cycle (compressive) elastic region. 182
Figure 206 - 4th cycle (compressive) elastic region. 182

List of Tables

Table 1 - Materials selection of both processes. 12
Table 2 – Types of lasers used in MAM and their properties. 16
Table 3 - Parameters of L-PBF manufacturing. 18
Table 4 - Main hazards of PBF machines. 23
Table 5 - Techniques for L-PBF post-processing. 27
Table 6 - Ni-Ti alloys advantages and limitations. 45
Table 7 - Types of SMA deformations. 53
Table 8 - L-PBF vs DED manufacturing in SMAs. 66
Table 9 - General properties expected through “conventional” non-AM techniques. 73
Table 10 - Sources of table 9. 74
Table 11 - General properties expected through MAM techniques, in particular, L-PBF. 74
Table 12 - Sources of table 11. 75
Table 13 - Chemical composition (in weight percentage). 79
Table 14 - Chemical composition (in atomic weight percentage). 79
Table 15 - Etching solutions used. 98
Table 16 – Results of the properties of the three traction specimens. 100
Table 17 - Properties of the three compression specimens. 103
Table 18 - E 23 Charpy absorbed energy. 106
Table 19 - DSC properties results. 110
Table 20 - Non-annealed samples hardness results. 112
Table 21 - Annealed samples hardness results. 112
Table 22 - Second procedure 22°C hardness results. 114
Table 23 - Second procedure 150°C hardness results. 114
Table 24 - Non-annealed porosity values. 120
Table 25 - Annealed porosity values. 120
Table 26 - Results of the SME test. 121
Table 27 - Deformation cycles overall properties. 123
Table 28 - The binding mechanism in L-PBF. 159

Acronyms

2D – 2 Dimensions
3D – 3 Dimensions
AGVs – Autonomous Guided Vehicles
AM – Additive Manufacturing
ASTM - American Society for Testing and Materials
CAD – Computer Assisted Design
CAGR – Compound Annual Growth Rate
CNC – Computer Numerical Control
CV - Conventional
CW – Continuous Wave
DED – Direct Energy Deposition
DMLS – Direct Metal Laser Sintering
DOD – Drop-on-demand
DSC – Differential Scanning Calorimeter
EBM – Electron Beam Melting
EB-PBF – Electron Beam Powder Bed Fusion
FDM – Fused Deposition Modelling
ILT – Institute for Laser Technology
L-PBF – Laser Powder Ned Fusion
LET – Laboratório de Ensaios Tecnológicos
LTM – Laboratório de Materiais Cerâmicos, Tratamentos Térmicos, Soldadura
MAM – Metal Additive Manufacturing
MMC – Metal Matrix Composite
OEM – Original Equipment Manufacturer
PBF – Powder Bed Fusion
PPE – Personal Protective Equipment
PW – Pulsed Wave
SEM – Scanning Electrode Microscopy
SLM – Selective Laser Melting
SLS – Selective Laser Sintering
SMA – Shaped Memory Alloys
SME – Shape Memory Effect
SMM – Shape memory materials
STL - Stereolithography
VDI – “Verein Deutscher Ingenieure” - The Association of German Engineers

1. Introduction

1.1. Objectives

This Master Thesis was conducted as part of the final project for the Master's degree in Mechanical Engineering, having as its main theme Metal Additive Manufacturing technologies and its role in the manufacturing of Shape Memory Alloys and its current applications. In particular, this thesis objective was the study of Nickel-Titanium alloys produced through Laser – Powder Bed Fusion technology, and subsequent evaluation of mechanical and metallurgical properties of test pieces produced through aforementioned technologies. This project was executed through an internship in a corporate environment, at Hypermetal Lda.

The thesis objectives are, therefore, the bibliographic review of metal additive manufacturing technologies and of Nickel-Titanium shaped memory alloys, with convergence of topics with 4D printing. Both these subjects have subsequent investigation of their industrial applications, regarding aeronautical, biomedical, automotive, energy and defence/military-industrial sectors. Lastly, there is an evaluation and discussion of the results obtained in manufactured test pieces, obtained through experimental means, with the aforementioned material composition and manufacturing technology, with analysis of various tests, defects, porosity, etc.

1.2. Hypermetal - Metal Additive Manufacturing

"Metal Additive Manufacturing, commonly known as Metal 3D Printing, is a technology used to obtain parts by metal powder sintering through a laser beam. It's a fascinating technology: fast, flexible, without waste and capable of producing parts that are impossible to obtain by any other technology." (Hypermetal website, 2024)

Hypermetal Lda., also known as Hypermetal – Metal Additive Manufacturing, is a SME located in Vila Nova de Gaia, near Porto, specialized in the production of metal parts through additive manufacturing, creating an assortment of parts depending on the client at hand. The clients are numerous and diversified, ranging from aerospace to automotive, passing through medical, industrial, and defence-related applications. Despite the (obvious) focus on metal additive manufacturing, there are also CNC capabilities, heat treatments (such as annealing and tempering), shot blasting post-processing, and various engineering consulting services (such as reverse engineering, virtual warehouse services, and topological optimization).

The company's CEO is Engineer Afonso Nogueira, with the company existing since 2016 and having an estimated social capital of 190.000€, being started through European Union grants for metal additive manufacturing companies and continued with the subsequent profits generated.

1.3. Master Thesis application

Metal additive manufacturing has been increasing in both patent development, technological sophistication, and capital stock at an exponential pace, especially in the last 10 years, and it has shown great economic viability for the production of parts of great complexity and low/medium volume productions, when comparing with more traditional processes such as subtractive or forming manufacturing technology. At the same time, shape memory alloys research provide unique characteristics that promise novel uses of thermo-mechanical applications for otherwise more complex engineering projects or processes that are currently in use, offering a dynamic model of material manipulation in crucial modern sectors.

The ever-increasing development of such novel technologies has been a key staple in industrial European policies of the last decades, with research grants being developed by the European Union for such ends. One of the key companies that such policies allowed was the start-up of Hypermetal Lda., which specializes in the aforementioned metal additive technologies, especially regarding L-PBF ones. Therefore, there is a study of the synergetic elements between the aforementioned technologies and its industrial viability for manufacture.

1.4. Structure and organization

This master thesis focuses, firstly, on a bibliographical review of metal additive manufacturing technologies, with the respective classification and subsequent focus on Laser-Powder Bed Fusion, the processing parameters, defects, post-processing, materials, various applications, and economical/market considerations. After such scope, there is the focus of shape memory alloys, in particular, Nickel-Titanium, also known as Nitinol, with its characteristics and development, and the modern and near-future applications of such alloy. The review finishes with 4D printing itself, a synergetic convergence of both fields.

After such state-of-the-art research and study, there is an experimental phase, with the determination and evaluation of the principal properties of the material, with documentation regarding the steps necessary, and comparing with the parameters given by the powder supplier, by examining the given properties and comparing with literature results.

Lastly, there is the visualization of the results and conclusions reached through such experiments, with evaluation of its properties and the influence of manufacturing parameters. Specimens were created and tested, so as to evaluate its mechanical properties, through metallic, metallurgical and application tests, with discussion of the results achieved, regarding the tensile properties, machinability, microstructure, and dimensional accuracy.

2. Bibliographic Review

2.1. Metal Additive Manufacturing

Additive manufacturing is, as defined by the ASTM society, and in particular, the F2792-12a standard, “a process of joining materials to make objects from 3D model data, usually layer upon layer, as opposed to subtractive manufacturing methodologies”, and, according to VDI 3405, as a “manufacturing process in which the workpiece is built up element by element or layer by layer”, with the geometry of the components in all additive manufacturing process being composed of individual layers (Gibson, Rosen, Stucker, & Khorasani, 5 - Powder Bed Fusion, 2021) (Squillace, 2023) (Schleifenbaum, 2023).

The additive manufacturing process differs from more conventional manufacturing processes in the method in which they build up the workpiece layer-by-layer, through successive joining of the material, instead of more traditionally subtractive or formative manufacturing, which subtracts or manipulates material, as can be seen in figure 1 (Squillace, 2023).

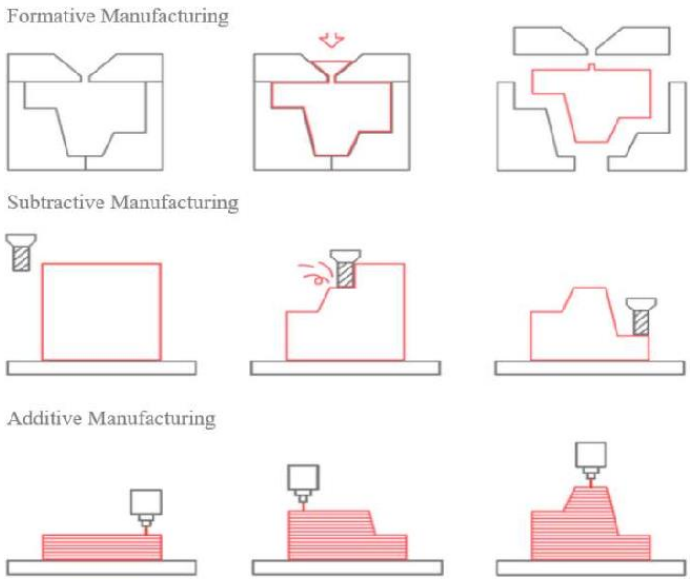


Figure 1 - Different types of manufacturing processes (Welfen, 2020).

Metal additive manufacturing technology has been gaining increased focus in the Western Industrial world, due to the adaptability and versatility inherent to such industrial procedure. With its very high level of technological and industrial expertise, this industrial region has been a key adopter of such technologies, making use of the vast intellectual capital at its disposal so as to better compete against the rising competitive Southeastern Asian markets, that have been gaining increased influence in global manufacturing quotas. Additive manufacturing allows unprecedent benefits regarding highly complex and/or low

volume production of parts, through the use of reduced manufacturing infrastructure, easily transferable digital-based designs, and versatility of modification of its design structure. (Gibson, Rosen, Stucker, & Khorasani, 5 - Powder Bed Fusion, 2021). Figure 2 shows the unit cost based on production volume.

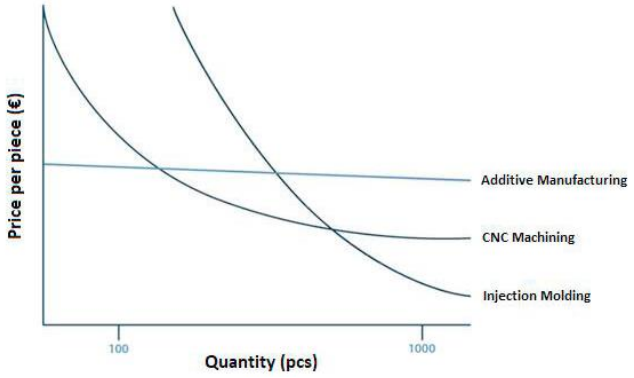


Figure 2 - Unit costs curves based on production volume (Vlamidir, Timko, Holubzak, & Novak, 2023).

2.1.1. Phases of Production

As a general rule, there are 7 mains steps that make a certain design transform itself from the virtual-based CAD characterization to the physical result of the product. These are shown in figure 3.

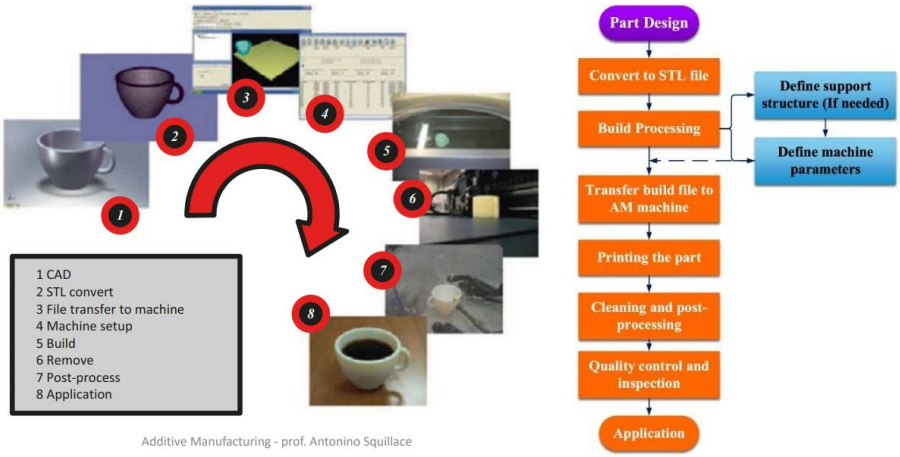


Figure 3 - Main steps of AM (left) and production phase (right) (Squillace, 2023) (Sefene, 2022).

In such technologies, parts are made by adding materials in layers, with each layer cross-section derived from a CAD part. As such, the major ways AM machines differ are in the materials that can be used, how the layers are created, and how the layers are bonded to each other. The creation process is very straight-forward, with a CAD design being converted to a .STL file, that is then transferred to the equipment, where there can be certain manipulation of some parameters, such as the correct size, position, and orientation for the build. The machine must be set up properly prior to the build process, with such

settings relating to parameters like the material constraints, energy source, layer thickness, timings, etc. (Gibson, Rosen, Stucker, & Khorasani, 5 - Powder Bed Fusion, 2021) (Squillace, 2023) (Schleifenbaum, 2023).

The .STL file has become the standard on this type of machines, where 3D modelling systems contain triangular-based representations of the given surfaces and have become "standard data inputs of rapid prototyping and manufacturing systems". In this technology, physical objects produced layer-by-layer are a 2D cross-section of the 3D mesh in STL format, through surface tessellation (Mátyási, 2023).

The build process is mostly automated, with only superficial monitoring of the machine needed confirm there are no errors present like power or software errors, running out of material, etc. Once the AM machine has completed the build, there is the need for the removal of the parts, which normally requires interaction with the machine, such as manipulation of safety interlocks. Once removed, the parts may require additional cleaning, removal of certain additional support structures, priming and or painting, various heat treatments, general improvement of weaker parts, etc. Post processing may be laborious or costly if the necessities are very demanding. After such manufacturing process, the parts are ready to be used, with possible assembly with other components, such as electrical or electro-mechanical ones (Gibson, Rosen, Stucker, & Khorasani, 5 - Powder Bed Fusion, 2021) (Squillace, 2023).

2.1.2. Classification and Technologies

There are a myriad of technologies regarding metal additive manufacturing (or MAM). According to the ASTM F-42 classification, there are seven different AM technologies, as can be seen in figure 4.

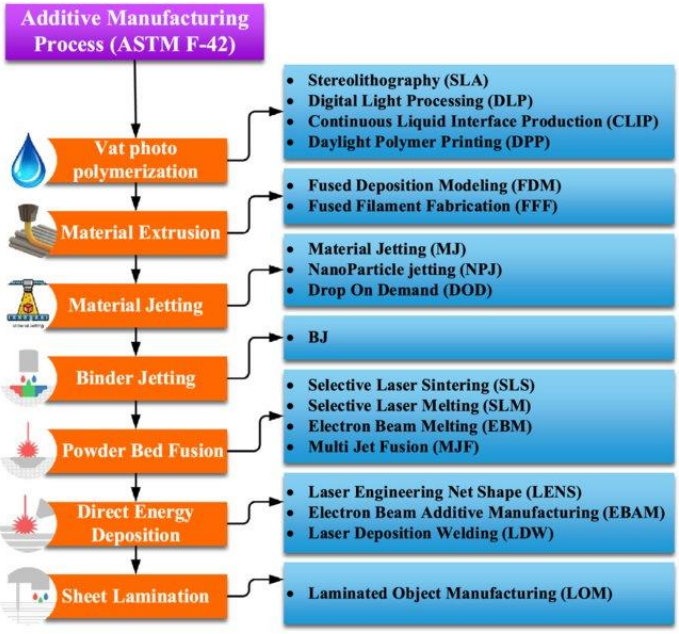


Figure 4 - AM categories (Sefene, 2022).

However, of these 7 categories, not all are fit for metal manufacture, with only 5 of the 7 categories being relevant for the MAM market, as can be seen in figure 5, and therefore having more emphasis in this document. These are Powder Bed Fusion, Direct Energy Deposition, Material/Binder Jetting and Material Extrusion.

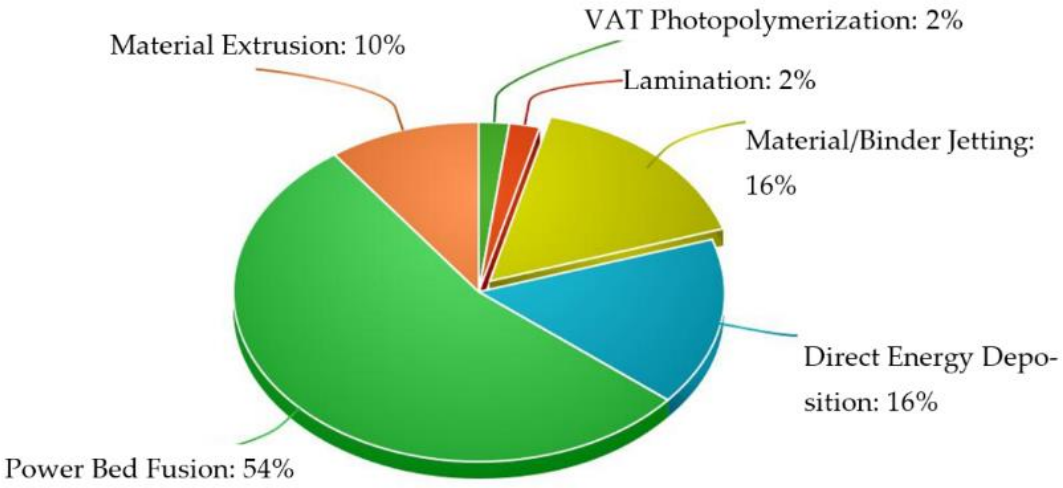


Figure 5 - Metal AM market (Vafadar, 2021).

More in-depth differences between non-PBF technologies are shown in Annex A, both in basic and hybrid form. Of note that Lamination and VAT Photopolymerization are not being discussed, since they represent such a small segment of the market.

2.1.3. Laser – Powder Bed Fusion

This report will mainly focus on Laser – Powder Bed Fusion, since it is the main manufacturing process for metal AM parts, representing the biggest quota of the metal AM market, with estimates of more than 50% of the market share (Vafadar, 2021).

According to ASTM 52900:2021, and as mentioned previously, Powder Bed Fusion can be defined as:

"An AM process in which thermal energy selectively fuses regions of a powder bed."

It is a renowned AM process that produces near-net-shape parts with good mechanical properties, good surface finish appearance and complex geometries. The high degree of freedom that L-PBF technology offers allows the creation of objects with unprecedent geometries and internal structures. This, when associated with topology optimization, allows for truly revolutionary design, that would otherwise be impossible before, being ideal for the fabrication of multifaceted parts with higher density of up to 99.9% by melting or sintering of metallic powder by high-powder-density lasers. (Gibson, Rosen, Stucker, & Khorasani, 5 - Powder Bed Fusion, 2021) (Schleifenbaum, 2023) (Laser Powder Bed Fusion, 2024). Such example of a machine can be seen in figure 6.

L-PBF processes were among the first commercialized additive manufacturing processes to be created, with SLS (selective laser sintering), a derivative of PBF technology, being created at the University of Austin, Texas, in 1986, with sponsorship made by the US government's Defense Advanced Research Projects Agency (DARPA), through the novel idea of fusing powder particles using a directed energy beam (SLS Inventor of the Year, 2015) (History of Selective Laser Sintering, 2023) .



Figure 6 - Renishaw RenAM 500Q (Renishaw AM 500Q, 2024).

The SLS method of powder particles fusion was initially only used for plastics however, with metal PBF only being partly achieved with the creation of Direct Metal Laser Sintering (DMLS) in 1994 by EOS GmbH, when they adapted their machine technology of SLS production so they could print metal parts from two component metal powders in a process of liquid phase sintering, with the possibility of melting now copper or bronze around steel particles. In the 1990s, high energy fibre laser experiments and research was being developed worldwide so as to melt one component metal alloys directly, with Fockele & Schwarze introducing the first SLM machine in 1999, finally making it possible for a complete metal PBF manufacturing procedure. Very soon after, Concept laser, EOS and Trumpf soon followed with their own laser-based particle alloy melting, with the creation of LaserCUSING, DMLS, and PBF respectively (Huckstepp, 2019) (Metal Additive Manufacturing History, 2024).

Some of the main corporations that work with this technology are Renishaw, SLM solutions, EOS, DMG Mori, Concept laser, TRUMPF, Sisma, 3D Systems, 3D4MEC, among others, with some of these having close partnerships with some of the most advanced R&D institutes around the world, such as the Fraunhofer ILT, the Massachusetts Institute of Technology, and the before mentioned US Government's DARPA. All of the early adopters of this systems still exist today, although some have been rebranded or bought, such as 3D Systems completing acquisition of DTM in 2001, and Concept Laser being bought by General Electric in 2016. Such examples can be seen in figure 7. (Squillace, 2023) (Sefene, 2022) (Metal Additive Manufacturing History, 2024) (Digital Alloys' Guide to Metal Additive Manufacturing, 2020).

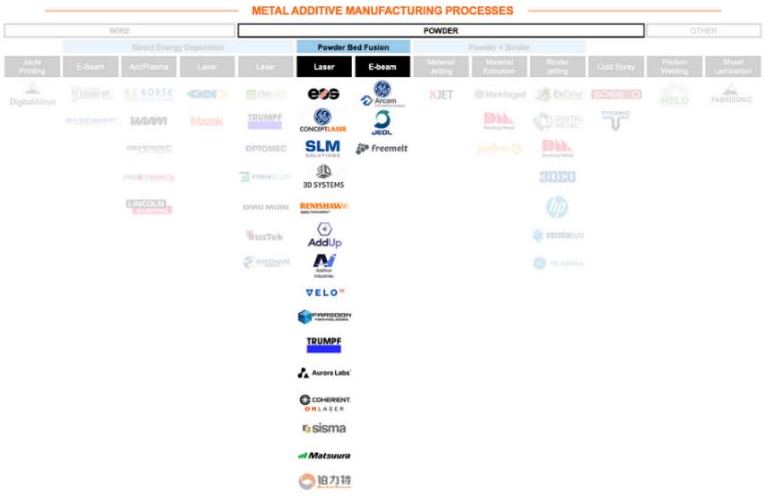


Figure 7 - Various international corporations serving the L-PBF market (Digital Alloys' Guide to Metal Additive Manufacturing, 2020).

2.1.3.1. Process Steps

There are several steps executed in a regular manufacturing procedure of this technology. The PBF process fuses normally thin layers of powder (normally between 0.075–0.1mm thick) which have been spread across the build area through the use of a counter-rotating powder levelling roller. The building process takes place inside an enclosed chamber filled with an inert gas for oxidation minimization and to prevent degradation of the powder material. Schematic is shown in figure 8 and 9 (Gibson, Rosen, Stucker, & Khorasani, 5 - Powder Bed Fusion, 2021).

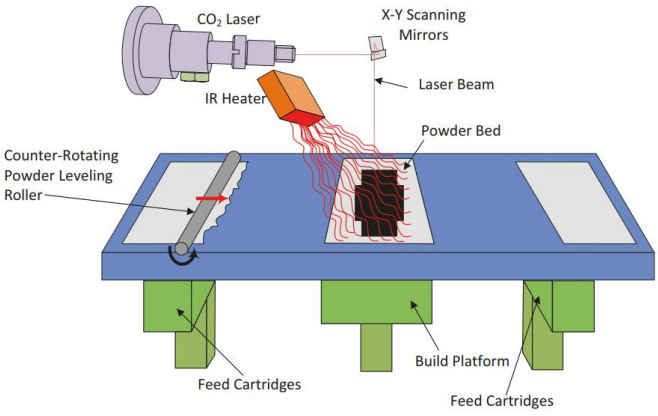


Figure 8 - L-PBF process schematic (Squillace, 2023).

Regarding the atmosphere's thermal characteristics, the powder is maintained at an elevated temperature below its melting point, but high enough for a preheating of its particles. Heaters are placed close to the platform in order to maintain a consistent high temperature in the part being formed and above the related feed platforms, so as to preheat

the powder prior to spreading, with cases where even the build platform is heated through the use of resistive heaters. Such stringent thermal requirements are necessary for minimization of the laser power requirements (since less laser energy is required for fusion, with application of effective preheating), and to prevent warping of the part during the build due to non-uniform thermal expansion and contraction (resulting in curling) (Gibson, Rosen, Stucker, & Khorasani, 5 - Powder Bed Fusion, 2021) (Schleifenbaum, 2023) (Squillace, 2023).

A focused laser beam is directed onto the powder and is moved through the use of galvanometers, thermally fusing the material to form the slice cross-section. After the completion of a layer, the build platform is lowered by one layer thickness, with a fresh new layer being laid and levelled using the counter-rotating roller. The beam then proceeds to scan the subsequent slice cross-section. This process repeats as many times as necessary until there is the full manufacture of the designated model (Gibson, Rosen, Stucker, & Khorasani, 5 - Powder Bed Fusion, 2021) (Schleifenbaum, 2023) (Squillace, 2023).

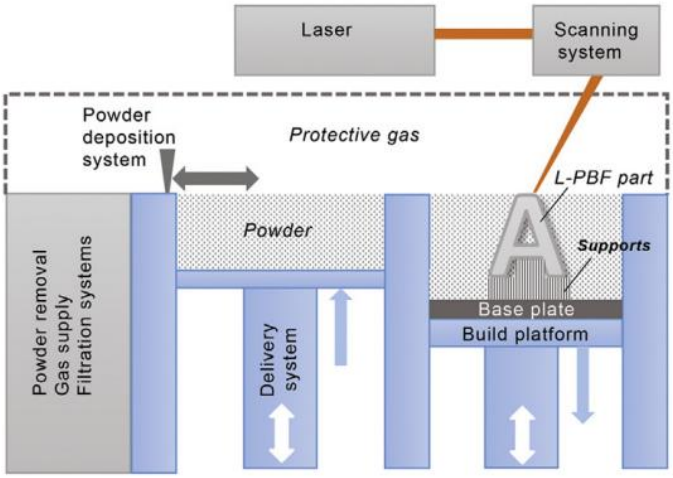


Figure 9 - Alternative L-PBF process schematic (Yadroitsev, Yadroitsava, MacDonald, & Plessis, 2021).

Although in polymers, the surrounding non-sintered powder remains loose and supports itself the subsequent layers (eliminating therefore the need for structural support), this is not true for metals, due to their higher weight and density, being such supports necessary when there is less than 45º of angle between the parts being built.

As a general rule, there is a requirement for a cool down period to allow the parts to cool to a temperature safe enough, not only for handling, but also for safe exposure to room temperature and atmosphere. If such cases are not respected and properly executed, there is a risk of industrial accidents, injuries regarding industrial personnel, degradation of the powder with presence with oxygen, catastrophic warp due to uneven thermal contraction, and others.

Finally, after all the process is completed, the loose powder is cleaned off the parts and there is further post-processing, when necessary, of the parts, with unfused powder being unused and (normally) reutilized, with possible purification (Squillace, 2023) (Sefene, 2022).

2.1.3.2. Subprocesses & variations

i) SLM vs DMLS vs LaserCUSING vs LMF

Scientific, as well as popular literature may use different nomenclatures for the L-PBF process, with the most well-known different terms being selective laser melting (SLM), direct metal laser melting (DMLS), LaserCUSING, and laser metal fusion (LMF) (Schleifenbaum, 2023).

These are regarded as different printing techniques of the same technical process, with different commercial names for what amounts to the same manufacturing technology – Additive Manufacturing of metal parts by fusion of a powder material through utilization of laser technology - having minimal variations between them, with differences only in very specific parameters. The development of this technology was made through different corporations and R&D firms, with sometimes very similar technological sophistication and expertise, with on-going efforts to capitalize on this emerging technological market while, at the same time, doing their best not to break patent infringement laws (Gibson, Rosen, Stucker, & Khorasani, 5 - Powder Bed Fusion, 2021) (Schleifenbaum, 2023) (Squillace, 2023).

As said before, the technologies are very similar fundamentally, changing only in certain parameters, such as the heating up of the particles until liquid phase sintering, instead of full melting, as an example. In figure 10 is shown the classification according to the german VDI standard.

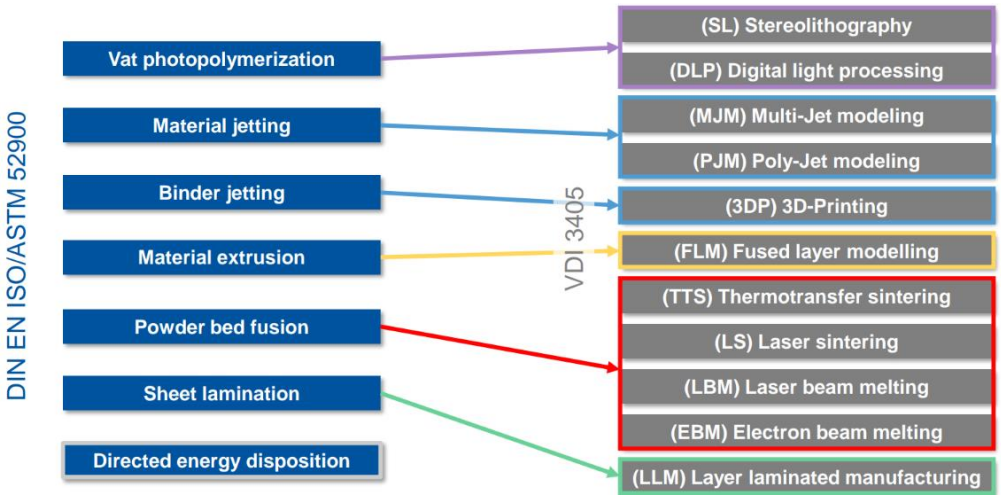


Figure 10 - Classification of AM-processes regarding DIN EN ISO/ASTM 52900 and VDI 3405. Of note that, according to the German VDI standard, Powder Bed Fusion encompasses a myriad of specific technological processes (Schleifenbaum, 2023).

It is worth nothing that there has been several advances in the last 20 years, with advancements becoming exponential in the last 10 years, in this field of metal additive

manufacturing, due to a myriad of factors such as, but not only: increasing knowledge of software systems, materials knowledge, laser technology and respective thermal processes involved, the emphasis of the Western World in adopting this myriad of technologies, so as to increase the versatility and complexity of its manufacturing processes, and the termination of patent laws protecting the corporations that developed them and had exclusive rights for them. The reasons for this growth are quite interesting and will be developed further in the relevant market and research sections.

Despite the relative low time of existence of L-PBF technology, with the EOSINT M160 DMLS machine being launched by EOS in 1994, and a basic ILT SLM patent being developed in 1997, just less than 30 years ago, this technology has come a long way, with possibilities nowadays of up to 4 lasers being able to create one part and build up areas of 800mm in length (Squillace, 2023) (Powder Bed Fusion, 2023) (Hybrid metal additive manufacturing: A state–of–the-art review, 2021).

ii) L-PBF vs EB-PBF

In the powder bed fusion process, there is a clear separation between laser-based powder bed fusion process (L-PBF or PBF-LB) and electron beam powder bed fusion (EB-PBF, PBF-EB or EBM). Although L-PBF is the main focus of this work, it is worth mentioning this variant and its overall differences.

While both processes utilize the principle of conversion of kinetic energy into thermal energy, the specific energy source is different in these processes, with L-PBF utilizing a focused beam of photons, while EB-PBF makes use of a focused beam of electrons. Both of these processes can be utilized for manufacturing of complex prototypes and for end-use metal parts with good resolution, reduced material wastage, and efficient recycling of the unmelted powder. Overall differences in design can be seen in figure 11 and material usage differences can be seen in table 1.

L-PBF is one of the oldest MAM processes, started being developed in 1986, and is a very mature MAM process, with extensive amounts of literature focused on the result of the final properties of the built parts made from an extensive choice of build parameters and an extensive range of metal alloys. In the L-PBF case, reflective mirrors are used to move the laser according to a specified and predefined two-dimensional scanning path, normally enclosed in atmospheres of argon or nitrogen, depending on the reactivity of the material being used. (Gibson, Rosen, Stucker, & Khorasani, 5 - Powder Bed Fusion, 2021) (Hybrid metal additive manufacturing: A state–of–the-art review, 2021)

The widespread use of this manufacturing technique, allied with the continuous improvement of various competing corporations and conglomerates, allows deposition

rates of up to 0.1 kg/h, and with surface roughness around 10–20 μm. (Campbell, Diegel, Kowen, & Wohlers, 2017).

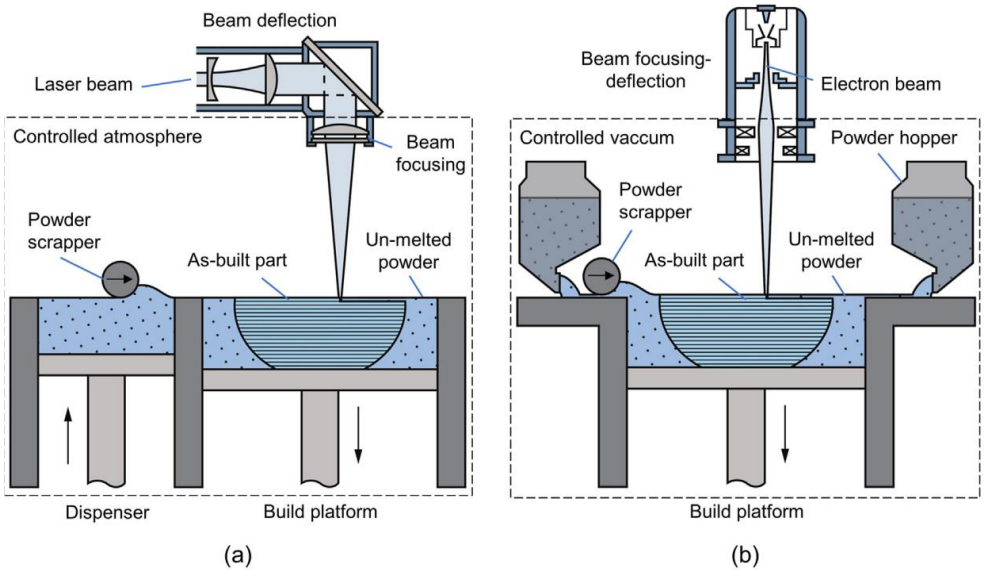


Figure 11 - L-PBF (a) vs EB-PBF (b) (Hybrid metal additive manufacturing: A state–of–the-art review, 2021).

Table 1 - Materials selection of both processes (Huckstepp, 2019) (Gibson, Rosen, Stucker, & Khorasani, 5 - Powder Bed Fusion, 2021).

Material	L-PBF	EB-PBF
Titanium (Ti6AL4V, grades 2, 5)	X	X
Titanium Aluminide		X
Cobalt Chrome (CoCr, CoCrMo, CoCrW)	X	X
Tool Steel (Maraging)	X	
Stainless Steel (316L)	X	
Inconel (625, 718, HX)	X	X
Aluminium (AlSi10Mg)	X	
Copper (CuSn10, Bronze)	X	X
Tungsten	X	
Precious Metals (Gold, Silver, Platinum)	X	

The EB-PBF process, meanwhile, was only developed in 2002 by ARCAM in Sweden, with the change in the source of thermal energy being accompanied by other key modifications to the equipment, so as to allow its production under controlled vacuum conditions, being therefore deflected through electromagnetic lenses, instead of mirrors. Of note that there is obligation of feedstock preheating to around 50% to 60% of its melting temperature, so as to avoid the effect of electrostatic charging, which can create unintended spread of the powder, also known as "Powder Push-away Phenomenon". (Murr, et al., 2012)Maximum deposition rates of EB-PBF are superior to L-PBF and are capable of reaching values up to 0.2 kg/h, double that of L-PBF, with surface roughness in 15-30 µm.

The EB-PBF process is not as common or widespread as the L-PBF process, in both scientific research and industrial production applications, however this electron-derived technology has been instrumental in the processing of materials that are difficult to handle, such as cobalt and nickel alloys, titanium aluminide, and niobium, to name a few, which are easier to process through this technology (cobalt and nickel alloys), if not the only possible in some cases (such as aluminide) (Huckstepp, 2019) (Gibson, Rosen, Stucker, & Khorasani, 5 - Powder Bed Fusion, 2021).

iii) Hybrid possibilities of L-PBF

Hybrid CNC-AM processes has the benefits of being fully automated, having very high surface quality and increased productivity due to the deep integration possible in Metal Additive Manufacturing, while coming with the drawbacks of being suitable only for metal parts, a higher waste production, increased investment costs, and the conditional of physical access into the parts being dictated by tool dimensions. (Schneck, et al., 2021) (AM 101: Hybrid Manufacturing, 2019) (Hybrid metal additive manufacturing: A state–of–the-art review, 2021). Typical machining operation can be seen in figure 12.

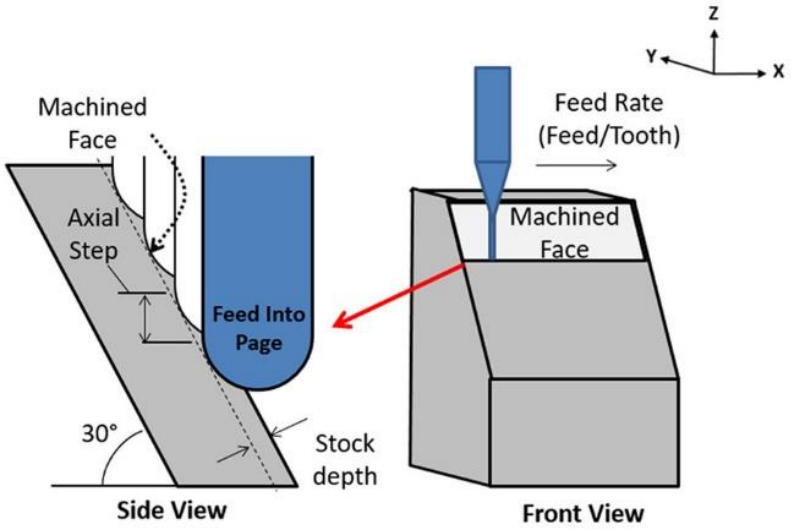


Figure 12 - Typical machining operation of hybrid L-PBF (Afazov, et al., 2021).

Hybrid L-PBF machines already exist on the current market, with examples such as the Matsuura LUMEX Avance-25, which typically deposits ten 50 µm layers before calling the machining operation. These can be seen in figure 13.

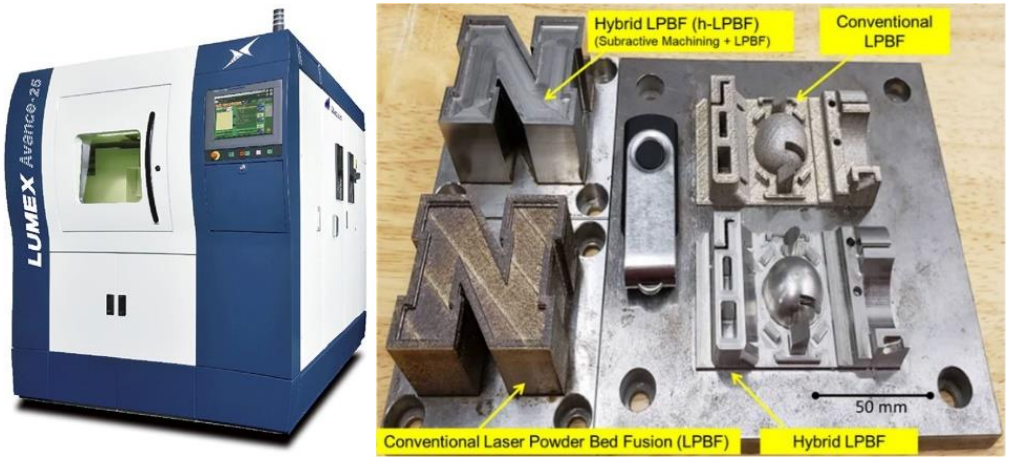


Figure 13 - Matsuura LUMEX Avance-25 hybrid L-PBF and its effects (LUMEX Avance-25, 2018) (Riensche, et al., 2022).

In 2021, the University of Sheffield utilized a hybrid L-PBF machine with micro-milling for increased versatility with the possibility of machining of internal surfaces, and the elimination of a refixing time between the AM and the milling part, with the limitation that combining L-PBF and micro-milling into a single system also increases complexity and generates more challenges and limitations - lubricants and coolant technologies cannot be applied during milling due to the surrounding powder and the possibility of contamination.

Of note that the design of the component must consider all aspects of the hybrid process and not just AM design rules, overhangs and sloped features, but also how supports could influence the access of the machining tool. Despite the challenges, the research concluded that the hybrid LPBF model allows the reduction of distortion by 60% in industrial manufacturing (Afazov, et al., 2021) .

In 2023, The European Society for Precision Engineering and Nanotechnology and the American Society for Precision Engineering developed a hybrid L-PBF process carried out on a pre-machined functional base. The main challenge was the calibration between both processes, with recommendations for further investigation into accuracy parameters and development, so as to minimize this factor, and reaching sufficient quality of the critical interface zone between the conventionally manufactured base and the L-PBF part (Metelkova J. , Paggi, Marco, & Sinico, 2023).

iv) Low-cost alternatives

As an example of integration with small-medium companies and attempts of minimizing cost of entry into industry, the Fraunhofer Institute of Production Technology created in 2019, through its spin-off company Laser Melting Innovations, the Alpha 140, a low-cost L-PBF industrial machine, costing around 100.000 €, in order to minimize entry costs for the market and to increase attraction to SMEs. The machine is shown in figure 14.



Figure 14 - LMI Alpha 140 unit (left) and inert gas and axis system (right) (Kurtz Ersa Alpha 140, 2021).

"The innovative system works in an argon/nitrogen inert gas environment and uses an air-cooled, fibre-coupled 200W diode laser with a wavelength of 915nm and a focus diameter of 140µm" (Fraunhofer ILT spin-off, 2019) (Kurtz Ersa Alpha 140, 2021).

2.1.3.3. Laser-Powder Mechanisms

The mechanism of manufacturing through powder bed fusion occurs through heat input to the powder material, by fusion of its particles. This process has variations on its method, being most commonly made through two different processes: "melting" and "sintering". Main primary mechanisms are shown in figure 15.

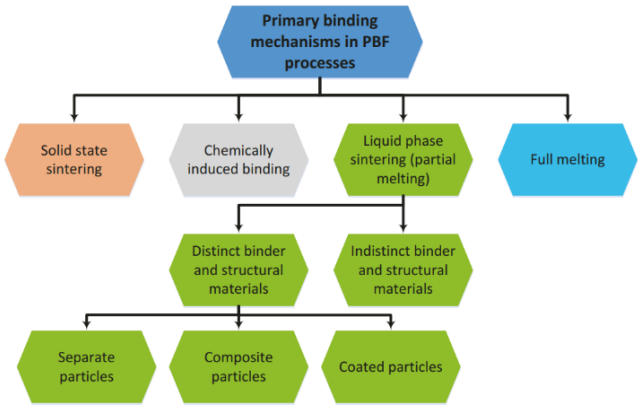


Figure 15 - Primary binding mechanisms in PBF processes (Gibson, Rosen, Stucker, & Khorasani, 5 - Powder Bed Fusion, 2021).

The use of a single word to describe powder fusion is inherently problematic as multiple mechanisms are possible, existing therefore four different fusion mechanisms which are present in PBF processes, which are: solid-state sintering, liquid-phase sintering, chemical-induced binding, and full melting. This last one tends to be the preferred one due to increased density of parts, and better mechanical properties achieved (Gibson, Rosen, Stucker, & Khorasani, 5 - Powder Bed Fusion, 2021) (Squillace, 2023).

More in-depth differences between the various mechanisms are shown in Annex B.

2.1.3.4. Laser Types

The category of laser used in the L-PBF machines are fundamental for the definition of the parameters of this technology manufacturing process, with the main laser types being the CO_2 (Carbon Dioxide) laser, the Nd:YAG (Neodymium-doped Yttrium Aluminium Garnet) laser, and the Yb (Ytterbium) fibre laser. The differences are shown in table 2.

Table 2 – Types of lasers used in MAM and their properties (Lee, et al., 2017) (Cobbinah, Nzeukou, Onawale, & Matizamhuka, 2021) (Santos, Shiomi, Osakada, & Laoui, 2005).

Property	CO2 Laser	Nd:YAG Laser	Yb-fiber laser
Wavelength (nm)	9400 / 10600	1060	1070
Efficiency (%)	5-20	10-20	10-30
Maximum Power Output (kW)	20	16	10
Pump Source	Electrical discharge	Flashlamp / laser diode	Laser diode
Operation Mode	CW / PW	CW / PW	CW / PW
Beam quality (mm.mrad)	3-5	0.4-20	0.3-4
Fiber delivery	Not possible	Possible	Possible
Maintenance period (hours)	2.000	10.000	25.000
Pulse duration	100s ns - 10s ms	1s ns – 10s ms	10s ns – 10s ms

CW - continuous wave
PW - pulsed wave
Ns - nanoseconds
Ms - milliseconds

The main difference is the wavelength used with such systems - with CO2 being around 10600nm, Nd:YAG around 1060nm, and Yb-fibre around 1070nm – and the transmission methods used – with CO2 using articulated mirror delivery assemblies, while Nd:YAG and Yb-fibre lasers are capable of transmitting light through optical fibre cables. This possibility of fibre cables is due to the shorter wavelength, meaning these last two can be guided with the laser source remotely from the L-PBF workstation. Additionally, the shorter wavelength is paramount to MAM since the absorptivity of most metals and MMCs increase inversely with laser wavelength (Lee, et al., 2017) (Cobbinah, Nzeukou, Onawale, & Matizamhuka, 2021).

Historically, CO2 and Nd:YAG lasers were the most common and ancient ones used, with recent advances in optomechanical and solid-state laser technology introducing the usage of Yb-fibre lasers. It is estimated that the energy efficiency of the L-PBF process will improve with advances in laser technology, with an increased use of Ytterbium (Yb) lasers as substitutes for Nd:YAG lasers, due to increased efficiency (Majumdar & Manna, 2012) (Olakanmi, Cochrane, & Dalgarno, 2015) (Lee, et al., 2017) (Cobbinah, Nzeukou, Onawale, & Matizamhuka, 2021).

Comparing to the CO2 lasers, both the Nd:YAG and the Yb-fibre lasers operate at lower scanning speed, due to the reduced interaction between beam, plasma and powder beds, which means a possibility of increasing the powder bed layer thickness to be melted. L-PBF processing with a Yb-fibre laser beam, in particular, yields a more stable and slightly larger scan track when comparing with CO2 laser beam, providing the ability to scan large tracks while maintaining the L-PBF build quality and speed, culminating in scan tracks with more uniformity and with less porosity (Majumdar & Manna, 2012) (Olakanmi, Cochrane, & Dalgarno, 2015) (Cobbinah, Nzeukou, Onawale, & Matizamhuka, 2021).

Comparing the Ytterbium doped fibre lasers to the Nd:YAG lasers, the first ones tend to have larger absorption bandwidth, longer maintenance lifecycles, and increased efficiency by the fact that they allow the ability to scan larger tracks while maintaining traditional speed and build quality, allowing very little porosity (Lee, et al., 2017) (Cobbinah, Nzeukou, Onawale, & Matizamhuka, 2021).

Although the optical fibres allow a myriad of advantages, they can also limit the performance of the laser, with the occurrence of fibre bending, vibrations, and temperature variations leading to alterations in polarization that can influence the laser output. This last topic is the reason why polarization maintaining optical fibres are suggested for current operations due to the improved environmental sustainability (although at a higher cost) (Olakanmi, Cochrane, & Dalgarno, 2015) (Lee, et al., 2017) (Cobbinah, Nzeukou, Onawale, & Matizamhuka, 2021).

2.1.3.5. Processing parameters

The usage of optimal processing parameters is crucial for the effective production of parts using the L-PBF process, with a broad field of manipulation possible, although it can be separated in 4 main categories: laser-related parameters, scan-related parameters, powder-related parameters, and temperature-related parameters. These are shown in table 3.

These parameter categories are mutually interacting and can be quite interdependent, with, as an example, the laser power increasing with an increase in the melting point of the powder bed material, and a decrease in the powder bed temperature, and varying with

the material's absorptivity characteristics, which, in turn, can be influenced by the material type, and the powder shape, size and packing density (Gibson, Rosen, Stucker, & Khorasani, 5 - Powder Bed Fusion, 2021) (Sefene, 2022).

Table 3 - Parameters of L-PBF manufacturing
(Oliveira, LaLonde, & Ma, 2020) (Gibson, Rosen, Stucker, & Khorasani, 16 - Post-Processing, 2021) (Squillace, 2023).

Category	Type	Specification
Laser	Thermal	laser power, spot size, pulse duration, pulse frequency, etc
	Electrical	
Powder	Material	particle shape, size and distribution, powder bed density, layer thickness, material properties, etc
	Metallurgical	
	Mechanical	
Scan	Electrical	powder bed temperature, powder feeder temperature, temperature uniformity, etc
Temperature	Thermal	
	Mechanical	

A more in-depth visualization of the different parameters is shown in Annex C.

2.1.3.6. Thermal relations

The melt pool formation and characteristics are primarily determined by the total amount of applied energy that is absorbed by the powder bed, when subjected to the laser beam interaction. It is worthy of note that energy input is different from the absorbed energy, as the first one is related to both the power, the speed of translation and the area of the heat source (such as the diameter of the beam), while the absorbed energy is a function of the heat source power, heat source speed, the diameter of the beam, the layer thickness, hatch distance, the absorptivity of the material, the thermophysical properties of the material, among others (Gibson, Rosen, Stucker, & Khorasani, 5 - Powder Bed Fusion, 2021).

More information regarding this part is shown in Annex D.

2.1.3.7. Advantages of L-PBF

Since L-PBF is a MAM technology, the latter ability of economic viability of creation of complex designs at comparatively low production volumes, and the low investment in infrastructure needed, also apply directly to L-PBF (Gibson, Rosen, Stucker, & Khorasani, 5 - Powder Bed Fusion, 2021).

This technology allows high production efficiency, especially regarding complex parts in small to medium production runs. The ability to consolidate multiple components into a single, integrated one has the effect of reducing assembling time and simplifying logistical chains, leading to reduced time of manufacturing, potential cost saving, and faster market application (Prima Additive L-PBF Benefits, 2023) (Kingsbury UK L-PBF Benefits, 2024).

Powder bed fusion allows the possibility of reduced material stage, by building up the part layer by layer, meaning it eliminates most of the waste associated with more conventional techniques, such as subtractive manufacturing. Although PBF manufacturing is considered slow, when compared with more conventional techniques, it allows increased versatility in the iterative process, with a complete part being able to be designed, manufactured, tested, re-designed and iteratively printed again in less effective time than the same process through metal injection molding or casting. This flexibility is paramount to innovative product development, with easy modifications to the products to be manufactured without heavy delays in time, capital, or simple infrastructure reinstallation (Prima Additive L-PBF Benefits, 2023) (Kingsbury UK L-PBF Benefits, 2024).

Regarding support structures, PBF requires very little support whilst printing of the part itself, due to the usage of unused powder for this end, meaning ease of creation of complex internal structures, such as cooling tunnels inside turbine blades, since excess powder can simply be poured out of these internal volumes. As mentioned previously, in metals, there is necessity of non-powdered support structures when the angle is less than 45º. In contrast to most other AM processes, L-PBF has a wide range of materials available for usage. As a general rule, if a metal can be welded, it can also be used through this technological process (Gibson, Rosen, Stucker, & Khorasani, 5 - Powder Bed Fusion, 2021) .

a) Generative design

The increased application of MAM processes translates into more developed practices for better usage of this technology, with techniques such as (generative) design for additive manufacturing being used for further weight reductions, less build jobs/assemblies, and reduced cycle times of manufacturing. Some of the practices in use for dfAM are shown in figure 16 (16 - AM for automotive industry, 2021).

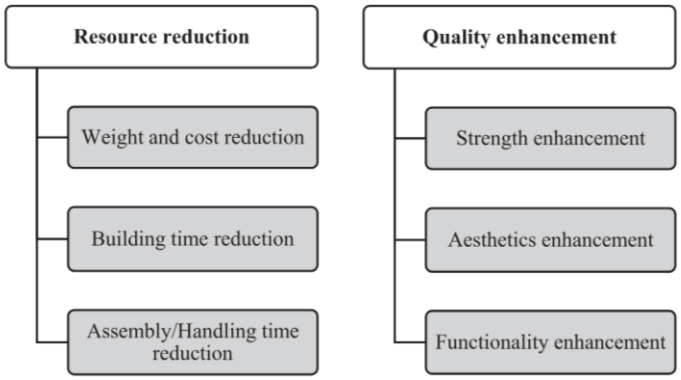


Figure 16 - Best practices for dfAM (16 - AM for automotive industry, 2021).

Such techniques are used extensively where mechanical performance must meet harsh operational conditions and the necessity of lightweight design, with focus on resource reduction requirements (raw material and time), as well as quality enhancement of the functionality of the system, through preliminary studies and process monitoring (16 - AM for automotive industry, 2021).

b) Topological optimization

Techniques such as topological optimization are crucial for better design parameters of MAM, with possibility of obtaining optimal structure configuration through a reasonable material distribution, satisfying specific load conditions, performance, and constraints. The topological optimization process is shown in figure 17.

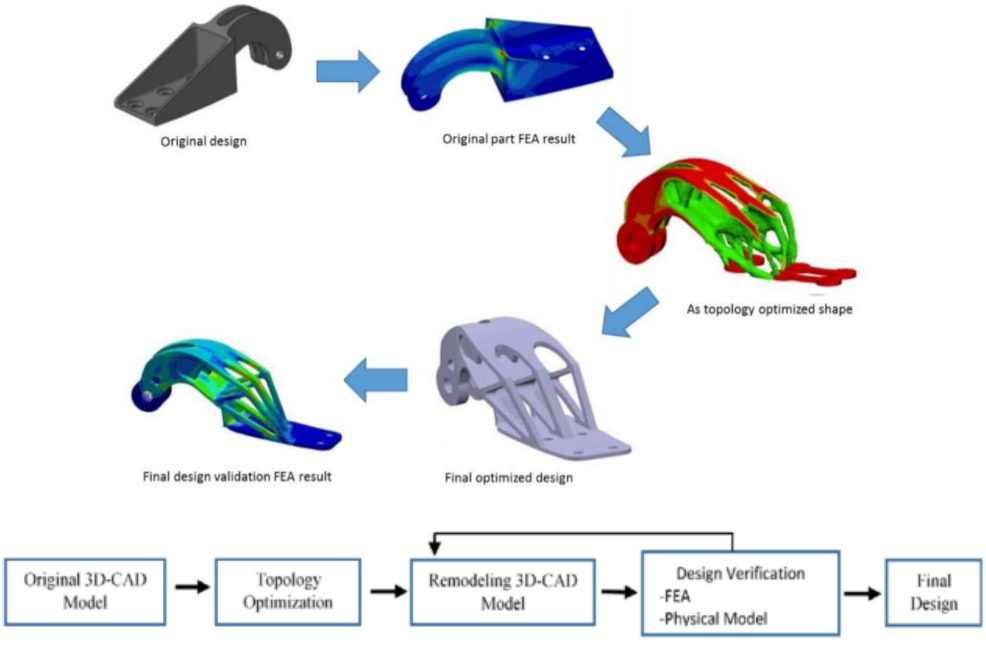


Figure 17 - Topological optimization process (Gebisa & Lemu, 2017).

Without necessitating for a diverse range of moulds or tools or any other complicated procedures, such technology can save significant investment regarding costs of production and cycle times, shortening the time-to-build. This translates into an effective approach for MAM designing, by utilizing what amount to a lightweight solution, whilst maintaining structural integrity of critical parts. An example is shown in figure 18 (Zhu, et al., 2021) (Prathyusha & Babu, 2022).

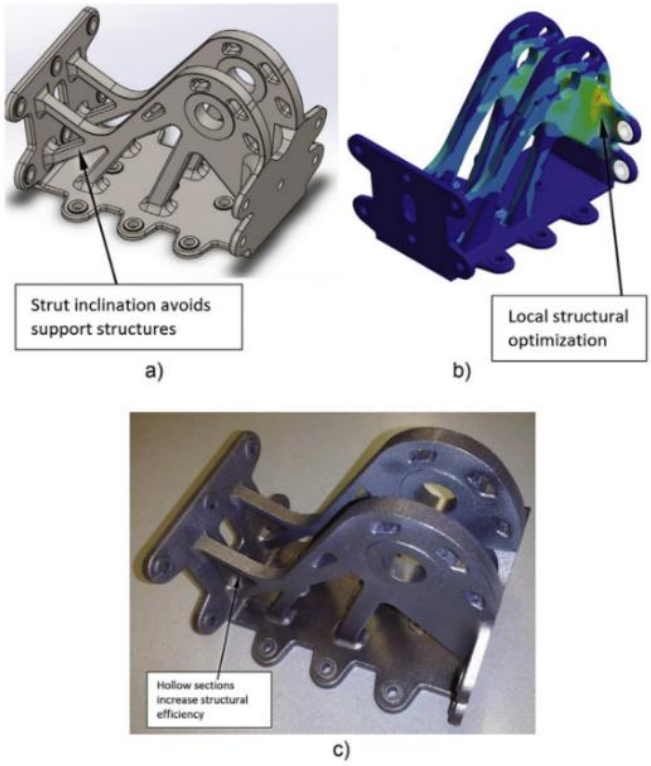


Figure 18 - High value aerospace bracketry: (a) topological optimization design: (b) parametric optimization of design details; (c) implementation of AlSi10Mg component (Yadroitsev, Yadroitsava, MacDonald, & Plessis, 2021).

This technique of iterative finite element analysis has been deeply appreciated in L-PBF design, and especially in the aerospace industry, as it manages to remove weight in this industrial field, ever so concerned with better thrust-to-weight ratios for improved performance of aeronautical and space vehicles, with the added benefits of improved buy-to-fly ratios. Therefore, it allows to minimize the amount of used material and strain of structures while maintaining the necessary mechanical strength, being excellent for synergistically combining itself with L-PBF (Zhu, et al., 2021) (Prathyusha & Babu, 2022).

2.1.3.8. Limitations of L-PBF

Although a promising technology, there are a myriad of limitations inherent to this manufacturing process. These can be divided into two categories: the disadvantages of the process, with an overview of the various drawbacks this technology offers against others; and manufacturing defects, with an overview of the most common defects and its effects on the parts for design.

Regarding the first, one of the most impactful disadvantages is the relatively high time necessary for direct production, with small parts taking hours for total manufacturing due the numerous layers needing to be sintered, which makes it less competitive against faster, high-developed methods such as injection molding. Although there is the possibility of design of intricate parts, it comes at a cost of smaller layers to manufacture, translating in

increased production time cycles. Meanwhile, surface quality and integrity of the printed part is heavily reliant in the powder material used, especially when discussing parameters such as grain size, purity, composition, and quality, and also thermal management of the laser-powder interactions (Squillace, 2023).

There is the frequent necessity for post-processing due to a typically semi-finished products, which need further processing in parameters such as rugosity, finishing, geometrical holes, etc, therefore finish machining operations are normally required to guarantee part assembly and the necessary surface quality. L-PBF suffers from certain drawbacks concerning reliability of repeated results and consistent quality in terms of dimensional accuracy, surface roughness and strength of the part (Dejene & Lemu, 2023).

Regarding manufacturing defects, one of the most common ones is related to porosity properties, which promotes cracking due to the so-called “notch effect”, with pores being able to develop over time due to the entrained gas, the chemical reactions, and supersaturated gases that were dissolved, creating air in the melt pool (Dejene & Lemu, 2023).

High residual stresses also are one of the most impactful phenomena that hinder the adoption of this technology into the industry, even 40 years after original creation. The stress is created through the significant thermal gradients formed by the laser system when melting the part, with the stresses created “freezing” upon solidification, as the part cools with the environment. Some of the effects are the overall presence of thermal stress cracking phenomena, which, and this is mostly significant, are impossible to correct with post processing. Shrinkage is also quite fundamental, causing a lack of dimensional accuracy and instability in geometrical constraints (Gibson, Rosen, Stucker, & Khorasani, 16 - Post-Processing, 2021) (Squillace, 2023).

Balling is a common defect in L-PBF manufacturing, whereas when surface tension forces overcome the combinations of adhesion, gravitational and dynamic fluid forces, the molten metal will have tendency to form a ball, with the effect being much more pronounced in metal powder manufacture, due to the greater surface energy that drives the material to limit the surface area to volume ratio (meaning, a tendency to form a sphere or ball). Such balling effect will possibly create broken tracks in the material, translating into reduced quality, consistency and density of parts (Gibson, Rosen, Stucker, & Khorasani, 16 - Post-Processing, 2021) (Squillace, 2023).

Dangers inherent to the industrials setting are also worth mentioning, as is shown in the table 4 below, with the associated type and details.

Table 4 - Main hazards of PBF machines
(Ferraro, Pirozzi, Annacondia, & Donato, 2019) (Gibson, Rosen, Stucker, & Khorasani, 16 - Post-Processing, 2021).

Type	Origin	Details
Mechanical	Moving elements	Powder levelling device
	Sharp edged surfaces, corners, rough surfaces	Overall industrial design
	Fall or projection of objects	Construction plates, gas equipment, powder cases
Electrical	Electromagnetic phenomena	Electrical circuits/devices
	Electrostatic phenomena	Produced by powder flowing, charge accumulation in powder
	Electrified parts	Internal circuits in maintenance, broken cables
Thermal	Hot surfaces	Heat in the unit / built part before extraction
Radiation	Optical radiation	Laser beams
Material	Powder	Micropowder, flammable/reactive materials, inert gases

2.1.3.9. Post-processing

The quality of the final part of the L-PBF product is determined by some characteristics such as microstructure, porosity, residual stresses, surface roughness and dimensional/geometrical accuracy. While the parts built by PBF systems may not meet all product requirements, post-processing operations can bridge the gap to achieve such criteria, with operations such as support material removal, surface texture improvements, accuracy improvements, aesthetic upgrades and property enhancements using a myriad of techniques. It is estimated that final finishing operations can absorb as much as 15% of total manufacturing costs, being one of the most labour intensive and uncontrollable areas of manufacturing (Rhoades, 1991).

One specific disadvantage of PBF systems is the relatively high surface roughness that comes with its built parts, as an example. In such cases, mechanical post-processing is widely used so as to counteract such flaws. The challenge therefore is to identify the methods for post-processing and get the best possible results from the point of view of the

surface roughness parameter. In order to achieve the desired microstructure, relieve residual stresses, and reduce porosity, appropriate heat treatments might be required. Post-processing may require the following steps: heat treatment to relieve residual stresses, annealing (argon or vacuum atmosphere), hot isostatic pressing, grit blasting, base plate removal, support removal, ultrasonic cleaning machining and polishing, among others (Gibson, Rosen, Stucker, & Khorasani, 5 - Powder Bed Fusion, 2021) (Gibson, Rosen, Stucker, & Khorasani, 16 - Post-Processing, 2021) (Squillace, 2023).

i) Support material removal

In MAM processes, there is the necessity of removal and separation of build material from the surrounding material before its use, in the situation where the part is fully enclosed by it. PBF processes are not the exception, requiring removal of the part from the loose powder surrounding it. (Gibson, Rosen, Stucker, & Khorasani, 16 - Post-Processing, 2021).

After the part being built, it is normally required to allow the part to go through a stage of cool-down, with the part remaining enclosed inside the powder for distortion minimization due to non-uniform cooling. The cool-down phase is dependent on several parameters, such as build material and size of the part in question. Once the cool-down phase is completed, there are several methods used to remove the required part from the surrounding structure. (Gibson, Rosen, Stucker, & Khorasani, 16 - Post-Processing, 2021).

Typically, the entire build part (the demanded build, the fused support parts, and the loose powders) are removed from the machine as a block and transported to a “breakout” station, where the parts are removed manually from the surrounding powdered material. Brushes, compressed air systems, and light head blasting are common methods for removal of loose powders, while tools similar to wood-working or dental cleaning tools are used for removal of the sintered powder structures used for support of the desired product (Gibson, Rosen, Stucker, & Khorasani, 16 - Post-Processing, 2021).

Internal cavities and hollow spaces might be quite difficult to achieve an effective cleaning, with solutions being developed as integration of loose powder cleaning systems unto the MAM manufacturing units, such as is the case in MTT SLM machines, or the Solukon SFM-AT800, as can be seen in figure 19 (Gibson, Rosen, Stucker, & Khorasani, 5 - Powder Bed Fusion, 2021).

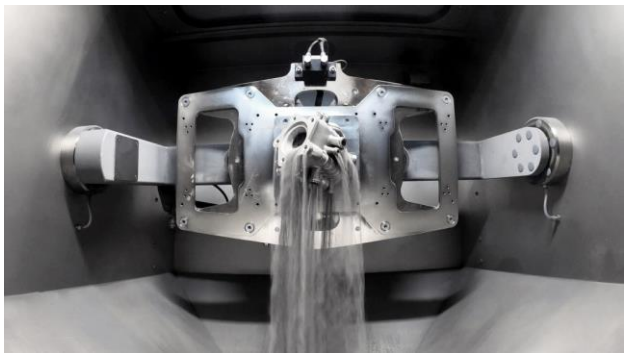


Figure 19 - Automated powder removal system in a Solukon SFM-AT800 (Kowen, 2019).

When discussing fused support parts, these metal supports are generally too strong to be removed by hand, necessitating the use of milling, bandsaws, cut-off blades, wire-EDM, and other diversified metal cutting techniques. An example of a dental frame before and after support removal is shown in figure 20.

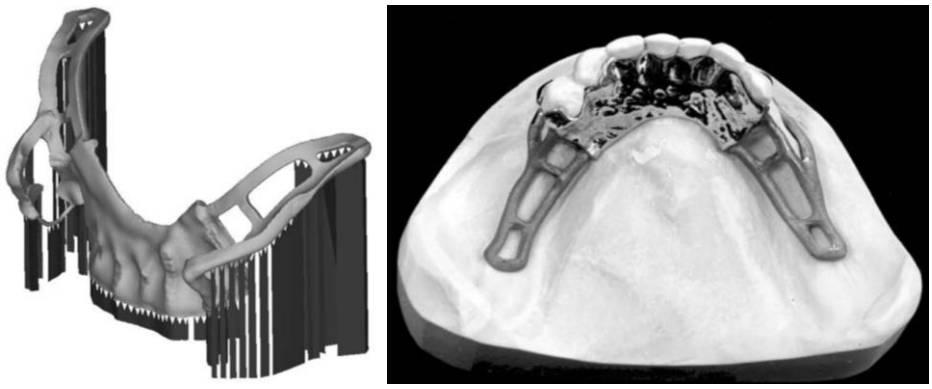


Figure 20 - Dental frame before (left) and after (right) post-processing support removal (Bibb, Eggbeer, & Williams, 2006).

Support generation and removal are significantly affected by the orientation of a part, particularly when relating to the primary build axis. If, as an example, a thin part is laid flat, it might consume an exceedingly high amount of powder just for support of its structural integrity. At the same time, the orientation of the support also affects the surface finish of the part, by leaving "witness marks" where the supports were attached (such as small bumps or divots). There is the possibility of small fragile features being broken if using supports in such regions and proceeding thereafter to its removal (Gibson, Rosen, Stucker, & Khorasani, 5 - Powder Bed Fusion, 2021).

ii) Surface texture improvements

There are common features related to surface textures that may need to be modified due to aesthetic preferences or actual performance reasons, with some examples being: stair-steps creation, powder adhesion, fill-patterns from the laser system, and witness marks from support material removal.

Stair-stepping is a fundamental, intrinsic issue to Additive Manufacturing and is quite difficult to overcome, although a common solution is the maximum practical and economical resolution possible, creating thinner layers, minimizing therefore the associated error at the cost of effective build time. Such geometry is shown in figure 21.

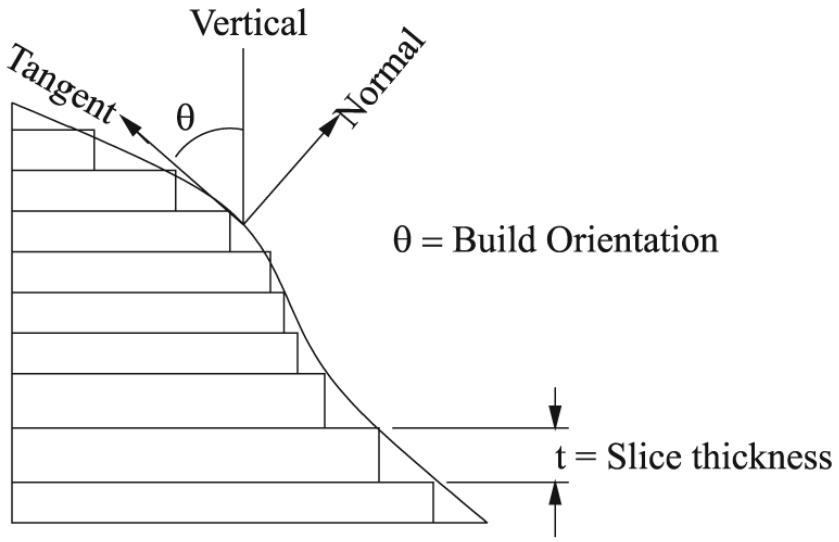


Figure 21 - Stair-stepping effect (Pandey, Nallagundla, & Dhande, 2003).

If there is a requirement for a smooth or polished finish, there will be application of posterior wet or dry sanding or even hand-polishing. In many cases, it is desirable to paint the surface prior to sanding or polishing, having the benefits of sealing porosity and (through viscous forces interactions) smoothing the stair-step effect, which also translates into an easier, more effective sanding and polishing. If there is the requirement for a matte finish, a simple bead blasting of its surface can even out the surface texture of the built part, remove sharp corners from stair-stepping and give the overall matte appearance.

There are several automated techniques possible for surface texture improvements, with two of the most utilized being the vibro-polishing technique for external features, and abrasive flow machining for internal features, with both managing to smooth surface features at the cost of small feature resolution, sharp corner retention and dimensional accuracy (Digital Alloys' Guide to Metal Additive Manufacturing, 2020) (Gibson, Rosen, Stucker, & Khorasani, 5 - Powder Bed Fusion, 2021).

iii) Accuracy improvements

Maximum resolution is directly dependent on the diameter of its laser beam (referred as spot-size), the layer thickness and the largest particles present in the metal powder itself, with overall having a resolution of 20 to 100 microns, as a general case. Typically, the larger the effective build volume and the faster the required or desired build speed, the worse the accuracy for a particular process. (Digital Alloys' Guide to Metal Additive Manufacturing, 2020) (Gibson, Rosen, Stucker, & Khorasani, 5 - Powder Bed Fusion, 2021)

There are a myriad of factors that play in such accuracy improvements, as seen in Annex E.

iv) Aesthetics

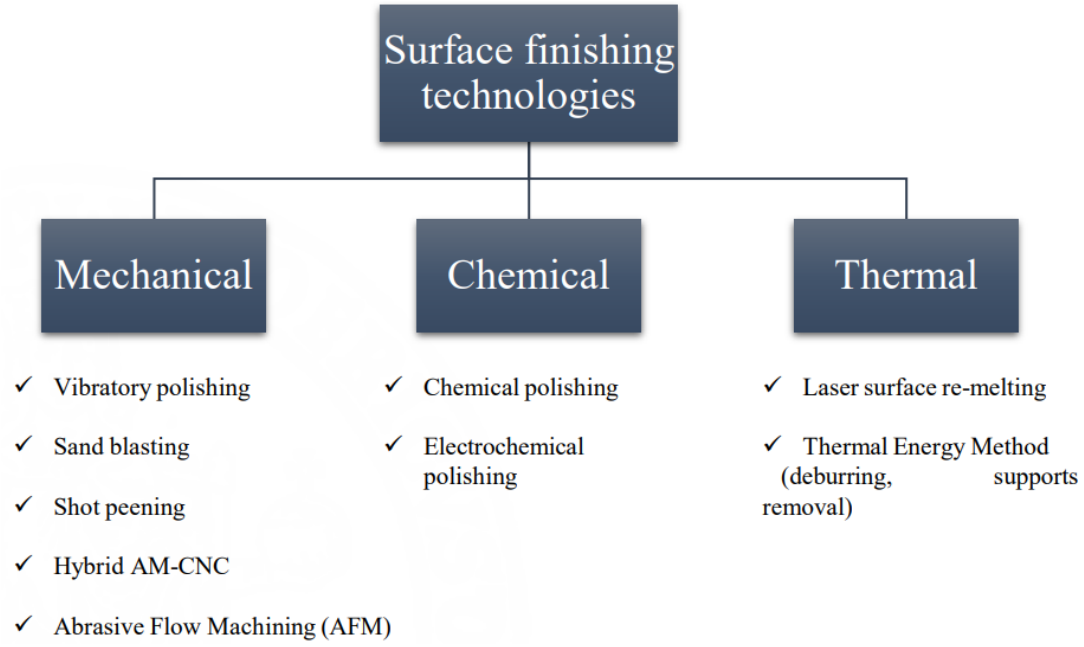
Many times, aesthetical considerations must be considered, simply due to the desired function of the part, or due to demands from the customer, ranging from market considerations to simple personal preferences. In such cases, the most common desired improvements relates to surface finish, where we can apply the already mentioned matte or polished finishing. In some cases, a difference in surface textures may be desired, which translates into finishing post-processing of selected specific surfaces, and not the overall part.

In situation where the colour is not of sufficient quality, there are a myriad of methods which can be used to improve part aesthetics. In parts created through powder beds, the inherent porosity leads to effective absorption of the coloured figments by simply dipping the part into a dye of appropriate colour, being extensively used, as an example, in automotive industry (Gibson, Rosen, Stucker, & Khorasani, 5 - Powder Bed Fusion, 2021).

v) Surface treatment technologies

There are a myriad of surface treatment technologies available for post-processing operations of the L-PBF built part, so as to better upgrade its inherent properties. The following table shows the different options available.

Table 5 - Techniques for L-PBF post-processing (Squillace, 2023).



These surface finishing technologies are better discussed in Annex F.

2.1.3.10. Materials

The material choice in L-PBF is quite broad, being able to use almost any type of metal compositions and alloys. Virtually any metal that can be turned into a powder through usage of a gas or plasma atomization process, can be used in this additive manufacturing method. MAM through L-PBF therefore works with a wide range of materials, such as Steel, Inconel, Aluminium, Copper, Gold, with the most common ones being Titanium, Nickel and Iron, and respective alloys, such as the Ti6Al4V alloy, Inconel's various subcategories, Steel derivatives such as stainless 316L, to name a few. The proportion is shown in figure 22 (Gibson, Rosen, Stucker, & Khorasani, 5 - Powder Bed Fusion, 2021) (Squillace, 2023) (Ali, Sabyrov, & Shehab, 2022).

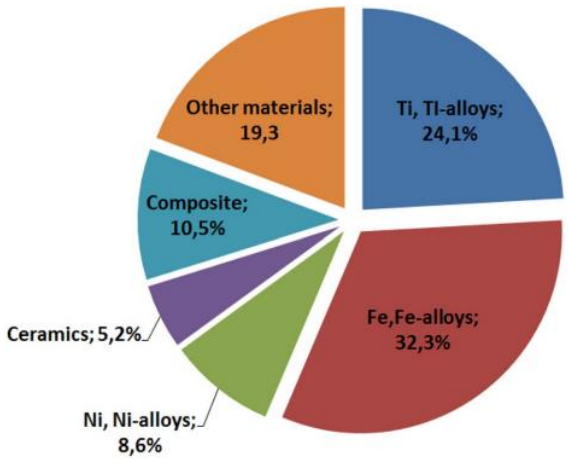


Figure 22 - Materials mentioned in publications regarding L-PBF additive manufacturing (Ali, Sabyrov, & Shehab, 2022).

One of the most useful materials for this technology is the utilization of Titanium (Ti), both in its pure form and as an alloy. Besides the more obvious advantages this material offers to the MAM process such as strong mechanical properties, good corrosion resistances and very attractive specific strength ratios, this material suffers from high wear when manufacturing it through subtractive technologies, such as machining, being therefore a prime material choice for L-PBF, since it manages to circumvent such problem (Ali, Sabyrov, & Shehab, 2022).

Iron (Fe) is quite popular, especially regarding alloy processing, since pure Ferrum is typically not much used. Various combinations of alloys are popular such as 316 stainless, Fe-Co-V, Fe-Ni-Si, Fe-Ti, between others, allowing a wide range of applications and parameters execution in such broad material alloy. 316 stainless is the most popular Fe alloy sued with L-PBF, with high level of corrosion resistance, good ductility characteristics and good strength properties (Ali, Sabyrov, & Shehab, 2022).

Nickel (Ni) is also quite appreciated in MAM technology, with excellent corrosion resistance, even at high temperatures, allied with the difficulty working this material in conventional machining. Their practical application comes from encompassing two very interesting fields: Nickel super alloys and Nickel-Titanium SMAs (Ali, Sabyrov, & Shehab, 2022).

In the first, the possibility of these super alloys means that materials that would lose resistance very quickly when subjected at high temperatures, in fields such as energy or aerospace, can maintain their integrity and resistance due to the special composition created, therefore not losing durability, due to the temperature opposition quality. There are several super-alloys, with the most common ones being Inconel (nickel-chromium) family type alloys. These are shown in figure 23 (Ali, Sabyrov, & Shehab, 2022).

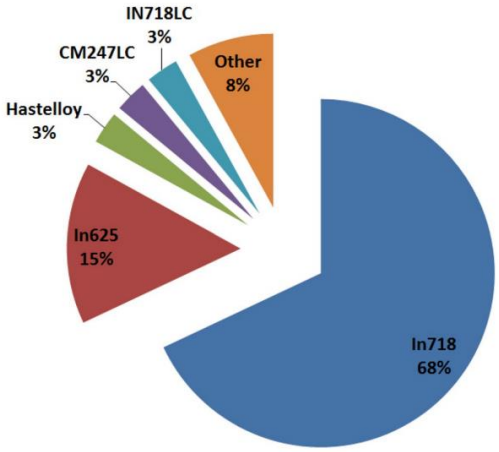


Figure 23 - Materials in studies regarding Nickel super alloys (Ali, Sabyrov, & Shehab, 2022).

Meanwhile, when Nickel is in use for SMAs, it allows for good corrosion and wear resistance, supreme ductility and elasticity, and the remarkable modification between two geometrical/dimensional parameters – translated in one in the austenitic phase and another in the martensitic phase, a quite interesting property due to potential and already existing uses in the field of engineering application (such considerations will be further developed in the work at hand) (Jani, Leary, Subic, & Gibson, 2014) (Pei & Loh, 2018) (Alagha, Hussain, & Zaki, 2021).

Other materials (Al, Cu, Mg) are also used, although at a smaller degree. Aluminium (Al) possesses appropriate strength parameters but is especially interesting when comparing strength-to-weight ratios, due to being cheap to manufacturing, tending to excel in applications where lightweight materials with sufficient hardness are required. Copper (Cu) is quite appreciated due to excellent electrical resistance, which can be paramount in electrical or electromechanical applications. Magnesium (Mg) has low density, high electrical/thermal conductivity, good electromagnetic radiation resistance (Ali, Sabyrov, & Shehab, 2022) .

2.1.3.11. Applications

As the technology matures and we increasingly make use of more complex and advanced manufacturing, and as material knowledge advances at frightening paces, the market for L-PBF will continue to grow.

Such a versatile technology is used in a multitude of different areas. Among the most utilized sectors, we can count on aerospace, automotive, biomedical, defense, and other high-tech areas, in applications as varied as rapid prototyping of parts and assemblies, commercial aerospace components, current and next-gen military technologies (including aerospace, logistical, naval, field maintenance and automotive applications), automotive engines and components, the creation of highly complex delicate objects, various selections of consumer products, auxiliary industrial machinery manufacturing, among others. There will be discussion of some fields of application of this industry.

i) Aerospace

One of the most applicable processes is the usage of this technology for aircraft mechanical part manufacturing, by minimizing the number for assembly into a single component, with optimization of weight parameters, in components such as turbine blades, fuel nozzles and guide vanes, allowing for efficient production of critical aerospace components that minimize weight, this being one of the key factors of the industry (Sefene, 2022).

As an example, GE Aviation has been producing fuel nozzles for its LEAP engine since 2013, applying L-PBF and managing to reduce the parts in such assembly from 20 to just 1, while also increasing the life of the fuel delivery system by a factor of 5 due to greater design freedom, and reducing weight by 25% (AM at GE Aviation, 2013) (Yadroitsev, Yadroitsava, MacDonald, & Plessis, 2021).

Another example is the combustion chamber for the ArianeGroup that was hot-fired in 2020 on the P8 test bench of the DLR Aerospace Center in Germany, as a Franco-German partnership, validating designs for future liquid propellant rocket engines. The combustion chamber was produced and tested under ESA's Future Launchers Preparatory Program, incorporating innovative manufacturing technologies and advance in cutting-edge propulsion technologies. Such as low-cost copper alloy cooling channels, an outer jacket made by cold gas spraying, and a single-piece injection head produced by L-PBF (Yadroitsev, Yadroitsava, MacDonald, & Plessis, 2021) (Sefene, 2022).

HPS GmbH, a specialist for space subsystems, produced, together with Fraunhofer ILT, an antenna with 400mm of diameter through L-PBF Ti6AL4V, with the topology-optimized L-PBF manufacture design reducing production time, minimizing weight and

allowing increased geometric freedom (Yadroitsev, Yadroitsava, MacDonald, & Plessis, 2021).

Meanwhile, in ESA's project "AAM21SH – Assessing the use of advanced manufacturing to improve and extend space hardware capabilities", the redesign, manufacturing and qualification of a metallic space bracket was achieved, with various topology optimization lessons being learned in the process, with reduced displacements of 55%, reduced mass by 68%, increasing minimum factor by 72%, with the demonstrator being qualified for technology level 5 (i.e. verification of technology in relevant environment). The component is shown in figure 24 (Yadroitsev, Yadroitsava, MacDonald, & Plessis, 2021).

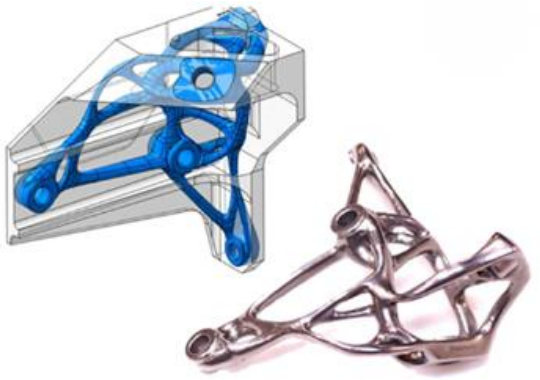


Figure 24 – L-PBF produced metallic bracket (Yadroitsev, Yadroitsava, MacDonald, & Plessis, 2021).

Again, for the ESA, with the project "Development of an AM mirror demonstrator for space applications", there was optimization of an AlSi40 mirror through L-PBF manufacturing, with an extensive development campaign, having final reductions of 40% of its weight and 20% better optical performance than the referenced part. This component is shown in figure 25 (Mueller, et al., 2019) (Yadroitsev, Yadroitsava, MacDonald, & Plessis, 2021).

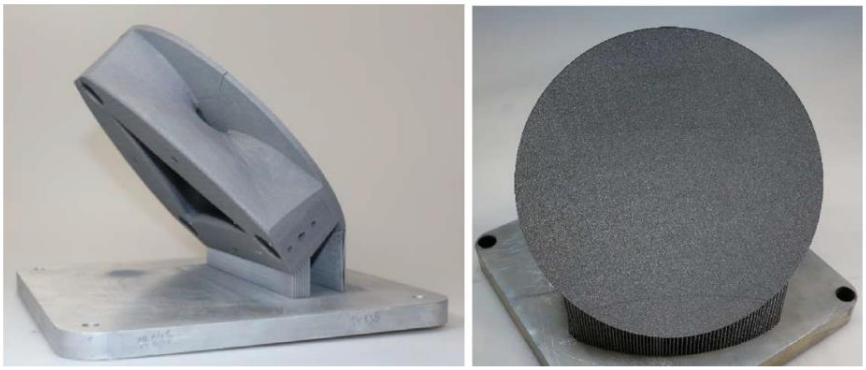


Figure 25 - AlSi10 mirror demonstrator for ESA (Mueller, et al., 2019).

Terma A/S, an aerospace company, as part of subcontracting for the Lockheed Martin F-35 Lightning II jet fighter, the premier Western jet fighter, managed to reduce the production time and necessary material for manufacturing of a particular (non-disclosed) component of the combat aircraft from 55 hours and 219 kg of steel to just 5 hours and 10 kg of powder, for a component that weighs seven kilograms at its final, through usage of L-PBF technology (Terma A/S F-35 AM reductions, s.d.).

In 2020-2021, GE Aviation, in conjunction with the US Army, selected the General Electric T901 turboshaft family of engines to replace the T700 family in the H-60 Black Hawk and AH-64 Apache helicopters, with the replacement being made due to possibilities of 50% more power and 25% less weight, by incorporating L-PBF technologies in the design process. This component is shown in figure 26 (GE and the U.S. Army conduct T901 Preliminary Design Review, 2018) (Additive Manufacturing and the U.S. Army's Improved Turbine Engine, 2021) (Boeing begins 3D-printing Apache helicopter parts, 2023).



Figure 26 - T901 turboshaft (Additive Manufacturing and the U.S. Army's Improved Turbine Engine, 2021).

So much was the success that the new design parameters of the engine allowed that the US Department of Defense (DoD) selected the turboshaft engines for the Future Vertical Lift (FVL) Future Attack Reconnaissance Aircraft (FARA) Competitive Prototype Program (GE and the U.S. Army conduct T901 Preliminary Design Review, 2018) (Additive Manufacturing and the U.S. Army's Improved Turbine Engine, 2021) (Boeing begins 3D-printing Apache helicopter parts, 2023)..

ii) Biomedical

Meanwhile, in biomedical applications, there is the possibility of manufacture of implant built with advanced bio-compatible materials that need to have complex surface structures so as to allow tissue to anchor on them, such as titanium hip joints. Some applications are shown in figure 27. Orthopedic implants are important high-technology applications that are manufactured mainly to standard (and less-than-ideal) sizes by using traditional more-conventional manufacturing technology.

Many clinical scenarios would be better answered through customized geometry of the parts – a situation which traditionally has been quite difficult, if not outright impossible to realize, due to the associated costs and the production time it would be needed to set up such manufacturing (Yadroitsev, Yadroitsava, MacDonald, & Plessis, 2021) (Sefene, 2022).

L-PBF technology is completely compatible with the clinical requirements, with medical implants being able to deliver, through smooth subcontracting or even with specialized manufacturing units in the actual hospital, the needed implants required for such biomedical procedures. A schematic is shown in figure 28. One of the main advantages of L-PBF technology is the possibility of processing a wide-range of materials, including medical ones, such as biomedical grade stainless steel, cobalt chromium, titanium, nickel, and such alloys (Yadroitsev, Yadroitsava, MacDonald, & Plessis, 2021) (Sefene, 2022).

The complex anatomies of human knee, hip, skull, dental and craniofacial tissues requires a precise design with high dimensional accuracy, so as to match and fit the implantation sites. Recent developments allow surgeons and material scientists to manufacture patient-specific custom medical devices, in nearly any type of geometry, within 24 hours, with even installation

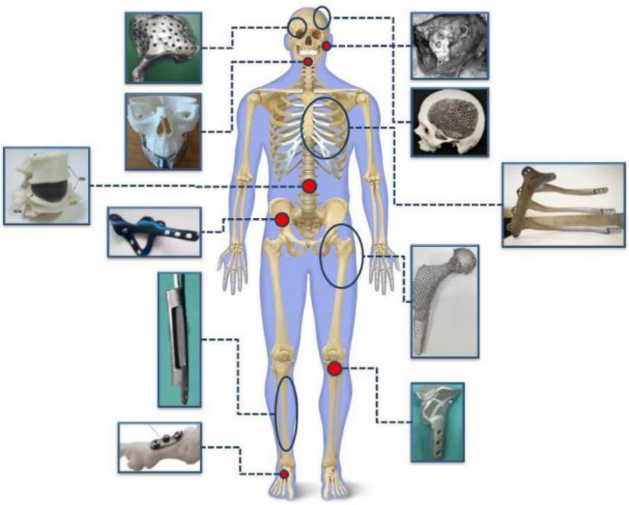


Figure 27 - Biomedical parts produced by L-PBF in the human body *(Ali, Sabyrov, & Shehab, 2022)*.

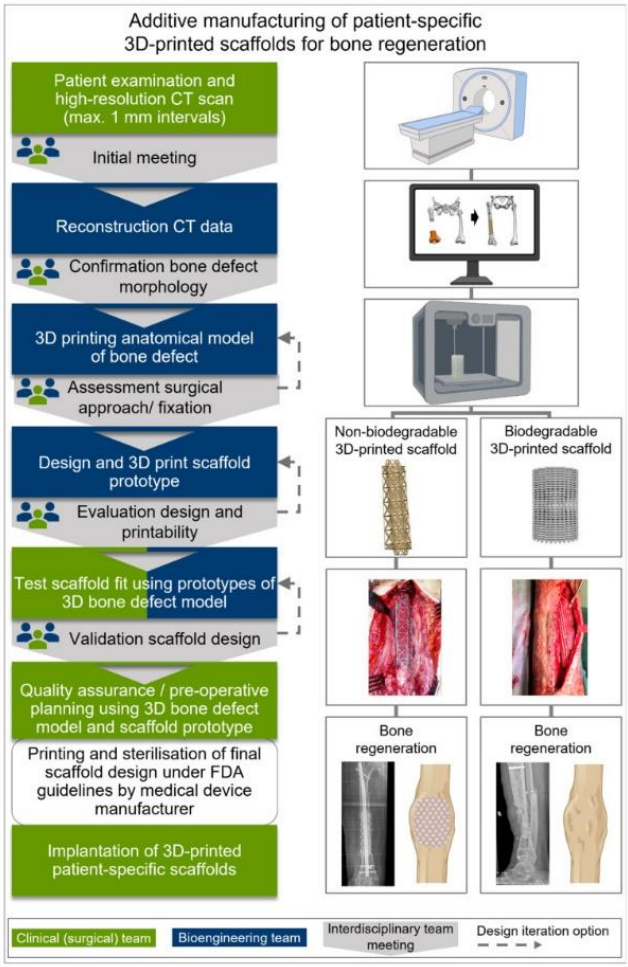


Figure 28 – Design, manufacturing, implant deployment and key bone regeneration of 3D-printed Ti-6Al-4V scaffold (Laubach, et al., 2023).

of the manufacturing units in the hospital themselves, particularly in the Southeast Asian medical industry (Munir, Biesiekierski, Wen, & Li, 2020).

One example is the treatment of bone defects, through application of titanium alloy parts manufactured through L-PBF, for better customization and less medical complications when comparing with convention medical techniques for bone correction deformations, with the main problems being "…to achieve consensus among the leading stakeholders in this field to eventually obtain high-quality findings that will lead to guidelines applicable to all treatment centers worldwide". (Laubach, et al., 2023) One example of such bone implants can be seen in figure 29.

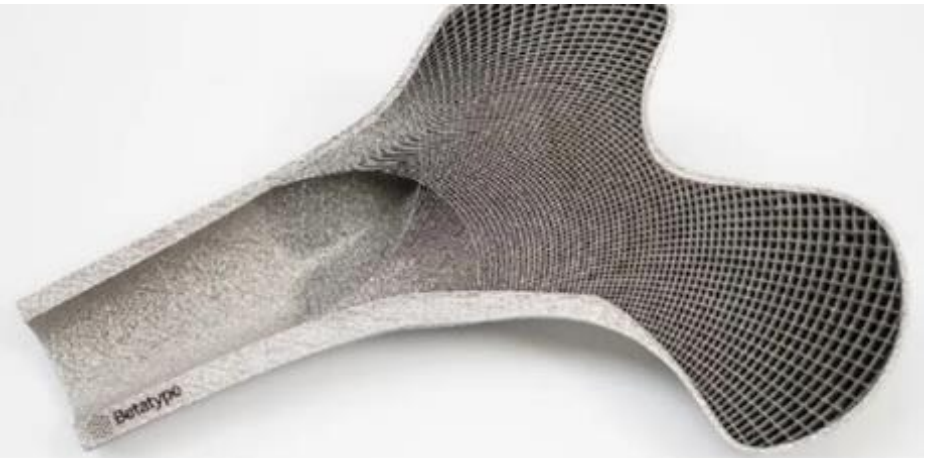


Figure 29 - Orthopedic implants of Renishaw (Renishaw AM Orthopedic implants, 2018).

iii) Automotive

In the automotive industry, L-PBF has been used from prototyping of components to full-scale production, in world-renown companies such as BMW and Porsche. It is also quite used in motorsports, where the cost of limited production is justified, in components such as brake pads with cooling ducts (Yadroitsev, Yadroitsava, MacDonald, & Plessis, 2021).

The Ford Motor Company created, in 2019, what it claimed to be "the largest 3D metal-printed part for a working vehicle in automotive history", a 6 kilograms aluminium manifold inlet that took 5 days to complete, printed on a Concept Laser X LINE 2000R from GE Additive, surpassing Bugatti's 2.9kg Titanium calliper that was printed using an SLM 500 machine, in a job lasting 45 hours, in 2017. The components can be seen in figure 30 (Yadroitsev, Yadroitsava, MacDonald, & Plessis, 2021).



Figure 30 - Bugatti brake Titanium calliper (left) & Ford Performance Aluminium Manifold Inlet (right) (Brake Calipper from 3D Printing, 2018) (Ford Performance 3D-printed inlet, 2019).

Another interesting example is the manufacturing of LED headlights by Betatype in 2021, which normally require large heatsinks that necessitate active cooling channels inside. Through L-PBF, the geometrical freedom allows the simplification of the total manufacturing chain from multiple processes to a single build job, reducing the cost from 30€ to 3€, and the build time from 444h to less than 30h (Yadroitsev, Yadroitsava, MacDonald, & Plessis, 2021) (Automotive Parts with L-PBF, 2021).

Since 2020, the BMW group has been vying to, through its BMW Group Additive Manufacturing Campus (AMC) research initiatives and through various industrial efforts, integrate MAM processes, and L-PBF in particular, in its chain of production.

In detail, there are focused efforts for the usage of 3D printed parts on exclusive small series production, the systematic integration of additive manufacturing into development and production, the generative design in component development process, and even the usage of machine learning and artificial intelligence for screening of components for additive manufacturability. Some examples can be seen in figure 31 (3D printing at BMW, 2020) (Automated AM for car parts, 2023).

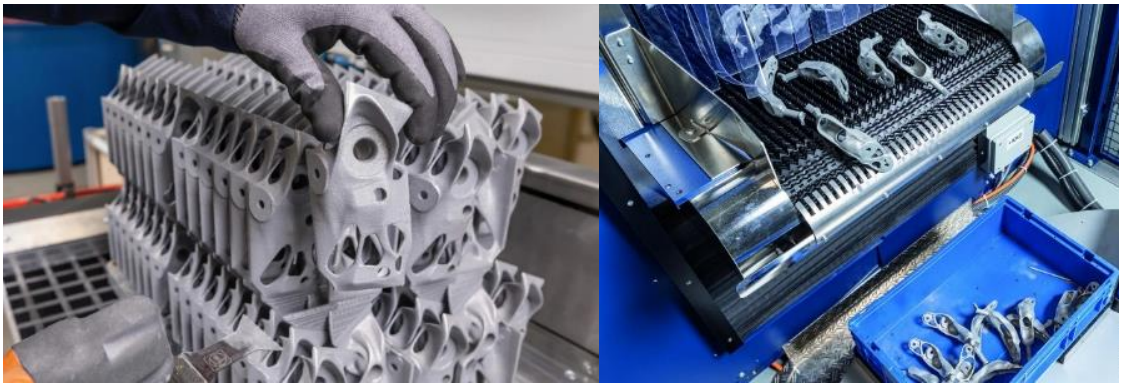


Figure 31 - BMWs components produced through L-PBF (3D printing at BMW, 2020) (Automated AM for car parts, 2023).

iv) Mould industries

Regarding the usage of the technology for industrial tool manufacturing, such processes such as L-PBF allows the incorporation of cooling channels into moulds, which eases the manufacturing of cooling systems. In injection moulding processes, these are typically the most time-consuming steps in manufacturing, with the adoption allowing increased production speed, higher quality moulded parts, and less scrap total produced (Asnafi, 2021) (Torok, et al., 2022) (Oliveira, Miranda, Oliveira, & Ferreira, 2022). Such processes creates positive feedback between the various entities involved, creating a self-sustained industrial cycle of development, as can be seen in figure 32.

The cooling efficiency of the moulds can be vastly improved due to the deep versatility and customization available through MAM. Such upgrades in the design can reduce the time for cooling for as much as 30% to 40% (Torok, et al., 2022).

Therefore, increased integration between various mould industries, and the MAM corporations will keep increasing, since the possible synergies between both technologies means upgraded cycle times. Using efficient design, the tooling in hot working and injection moulding can be made more competitive through L-PBF integration, with generative design/topology and lattice structure optimization for lightweight designs of such tooling components.

Although there can appear high tooling costs at first, the total costs are competitive due to reduced cycle times possible due to upgraded cooling parameters (Asnafi, 2021) (Oliveira, Miranda, Oliveira, & Ferreira, 2022).

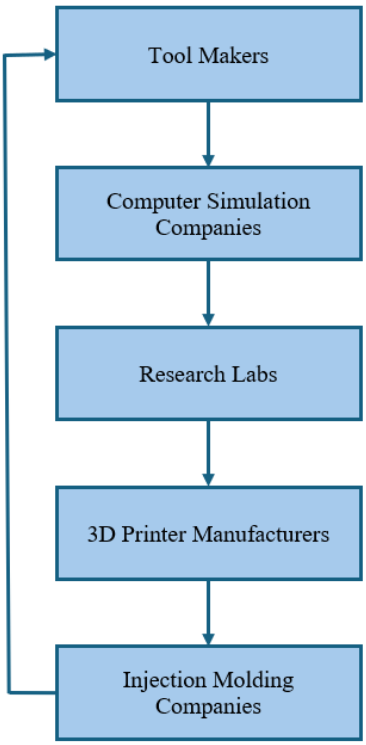


Figure 32 - Supply chain for fabrication of tooling for injection molding (Buxani, 2018).

v) Energy sector

The energy sector, extremely vital for the modern industrial-technological society, has been ever-increasing the role of this technology on its manufacturing processes. One example comes in 2021, with the 3D printing of turbine vanes, developed by the Siemens Corporation, so as to replace the 25-year-old combined cycle power plant with three Siemens V64.3 gas turbines in the town of Dresden, for the DREWAG AG municipal utility authority, for a lifetime extension and modernization upgrade package. Components can be seen in figure 33 (Yadroitsev, Yadroitsava, MacDonald, & Plessis, 2021).

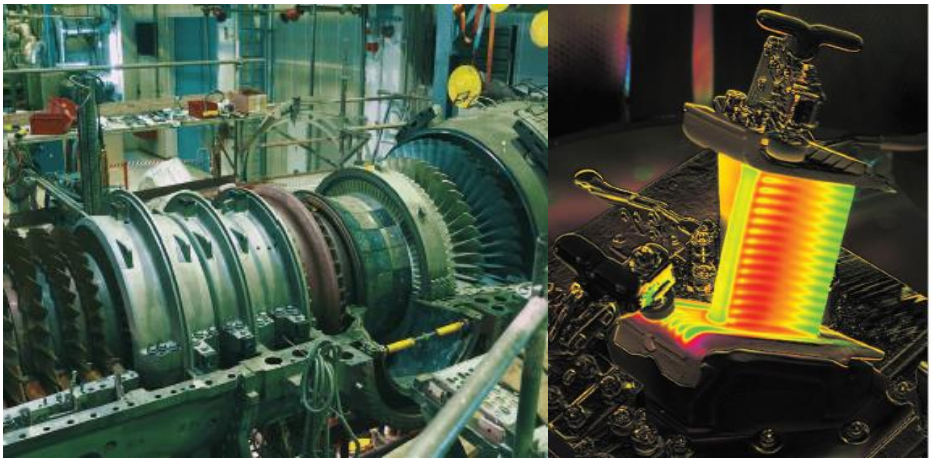


Figure 33 - Siemens 60MW V64.3 turbine (left) and thermal image of redesigned turbine vane (right). (AM in turbines, 2024)

The project consisted of two stages, with the first being the reproduction of the vanes in its original design, and the second one was the development of the upgraded redesigned vanes for installation. The vanes, produced by Material Solutions, a company of Siemens, resulted in high accuracy results, with excellent operating behaviour after 8000 hours of operating time, with the added upgrades of advanced air-cooling design, for better efficiency and less environmental harming emissions.

Another impressive example provided by Material Solutions is the additively manufactured turbine blade of the SGT-400 gas turbine, managing to reduce costs by 70% and cutting lead times by 75%. Components can be seen in figure 34 (Siebold, 2019).

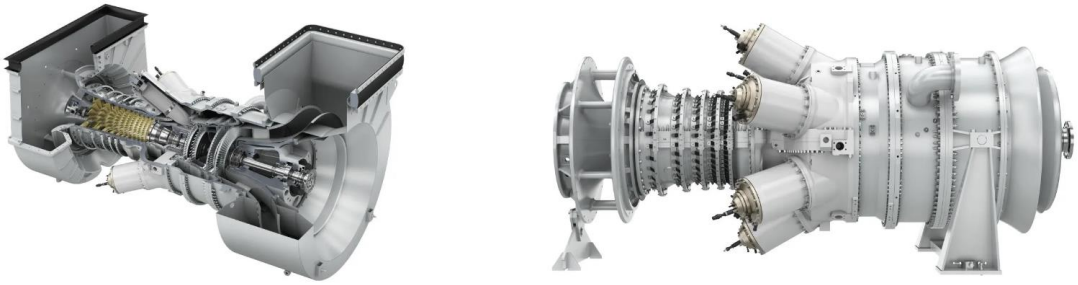


Figure 34 - Siemens SGT-400 industrial gas turbine: cut section (left) and core engine (right) (Siemens Gas Turbines, 2024).

Since 2016, that burner components for gas turbines of the SGT-1000F have been manufactured on a commercial scale in additive production. In 2013, the gas burner tips for both the SGT-700 and SGT-800 gas turbines were repaired on a commercial scale using L-PBF technology, with the damaged part of the torch tip being cut off and then reprinted, reducing estimated repair times in 60%. Since 2017, the burner rigs have been totally redesigned through L-PBF, reducing the parts from 13 to just 1, eliminating 18 different

welding operations, and increasing functionality by inclusion of the gas supply component as part of the burner head, resulting in increased service life. Components can be seen in figure 34 (Yadroitsev, Yadroitsava, MacDonald, & Plessis, 2021).

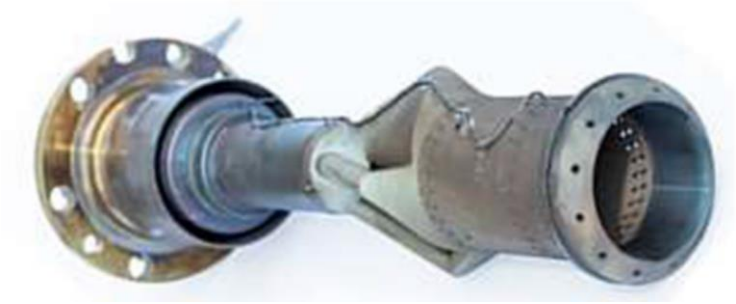


Figure 35 - 3D Gas burner from Siemens for the SGT-700 gas turbine in the E.ON-GuD power plant Philippsthal (Yadroitsev, Yadroitsava, MacDonald, & Plessis, 2021).

One practicality of L-PBF manufacturing is the possibility of a fast and sustainable creation of replacement parts for the turbines. While conventional manufacturing proves difficulty at providing spare parts due to the rather low (but critical) and varied requirements for preventive and corrective maintenance, with the necessity of entirely new casting moulds in some cases, the switching of production to Additive Manufacturing offers maximum supply security without the constraint of maintain very expensive warehousing or tooling (Yadroitsev, Yadroitsava, MacDonald, & Plessis, 2021).

vi) Defense and Military technology

Defense and military technology can also use metal additive manufacturing processes, with companies such as General Dynamics Land Systems and Rheinmetall Landsysteme using such procedures for manufacturing of specialized components, or for ease of maintenance in specialized components, as evidenced by the conjunction of GE Additive with General Dynamics, and the existence of Rheinmetall 3D TechCenter. Component manufacturing can be seen in figure 36 (Rheinmetall turns to SLM, 2017).

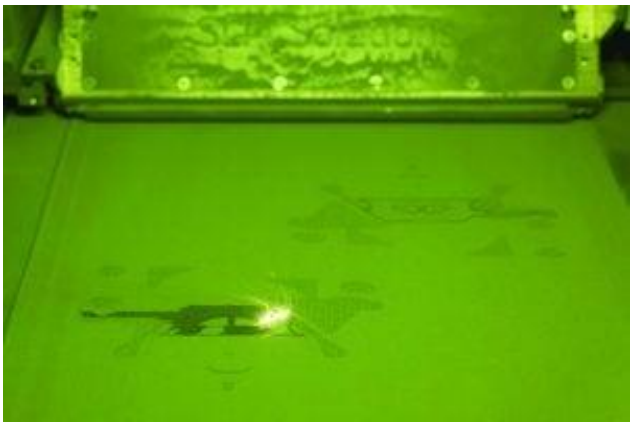


Figure 36 – L-PBF techniques used in Rheinmetall manufacturing units, at the Rheinmetall 3D TechCenter (Rheinmetall turns to SLM, 2017).

"General Dynamics is always looking for innovative technologies to enhance our products, and additive manufacturing holds real promise in the near term. We'll continue teaming with leading suppliers such as GE Additive as we uncover additional applications

for this exciting technology," - Process & Technology Development, General Dynamics. Components can be seen in figure 37 (GE Additive Print Services selected by General Dynamics Land Systems, 2019).



Figure 37 - General Dynamics Land Systems and GE Additive representatives (left) discussing integration of MAM for automotive combat systems applications (right)
(GE Additive Print Services selected by General Dynamics Land Systems, 2019).

Similar to automotive and aerospace sectors, defense and military technology can receive a more versatile and diversified design and manufacturing capabilities by working through such systems, especially when regarding titanium alloys applications, due to the great utilization of this alloy due to superior strength-to-weight ratios, and the difficulty working it through conventional manufacturing techniques.

ThyssenKrupp GmbH, world leader in diesel engines for military technology applications, especially regarding submarine applications, is also increasingly using this technology due to the versatility of the designs possible and for reductions in weight, with Dr. Luis Alejandro Orellano, Chief Operating Officer of ThyssenKrupp Marine Systems, giving an example that "using a 3D printer to make the hydraulic block for a submarine, 83 percent of the weight was saved". Such components are made at ThyssenKrupp TechCenter Additive Manufacturing, as can be seen in figure 38 (Submarine Components from 3D Printers, 2020) (ThyssenKrupp TechCenter AM, 2024).



Figure 38 - Submarine components for ThyssenKrupp (left) and engineers of the corporation leading to its manufacture (right) (Submarine Components from 3D Printers, 2020) (ThyssenKrupp TechCenter AM, 2024).

2.1.3.12. Market & Economical Considerations

Regarding market considerations, metal additive manufacturing is experiencing an unprecedent economic and technological boom, with a 15.5% median CAGR (compound annual growth rate), with just last year achieving a groundbreaking 24.4% growth in sales of metal AM systems alone, as can be seen in figure 39 (Wohlers Report, 2024).

It is estimated that current market trends with continue with the industry, nowadays evaluated at 4.64 billion USD in 2023 to 5.36 billion in 2024 and is expected a 9.74 billion size in 2028, with a total median 16.1% CAGR (Metal Additive Manufacturing Global Market Report, 2024).

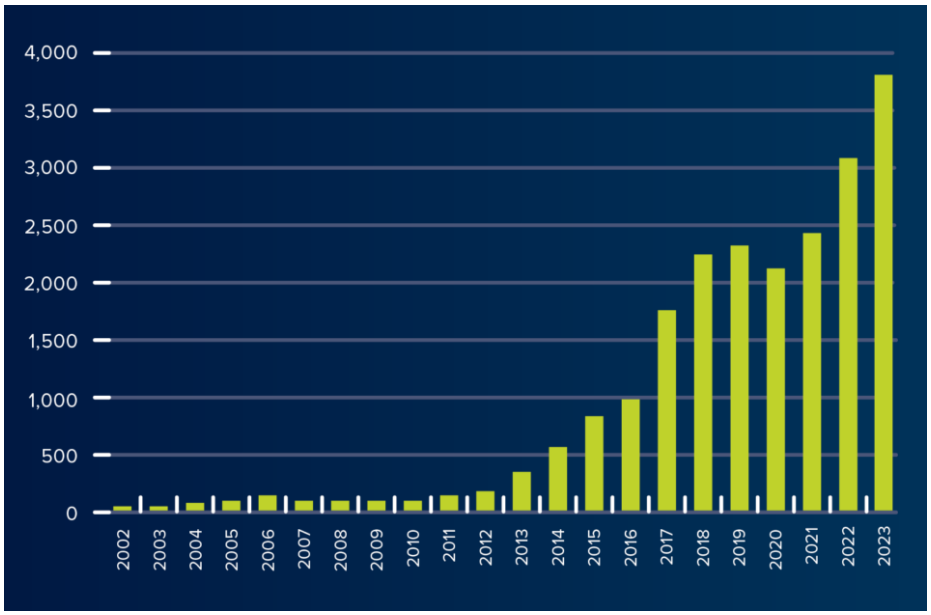


Figure 39 - Metal AM solutions total sales for the last 20 years (Wohlers Report, 2024).

AM Power report states that the total AM market and forecast have a 13.9% CAGR on market value, with part manufacturing taking the biggest share, which is followed by the specialized material and equipment, as can be seen in figure 40 (AMPOWER Report 2024, 2024).

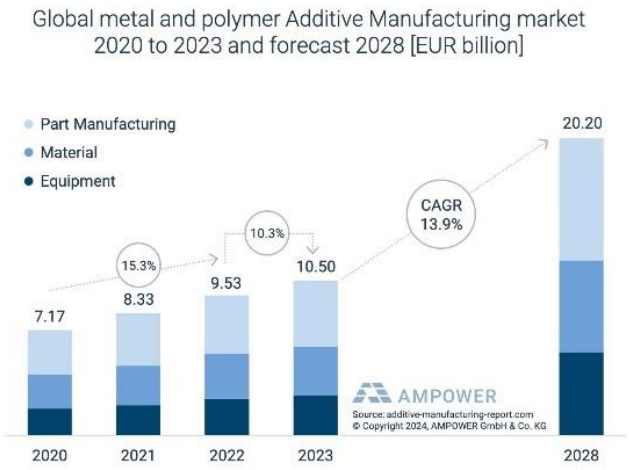


Figure 40 - Global AM market projections (AMPOWER Report 2024, 2024).

Some of the key factors are the increased adoption in aerospace and defense industry, that has seen an increase in sales due to current global political instability; a surge in EV (electric vehicle) development, with on-demand production and reduced dependence on complex supply chains, which are particularly beneficial to this market; the increased automation and robotization of these manufacturing units, such as the US-based ADDiTEC AMRC-P (additive manufacturing robot cell-portable); and the increased integration of the technology both in global manufacturing as well as global attention and investment on it (Metal Additive Manufacturing Global Market Report, 2024).

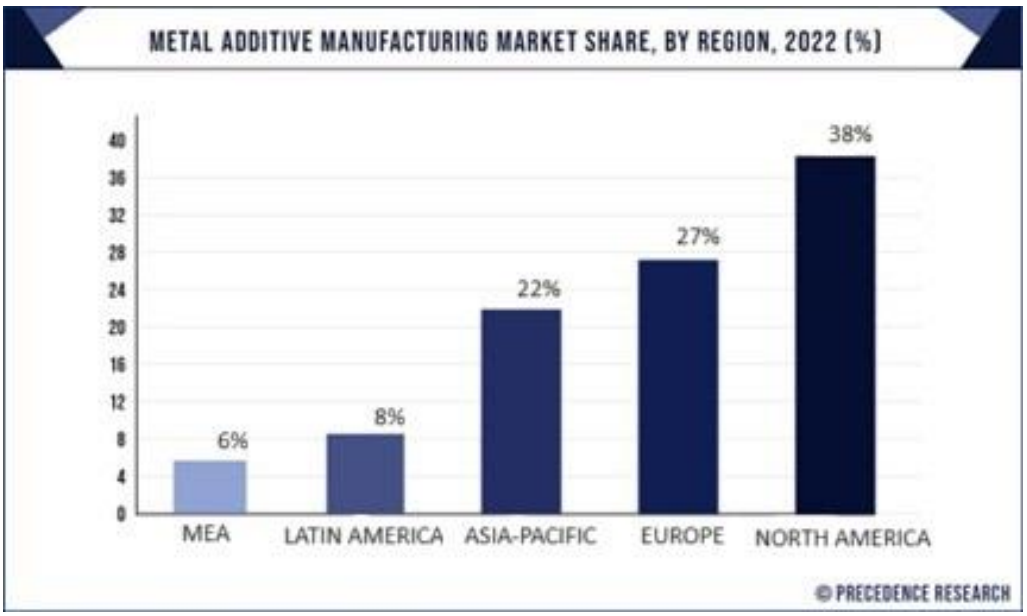


Figure 41 - MAM market share, by region, in 2022
(Metal Additive Manufacturing Market Size, Share, Report 2023-2032, 2024).

The key regions of adoption of this technology are North America (specially the US) and Europe (specially Germany, France, and Italy), which represent, by far, the ones most developed and integrated with such technology, due to high technological expertise, focus on human capital, and R&D efforts, however it is projected for Southeast-Asian markets to be the ones with most growth due to the fast beginning of adoption on these regions (Metal Additive Manufacturing Market Size, Share, Report 2023-2032, 2024).

2.2. Shape Memory Alloys

Shape memory materials (SMMs) are unique materials with the ability to sense and respond to stimulus such as heat, electricity, vibrations, and electromagnetism. Shape memory materials are divided in various subgroups, like shape memory alloys (SMAs), shape memory ceramics (SMC), shape-memory polymers (SMP) and shape memory composites (SMC).

When the stimuli of such materials are changed or removed, these materials are able to recover their predefined shape, allowing for unprecedent versatility in its interactions with the physical world, when properly designed and manufactured. Some of the temperature ranges are shown in figure 42, where the versatility of Ni-Ti alloys ("Titanium-nickel") can be seen (Alagha, Hussain, & Zaki, 2021).

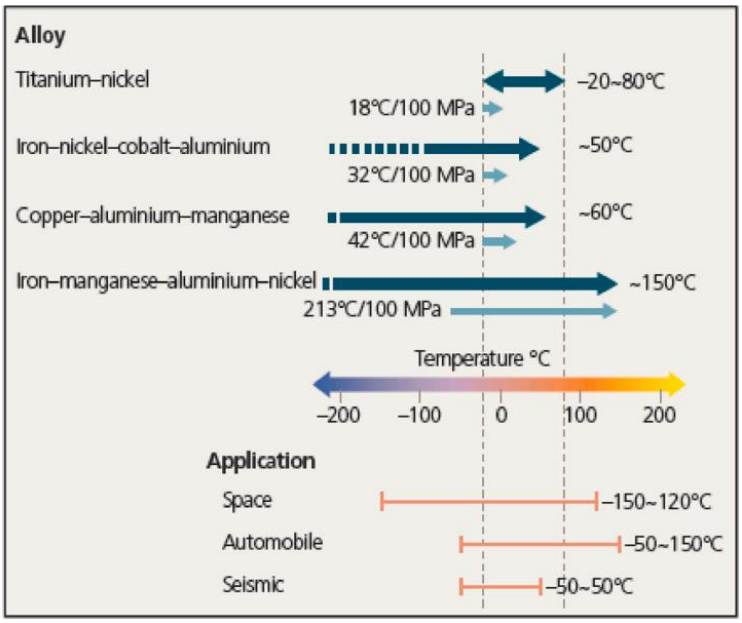


Figure 42 - Operational temperature of some examples of SMAs and their applications (Omori, et al., 2011).

Due to the characteristics of the materials, these is increased attention in its potential, with SMAs being the most important and with the biggest focus among industrial and scientific research (Pei & Loh, 2018).

Shape memory alloys, or SMAs, are metallic-based materials with the ability to recover inelastic strains in a bigger magnitude than other, more conventional, alloys. In such alloys, the shape recovery is operated by heating, with the resulting behaviour being called "shape memory effect" or by mechanical stress, with the resulting behaviour being called "superelasticity" (Jani, Leary, Subic, & Gibson, 2014) (Alagha, Hussain, & Zaki, 2021).

In SMAs, the crystallographic structural change is the responsible for the shape-recovery behaviour, with a predefined shape at a certain temperature/stress level, and a subsequent restoration of its initial shape when loaded or heated until a certain critical condition. There is normally the existence of a low-temperature martensite phase and a high-temperature austenite phase (Jani, Leary, Subic, & Gibson, 2014).

Among them, the most used are Nickel Titanium alloys (also known as Ni-Ti or Nitinol), and, as such, will be the focus on this work, but it is worth noting that there are far more materials with shape memory behaviour, with some of the most common being the copper-zinc-aluminium (Cu-Zn-Al), the copper-aluminium-nickel (Cu-Al-Ni), and the iron-manganese-silicon (Fe-Mn-Si) alloys (Jani, Leary, Subic, & Gibson, 2014) (Alagha, Hussain, & Zaki, 2021).

2.2.1. Ni-Ti alloys

Nickel-Titanium alloys, commonly referred as Nitinol, are materials with (originally classified as) near-equiatomic composition of Titanium and Nickel content (50-50 ratio), with this material being part of the class of SMAs that manage to have deformations at low temperature and are able to recover their original shape when exposed to high temperatures (through, for example, the resistance created through electrical input).

Figure 43 shown Ni-Ti alloys with various different chemical compositions.

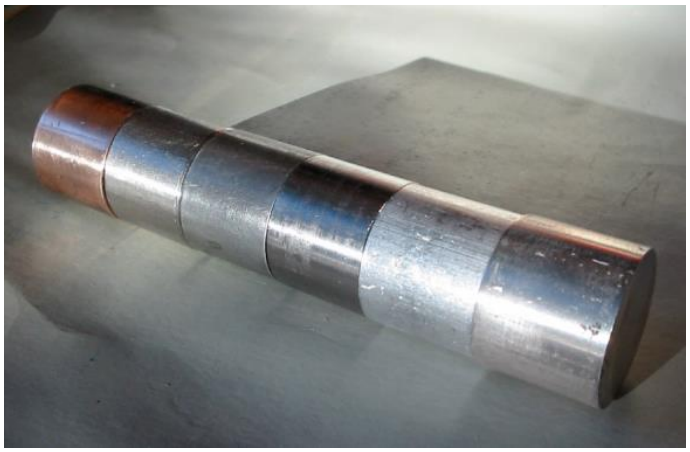


Figure 43 - Ni-Ti alloys (various compositions) (Ni-Ti SMA, 2002).

Of note that, nowadays, Nickel weight content can go from 49% to 57%, as a general rule, due to increased manipulation of this alloy, with alloys such as Nitinol-50 (50% Ni content) and Nitinol-55 (55% Ni content) being common (Alagha, Hussain, & Zaki, 2021) (Patel, Dubey, Roshan, & Behera, 2023) .

In such materials, there are two main phases, the B2 cubic austenitic high-temperature phase, and the B19' monoclinic martensitic low-temperature phase, which will significantly alter its properties through deformation and/or thermal alterations of the structure. Of note, that additionally, there is a third state – called the R-phase – which might appear temporarily between the mentioned states and is explained further in the document (Sittner, Landa, Lukas, & Novak, 2006).

Although the more technical term is Ni-Ti alloys, it is often referred as Nitinol due to the discovery in 1959 at the Naval Ordinance Labs (NOL), as a material research grant for US Navy technologies, with metallurgist William J. Buehler giving hence the name of the alloy as Nickel-Titanium Naval Ordinance Laboratories – Nitinol, while working on a project for development of the UGM-27 Polaris missile system – a two-stage solid-fuel nuclear-armed submarine-launched ballistic missile - and, more specifically, a nose cone

capable of resisting the heat of re-entry into Earth's atmosphere (Patel, Dubey, Roshan, & Behera, 2023).

It is worth noting that, in Ni-Ti alloys, the increase of Nickel content in the mentioned 8% atomic weight of margin can induce decreases in transformation temperature and increases in yield strength of the alloy (in both austenitic and martensitic phases), as more of this chemical element is added (Alagha, Hussain, & Zaki, 2021).

Most Ni-Ti applications regarding the medical field rely on superelasticity while more actuator-based and heat engine applications use the shape memory effect. Such effects will be heavily influenced by composition of alloy, with higher Ni content lowering transformation temperature and bestowing superelastic properties on the material, whereas higher Ti content results in higher transformation temperature and a prominent shape memory effect (Chekotu, Groarke, O'Toole, & Brabazon, 2019).

Nitinol is, by far, the most widely used SMA due to several reasons, including superior functional stability, the immense biocompability, its damping characteristics, and its high resistance to oxidation, along with his very useful temperature transformation bracket. Some of its qualities are shown in figure 44 (Tanzi, Farè, & Candiani, 2019) (Omori, et al., 2011) (Parvizi, Hashemi, & Moein, 2022).

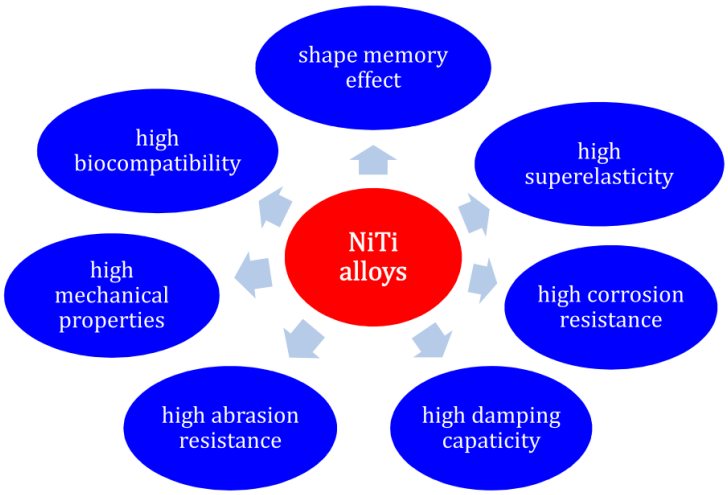


Figure 44 - Main properties of Ni-TI alloys (Parvizi, Hashemi, & Moein, 2022).

Despite these advantages, Nitinol suffers from poor workability, resulting in high tool wear in its manufacturing, making it difficult to shape into complex structures using conventional techniques. Such circumstances make additive manufacturing unique in its ability to circumvent such problems, avoiding not only the need for the mentioned tooling, but also allows its fabrication directly from CAD files, with no downside to the creation of complex shapes, as will be discussed further (Alagha, Hussain, & Zaki, 2021).

In the next table, we can see some of the main advantages and limitations of this type of alloys, and how its usage is conditioned by the following criteria.

Table 6 - Ni-Ti alloys advantages and limitations (Mehrpouya & Bidsorkhi, 2016).

Advantages	Limitations
High mechanical performance	Low energy efficiency
High power-to-weight ratio	Complex thermo-mechanical behaviour
Large deformation	Complex motion control
Large actuation force	Expensive material
High damping capacity	Temperature dependent effect
High wear resistance	Poor fatigue properties
High corrosion/chemical resistance	Low operational speed
High specific strength	---
Compactness /lightness	---

2.2.2. Ni-Ti phase diagram

The binary phase diagram of Ni-TI is a useful tool for understanding the exact microstructural changes with given heat treatments and with changes in the alloy composition. As said before, Ni-Ti alloys generally have percentages of Nickel from 49% to 57% in atomic weight, with normally metastable compositions until room temperature, therefore not requiring post-treatment or quenching processes.

The temperature at which one phase is transformed into the other is called the transformation temperature and, as can be seen on the phase diagrams of figures 45 and 46, it will heavily depend on the actual alloy content. It is worth noting that contaminants such as carbon and oxygen can vary the transformation temperature and affecting the mechanical properties, therefore increased attention must be taken to prevent such occurrences (Alagha, Hussain, & Zaki, 2021) (Parvizi, Hashemi, & Moein, 2022).

As can be seen on the Ni-Ti phase diagrams, the B2 austenitic phase, at 950ºC, goes from 49% to 57% Ni, with its left border a straight line, almost perpendicular to the concentration axis of the diagram, while the Ni-rich border of B2 has a positive slope, meaning increased solubility of Ni at higher temperatures. Of note that nickel rich B2 compositions are not stable at low temperatures, and precipitation reactions frequently occur in such cases. As a general rule, increased nickel content will decrease the transformation temperature of the martensite-to-austenitic phase (Parvizi, Hashemi, & Moein, 2022).

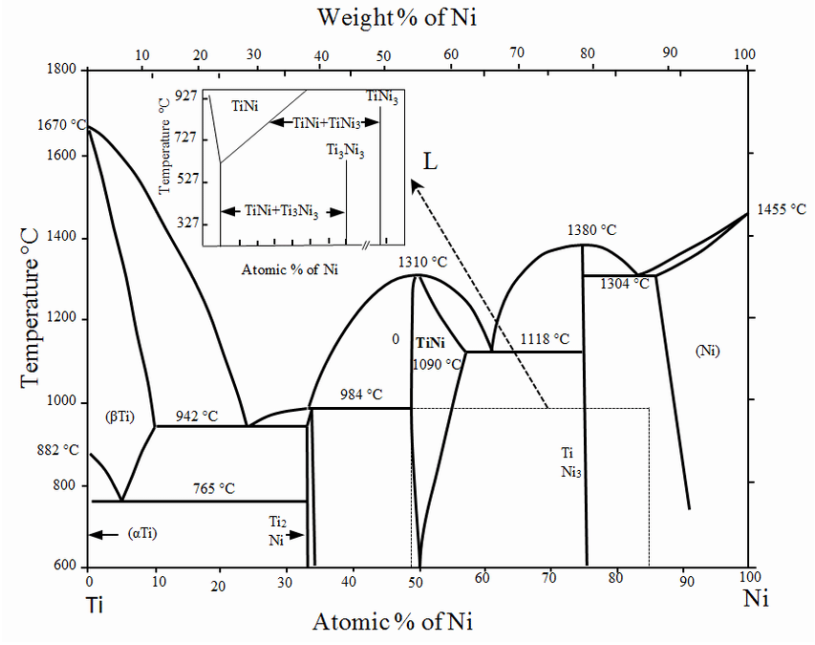


Figure 45 - Ni-Ti phase diagram 1 (Ternik, Zadravec, & Rudolf, 2017).

It is known that the solubility limit of the Ni-Ti phase is around the 900ºC, meaning that the solubility of such composition does not change with increasing the temperature. When decreasing the temperature below this limit, the boundary between the Ti-rich region and the single Ni-Ti phase becomes sloped, meaning less titanium is dissolved in the Ni-Ti composition. As can be visualized from the phase diagrams, the highest possible dissolution of Ni occurs at the eutectic point with 57% Ni, at 1118ºC. In turn, the lowest possible dissolution is around 49% Ni, at 950ºC (Parvizi, Hashemi, & Moein, 2022).

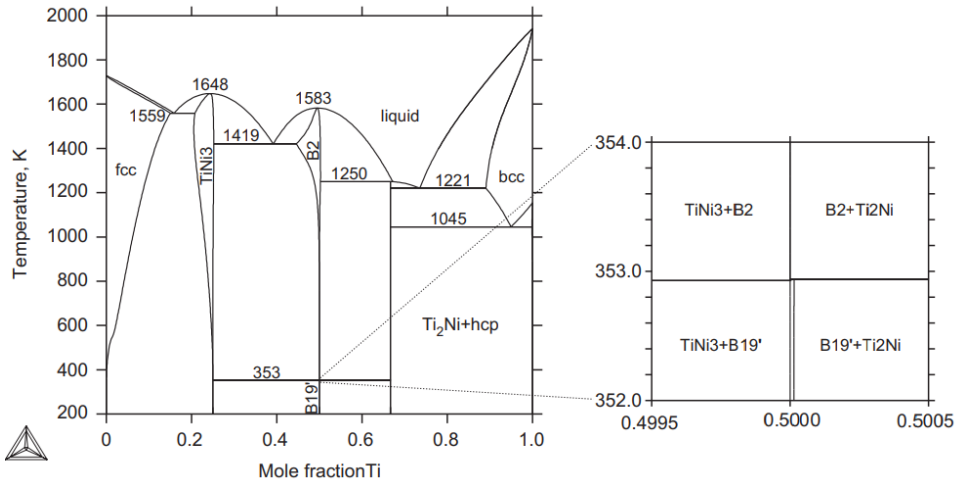


Figure 46 – Ni-Ti phase diagram 2 (Povoden-Karadeniz, Cirstea, Lang, Wojcik, & Kozeschnik, 2013).

In some cases, unwanted phases, and impurities like Ni3Ti and Ti2Ni are possible, with these compositions appearing if oxygen content infiltrates the alloy during the

production process. Such phases suppress the shape memory effect and are therefore barriers to the martensitic transformation. As such, rigorous production criteria must be observed for elimination of such impurities (Gangil, Siddiquee, & Maheshwari, 2020) (Parvizi, Hashemi, & Moein, 2022) .

2.2.3. Mechanism classification

Various mechanisms are present in shape memory alloys, which were deemed significant for explanation.

When martensite Ni-Ti is heated, it starts changing into austenite at a temperature called “Austenite start temperature” (As). The temperature at which this phenomenon ends is called “Austenite finish temperature” (Af). When, in turn, austenite is cooled, it begins changing into martensite, at a temperature called “Martensite start temperature” (Ms). The temperature at which martensite is again completely reverted is called martensite finish temperature (Mf). There is also “Austenite speak temperature” (Ap) and “Martensite peak temperature” (Mp), however these are not as important (ASTM F-2005, 2000) (Tanzi, Farè, & Candiani, 2019).

2.2.3.1. R-phase

Equiatomic Ni-Ti alloys can transform, when in cooling or when stressed, from an austenite B2 phase into two structures: the commonly known B19’ monoclinic structure known as martensite, or the rhombohedral distorted martensite, which is known as the R-phase.

While the simple martensite is more stable, the R-phase phenomenon has less barrier and conditions for its creation, creating a possibility of austenite transforming into R-phase, and then alter into martensite, creating therefore an intermediate stage of martensite – simple martensite has thermodynamical preference, however, R-phase has initial phase creation due to presenting lower activation energy, being therefore kinetically preferred (Sittner, Landa, Lukas, & Novak, 2006) (Duerig & Bhattacharya, 2015).

The R-phase can be “R-phase start temperature” (Rs), “R-phase finish temperature” (Rf), and “R-phase speak temperature” (Rp) (ASTM F-2005, 2000) (Tanzi, Farè, & Candiani, 2019).

Figures 47 and 48 show the transformation temperatures without and with R-phase existence.

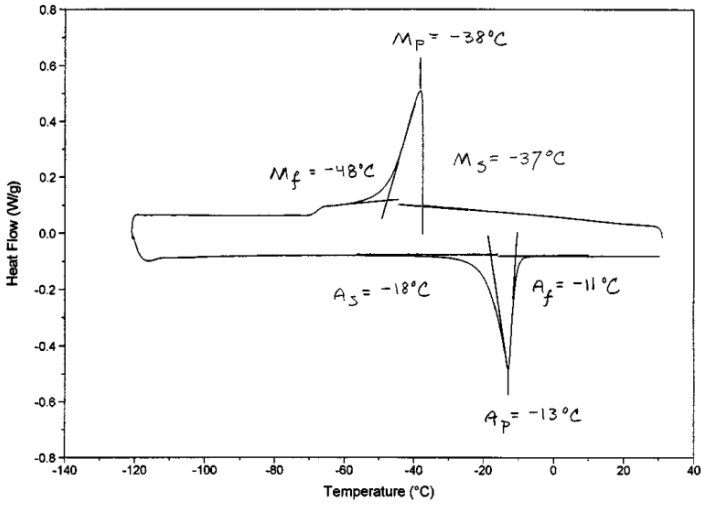


Figure 47 - Example of a single-stage transformation (without R-phase) (ASTM F-2005, 2000).

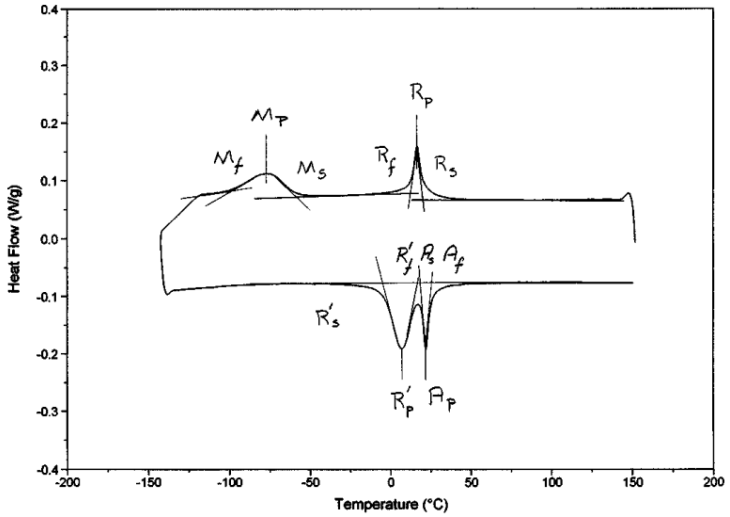


Figure 48 - Example of a two-stage transformation (with R-phase) (ASTM F-2005, 2000).

Such possibility means that shape memory alloys might have a single stage transformation or actual two-stage transformation, depending on the existence of the R-phase and how it relates to the twinning and detwinning of the martensite when subjected to deformation or heating alterations.

2.2.3.2. Shape memory effect (pseudoplasticity)

The shape memory effect of Ni-Ti is related to the existent transformation phases, which is divided in two main phases, the low-temperature martensitic and the high-temperature austenitic. This phenomenon relates to the condition when the operating temperature is lower than the martensitic phase transformation temperature. In such condition, the dominant structure is the distorted derivative (or twinned) structure of

martensite, which forms itself during the transition from the austenitic state to martensitic, which appears to intend to minimize the overall shape change of the structure (Gangil, Siddiquee, & Maheshwari, 2020) (Parvizi, Hashemi, & Moein, 2022).

When there is the existence of applied stress, the domain twin's walls start to shift, producing macroscopic strain by detwinning the martensitic structure. During release of applied stress, the stable phase would be the detwinned martensite, until the material is heated and the austinite phase is stable (Gangil, Siddiquee, & Maheshwari, 2020) (Parvizi, Hashemi, & Moein, 2022).

In such a phase, the transformation proceeds from martensite to austenite upon heating, with the macroscopic strain related to the twinning/detwinning of the process disappearing, therefore initial shape is recovered. During cooling, without application of external stresses, the material falls back into the original "twinned martensite" structure, keeping its original shape, as shown in the figure 49 (Gangil, Siddiquee, & Maheshwari, 2020) (Parvizi, Hashemi, & Moein, 2022).

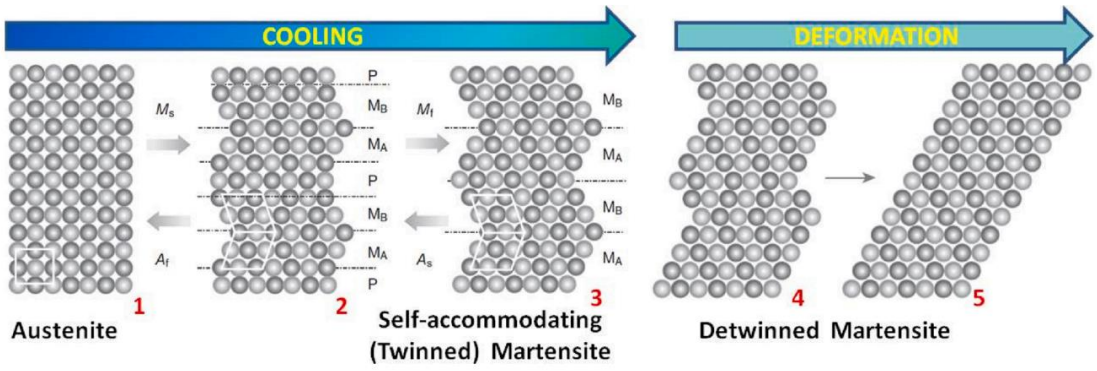


Figure 49 - Microstructural state in SME (Gangil, Siddiquee, & Maheshwari, 2020).

At the highest temperature phase of the Ni-Ti shape memory alloys, there is the arrangement of the atoms in orderly manners, in a body-centered cubic crystal structure, in the austenitic phase (also referred as B2). In such a phase, the alloy resists attempts to twist and bending actions (ASTM F-2005, 2000) (Tanzi, Farè, & Candiani, 2019). At the lowest temperature phase of the Ni-Ti shape memory alloys, there is existence of a martensitic phase, with a monoclinic (distorted) crystal structure (also referred as B19). This phase is suited for deformations on its structure, with the recoverable part happening in the austenitic phase (ASTM F-2005, 2000) (Tanzi, Farè, & Candiani, 2019). The mechanism is shown in figure 50.

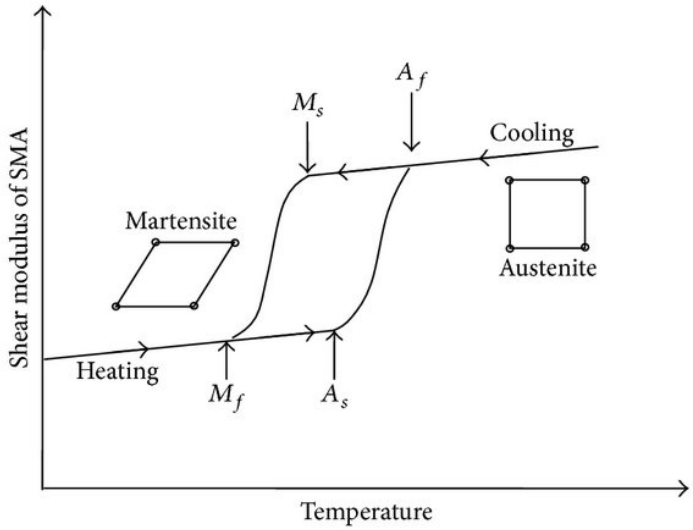


Figure 50 – Shear modulus–temperature graph of Ni-Ti (Ma, Huang, & Huang, 2013).

When martensite Ni-Ti is heated, it starts changing into austenite at a temperature called "Austenite start temperature" (As). The temperature at which this phenomenon ends is called "Austenite finish temperature" (Af). When, in turn, austenite is cooled, it begins changing into martensite, at a temperature called "Martensite start temperature" (Ms). The temperature at which martensite is again completely reverted is called martensite finish temperature (Mf) (ASTM F-2005, 2000) (Tanzi, Farè, & Candiani, 2019).

Therefore, the shape memory effect is the ability of the material to recover the initial and predefined shape against an external stimulus like temperature, electromagnetic field, or stress, with the possibility of Ni-Ti SMAs applying, during the shape recovery process, energy as high as several hundred Megapascals, as recovery stress. In other words: SME is the ability to recover the original shape after deformation following a thermal cycle (Tanzi, Farè, & Candiani, 2019) (Parvizi, Hashemi, & Moein, 2022).

2.2.3.3. Superelasticity (pseudoelasticity)

Superelasticity, also known as pseudoelasticity, is a phenomenon that occurs when the functional temperature is above the Austenite finish temperature or between the Austenite start and finish temperature.

In such conditions, the application of stress on the structure will stabilize the structure in the martensitic phase, and, by removal of the stress, martensite will become thermodynamically unstable, therefore the alloy will revert to the austenitic phase, with recovery of the original shape. This translates, in practical applications, that no thermal cycling is needed for transformation and that large strains applied by loading can be recovered by simple unloading of the alloy, as can be seen in figure 51 (Jani, Leary, Subic, & Gibson, 2014) (Tanzi, Farè, & Candiani, 2019) (Parvizi, Hashemi, & Moein, 2022).

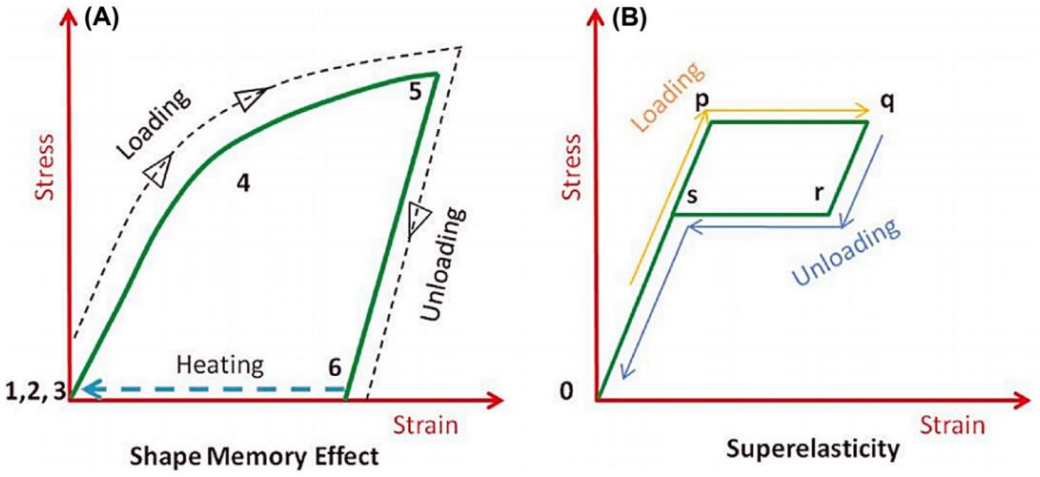


Figure 51 – One-way shape memory effect (left) and superelasticity (right) (Gangil, Siddiquee, & Maheshwari, 2020).

Such mechanism is created by deforming the SMA in a martensitic state below Mf and subsequent heating of the alloy to temperatures higher than As or Af. By loading below the critical stress, the austenitic phase will transform into a two-phase structure of martensite and austenite (Jani, Leary, Subic, & Gibson, 2014) (Tanzi, Farè, & Candiani, 2019) (Parvizi, Hashemi, & Moein, 2022). Another example of the superelasticity phenomena can be seen in figure 52.

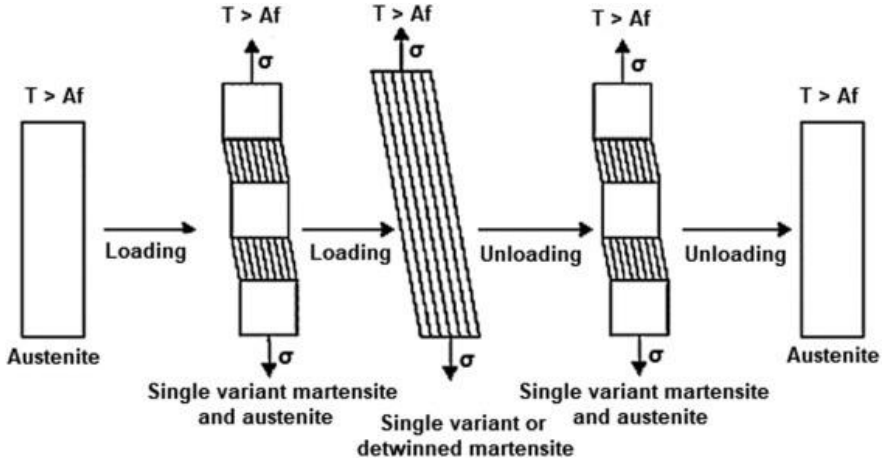


Figure 52 – Superelasticity phenomena (Parvizi, Hashemi, & Moein, 2022).

2.2.3.4. Two-way SME

When discussing the subject of shape memory behaviour, there are three main responses observed: One way shape memory (OWSMA), two-way shape memory (TWSMA) and full shape memory alloys (FSMA) (Jani, Leary, Subic, & Gibson, 2014) (Tanzi, Farè, & Candiani, 2019) (Parvizi, Hashemi, & Moein, 2022). Schematics of the mechanism can be seen in figure 53.

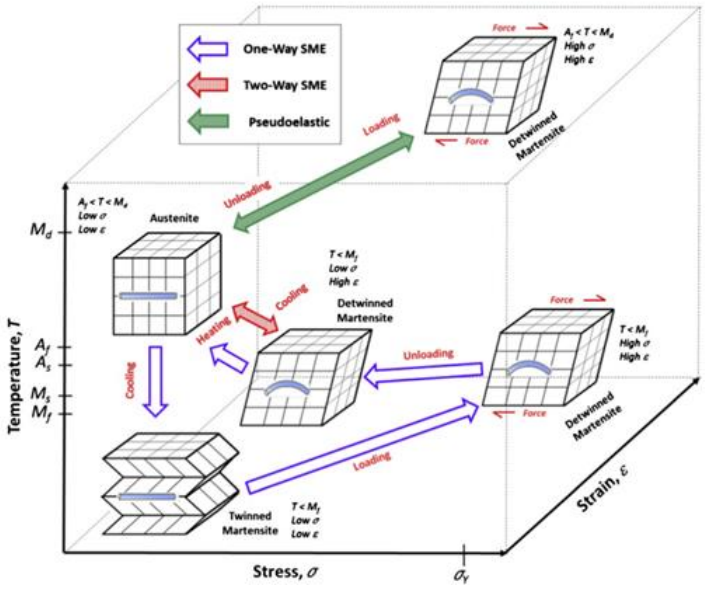


Figure 53 - SMA phases & crystals structure (Jani, Leary, Subic, & Gibson, 2014).

In the subchapter before, there was discussion of the memorization of the austenitic phase, however, there is the possibility of memorization of the martensitic phase – a two-way shape memory effect. TWSMA is the shape recovery of Ni-Ti both in heating and in cooling phases, without the necessity of any applied stress – this means that only thermal cycles are needed for the completion of the total strain cycle and there is not the necessity of mechanical deformations for such cycling effect. This translates into the remembering of the phases both in low temperature (martensitic) and high temperature (austenitic) (Jani, Leary, Subic, & Gibson, 2014) (Tanzi, Farè, & Candiani, 2019) (Parvizi, Hashemi, & Moein, 2022). Examples of OWSMA vs TWSMA can be seen in figure 54.

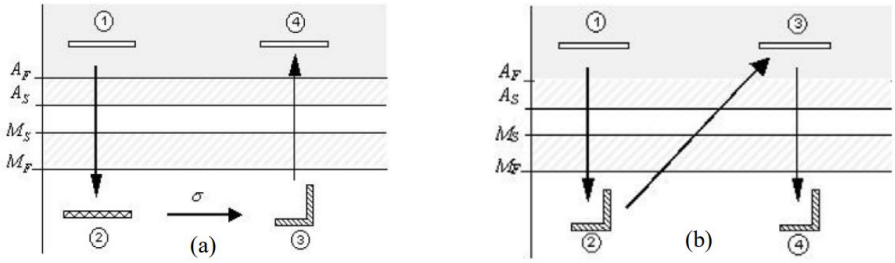


Figure 54 – OWSMA (a) vs TWSMA (b) (Pereira, 2009).

TWSMA is only present in alloys exposed to specific thermomechanical treatments, unlike OWSMA which is present in all Ni-TI alloys. If the arrangement of variants during cooling is suitably controlled, a shape change during cooling can therefore be attained. *(Jani, Leary, Subic, & Gibson, 2014) (Tanzi, Farè, & Candiani, 2019) (Parvizi, Hashemi, & Moein, 2022)*

2.2.3.5. Full-way SME

Regarding FMSA, when at low temperatures and when there is deformation, the structure of the twinned martensite is transformed into detwinned martensite. When the temperature rises above the austenite finish temperature, the transformation of martensite to austenite will occur and the original shape will be completely recovered. During cooling cycle, different behaviour will occur with the inverse shape being recovered. Therefore, this will correlate with the R-phase existence, where the R-phase is a form of twinned martensite (Gangil, Siddiquee, & Maheshwari, 2020). The different types of SMA deformations can be seen in table 7.

Table 7 - Types of SMA deformations (Gangil, Siddiquee, & Maheshwari, 2020).

SMA	Original shape	Low-temperature deformation	High-temperature deformation	Cooling deformation
One-way SMA				
Two-way SMA				
Full SMA				

2.2.4. Applications

The applications regarding this type of material are numerous, ranging from biomedical implants, to automotive, aerospace, and energy sector applications, as can be seen in figure 55.

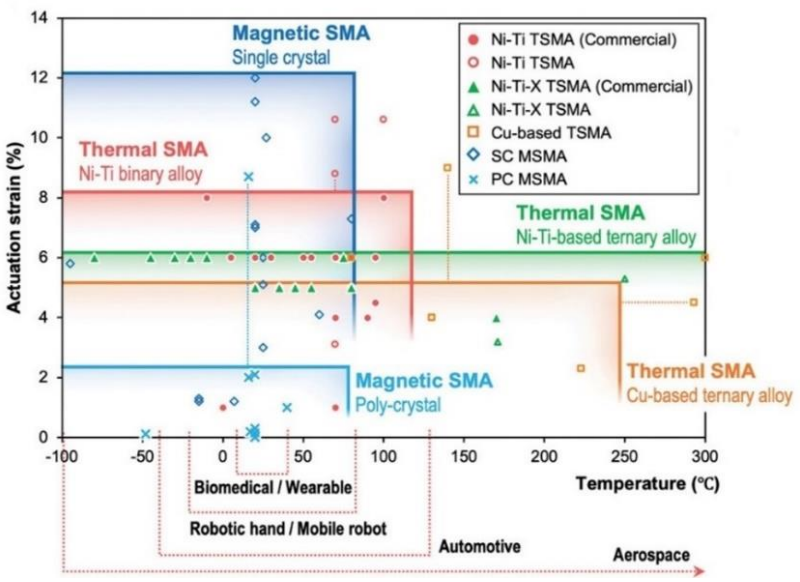


Figure 55 - Comparison of different SMA materials in terms of actuation strain and temperature. Of note is the versatility of Ni-Ti binary alloys, which explains its high usage (Kim, et al., 2023).

The temperature range related to the overall transformation temperatures of Ni-Ti alloys allow for increased versatility, and increased usage and focus of this particular SMA when related to other SMM (Kim, et al., 2023) (Parvizi, Hashemi, & Moein, 2022).

The usage of SMAs are varied, being able to be used in a wide range of applications, from wearable devices, mobile robots, robotic hands, automotive/aerospace appliances,

biomedical devices, among others, with the unique properties allowing great versatility of use on its usage (Kim, et al., 2023). Examples can be seen in figure 56.

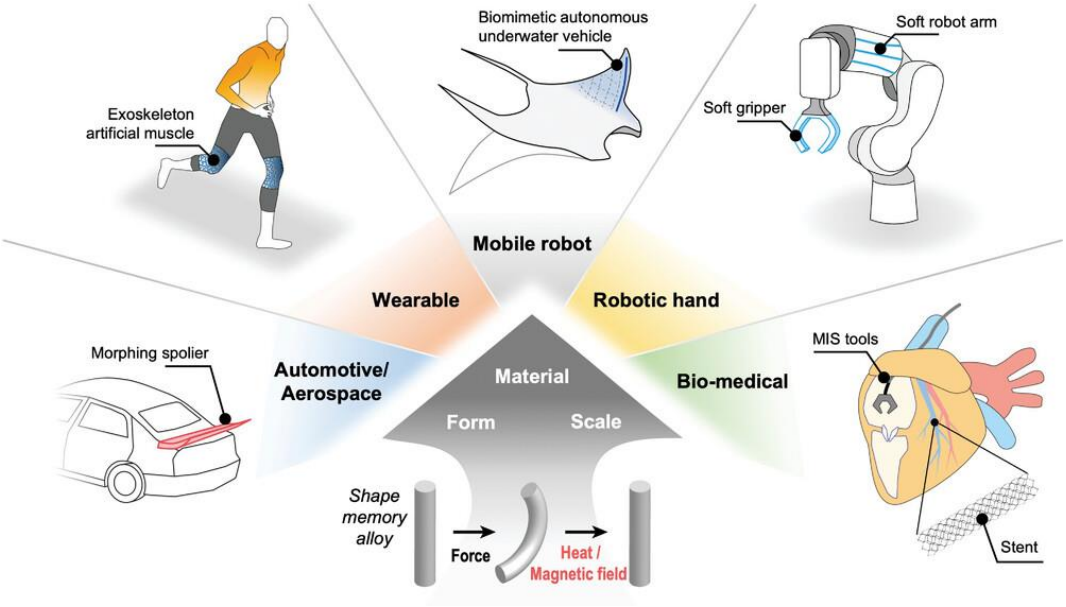


Figure 56 - Wide range of applications of SMAs (Kim, et al., 2023).

i) Couplings

Coupling systems, such as seen in figure 57, are one of the main uses of Ni-Ti SMAs, with the advantages of easy tooling installation, design simplicity, no corrosion in the coupler, possibility of joining of dissimilar materials, minimal leakages, looser tolerances necessary for joining process and easy engagement and disengagement, coming at the disadvantages of high cost of material, and necessity of transportation of the coupler at cryogenic temperatures (prior to installation).

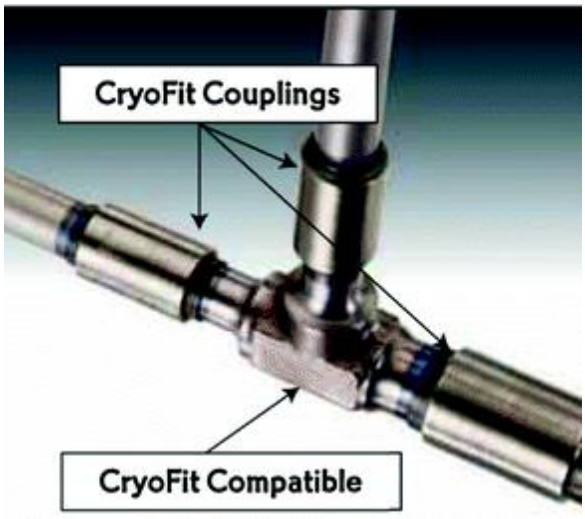


Figure 57 - Cryofit coupling system (Prasad & Wanhill, 2016).

One of its first uses being in 1969, when it was applied in hydraulic components for the Grumman Aerospace Corporation regarding the development of the US Navy's F-14 fighter aircraft, with the usage of the Cryofit tube coupling system (Prasad & Wanhill, 2016) (Barik & Samal, 2022). In such system, the expanded coupling have inside diameters slightly larger than tube outside diameters. Meanwhile, as the coupling warms up from a liquid nitrogen bath, when exposed to room temperature, they contract,

generating a lightweight, simplified metal-to-metal seal (Junior, Jr, & Savi, 2016) (Gangil, Siddiquee, & Maheshwari, 2020). Schematic example is shown in figure 58.

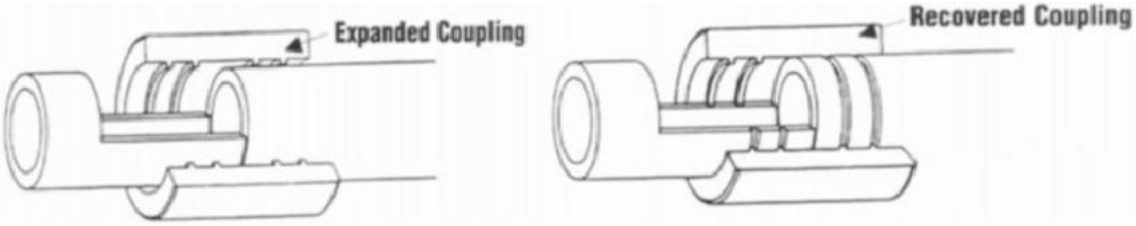


Figure 58 – SMA coupling mechanism (Junior, Jr, & Savi, 2016).

This type of couplings allow to sidestep the necessity of perfectly alignment, as seen in conventional sleeve, flange and split muff couplings, since the dimensions of both sides of the coupling system can be manipulated through thermal manipulation. In addition, certain post-processing such as soldering or brazing used in conventional couplers can in fact weaken the connection, reducing its strength, due to development of heat-affected zones where coarse grain formations might take place. There is also the possibility of reduced vibrations, adding value to such coupling systems, especially in shipbuilding, offshore and aerospace, due to simplified part assembly and mechanics (with the caveat of absence of high-frequency vibrations) (Barik & Samal, 2022). Examples are shown in figures 59 and 60.

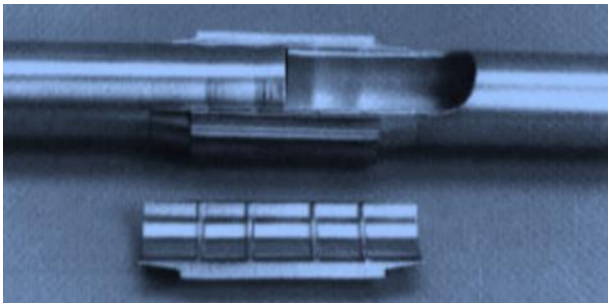


Figure 59 - Ni-Ti pipe coupler of a Y12F hydraulic system (Barik & Samal, 2022).



Figure 60 - SMA coupler in offshore applications (Barik & Samal, 2022).

ii) Aerospace

A popular aerospace application of SMAs is the usage of morphing wings, which involve structural modifications to the aircraft airframe, so that certain specifications can be met in different utilization conditions (for example, variable wing design depending on Mach speed of the aeronautical vehicle) (Constanza & Tata, 2020).

Some of the advantages are increased speed and efficiency, with reduced power consumption and increased roll control. Such projects normally require drawbacks such as surface discontinuity and severely increased weight due to the necessary control surfaces – this can be greatly reduced with the usage of SMA materials, such as seen in the projects of DARPA (as can be seen in figure 61) – the Smart Wing Program (SWP) and Smart and Aircraft and Marine Propulsion System Demonstration (SAMPSON) – with the first relating to applications regarding lifting devices and the second the research of new shape-adaptive structures for next gen aircraft (Hartl & Lagoudas, 2007) (Savi, Paiva, Araujo, & Paula, 2016) (Constanza & Tata, 2020).

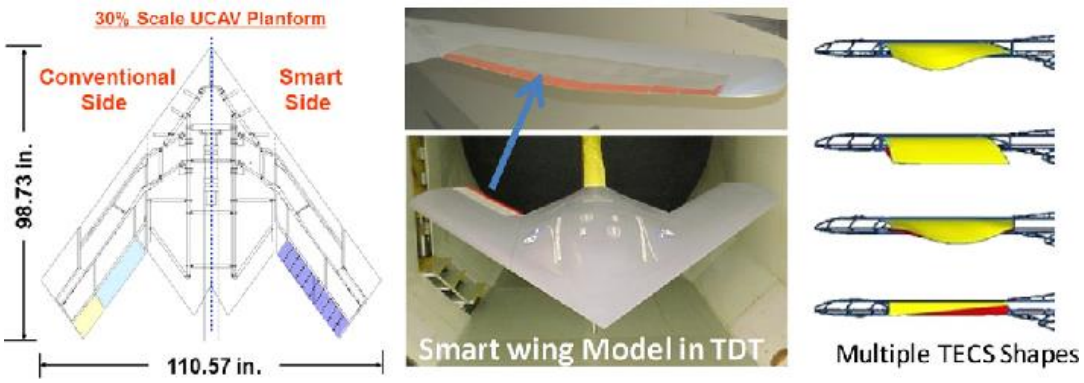


Figure 61 - Overview of the DARPA Smart Wing program (Carman, Inman, Kudva, & Leo, 2015).

The usage of chevron variable geometry at the rear end of the chevron nozzle allows for reduction in jet noise at take-off, reducing noise pollution. Despite this, such device negatively affects cruising speed, by reduction of thrust and increase in drag.

Due to this, a solution was reached through a Variable Geometry Chevron (VGC), as can be seen in figure 62, allowing all-out bending during take-off and landing and minimum applied deflection while in cruise speed parameters, so that flight efficiency could be maintained, while also allowing for noise reduction at take-off and landing



Figure 62 - Variable Geometry Chevron demonstration (Hartl & Lagoudas, 2007).

(Hartl & Lagoudas, 2007) (Constanza & Tata, 2020).

In addition, lifting bodies adaptation can also be achieved, for a modification of intrinsic vibration frequencies, and reinforcing of complex matrix structures, with insertion of Ni-Ti wires into Kevlar fiber epoxy matrixes (Constanza & Tata, 2020).

iii) Blast protection

In 2003, a US patent was made for a lightweight armor with repeated hit absorption capabilities regarding high energy transfers, with a capability of "reversible change phase and/or an elastic deformation of at least 5%", based on a Ni-Ti alloy, as replacement for titanium, ceramic or reactive based armors, since armor piercing projectiles are currently surpassing protective vehicles capabilities. By tailoring the composition of Ni-Ti, it is possible to tailor the transformation temperature, or in other words, the energy input, from austenitic to martensitic phase (U.S.A. Patent No. US7082868B2, 2003). The patent is shown in figure 63.

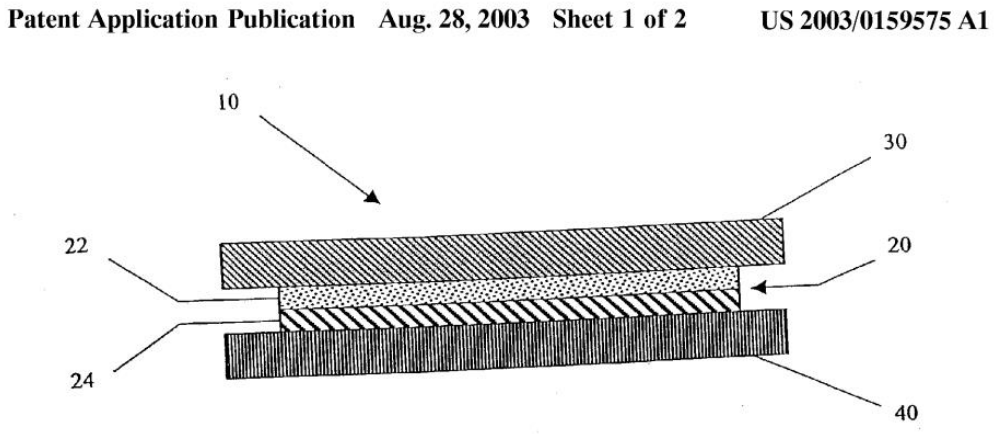


Figure 63 - Example of the blast protection mechanism in the patent. Several variations are possible, such as one where plate 30 was composed of Ni-Ti, and, in other instance, 30 being Ti6Al4V and 20 being Ni-Ti (U.S.A. Patent No. US7082868B2, 2003).

In 2006, Sino-Japanese researchers investigated the possibility of porous Ni-Ti SMAs for high energy absorption applications, with the possibility for incorporation of this material for blast protection in armoured vehicles. In particular, porous Ni-Ti was lighter than dense Ni-Ti alloys but had similar capabilities of resistance to energy discharges, being possible its application to also naval and aerospace sectors. In such applications, it recovered the form in low-impact energies and served a critical energy absorber/dampening effect in high-impact energy considerations (Lagoudas, Ravi-Chandar, Sarh, & Popov, 2003) (Zhao, Taya, Kang, & Kawasaki, 2005) (Yang & Qiao, 2010).

The energy dissipated through under the given adiabatic loading condition is shown in the next figure. As it can be seen, there was dissipation of 85% of input energy through the SMA phase transformation, as can be seen in figure 64.

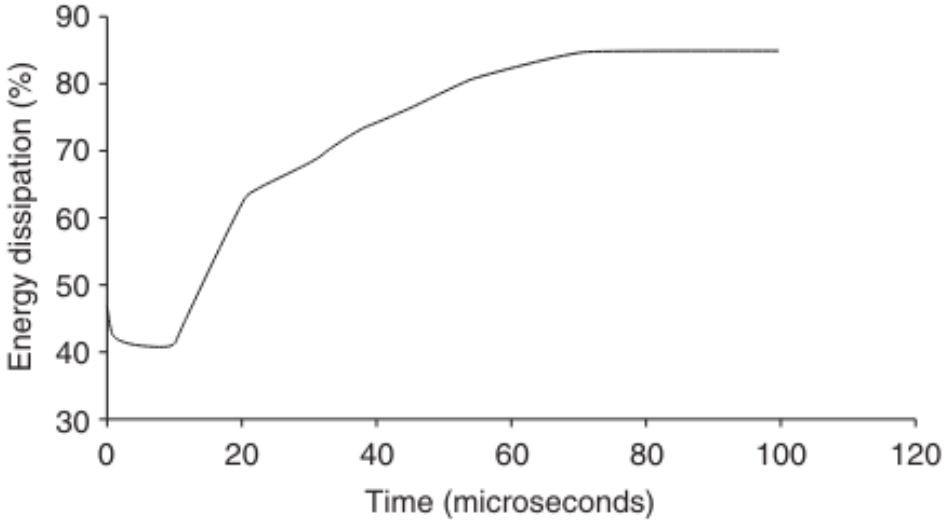


Figure 64 - Energy absorbed by a SMA rod under adiabatic conditions (Lagoudas, Ravi-Chandar, Sarh, & Popov, 2003).

The energy dissipated through the SMA rod under the twinning loading condition is shown additionally, with about 85% of the input kinetic energy has been dissipated under twinning condition, as can be seen in figure 65.

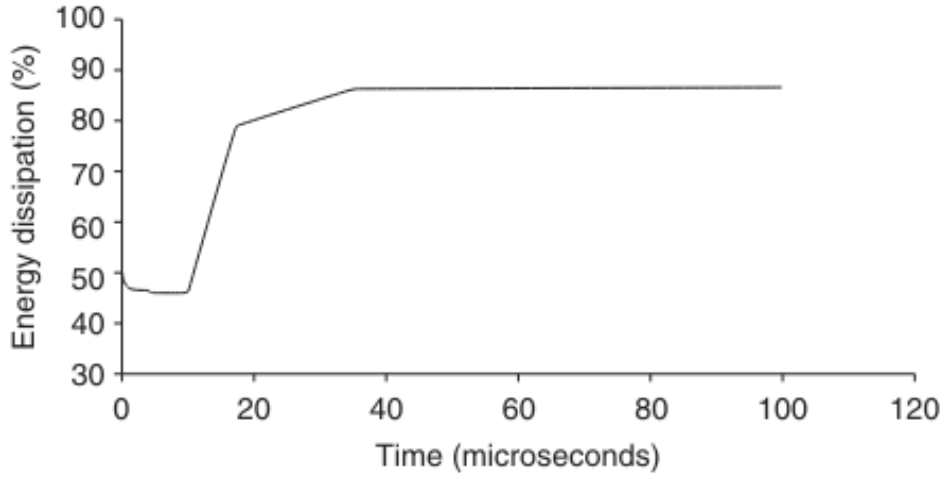


Figure 65 - Energy absorbed by a SMA rod under twinning conditions (Lagoudas, Ravi-Chandar, Sarh, & Popov, 2003).

In 2016, BAE Systems unveiled a “memory metal suspension system” for its line of armoured vehicles, simplifying the suspension system and increased protection capabilities, through a “wishbone suspension that can not only pop back into shape after being badly bent in an explosion, but which is flexible enough to do away with the springs entirely, resulting in a simpler design”, as can be seen in figure 66.

It is not specified which vehicles of the corporation had this technological development of a “new bendable titanium alloy suspension concept” applied or whether industrial competitors have similar R&D programmes with SMAs also being applied (Memory Metal Suspension for Military Vehicles, 2016).

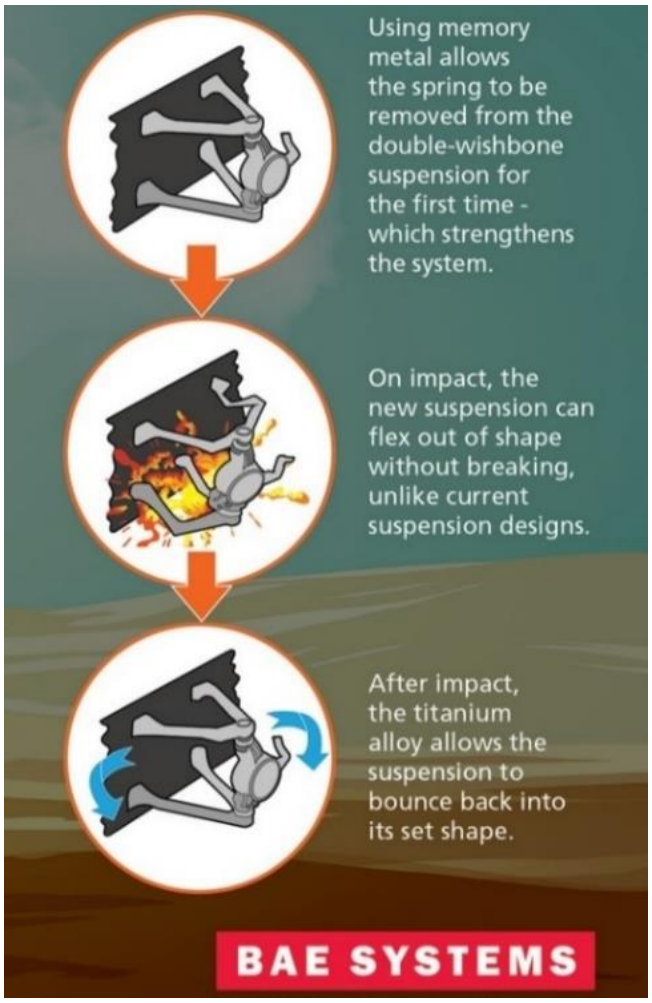


Figure 66 – “Memory Metal” technology (Memory Metal Suspension for Military Vehicles, 2016).

iv) Actuators

Demands for safety and comfort in modern vehicles led to an increase in sensors and actuators in automotive vehicles, which also allow better performance of the vehicles, with smart memory alloys allowing greater opportunities than simple electromagnetic, pneumatic, or hydraulic ones, through reduction of cost and weight and providing significant performance improvements (Khidir, Mohammed, Nor, & Mustafa, 2007) (Behera, Sahoo, & Mohapatra, 2022).

SMA linear actuators are a common and popular application of this material, with high electrical resistivity, excellent corrosion resistance and high mechanical strength and the possibility for electrical or thermal activation being used in a myriad of applications in industries, from aerospace to automotive (Khidir, Mohammed, Nor, & Mustafa, 2007) (Behera, Sahoo, & Mohapatra, 2022) (Parvizi, Hashemi, & Moein, 2022). Examples are shown in figure 67.

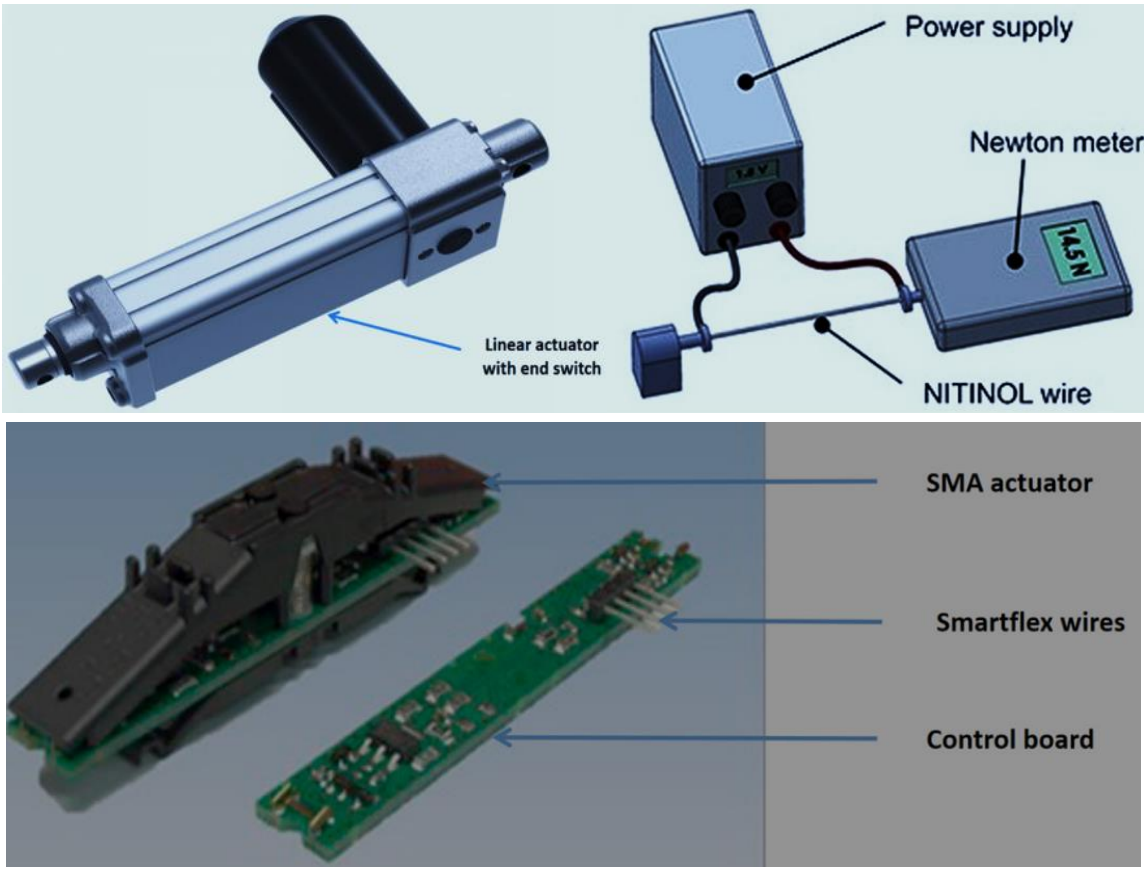


Figure 67 - Various examples of actuators used with Ni-Ti, such as for a battery module (left), with wires (right), and through a control board (down) (Behera, Sahoo, & Mohapatra, 2022).

This application can be used in thermal valves, acting as both actuator and sensor; in the replacement of general actuators such as robotic servo motors (as can be seen in the Stilito robot); has also become an industry standard in pneumatic valves for comfort seating; and can be used as optical image stabilizer in mobile phones and an autofocus actuator in action cameras (Behera, Sahoo, & Mohapatra, 2022).

v) Automotive

There are a myriad of automotive companies utilizing smart material in the manufacturing of their vehicles. The applications of smart hybrid materials in various parts of vehicles and in the automotive industry are discussed below. (Behera, Sahoo, & Mohapatra, 2022) (Parvizi, Hashemi, & Moein, 2022).

As can be seen in figure 68, examples of applications of this material in the sector can include equipment such as (1) fog lamp, (2) engine hood lock, (3) transmission control, (4) seat belt adjustment, (5) shock absorber adjustment, (6) trunk lock, (7) filler inlet lock, (8) central locking system, (9) rear-view mirror adjustment, (10) wiper pressure control, (11) climate control, (12) seat belt adjustment, (13) transmission control, and (14) engine control (Behera, Sahoo, & Mohapatra, 2022) (Parvizi, Hashemi, & Moein, 2022).

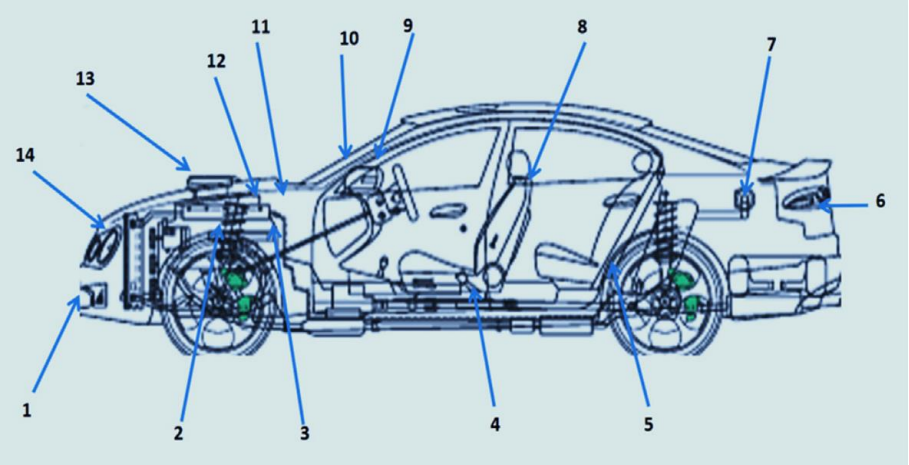


Figure 68 - Various uses of SMAs in automotive industry (Behera, Sahoo, & Mohapatra, 2022).

Practical examples include a smooth gear shifting upgrade for a Mercedez Benz transmission system and SMA pneumatic valves for car seats in Mercedez Benz, Ford, Volkswagen, General Motors, and BMW products (Leary, Huang, Ataalla, Baxter, & Subic, 2013) (Behera, Sahoo, & Mohapatra, 2022) (Parvizi, Hashemi, & Moein, 2022).

Chevrolet reduced its Corvette automotive products weight by more than 40kg, through replacement of existing actuators with SMA based ones, with as much as 200 components in the car being possible for replacement by SMA actuators. One example is the replacing the hatch vent that releases air from the trunk part, through an SMA actuator that utilizes heat input from an electric current. When activated, the Ni-Ti wire contracts and moves a lever arm to open the vent. Once it is no longer needed, the electrical current switch off, colling the wire and returning to its original shape. This component is 0.5 kilograms lighter than its conventional motorized system predecessor (GM's first use of heat-activated shape memory alloy to replace heavier motorized part, 2013) (Chevrolet Corvette SMA, 2013).

vi) Biomedical

Biomedical applications have suffered extensive research efforts with this technology, due to the possibilities regarding the shape memory effect allied with excellent corrosion resistance, good biocompatibility (the ability of a material to perform a specific application similarly to the host body), overall similar elastic modulus to bone, and high strength characteristics (Manik & Sahu, 2022).

Biomedical devices such as self-expanding vascular stents represent a very interesting application of SMAs, with Ni-Ti stents being able to have a small diameter prior to insertion into the delivery system of a body, with recovery of the permanent shape (larger diameter, for example) happening with thermal input of the body temperature, allowing

for a minimally invasive approach, as the stent can remember the shape at the austenitic phase at elevated temperature. There is also tweezers for eliminating foreign objects through small incisions, and anchors for tendon fixation techniques, among other examples (Tanzi, Farè, & Candiani, 2019).

Example of the stent is shown in figure 69 and a myriad of implants are shown in figure 70.

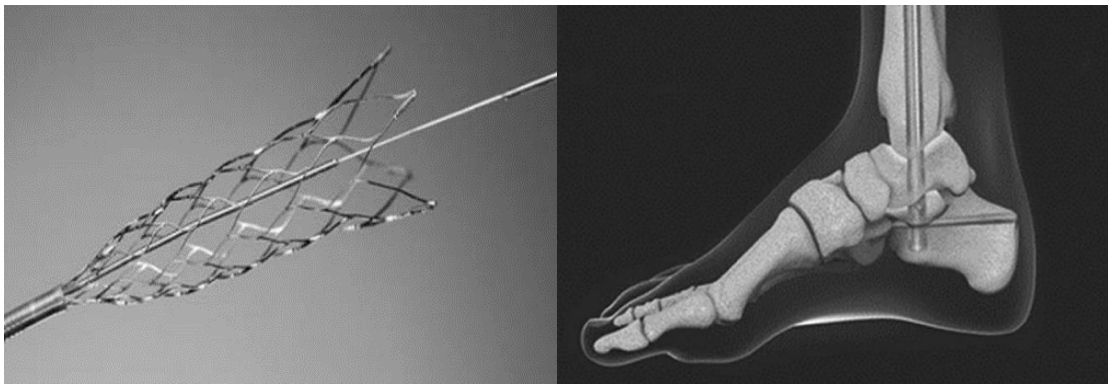


Figure 69 - NiTi self-expandable neurosurgical stent (left) and bone-implant (right) (Petrini & Migliavacca, 2011) (Patel, et al., 2020).

In applications such as orthodontics, drug delivery systems and implant devices, it is also used due to the biocompatibility, corrosion resistance and the MRI (magnetic resonance imagery) compatibility they offer. The high nickel content is the main reason why such biocompatibility is possible, being recorded as a very safe biomaterial for use in implants (Manik & Sahu, 2022) (Sathishkumar, et al., 2023).

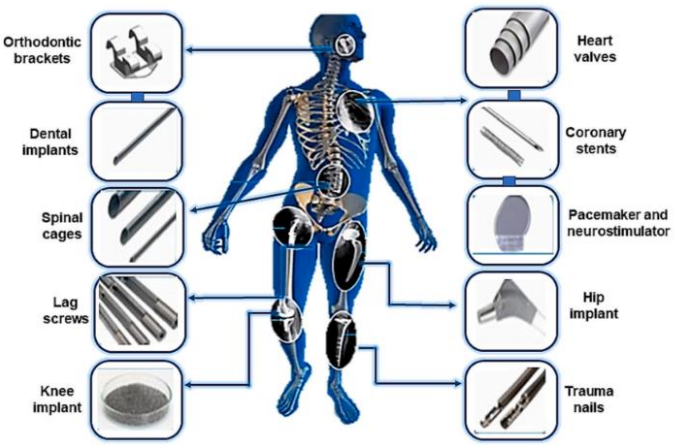


Figure 70 - Applications of Ni-Ti in biomedical (Sathishkumar, et al., 2023).

Ni-Ti alloys impart mechanisms very similar to bone structure (due to similar elastic modulus) when used as implants and have replaced 316L stainless steel due to the better overall mechanical properties and hysteresis behaviour. Another reason for such adoption is the capability of human bone to exhibit a recoverable strain limit superior to 1%, while Ni-Ti can reach around 8%, meaning it will not be an inferior strength body part when compared with typical bone structure (Petrini & Migliavacca, 2011) (Patel, et al., 2020) (Manik & Sahu, 2022).

2.2.5. Market & Economical Considerations

SMAs in general, and Ni-Ti alloys in particular, have extensive usage in modern society, due to their unique characteristics and versatility. With rapid increases in worldwide population, it is expected that this market will grow considerably due to the focus of such alloys in medical and transport industries (mainly aerospace and automotive) (Global Shape Memory Alloys Market Size, Industry Report, 2019-2025, 2018).

Biomedical applications are paramount on the usage of this type of materials due to increased biocompatibility, versatility of form, and the necessity of reduction of invasive surgeries. In the automotive sector, increased demands for performance, comfort and safety is contributing to the development of advanced sensors, microcontroller, and actuators, increasingly replacing more conventional actuator design (pneumatic and hydraulic). Aerospace and defense market is also increasing its usage of these alloys, with main usage in sensors, actuators, and structural members, for attempts at simplifying components while reducing weight *(Global Shape Memory Alloys Market Size, Industry Report, 2019-2025, 2018)*.

The international market is currently evaluated in 14 billion USD and is expected to grow at a 14.02% CAGR, as can be seen in figure 71, reaching almost 45 billion USD in 2030. Increased global industrial output and population, allied with increased demands in biomedical, aerospace, defense and automotive industries are the key drivers of this technology (Shape Memory Alloys Market Research Report 2018-2030, 2018).

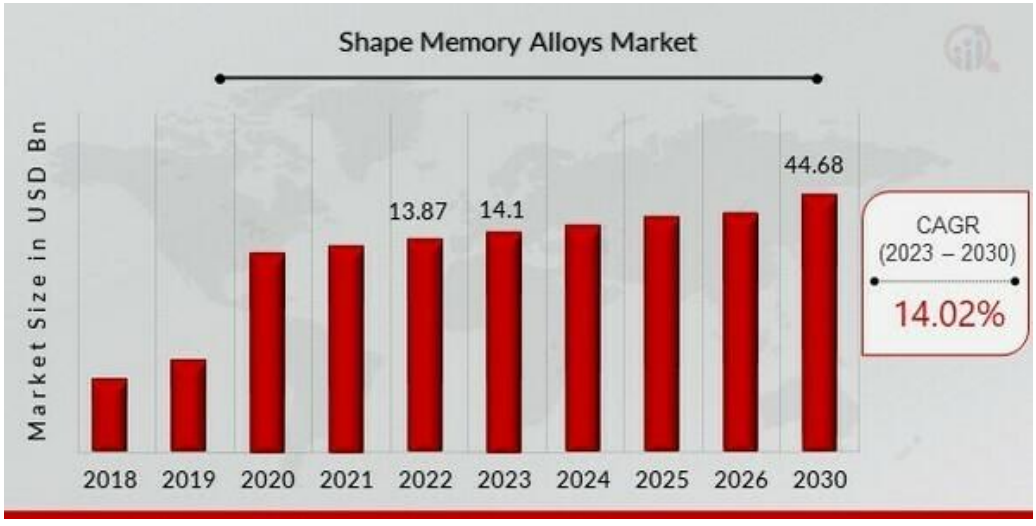


Figure 71 - SMA market, from 2018 to 2030 (Shape Memory Alloys Market Research Report 2018-2030, 2018).

The global shape memory alloys market share, in 2018, is shown in figure 72, with distinction between several key industries of the current era. Biomedical applications accounted for 60.7% of the market in 2018, with estimations to continue such primary place in the sectors. Automotive sector is expected to also increase due to rising demand

of enhanced performance, safety, and comfort of modern vehicles. It is worth noting that advancements in such technology are both from government entities (such as NASA) as well as private-owned corporations (such as SAES Getters) (Global Shape Memory Alloys Market Size, Industry Report, 2019-2025, 2018).

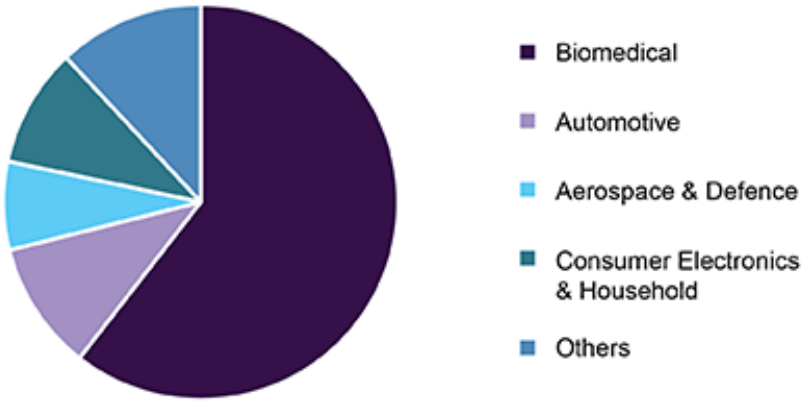


Figure 72 - Global SMA market share, by end use, in 2018 (Global Shape Memory Alloys Market Size, Industry Report, 2019-2025, 2018).

Meanwhile, the publications regarding the different areas, from 1990 to 2013, as shown in figure 73, make it clear that engineering and material science area are the departments most interested in such technology, with physics and strictly medical fields also being interested in the possibilities of such technology (Fang & Wang, 2020).

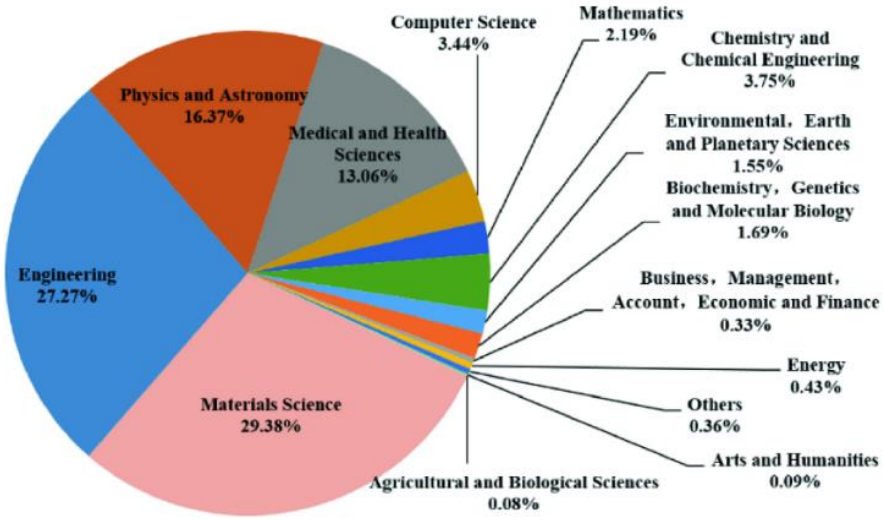


Figure 73 - SMA publications by subject areas, from 1990 to 2013 (Fang & Wang, 2020).

Some of the key corporations related to the SMA market are SAES Getters S.p.A, TiNi Alloy Co, Ultimate NiTi Technologies Inc, DYNALLOY, Inc., EUROFLEX GmbH, Confluent Medical Technologies, Inc, Burpee Materials Technology LLC., TiNi Aerospace, FURUKAWA ELECTRIC CO. LTD, Aerofits Products Inc, Baoji Titanium Industry CO., LTD, and XSMA, Inc. (Shape Memory Alloys Market Research Report 2018-2030, 2018)

2.3. 4D printing

With the significant advancements in MAM technology, and the overall progress and increased interest in SMMs, specially regarding automotive, aeronautical, and biomedical industries, the term 4D printing is introduced so as to combine the synergy of both processes. 4D printing therefore is a blend between 3D printing manufacturing techniques and the added dimension of time itself – smart materials printing that can react to external stimuli (Saritha & Boyina, 2020). Figure 74 shows an example of the transformation.

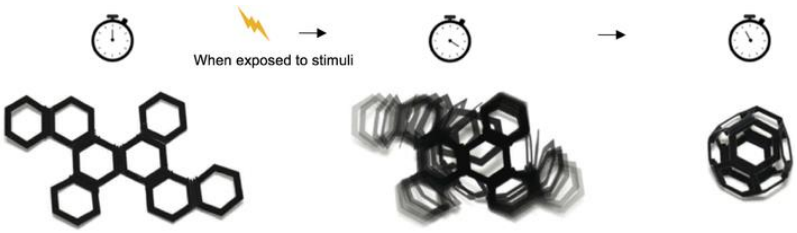


Figure 74 - 4D-printed self-folding truncated octahedron with "transformation over time" effect (Pei & Loh, 2018).

Additive manufacturing was found quite effective at manufacturing of complex Ni-Ti geometries with homogeneous composition, pre-designed porosity and overall, more desirable properties, when compared with more traditional conventional techniques. Such technique is able to achieve structures with high density and near net shape, with little processing required posterior to manufacture. Of note that AM process parameters can be manipulated to create comparable properties to those of conventionally processed Nitinol, including surface morphology and shape memory characteristics. (Chekotu, Groarke, O'Toole, & Brabazon, 2019). Figure 75 shows the main differences between 3D and 4D printing.

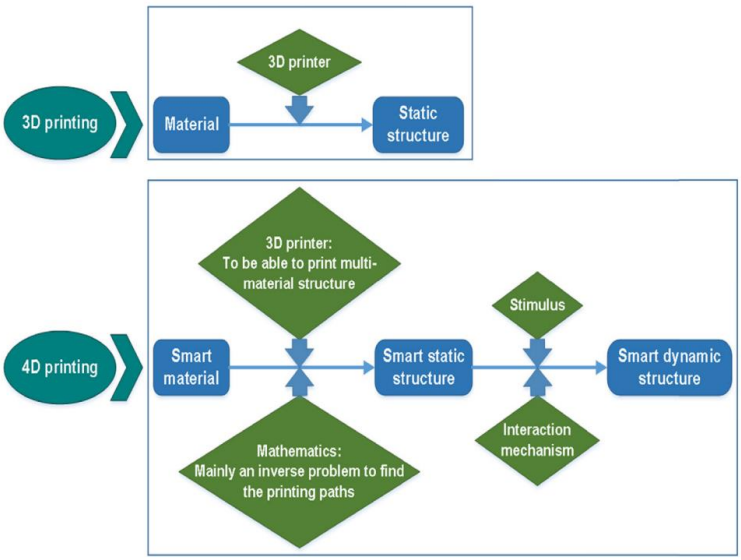


Figure 75 - Difference between 3D and 4D printing (Patil & Sarje, 2021).

A key advantage is the potential combination of such technologies is that they allow vastly increased ease of manufacture of SMAs, when having materials difficult to process through more conventional manufacturing techniques, such as the case of Ni-Ti, which is quite difficult to manufacture due to the high content of titanium (between 40% to 50%) – an element known for the high wear on milling tools and for low overall machinability. In addition to the usage of MAM techniques allowing for more complex geometries and increased freedom of design, it is stated that additive manufacturing can be used to process Ni-Ti components with little post-processing required, allowing high densities and near-net shapes, creating structures with pre-determined porosity, properties, and composition (Chekotu, Groarke, O'Toole, & Brabazon, 2019) (Patil & Sarje, 2021).

The main processes used for 4D printing, regarding metal solutions, are L-PBF and DED. As a general rule, L-PBF allows for a better and more controllable composition of Ni-Ti allows, being the preferred method of manufacturing due to its superior processing characteristics and having the most extensive research conducted (Chekotu, Groarke, O'Toole, & Brabazon, 2019) (Patil & Sarje, 2021). Table 8 shows the key differences between both technologies.

Table 8 - L-PBF vs DED manufacturing in SMAs (Chekotu, Groarke, O'Toole, & Brabazon, 2019).

L-PBF	DED
Homogeneous composition from feedstock composition	Composition varies spatially and may differ from feedstock composition
Columnar grains (due to orientation in build direction)	Equiaxial grains (more uniform orientation of the build)
Uniform strain accumulation (due to homogeneity of material structure)	Heterogeneous strain accumulation (heterogeneity of material structure)
Shape recovery require temperature increase - more stable detwinned martensite	Residual martensite recovers on heating – less stable detwinned martensite
Stress-strain curve shows plateau when critical stress is exceeded	Stress-strain curve shows strain-hardening response when critical stress is exceeded

This technology is not without its flaws however, with the main challenges of manufacturing of Ni-Ti through conventional means, as well as through additive ones, being: the production of complex structures, the creation of a uniform and homogeneous composition, a low level of machinability (due to the high elastic and abrasive nature of Ni-Ti), the acquisition of good Ni-Ti material (free of oxides and inclusions), the provision of an inert atmosphere (so as to avoid oxidation), avoiding impurities (affecting transformation temperatures, mechanical resistance and crack propagation), avoidance of

flaws and porosity (due to crack propagation mechanics and reducing of total possible load) (Lu, et al., 2019) (Chekotu, Groarke, O'Toole, & Brabazon, 2019).

Despite such potential, with great flexibility of design, there is a contradiction occurring in L-PBF – there is the necessity for high enough levels of laser power input so as to melt the powder particles of Ni-Ti and obtain parts with full density, while there is also the necessity of low enough levels of laser power input so as to minimize the temperature gradient and residual stress between the melt pools and the particles of the powder, so as to avoid cracking tendencies. This can occur in a myriad of materials in fact but is especially evident in Ni-Ti alloys due to the low thermal expansion and thermal conduction of their main phases – the B2 and B19' specifically – too high or low energy densities result in impurities, increased porosity, and less-than-ideal surface finish. Therefore, extra care must be given, if possible, to change laser parameters of the manufacturing units, which can be hardlocked or severely restricted by the manufacturer of such units due to safety/optimization concerns (Lu, et al., 2019).

2.3.1. Modern and near-future applications

Such technology has immense capacity for the generation of complex and dynamics structures, with increasing usage in aerospace, automotive, medical technology, consumer products, organ engineering, and tissue repair applications, as can be seen in figure 76 (Saritha & Boyina, 2020).

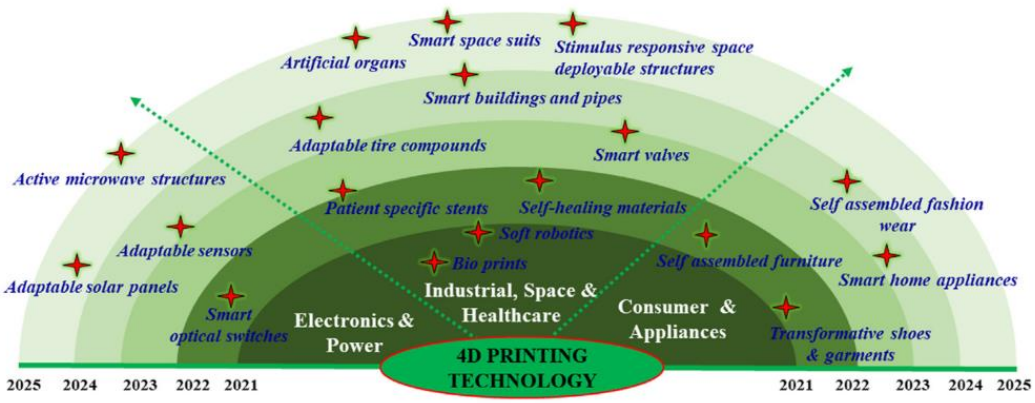


Figure 76 - Current and near-future applications of 4D printing (Samal, Jena, Varshney, & Kumar, 2023).

During the troubled times of the world pandemic, 3D printing largely attenuated the complete seizure of the supply chain apparatus, through printing of personal protective equipment and devices. 4D printing can take such a step even further, through smart masks with better ergonomics for each distinct person, and tissue regeneration technologies. Drug delivery systems can also be vastly applied and simplified due to the inherent nature of the process, allowing invasion free and more compatible medication systems (Samal, Jena, Varshney, & Kumar, 2023) (Sajjad, et al., 2024)

This technology can be applied on consumer appliance, with uses as dynamics jewellery and shoes, transformative futuristic fashion wear (with vastly improve comfort due to flexible properties), and household appliances, to name a few, with examples being furniture and domestic tools being auto assembled when exposed to, as an example, hydric-based stimulus (Sajjad, et al., 2024).

In space technology, the necessity for tribology-free elements and the overall low rate of production and complex designs also becomes transformative in such a setting, with ease of creation of space-deployable structures, self-healing materials, simplified coupling and actuators, simplified thermal sensors, to name a few (Samal, Jena, Varshney, & Kumar, 2023) (Sajjad, et al., 2024).

Industrial technology applications allow smart valves, couplings, sensors and actuators, soft robotics, shape-changing mechanical metamaterials, optical switches, and others. Worldwide logistical capabilities can be greatly increased, with certain components being able to be deployed on site, with transportation being in a reduced minimized state, translating into reduced transportation costs and better delivered in the same volume, increasing the effectiveness of national and international trade dynamics (Momeni, Seyed, Medhi, Liu, & Ni, 2017) (Ahmed, Arya, Gupta, Furukawa, & Khosla, 2021) .

4D printing is considered part of Industry 4.0, which translates into smart manufacturing, industrial flexibility, and overall simplified logistical supply chains, where 4D printing will have a crucial role in fields as robotics, human augmentation /cybernetics, advanced manufacturing advances, next-generation sensors, and others (Deloitte, 2016) (McKinsey, Technology deep dive: 3-D or 4-D printing, 2021) (McKinsey, What are Industry 4.0, the Fourth Industrial Revolution, and 4IR?, 2022).

Such technology is deeply embedded in Industry 4.0 advancements, which are composed of four core foundational technological achievements: connectivity, data and computational power technologies (cloud technology; advanced sensors; blockchain); analytics and artificial intelligence technologies (machine learning and artificial intelligence); human-machine interaction technologies (virtual reality, augmented reality, robotics, AGVs, and automation); and advanced engineering (3D and 4D printing, nanotechnology, metamaterials) (Deloitte, 2016) (McKinsey, Technology deep dive: 3-D or 4-D printing, 2021) (McKinsey, What are Industry 4.0, the Fourth Industrial Revolution, and 4IR?, 2022).

A Gartner hype cycle regarding such trends in research efforts and market receptiveness to such disruptive technologies is shown in figure 77.

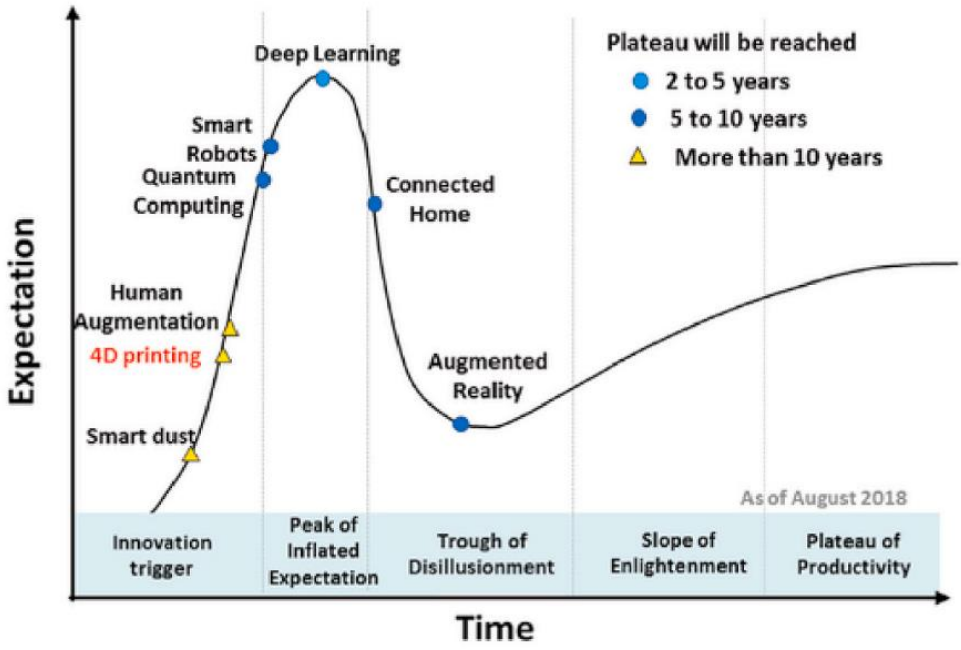


Figure 77 - Gartner hype cycle of the year 2018 (Kuang, et al., 2018).

2.3.2. Research developed

There is increasingly on-going research regarding the development of 4D printing, with L-PBF methods being primarily used when against the other additive manufacturing techniques, and with an ever increasingly number of additive manufacturing Ni-Ti publications being released, as there is more maturity in such technology (figure 78).

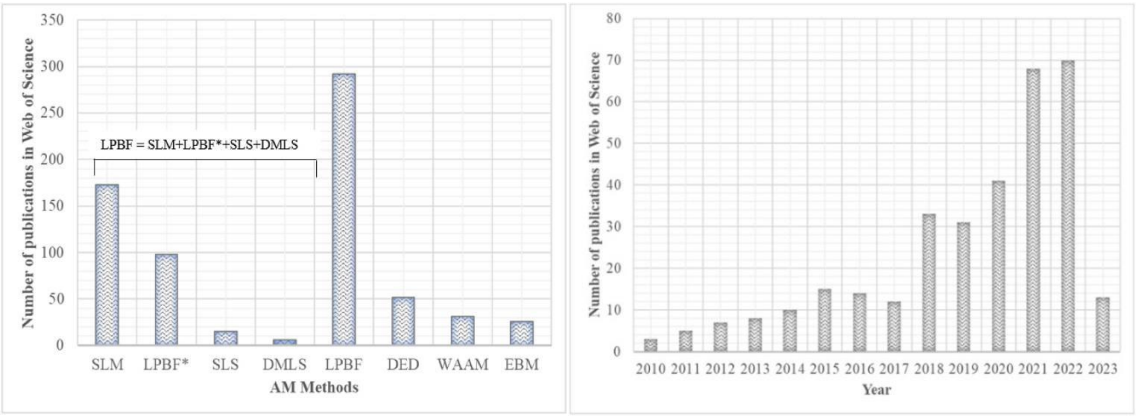


Figure 78 - Methods used to manufacture Ni-Ti alloys and corresponding number of publications (left) and number of annual AM Ni-Ti alloy publication outputs in Web of Science database (right) (Dzogbewu & Beer, 2023).

2.3.3. Market & Economical Considerations

The increased technological sophistication of MAM, allied with ever-increasing technological requirements of the modern world, have greatly increased R&D efforts of this symbiotic technology, as seen by the increase in number of articles published in the last 10 years (Cataldi, Liu, Bissett, & Kinloch, 2022).

We can see, in figure 79, the number of articles published in the last 8 years on the subject and its relation to 3D printing in general – we can see the relation between such related topics.

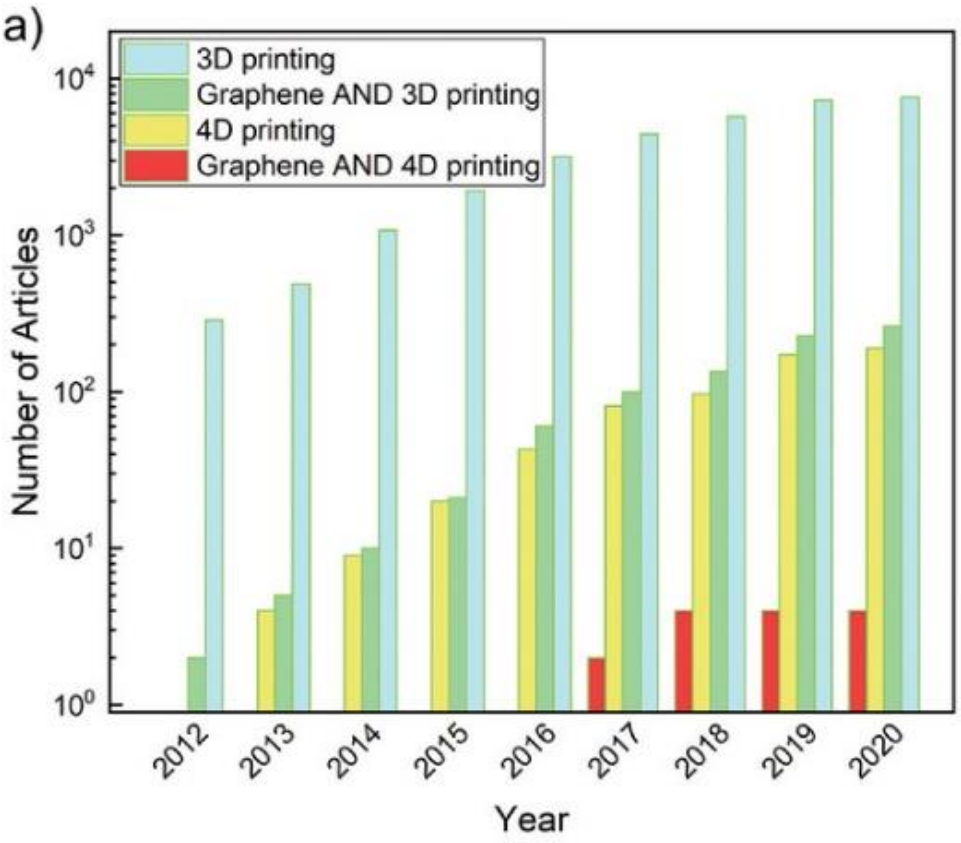


Figure 79 - Number of articles from 2012 to 2020 regarding "3D printing", "graphene and 3D printing", "4D printing", and "graphene and 4D printing" (Cataldi, Liu, Bissett, & Kinloch, 2022).

Meanwhile, it is projected for an exponential increase in the market share of this technological development, with a CAGR of 36.2%, from 137 million USD in 2022 to almost 3000 million USD in 2032, as can be seen in figure 80 (4D Printing Market - Global Industry Analysis 2023 – 2032, 2023).

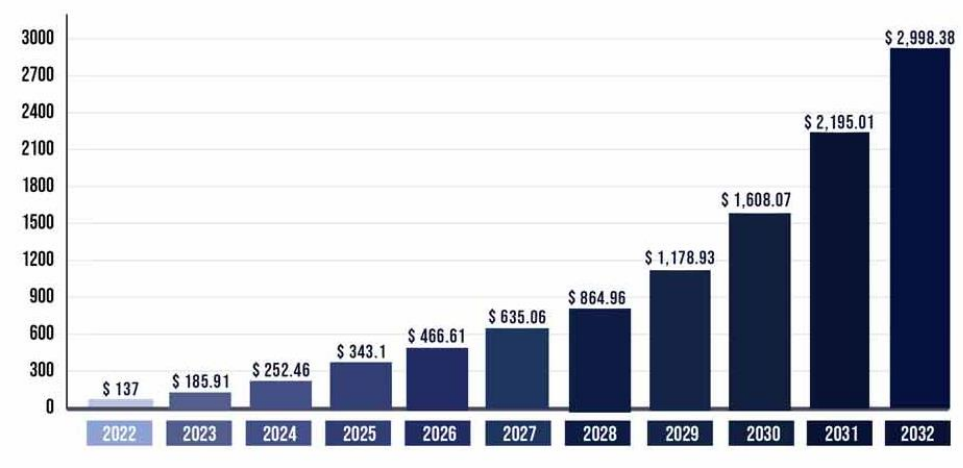


Figure 80 - 4D printing market size, in billion USD (2022-2032) (4D Printing Market - Global Industry Analysis 2023 – 2032, 2023).

Such increase is projected to happen due to biomedical, robotics and aerospace applications of this type of materials, increased societal digitalization and better simulation software of this type of materials, and maturing/understanding of the mechanism involved, through advances in material science and manufacturing techniques. The advances in MAM technology have greatly increased their usage in the myriads of industries, with SMAs being affected in such regard (4D Printing Market - Global Industry Analysis 2023 – 2032, 2023).

4D printing market shares are fairly fragmented, with a number of large and medium-sized players accounting for major revenue sources. Some of the main corporations are 3D Systems Corporation, Autodesk Inc., Hewlett-Packard Company, Organovo, Materialise NV, EnvisionTEC Inc., Dassault Systèmes, ExOne, Heinejken N.V., Stratasys, Aerojet Rocketdyne Holdings Inc., among others. This is in contrast with either smart material and 3D printing markets, which are composed of more settled and definitive global-renowned corporations, which could be possibly explained by the yet-to-be matured technology. (4D Printing Market Size & Share Analysis - Growth Trends & Forecasts (2024 - 2029), 2024) (4D Printing Market - Global Industry Analysis 2023 – 2032, 2023) .

It is worth noting that although the Western markets provide the biggest market share, especially North America and Western Europe, the Southeast Asian market represent the biggest research and development by publications. (4D Printing Market - Global Industry Analysis 2023 – 2032, 2023) (4D Printing Market Size & Share Analysis - Growth Trends & Forecasts (2024 - 2029), 2024) (figure 81).

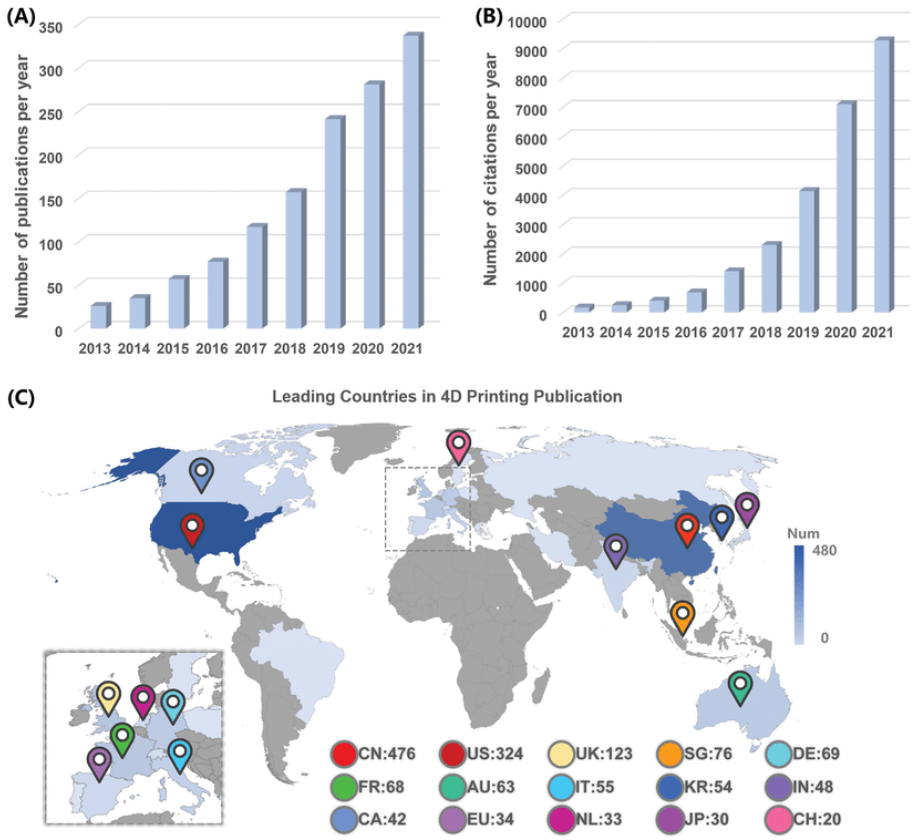


Figure 81 - Statistics of publications on 4D printing, from Web of Science (Wang, et al., 2022).

2.4. Expected Properties

Ni-Ti with 55% weight composition of Nickel values can be compared for analysis of its properties. These are, however, dependent on the manufacturing techniques used therefore with a main distinction being made between conventional and non-conventional (i.e. additive manufacturing) techniques.

Conventional (CV) techniques are those not covered by metal additive manufacturing. These are varied and been in use since the discovery of the alloy. There is melting and casting of the alloy itself, with normally either vacuum-induced melting, levitation melting, and consumable / non-consumable arc melting being used.

Afterwards, there is the usage of either hot or cold working of the alloy. Such manufacturing techniques can include hot working by rolling, forging, extrusion or swaging. Cold working can include wire drawing and cold rolling. The different manufacturing techniques create different variations of the mechanical properties of the alloy, however the properties themselves are of more interest to the thesis, since they serve as a base of knowledge for the experimental analysis, and comparison with L-PBF manufacturing values (NASA, 1972)

In the next table, are the conventionally manufactured expected values, which come from the aforementioned variety of sources.

Table 9 - General properties expected through "conventional" non-additive manufacturing techniques.

Property (Conventional)		Martensite	Austenite
Elastic Modulus (GPa)		25-40 [2] [3] [5] [6] 21-69 [4]	60-83 [1] [3] [6] 75-83 [2] [5] 70-110 [4]
Tensile yield strength (MPa)		70-140 [2] [5] 275 [7]	225-560 [1] 195-690 [2] [5] 400 [7]
Ultimate Tensile strength (MPa)		103-1100 [4] 895 [5] 450 [7]	750-965 [1] 800-1500 [4] 800 [7]
Transformation Temperature (ºC)	Start	24.9 [1]	54.8 [1]
	Finish	4.7 [1]	69.6 [1]
Compressive yield strength (MPa)		275 [7]	550 [7]
Ultimate compressive strength (MPa)		400 [7]	800 [7]
Hardness (HV)		225 - 250 [1] [8]	400-420 [8]
Max elongation/strain (%)		6 – 9 [1] [6] [7]	6 – 8 [6] [7]
Max compressive strain (%)		4.5 – 6 [6] [7]	5.5 – 6.5 [6] [7]
Coefficient of Thermal Expansion (K^-1)		$11x10^{-6}$ [2] [3] [5]	$6.6x10^{-6}$ [2] [3] [5]
Thermal Conductivity (W/(m·K))		8-10 [3] [5]	18 [3] [5]
Density (g/cm^3)		6.45 [1] [2] [5]	

Table 10 - Sources of table 9.

Number	Source
[1]	(NASA, 1972)
[2]	(Vemury, Corradi, Abozaid, Charles, & Hughes, 2021)
[3]	(Stachiv, Alarcon, & Lamac, 2021)
[4]	(MIhálcz, 2001)
[5]	(Jani, Leary, Subic, & Gibson, 2014)
[6]	(Zaki, Moumni, & Morin, 2011)
[7]	(Zaki, Moumni, & Morin, 2011)
[8]	(Huang, Nohava, Zhang, & Ramirez, 2016)

In table 10, are the MAM expected sources, in particular, through laser-powder bed fusion manufacturing.

Of note that both the thermal conductivity and the coefficient of thermal expansion do not vary due to additive manufacturing processes, however the density might be lower in the L-PBF manufacture due to possible porosity in the material.

Table 11 - General properties expected through metal additive manufacturing techniques, in particular, L-PBF.

Property (L-PBF)		**Martensite**	**Austenite**
Elastic Modulus (GPa)		56 [6]	40-60 [6] 36 [6] 47 [6]
Tensile yield strength (MPa)		215 [7]	100-150 [4]
Ultimate Tensile strength (MPa)		400 [7]	600-800 [4] [5] 1224 [6]
Fracture Toughness (J)		---	W = 10.84 J [2] Wi = 4.04 J [2] Wp = 6.80 J [2]
Transformation Temperature (ºC)	Start	8.3 [1] 16 [7]	-4.3ºC [1] -6.2ºC [3]
	Finish	-35.1ºC [1] -29.31ºC [7]	26.1ºC [1] 30.8 [3]

Compressive yield strength (MPa)	250-300 [9]	400 [9]
Ultimate compressive strength (MPa)	800 [9]	600 - 800 [5] [9]
Hardness (HV)	---	380 HVN [1]
Max elongation/strain (%)	7 [7]	8 - 15 % [4] 6.5 - 10.5 [5]
Max compressive strain (%)	6% [9]	5-6 % [4] 6.5% [9]
Density (g/cm^3)	6.4-6.45 [8]	

Table 12 - Sources of table 11.

Number	Source
[1]	0º build data (Zhang, et al., 2024)
[2]	45º build data (Zhang, et al., 2024)
[3]	(Farber, Zhu, Popovich, & Popovich, 2020)
[4]	(Wei, et al., 2023)
[5]	(Dzogbewu & Beer, 2023)
[6]	(Saedi, et al., 2018)
[7]	(Yang, et al., 2019)
[8]	(Cao, et al., 2020)
[9]	(Saedi, Moghaddam, Amerinatanzi, Elahinia, & Karaca, 2018)

Of note that values in reference [1] and [2] of the L-PBF table was dependent on build angle of geometry. In such report, (Zhang, et al., 2024), there was usage of traction and charpy specimens at 45º build angle, while compression test pieces used 0º angle with X axis. It is worth noting also that in the same report, there is distinction between total impact absorbed energy (W), crack initiation energy (Wi) and crack propagation energy (Wp). This was to be measured however, there was not infrastructure for detailed fracture toughness analysis, and crack initiation energy was the only one measured.



Figure 82 – Example of a thermomechanical actuator of CSEM with Ni-Ti SMA alloy usage (courtesy of CSEM).

3. Experimental part

In this experimental stage of the thesis, there will be production of test pieces of Nickel-Titanium, with posterior ASTM tests being conducted so as to characterize the piece itself.

One of the main objectives of this work is to check the viability of production with 4D printing technology, with the effects of the manufacturing on the mechanical, geometrical, and metallurgical dimensions of the material.

Therefore, the main objective of the experimental part is to analyse the viability of the L-PBF process on the manufacturing of Ni-Ti test pieces, with analysis of any characteristic and defects that may appear in the test pieces, with subsequent discussion of the results given.

The analysis encompassed therefore a myriad of different properties. For the total of 12 test piece, there is division of 4 groups: 3 specimens for tension testing through ASTM F2516 standard; 3 specimens for compression testing through ASTM E9 standard; 3 specimens for energy absorption during fracture through ASTM E23 standard; and 3 specimens for transformation temperature determination by utilization of a DSC through ASTM F2004 standard. There was also subsequent evaluation of the microstructure, hardness, porosity, and defects.

Overall, there were more tests planned to be executed through more test pieces manufacturing (regarding the ASTM F2082 standard, and other subspecimens of both F2516 and E9 standards), however a lack of available infrastructure and economical impracticability meant such possibilities were discarded.

Of note that overall, these test pieces were also divided in three main groups: one for martensitic status determination – **group 1**; another for austenitic status determination – **group 2**; and other for effects of annealing on the material – **group 3**.

The impossibility of using temperatures below the ambient range, due to lack of infrastructure at FEUP, until the purchase of Nitrogen until mid-July, meant that there was a compromise, and the group used for martensite study had to be done at room temperature, which proved to be suboptimal. This meant that the specimens had the possibility of a partially martensite, partially austenite phase at the moment of testing.

3.1. Materials and Methods

In this section, there will be discussion regarding the materials and methods necessary for the experimental part, passing through general overview, material composition, properties expected, ASTM tests and production – in particular, additive manufacturing,

machining post-processing, corrective measures, annealing treatments, clamp creation, and infrastructure for analysis.

3.1.1. General overview

This is the general overview of the fluxgram of the general work, which can be seen as follows, in figure 83.

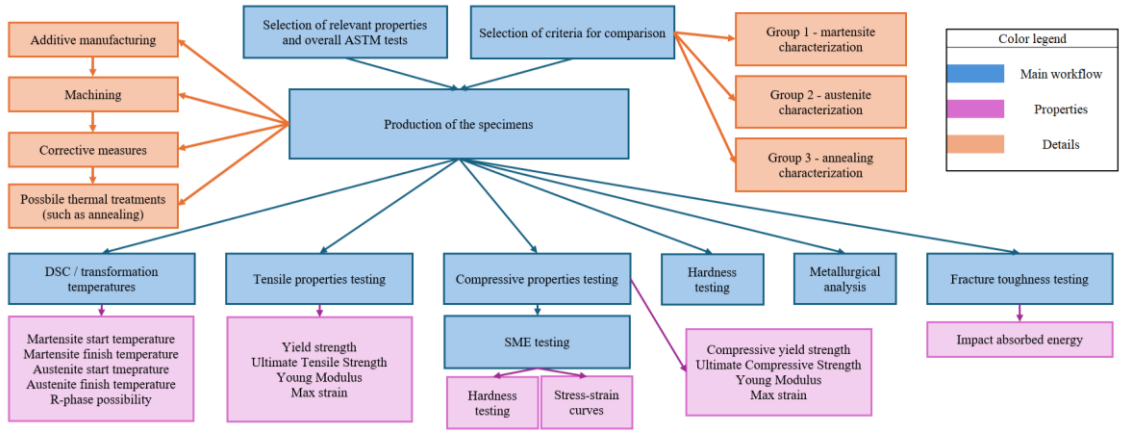


Figure 83 - Work order plan fluxgram.

Of note that this was the planned work order, and real-life circumstances dictated different approaches – the most notable ones being the difficulty and delay developing the DSC tests, which meant that tensile and compressive properties testing were made prior to full DSC characterization.

At the same time, the impossibility of the resin used in hardness testing meant certain temperatures were deemed practically impossible (at 150ºC the resin started to melt, and there was not enough nitrogen for hardness characterization at -10ºC).

There were several difficulties relating to the etching solution for metallurgical analysis. Additionally, tests where thermal variations were involved regarding properties characterization (hardness dependent on temperature, for example) had constraints due to the inadequate infrastructure for such tests – an oven could very well be at, as an example, 100ºC, and the specimens at a similar temperature, however the moment the oven was open for retrieval of the specimens unto the charpy test machine, there was already a drop in the temperature of the specimens.

3.1.2. Material composition

The material composition of the Ni-Ti alloy powder is shown in the next table. This powder was given by CATEC as a 2-gram sample.

The Ni-Ti alloy is very similar to Nitinol-55 in composition (weight percentage wise), as can be seen by looking at the composition. There was conversion of the wt% to at%, so as to better locate the properties of the material itself. Tables 13 and 14 show the compositions.

Table 13 - Chemical composition (in weight percentage).

Chemical element	Composition (wt%)
Ti	Bal. (44.367)
Ni	55.6
O	0.01
N	0.002
Fe	0.02
H	0.001

Table 14 - Chemical composition (in atomic weight percentage).

Chemical element	Composition (at%)
Ti	49.48
Ni	50.52
O / N / Fe / H	<0.01

3.1.3. Additive manufacturing

The test pieces were initially going to be manufactured at Hypermetal Lda., in a Renishaw AM 500S L-PBF production unit, however, the necessary industrial and economic conditions of the private company made such procedure unviable. The L-PBF production units used were therefore subcontracted to CATEC ("Centro Avanzado de Tecnologías Aeroespaciales" – Center for Advanced Aerospace Technologies), with their Renishaw AM 250 units (figure 84), with the maximum allowed height for specimens being around 50mm for production, since the overall maximum fabrication volume was 250x250x270mm. This meant the remodelling of several specimens, and, as mentioned previously, the impossibility of some of them.

The necessary minimum threshold for commercial purchase of Ni-Ti powder (around 200kg) largely exceeded the necessary amount for the test pieces (which amount to, at most, 15 test pieces). Additionally, the necessary retooling for one of the production units, with the impossibility of working in other projects meanwhile (due to total replacement of the powder in a machine for a new one - meaning a third of total production effectively stopping), meant the outsourcing of the specimens manufacturing to CATEC, based in Sevilla, capital of the Andalucian region of Spain.



Figure 84 - Renishaw AM 250 of CATEC.

The industrial connection between both entities had prior been established with a myriad of other projects, and the project was therefore accorded between both companies for manufacturing of the test pieces in Sevilla, and posterior shipment to Porto.

The test pieces were manufactured with a laser power of 200W, a scan velocity of 1000mm/s, and a layer thickness of 30µm, in a meander-type laser patter. Such pattern followed prior experience of CATEC, which had prior been working on Ni-Ti alloys for various aerospace applications in Spain. The pattern and strategy used for manufacturing can be seen in figure 85.

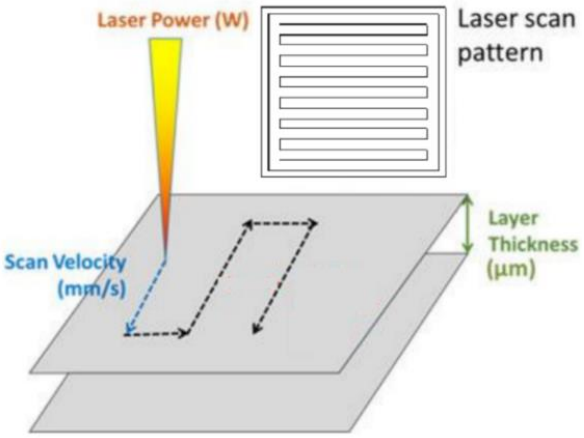


Figure 85 - Strategy used for manufacturing (CATEC data regarding Ni-Ti build job manufacturing, 2024).

Due to constraints related with economic considerations, infrastructure needed for the necessary tests, and the impossibility of pieces with length superior to 50mm, there was manufacturing of three cylindrical test pieces of ASTM E 8M (which would be used for ASTM F 2516), three short specimen types of ASTM E 9, the three specimens of ASTM F 2004, and the three specimens related to ASTM E 23. The test pieces related to ASTM F 2082, the thin sheet specimen of ASTM F 2516, and the medium and long-length specimens of ASTM E 9 were discarded for manufacturing, due to lack of infrastructure in the first, and the hard limit of length of specimens of 50mm for the later ones. Of note that there was also requisition of a small container with 2 grams of the Nickel-Titanium powder, mentioned previously in the materials subsection, so as to better analyse its properties through optical microscopy means and for a better composition result.

Images 86, 87 and 88 show the manufactured specimens.



Figure 86 - F2516/E8 specimens (left) and E9 specimens (right).

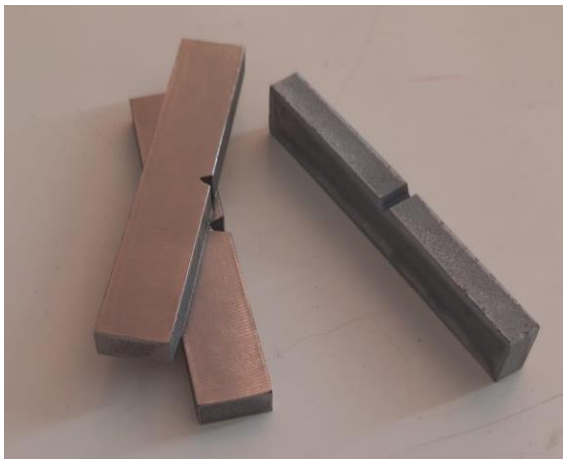


Figure 87 - E23 specimens. Of note that the photos were taken after the right one has been annealed.



Figure 88 – Container with 2 grams of Ni-Ti powder (left) and F 2004 specimens (right).

3.1.4. Post-processing

There was necessity of post-processing in the specimens, for better surface properties or the facing for better consistency of results.

There was the necessity of part facing of the top and bottom bases of the E 9 test pieces, due to necessity of better surface roughness for better analysis of compressive properties. The HAAS ST10 (figure 89) was used for part facing of the E 9 pieces, since hydraulic operation would not negatively impact the structural integrity of the part.



Figure 89 - HAAS ST10 machine, located at DEMEC machine shop.

There was also the necessity of machining at both ends of the E 8M test pieces prior to testing relevant to the F 2516 due to the necessity of threaded clamps in such environment. The GE Fanuc OT (figure 90) was chosen for this operation, due to better control of the process. Comparing with the HAAS S10, the GE Fanuc OT allows only the support of one of the ends of the test piece, a significant disadvantage which is only compensated by the possibility of less torque, meaning less possible warping of the parts.



Figure 90 - GE Fanuc OT machine, located at DEMEC machine shop.

The E8M test piece started to harden at the start of the threading operation, which gave a preliminary analysis on the possibility of of austenitic to martensitic transformation due to the deformation applied (superelasticity effect), since it was reported that the piece

started to harden moments after the beginning of the first threading on the test piece. Another method therefore would have to be used for the creation of supports for the realization of traction tests.

3.1.5. Clamp creation

There was the necessity of special built clamps for the possibility of realizing the tensile tests. The clamps were made with CK45 carbon steel. There was subsequent hardening of the pieces, through a 2-hour heating until reaching 850ºC, for a stage of 30 minutes with subsequent cooling in quenching oil, and posterior tempering for 2h at 150ºC. This overall process increased the hardness of the pieces from 210 HV to 285 HV. This was crucial so that the clamps would hold the F2516 traction test pieces, so that the test could continue given its parameters. Clamp images can be seen in figures 91, 92 and 93.



Figure 91 - Clamps for both bases of the F2516 specimens.



Figure 92 - Clamp in the open positions (left) and locked position (right).

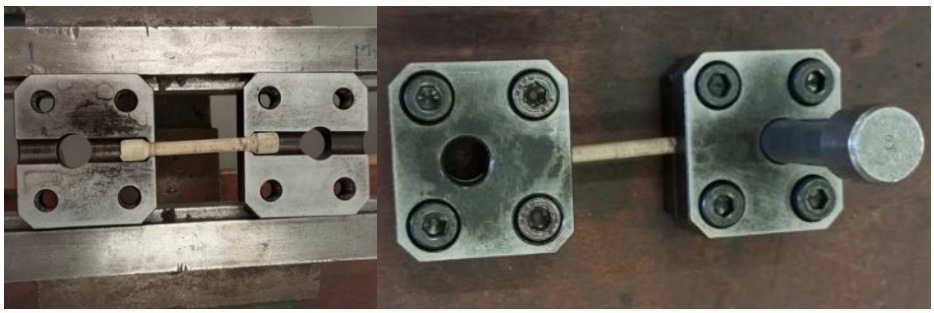


Figure 93 - Specimen in the clamp system before locking (left) and after locking (right).

3.1.6. Annealing

There was necessity of annealing operations in some of the test pieces, so as to better induce the transformation effect, or due to actual necessities of the ASTM tests procedures.

Such treatments were made at Hypermetal Lda., by usage of their industrial furnace – a Nabertherm Model N41/H (figure 94), operating on an argon atmosphere so as to prevent oxidation. The argon gas flow was of 25L/min.



Figure 94 - Nabertherm N41/H industrial furnace.

In the main annealing operation, the specimens were divided into 3 groups: group A – consisting of two DSC F 2004 specimens; group B – consisting of one F 2516 specimen and one F 2004 specimen; and group C – consisting of one E 23 specimen. Each of these had a direct connection to the thermocouple for accurate thermal characterization during the annealing treatment.

The specimens were placed in tiles so as to prevent soldering effect with the oven. Relevant images can be seen in figures 95 and 96.



Figure 95 - Assembly of the thermocouple unto a personal computer for data recovery.

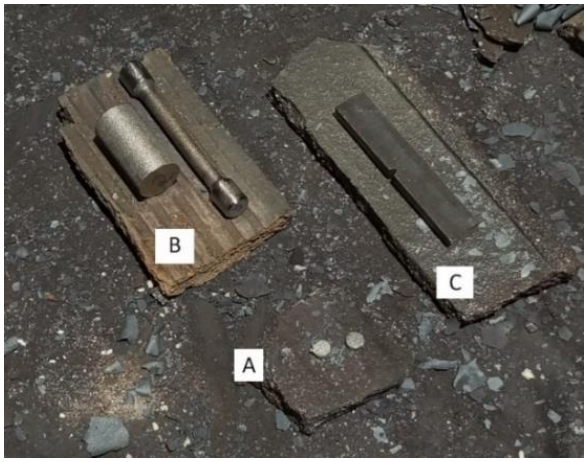


Figure 96 – Main annealing groups.

The annealing chart showcases the given order for the thermal treatment. There is initial pre-heating of the oven from nominal room temperature of 25ºC to 200ºC, which lasts 1 hour, at the maximum possible heating rate (10ºC/min). Afterwards, there is heating from 200ºC to 800ºC, at a rate of 5ºC/min, where there is a 1-hour stage at the 800ºC temperature. Subsequently, there is cooling of the specimens at nominal air conditions, reaching 25ºC in approximately 1h15. Figure 97 shows the main annealing temperature vs time chart.

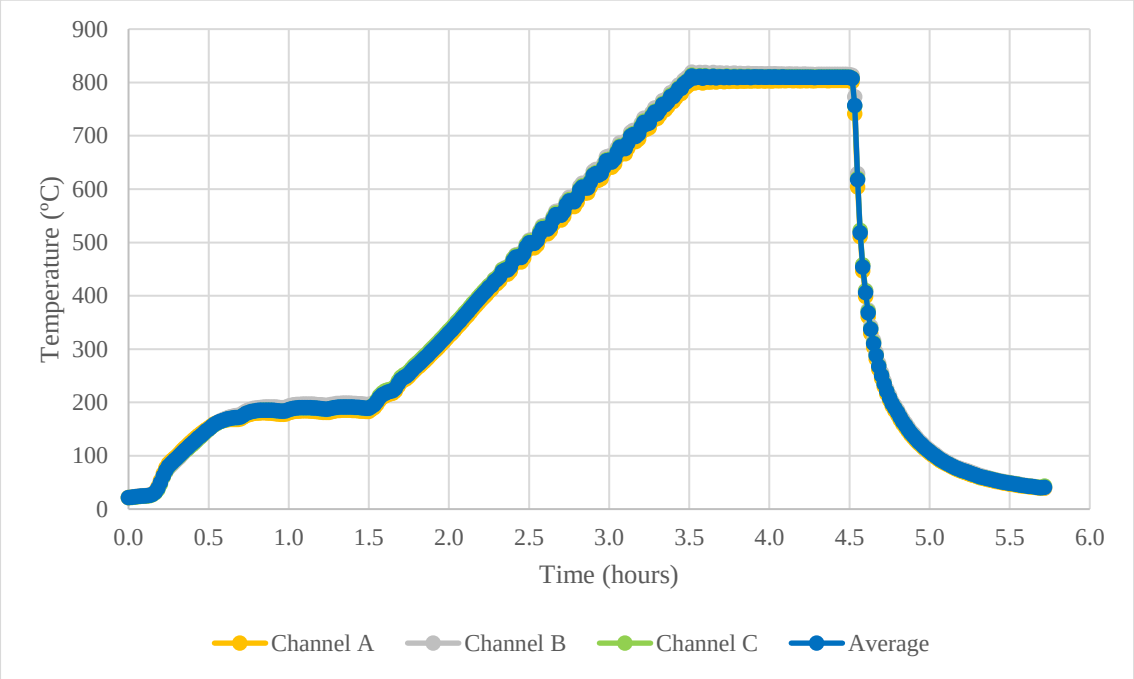


Figure 97 – Main annealing chart: temperature vs time.

The argon gas had introduction at the end of the pre-heating, around the 1.5-hour mark, and was subsequently closed when around the end of the cooling operation, around the 5-

hour mark. Additionally, it is worth noting that the specimens had their temperature registered, through the thermocouple apparatus, every sixty seconds. The resulting specimens are shown as follows, after the air-cooling operation.

Such specimens are part of group 3 – related to analysis of the effect of the annealing treatment in the test pieces throughout the various physical, mechanical and metallurgical properties (figure 98).

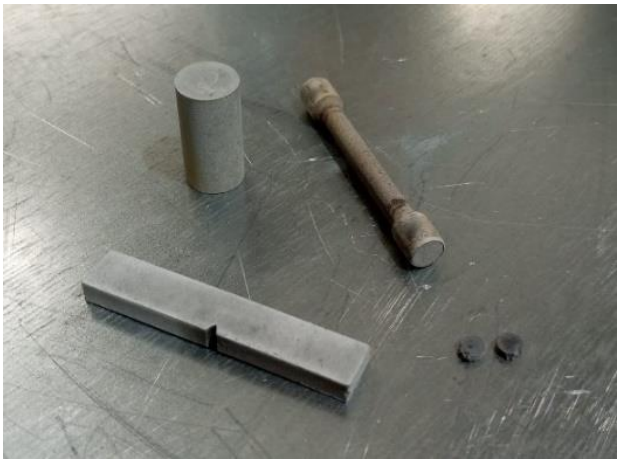


Figure 98 – Group 3 specimens post-annealing. Of note the slight oxidation created at their surface.

There was another annealing operation, with F2004 test specimens, regarding annealing influence on transformation temperature of the specimens, and the effect of double annealing treatment, since it was interesting to visualize the effect of annealing on the transformation behaviour of Ni-Ti (Huang & Liu, Effect of annealing on the transformation behavior and superelasticity of NiTi shape memory alloy, 2001). This was only done on two of the samples, and can be seen in figure 99.

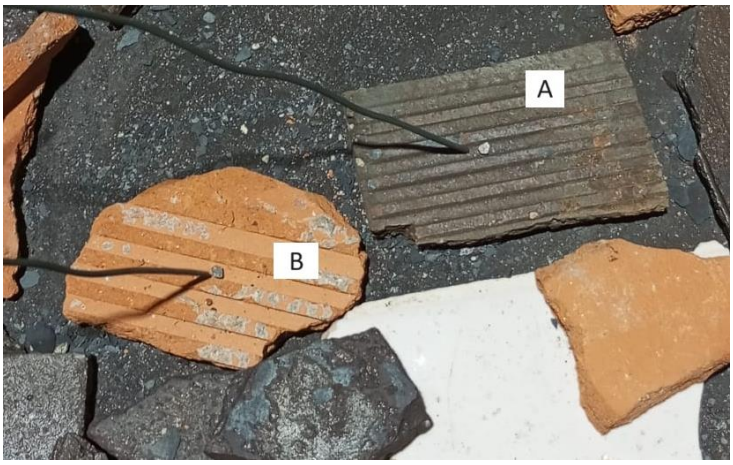


Figure 99 - Secondary annealing groups.

After the previous 1-hour 800ºC annealing done, and subsequent related tests, there was a new, 1-hour 500ºC annealing executed, with equal general parameters (heating rate, argon gas protection, etc.) to the previous one, with main difference being the lower maximum temperature of 500ºC.

The annealing chart showcases the given order for the thermal treatment. There is initial pre-heating of the oven from nominal room temperature of 25ºC to 200ºC, which lasts 1 hour, at the maximum possible heating rate (10ºC/min). Afterwards, there is heating from 200ºC to 500ºC, at a rate of 5ºC/min, where there is a 1-hour stage at the 500ºC temperature. Subsequently, there is cooling of the specimens at nominal air conditions, reaching 25ºC in approximately 2 hours. Figure 100 shows the main annealing temperature vs time chart.

The treatment, despite having lower thermal temperatures, ended up taking more time, due to the usage of more inert argon atmosphere. The bottle was completely full and there was better control of the process. In the main annealing treatment executed previously the argon was at the end and was turned off sooner.

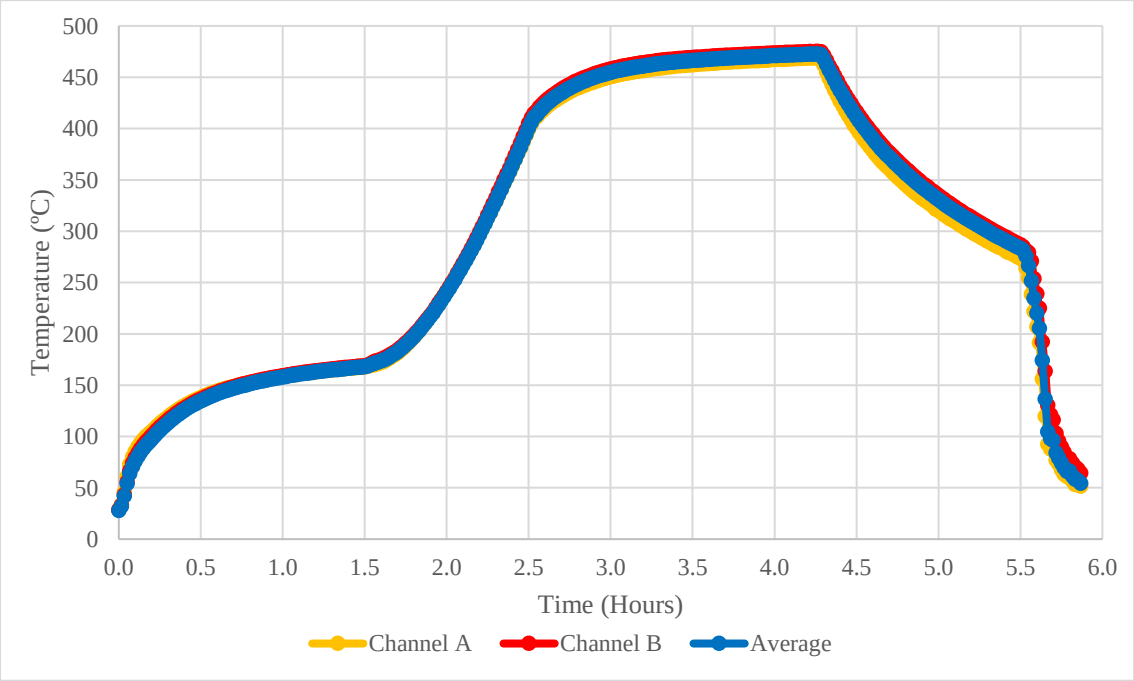


Figure 100 - Secondary annealing chart: temperature vs time.

There was usage of inert argon gas so as to prevent oxidation, which was used from the 1.5-hour mark until the 6-hour mark. As previously, each of the specimens had a direct connection to the thermocouple, in conditions equal to the previous operation. The specimens had their temperature registered, through the thermocouple apparatus, every sixty seconds.

3.1.7. Development, modelling and testing

As mentioned previously, there was production of three equal test pieces per test to be conducted, so as to better compare with the overall. Of note that some tests are highly dependent of the infrastructure available at a given time for its development. The L-PBF machine had a maximum production length of 50mm, and dimensions were chosen accordingly for allowance of its manufacturing.

The tests which are to be conducted are ASTM F 2516 “Standard Test Method for Tension Testing of Nickel-Titanium Superelastic Materials” (ASTM F-2516, 2022), ASTM E 9 “Standard Test Methods of Compression Testing of Metallic Materials at Room Temperature” (ASTM E-9, 2000), ASTM E 23 “Standard Test Methods for Notched Bar Impact Testing of Metallic Materials” (ASTM E-23, 2016), and ASTM F 2004 “Determination of Transformation Temperature of Nickel-Titanium Shape Memory Alloys by Thermal Analysis” (ASTM F-2004, 2017). These tests are to be additionally supported by metallurgical tests, such as microscopical and hardness test, and by extensive documentation supporting such procedures, not only of the ASTM tests referenced prior, but also of ASTM E 8M “Standard Test Methods for Tension Testing of Metallic Materials” (ASTM E-8M, 2022), as support for ASTM F 2516, and ASTM F 2005 “Standard Terminology for Nickel-Titanium Shape Memory Alloys” (ASTM F-2005, 2000), as support for the Ni-Ti related procedures.

Despite the interest in the realization of ASTM F 2082 “Standard Test Method for Transformation Temperature of Nickel-Titanium Alloys by Bend and Free Recovery”, and the possibility of creation of custom test pieces for the metallurgical tests, this was later abandoned due to economic considerations, lack of infrastructure available for its realization and the length of the specimen being superior to the available length of the manufacturing unit.

The ASTM tests were paramount so as to conduct research in a standardized manner and with a guide of reference, however in parameters such as hardness and shape memory effect analysis through deformation cycles, there was not any conductive ASTM procedures one could follow.

The modelling of the test pieces was designed through SOLIDWORKS software, whilst following ASTM test measurements and related geometric/dimensional directions. The modelling of these test pieces will be shown as follows.

3.1.7.1. Tensile Testing

The ASTM F 2516 “Standard Test Method for Tension Testing of Nickel-Titanium Superelastic Materials” (ASTM F-2516, 2022) covers the methods of determination of upper and lower plateau strength, residual elongation, tensile strength, and elongation, for

superelastic nickel-titanium materials. Such test specimens base themselves on the E8M test method. There was the development and modelling of cylindrical and rectangular type test specimens.

The cylindrical test piece is a threaded specimen type from the ISO 6982 guideline manual, which can also been found on "For Test Specimens with Gauge Length Five times the Diameter" table of ASTM E 8M. Such manufacture will require machining of the threaded part (the head – M8 threaded) posterior to the additive manufacture process. The modelling can be seen in figure 101.

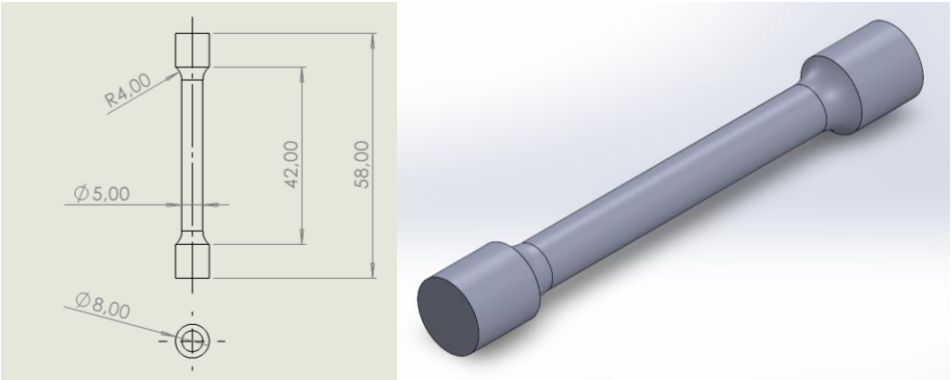


Figure 101 – Modelling of the cylindrical test specimen for F 2516.

The ASTM F 2516 tension testing procedure is realized by pulling the material until 6% strain, unloading to less than 7 MPa, and pulling to failure. The velocity of the first phase until 6% strain was of 0.25mm/min, and the failure phase was recorded with a velocity of 2.5mm/min.

For testing at room temperature, there was utilization of an MTS 810 servo hydraulic computer-controlled universal material testing machine (figure 102), due to their possibilities with tensile and compressive testing procedures. Software for monitorization and analysis is included in the machine infrastructure.

For the possibilities regarding heated specimens there was usage of a Instron 3367 testing machine (figure 103), located at LTM, which allowed the heating of specimens to upwards of 100ºC, however having the limitation of a maximum applied force of 30 KN.



Figure 102 - MTS 810 testing machine, located at LET.



Figure 103 - Instron 3367 testing machine, located at LTM (left), and with its heated chamber procedure being used (right).

3.1.7.2. Compressive testing

The ASTM E 9 "Standard Test Methods of Compression Testing of Metallic Materials at Room Temperature" (ASTM E-9, 2000) covers the methods for axial-load compression testing of metallic materials at room temperature, along with apparatus and specimens necessary. The short piece is a 13mm per 25mm from "Suggested Solid Cylindrical Specimens" subcategory of ASTM E9, with an approximate L/D ratio of 2.0. The modelling can be seen in figure 104.

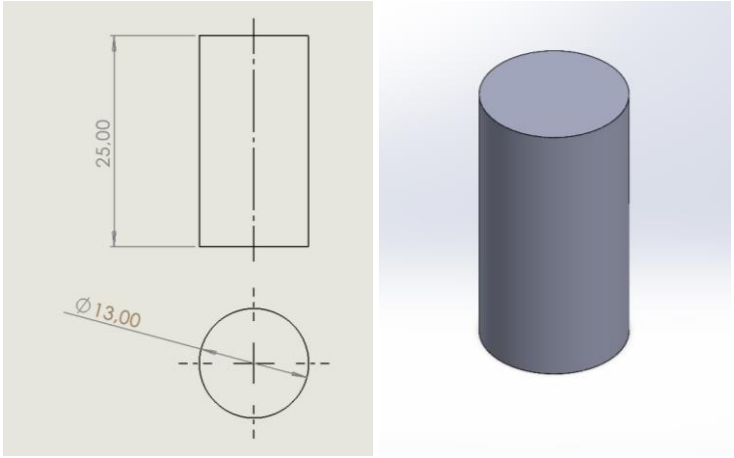


Figure 104 – Modelling of the short-length specimen for E 9.

The ASTM E 9 compression testing procedure allows axial-load compression testing of metallic materials at room temperature, providing information relative to the yield strength, the yield point, Young's modulus, the stress-strain curve, and the compressive strength. Such procedure is realized by subjecting the material to an increasingly axial compressive load, and monitorization of both load and strain parameters.

For testing at room temperature, similarly to the tensile testing, there was utilization of an MTS 810 servo hydraulic computer-controlled universal material testing machine (figure 103), due to their possibilities with tensile and compressive testing procedures. Software for monitorization and analysis is included in the machine infrastructure.

For the possibilities regarding heated specimens, again similarly to the tensile testing, there was usage of a Instron 3367 testing machine (figure 104), located at LTM, which allowed the heating of specimens to upwards of 100ºC, however having the limitation of a maximum applied force of 30 KN.

The velocity of the testing machine on both cases was of 0.15mm/min.

3.1.7.3. Fracture toughness testing

The ASTM E 23 "Standard Test Methods for Notched Bar Impact Testing of Metallic Materials" (ASTM E-23, 2016) covers the method of impact testing relating specifically to the behaviour of metal when subjected to a single application of force, resulting in multi-axial stresses associated with a notch, coupled with high rates of loading. Such procedure results in accurate predictions relating to accurate brittle fractures, and hardness determination. The test piece is a simple-beam impact test specimen, with a base of 5mm per 10mm and height of 55mm from Charpy type-2B V-notch specimens. The modelling can be seen in figure 105.

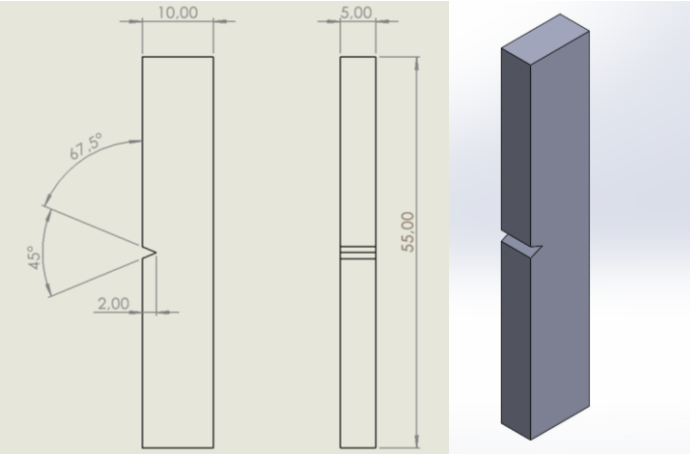


Figure 105 – Modelling of Charpy V-Notch specimen for E 23.

Such procedure is realized by usage of a suitable specimen, a set of anvils, and specimen support on which the test specimen can be placed so as to receive the blow of the moving mass, with sufficient energy for breaking it, and device for measurement of the energy absorbed by the broken specimen.

Corrective measures had to be undertaken for the better dimensioning of the specimens, with more drastical alterations made, when compared with post-processing machining operations. Another necessity of post-processing operation was the mechanical grinding of the Charpy test pieces, since their roughness could potentially interfere with the test. For that end, the machine shop of DEMEC was critical at the operation for smoothing of the specimens.

The first overall smoothness operation was deemed suboptimal for two of the test pieces, which were subsequently remachined for better dimensions – in particular the notch itself, which was inadequate for the task at hand. The other specimen was used meanwhile for testing. Figure 106 shows the results post-smoothing.

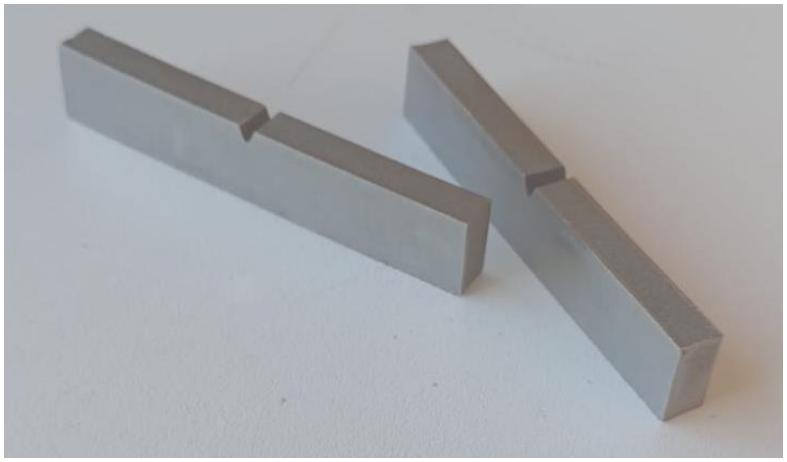


Figure 106 - E23 charpy specimens with improved smoothing.

For the E 23 Charpy test, there was utilization of a standard pendulum type of rigid construction, with related infrastructure (figure 107), for impact testing according to the Charpy method.

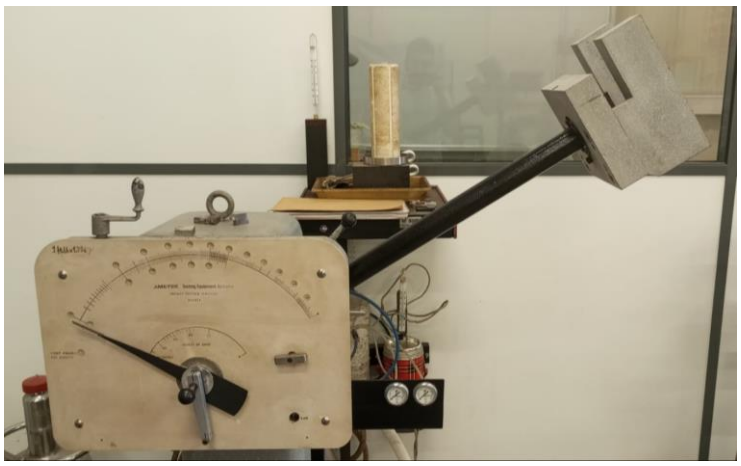


Figure 107 - E23 Charpy test machine (in ready position with the weight), located at LET.

3.1.7.4. Transformation temperature testing

The ASTM F 2004 "Standard Test Method for Determination of Transformation Temperature of Nickel-Titanium Shape Memory Alloys by Thermal Analysis" (ASTM F-2004, 2017) covers the procedure for determination of a martensite-to-austenite and austenite-to-martensite transformation temperature of Nickel-Titanium alloys through DSC (differential scanning calorimetry).

There was analysis of the powder material, and of samples without annealing, with annealing done at 800ºC, and with a double annealing of 800ºC and 500ºC.

The test piece is a 5mm per 1.7mm strip, as advised by members of ISQ ("Instituto de Soldadura e Qualidade" – Welding and Quality Institute) installations, in Oeiras. There was initial idea of doing the DSC in the installation of the institute however doing such procedures at FEUP was eventually chosen due to better/more practical conditions. The modelling can be seen in figure 108.

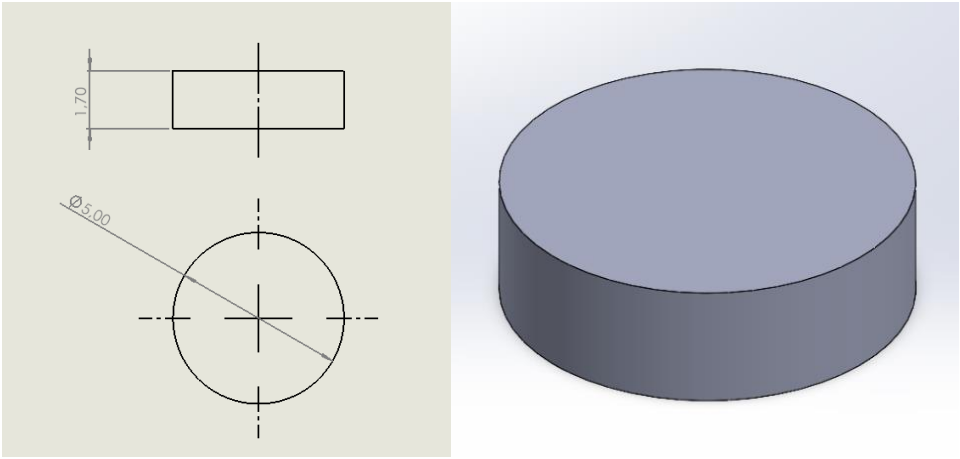


Figure 108 – Modelling of the specimen for F 2004.

This procedure is realized through heating and cooling of the specimen at a controlled rate in a controlled environment, with the heat flow between the test material and a reference material due to energy changes continuously monitored, with absorption of energy resulting in an endothermic peak on heating and a release of energy resulting in an exothermic peak on cooling, due to the phase transformation mechanism.

Corrective measures had to be undertaken for the better dimensioning of the specimens, with more drastical alterations made, when compared with post-processing machining operations.

Despite advice from ISQ to use 1.7mm diameter per 5mm cylindrical test pieces for the DSC tests, the specimens were too big for its usage in DSC equipment. The ASTM tests advised specimens with mass between 10 and 65 milligrams, while the manufactured

specimens, after measurement of its weight achieved between 145mg and 165mg total. Therefore, there was grinding at the FEUP facilities to values more acceptable, with the test pieces reaching for the non-annealed sample, 52.9 mg, and for the annealed samples, 57.8 mg. This was deemed acceptable, both in dimensions (being able to fit the enclosure for the DSC test) as well as weight (being close enough to the F 2004 parameters of specimens regarding weight, and by consulting of informed technicians related to the matter).

The ASTM F 2004 was conducted through a differential scanning calorimetry analysis at the installations of FEUP, in the materials department, through use of a Netzch DSC 214 Polyma (figure 109), and auxiliary Netzch Proteus Thermal Analysis software.



Figure 109 - Netzch DSC 214 Polyma machine, located at the Department of Metallurgical and Materials Engineering.

The ASTM F 2004 thermal analysis procedure allows determination of the transformation temperatures of nickel-titanium shape memory alloys, providing information relative to the phase transformation from martensite to austenite, through a differential scanning calorimeter.

This procedure is realized through heating and cooling of the specimen at a controlled rate in a controlled environment, with the heat flow between the test material and a reference material due to energy changes continuously monitored, with absorption of energy resulting in an endothermic peak on heating (and where we can see the martensite values) and a release of energy resulting in an exothermic peak on cooling (and where we can see the austenite values), due to the phase transformation mechanism.

There was analysis of the powder material, and of samples without annealing, with annealing done at 800ºC, and with a double annealing of 800ºC and 500ºC.

3.1.7.5. Hardness testing

There was realization of hardness tests for better visualization of hardness values achieved, and for cross-referencing with the DSC tests regarding transformation temperature values. This was made with two different procedures, one with specimens in resin, and other without resin embedded. These methods and results will be explained as follows in the next subchapters.

There was usage of a “Dia Testor 2Rc” hardness tester, manufactured by Wolper, which can be seen in figure 110.



Figure 110 - Wolpert Dia Testor 2Rc hardness tester, similar to the one located at LET (Hardness tester WOLPERT, type Dia-Testor 2RC, 2024).

i) First procedure

Tests were made at different temperatures: first at room temperature, then subsequently through temperatures of 70ºC and 100ºC, with use of a Sapratin model 29 PRT II industrial oven.

There was reutilization of the specimens used before in the different tests, in particular, specimens CR1 and CR2 are parts of the E9 compression test (base and lateral samples), specimens TR1 and TR2 are parts of the F2516 tension test (base and lateral samples), and specimens CH1 and CH2 are parts of the E23 charpy test (of each side).

There was division, when inserted in resin moulds, between the non-annealed and annealed samples, with the resin used, as can be seen in figure 111, being a clear acrylic system with a 15-minute cure time, with designation “Buehler VariKleer”.

The resin mould disposition and overall configuration can be seen in figure 112.



Figure 111 - Resin used for hardness testing support.



Figure 112 – Non-annealed and annealed samples in resin moulds (left) and the designation of the specimens (right).

ii) Second procedure

There was a plan to make hardness testing with the samples of the previous procedure at temperatures of 150ºC and -10ºC (so as to better compare the hardness progression by having bigger thermal margins), however this ultimately revealed itself to be impossible since the resin started melting at 150ºC, making impossible the indentation operations, and the nitrogen was not in enough supply for the negative temperature tests, therefore such plans were discarded.

The alternative therefore was the measurement of hardness at room temperature (22ºC) and at 150ºC, so as to check for not only confirmation of the hardness values of the alloy, but also to visualize if there was significant hardness variations, which would indicate differences between a martensite and austenite phases. For heating of the specimens until 150ºC, there was a direct heating until the temperature, where it stayed in such temperature for 1 hour. There was usage of the Sapratin Type 29 PRT II industrial oven available at LET.

There was the usage of non-annealed charpy specimens, named samples 1 and 2, and annealed charpy specimens, named samples 3 and 4 (figure 113).



Figure 113 - Non-annealed (left) and annealed (right) samples used for the second hardness procedure.

3.1.7.6. Shape memory recovery testing

Regarding shape memory recovery possibilities, there was usage of the post-deformation E9 compression samples so as to see the possibilities regarding such mechanisms – economic viability of purpose-built specimens for such testing was not practical due to additional cost, therefore there was usage of the aforementioned compression specimens for this particular testing. In particular, the schematic of operations (in the form of a fluxgram) is shown as follows, for each deformation cycle.

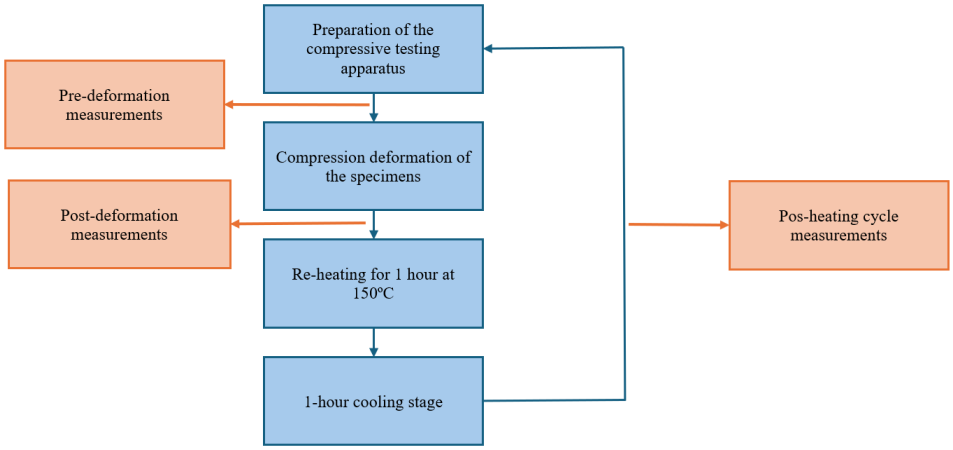


Figure 114 - Fluxgram of the SME testing plan.

There was a heating of the samples to 150ºC, with subsequent deformation, and re-heating, iteratively making such process. The temperature for the oven was chosen due to being more than 50ºC above the austenite finish temperature, proving adequate for the full testing of the shape memory effect. The compression testing followed similar guidelines to the E9 compression test, with a total exerted force of 150 KN.

3.1.7.7. Microstructure testing

Microstructure analysis was executed as to allow observation of the microstructure, defects and possible porosity. This was divided in non-annealed and annealed samples and in compression, tension and charpy specimens. A relevant fluxgram is shown in figure 115.

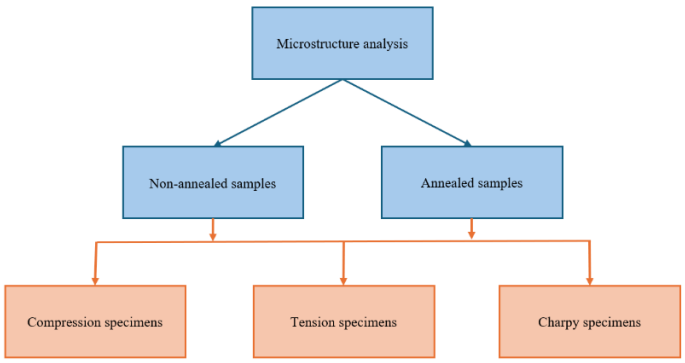


Figure 115 - Microstructure analysis fluxgram.

So as to better visualize and analyse the microstructure of the specimens, there was a necessary etching of the parts, however this proved ineffective.

There was an attempt with three different solutions. These are shown in the next table.

Table 15 - Etching solutions used.

Attempts	Solution	Composition ratio	Solution-to-water ratio
1st	HCl + HNO3	1:3	1:4
2nd	HF + H2O2	1:1	1:20
3rd	Kroll's reagent	Water 92.82% Nitric Acid 6.11% Hydrofluoric Acid 1.07%	

The solution advised for the first attempt was a 200 cubic centimetre solution based on chemical etching of nitinol stents for medical applications, in particular self-expanding stents for cardiovascular applications (Katona, Bognár, Berta, Nagy, & Hirschberg, 2013). Second attempt was a 22 cubic centimetre solution based on a wet-chemical etching solution guide from MicroChemicals GmbH (MicroChemicals GmbH, 2024), which explained how nickel and titanium alloys can be treated with the aforementioned solution – there was therefore usage of the titanium solution in the guide. The third attempt was a Kroll reagent, containing "water 92.82%, nitric Acid 6.11%, hydrofluoric acid 1.07%", advised by the technician of the etching laboratory.

The microstructure analysis used the resin embedded specimens, which were also used for the first procedure of hardness testing. The fluxgram as follows better represents the microstructure analysis choice.

3.1.7.8. Porosity testing

For analysis of the porosity on the specimens, six images were chosen in the non-annealed and annealed samples, and were subjected to ImageJ software (version 1.53K) treatment, through a brightness interval of [0;90] at the colour threshold, and subsequent analysis of the highlighted areas – dark spots would translate into a certain area volume, which would give the percentage of porosity existent on images, and by transposing, the specimens overall porosity.

3.2. Results and discussion

The analysis encompassed therefore a myriad of different properties. As mentioned previously, for the total of 12 test piece, there is division of 4 groups: 3 specimens for tension testing through the F2516; 3 specimens for compression testing through the E8M standard; 3 specimens for energy absorption during fracture through the E23 standard; and 3 specimens for transformation temperature determination by utilization of a DSC through the F2004 standard. There was also subsequent evaluation of the microstructure, hardness, and defects. In most cases, each of these groups were further subdivided into three sections: one for martensitic status determination – **group 1**; another for austenitic status determination – **group 2**; and other for effects of annealing on the material – **group 3**, however such procedures would depend on the character of the testing – some tests were better suited to compare austenite vs martensite differences, and other non-annealed vs annealed differences.

3.2.1. Tensile properties

The results of the tensile test carried out are shown as follows.

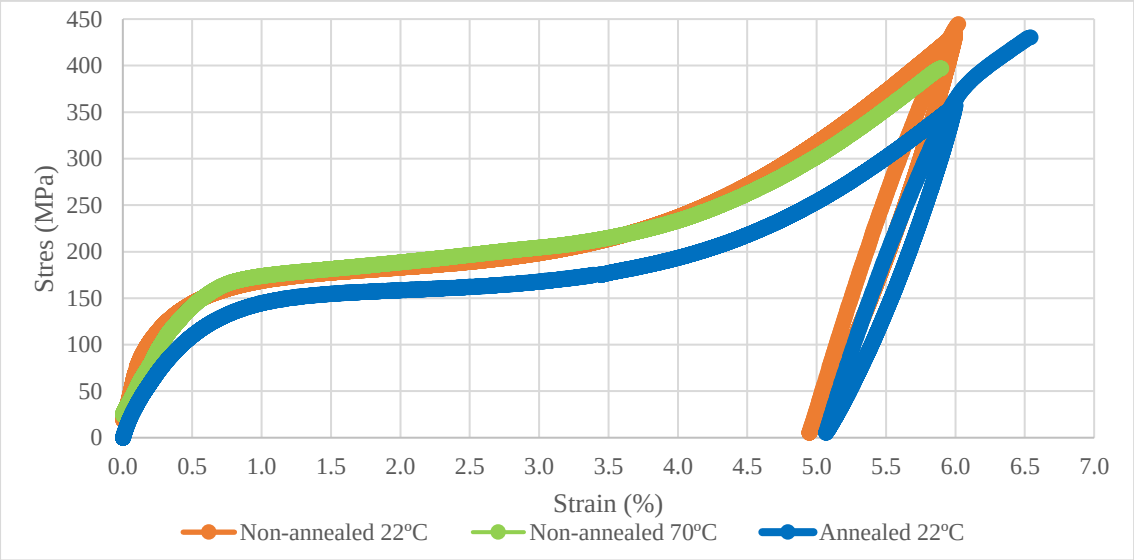


Figure 116 – Graphical result of the three traction specimens.

There is the creation of the table with a myriad of different properties which could be collected from the stress-strain curve. Calculation related to these properties can be seen in annex G.

Table 16 – Results of the properties of the three traction specimens.

Mechanical properties	Non-annealed		Annealed
	22ºC	70ºC	22ºC
Yield strength (MPa)	145	170	120
Upper plateau strength (MPa)	189	197	162
Tensile strength before recovery (MPa)	440	-	357
Ultimate Tensile Strength (MPa)	460	397	430
Young Modulus (GPa)*	57.2	27.1	26.6
Max Strain (%)	6.1	5.9	6.6

*Since there was not the recovery of the specimens in a way suitable for the test, lower plateau strength was discarded.

Regarding the non-annealed 22ºC sample, the material goes into the 6% strain, reaching 440 MPa, where it recovers partially to 4.9% of elongation, and afterwards it is subsequently pushed into 6.1% strain, where it fractures. Through a parallel curve around 0.2% strain, there is the visualization of the yield strength around 145 MPa, and an ultimate tensile strength of 460 MPa.

Meanwhile, in the non-annealed 70ºC sample, the material goes into the 5.9% strain, reaching 397 MPa, where it fully fractures, making it unable to see the recovery possibility of the material, which would start at 6% strain. Through a parallel curve around 0.2% strain, there is the visualization of the yield strength around 170 MPa, and (as mentioned) an ultimate tensile strength of 397 MPa.

Lastly, in the annealed 22ºC sample, the material goes into the 6% strain, reaching 357 MPa, where it recovers partially to 5.1% of elongation, and afterwards it is subsequently pushed into 6.6% strain, where it fractures. Through a parallel curve around 0.2% strain, there is the visualization of the yield strength around 120 MPa, and an ultimate tensile strength of 430 MPa.

The initial traction tests were made with different values than expected (see figure 117). The values of group 1 and 2 were quite similar, and both had fracture at the section between the head of the specimen and the cross-section of it. This means that there were defects present at the specimens in question – if not, there would be a fracture in the middle of the specimen, and not in the end of the shaft. Meanwhile, group 3, being annealed, showed better total strain capabilities, however also breaking at the end of the shaft.

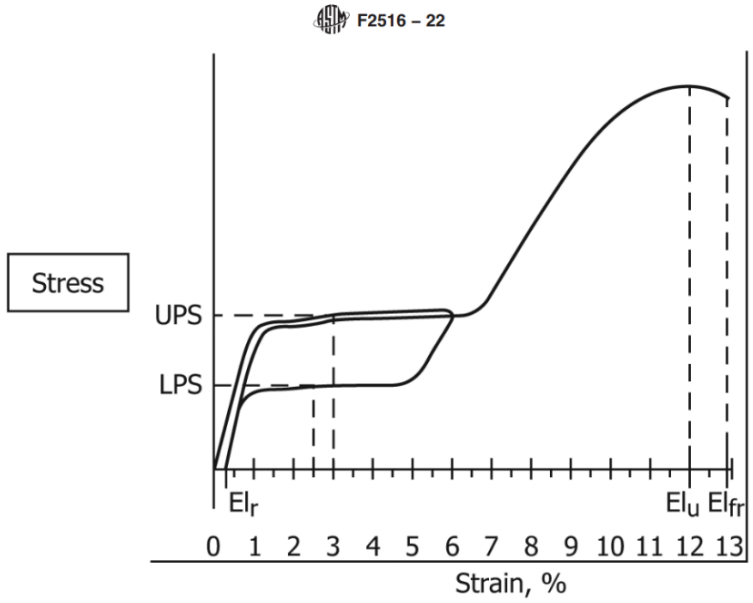


Figure 117 - Theoretical (expected) progression when with adequate manufacture, according to ASTM F2516.

Overall, the feasibility of the tests is inconclusive since the fracture was at the end of the shaft section (figure 118) – meaning possible manufacturing defects of the test pieces and no compliance with the procedures necessary for an accurate result. Despite this, it is obvious to see the annealing reduces UTS and increases maximum strain – meaning a decrease in resistance and an increase in ductility of the material.



Figure 118 - Fractured non-annealed specimens.

Therefore, one can assume manufacturing errors with the F2516 specimens, which can be attributed to a myriad of factors. At the time of manufacture, due to constraints related to the height of the build chamber (maximum height of 50mm – with the traction specimens having a total height of 58mm), these traction specimens were built with a certain inclination. Additionally, it was revealed that supports were given only at the head of the specimens, and this could have created internal stresses which weakened the resistance of the specimen – it was later confirmed by impossibilities regarding machinability of the heads of the specimens due to a bending phenomenon that made the

necessity of special adapter clamp supports (which were referenced earlier), due to a non-linear total geometry.

At the same time, temperature gradients could have been created at this part of the specimens, also contributing to its overall weakness. While the compression specimens were made with a 0º inclination and the DSC specimens were made with a 90º inclination, both not being affected regarding possible created stresses, the possibilities regarding the inclination of the traction specimens (as well as the charpy specimens) - with an inclination of 45º - could have severally impacted the mechanical properties of the test pieces, due to possible loads sustained. This is just educated guesses, however.

After lengthy deliberation with CATEC regarding the specimens, and with their full cooperation and support, it was shown the following images regarding the traction specimens, through use of CT scanning technology (figure 119). In such operation and after analysis, despite the bulk being in good conditions, the border is suboptimal – this is due to the different laser parameters used, which would explain the premature failure of the specimens. However, it is not enough for explanation on why they fractured all at the same part, although it does explain the insufficient strain that the specimens possessed and why they failed earlier than expected.

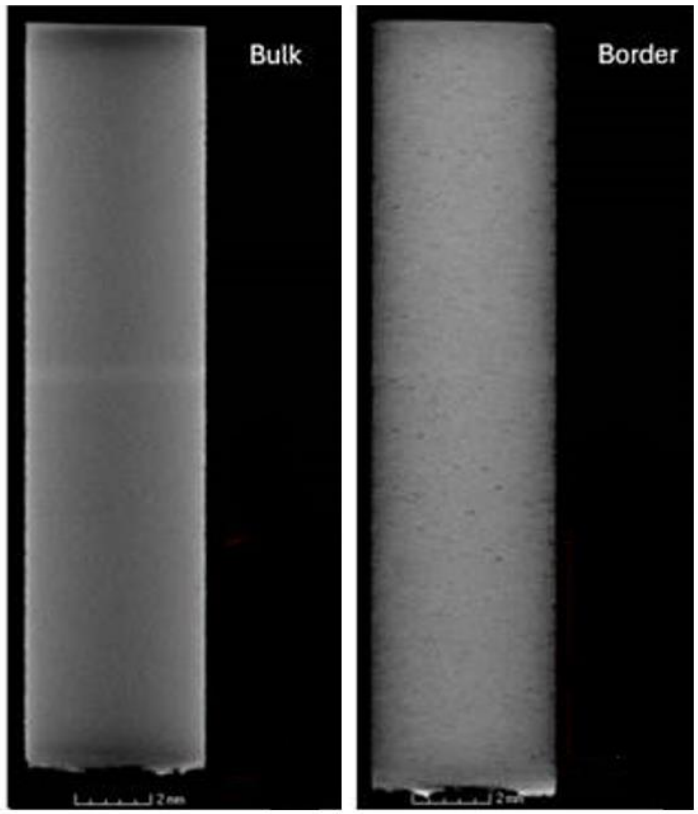


Figure 119 - Bulk vs border CT scan (courtesy of CATEC).

The defect between the lack of uniformity between the border and the bulk regions might contribute to such fracture, however – it could be explained as the initiator of the crack, but not its main propagator - when mounting the samples on the testing machine, any twisting or pulling force might have created or intensified a microcrack which was itself only propagated when the testing load was applied.

3.2.2. Compressive properties

Results of the compressive tests are shown as follows.

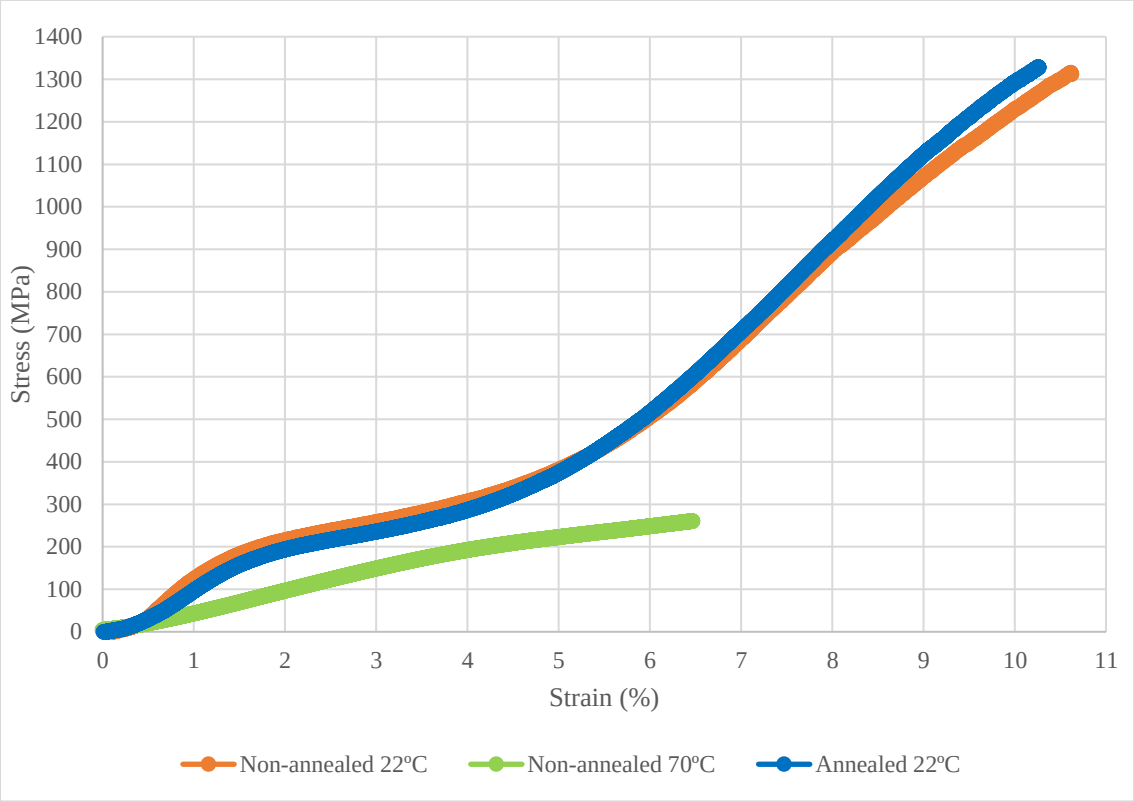


Figure 120 – Total results of the three compression specimens.

There is the creation of the table with a myriad of different properties which could be collected from the stress-strain curve. Calculation related to these properties can be seen in annex H.

Table 17 - Properties of the three compression specimens.

Mechanical properties	Non-annealed		Annealed
	22ºC	70ºC	22ºC
Compressive Yield strength (MPa)	180	200	180
Ultimate Compressive Strength (MPa)	>1300	>260	>1300
Young Modulus (GPa)	10.8	4.7	12.7
Max Strain (%)	10.6	6.5*	10.3
Stress at 6.5% Strain (MPa)*	590	261	607

* Due to the impossibility of reaching more than 30 KN in the heated chamber testing machine, there was not a possibility of increase the strain of group 2 specimen to more than 6.5%. Therefore, we can only make a successful comparison until this strain value, when comparing the total specimens utilized.

Regarding the non-annealed 22ºC sample, through application of maximum force of 150 KN, there was creation of the graph as shown. Compressive yield strength will have values of 180 MPa, with ultimate compressive strength being superior to 1300 MPa, and reaching value superior to 10.5% elongation. The test, for safety reasons, was interrupted at around 150 KN of force.

Meanwhile, in the non-annealed 70ºC sample, through application of maximum force of 30 KN, there was creation of the graph as shown. Compressive yield strength will have values of 190 MPa, with ultimate compressive strength being superior to 260 MPa, and reaching values superior to 6.5% elongation. The test, for safety reasons, was terminated at around 30 KN of force due to the use of a different machine, available at LTM.

Lastly, in the annealed 22ºC sample, through application of maximum force of also 150 KN, there was creation of the graph as shown. Compressive strength will also achieve values of 185 MPa, with ultimate compressive strength being superior to 1300 MPa, and reaching value superior to 10% elongation. The test, for safety reasons, was terminated at around 150 KN of force.

Compression tests allowed partial visualization of the difference between room temperature (22ºC) compressive stress and stress behaviour in austenitic phase temperature (70ºC). While group 1 and 3, which were made at room temperature, showed 6.5% strain around 600 MPa, group 2, which had a test conducted at 70ºC, and therefore can be theorized to reach an austenitic phase - behaved in a quite different way, reaching 250 MPa at the same strain percentage. This could be attributed to the fully austenitic phase of the specimen in group 2, having quite different stress-strain curve behaviour – there is a clear case of stiffness reduction when in austenitic phase – this means that, when in compression and in austenite phase, the specimens will have less resistance to elastic deformation, stretching more easily.

Such results are significant since the austenite phase is thought to be stiffer than the martensite phase, as a general rule, in shaped memory alloys. The results, however, agree instead with the work of (Bucsek, Paranjape, & Stebner, 2016), where it is explained that “Nitinol martensite prefers to behave stiffer under compressive loads and more compliant under tensile loads.” – a significant asymmetric behaviour of this material and which explains the results.

According to the same report, and as can be seen in figure 121: "*The truth is martensite crystals may be more compliant, equally stiff, or stiffer than austenite crystals, depending on the orientation of the loading direction with respect to the unit cells*." (Bucsek, Paranjape, & Stebner, 2016)

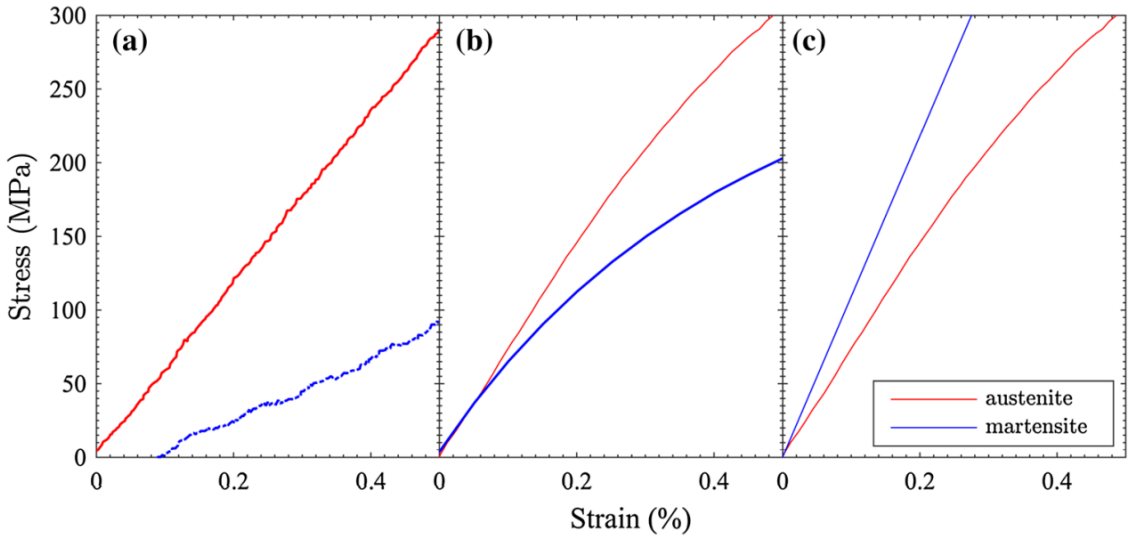


Figure 121 - Nitinol stiffness and relation with phases: (a) highly worked & textured Nitinol wire (austenite appears stiffer); (b) random texture, hot extruded martensite (appearing initially as stiff in both phases); (c) random-texture, as-cast Nitinol (martensite appears stiffer) (Bucsek, Paranjape, & Stebner, 2016).

This requires further research, however there is the possibility that additive manufactured nitinol has mechanical behaviour similar to, in this case, casting processes, and not to extrusion processes, and that the build direction might severely affect the properties – in this case, the compression specimens were built with 90ºC angle, however such properties might be different with specimens manufactured at various different angles – 30º, 45º, 0º, etc.

As says the aforementioned report "*The Young's Modulus of polycrystalline Nitinol is not a fixed number—it changes with both processing and in operando deformations. Nitinol martensite prefers to behave stiffer under compressive loads and more compliant under tensile loads.*" (Bucsek, Paranjape, & Stebner, 2016)

More research is required and is an opportunity for further projects regarding this matter - the unique relations of Ni-Ti according to its manufacturing orientation and process and how it dynamically impacts such properties.

3.2.3. Toughness properties

The results of the fracture toughness test are shown as follows.

The specimens used a potential energy of 300 Joules, with the non-annealed 22ºC sample achieving an absorbed energy of 4 Joules, the non-annealed 70ºC sample achieving an absorbed energy of 2.7 Joules, and the annealed 22ºC sample achieving an absorbed energy of 3.5 Joules. It is worth noting that all specimens had brittle fractures (figure 122), meaning that the specimens fractured abruptly due to a lack of significant plastic deformation capabilities, and overall low energy absorption capacity, translating into a lack of ductility in the material, both at nominal room temperature and in the heated state.

Table 18 - E 23 Charpy absorbed energy.

Chosen Group		Non-annealed		Annealed
		22ºC	70ºC	22ºC
Total impact absorbed energy	Foot-pound	3 ft-lb	2 ft-lb	2.6 ft-lb
	Joules (J)	4 J	2.7 J	3.5 J

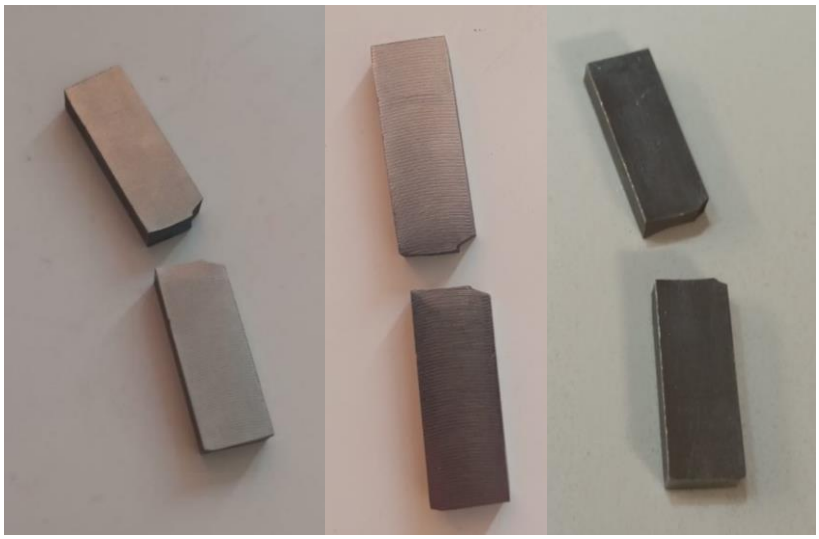


Figure 122 - Group 1 (left), group 2 (middle) and group 3 (right) specimens after impact.

It is worth noting that all specimens had brittle fractures (figures 123, 124 and 125), meaning that the specimens fractured abruptly due to a lack of significant plastic deformation capabilities, and overall low energy absorption capacity, translating into a lack of ductility in the material.

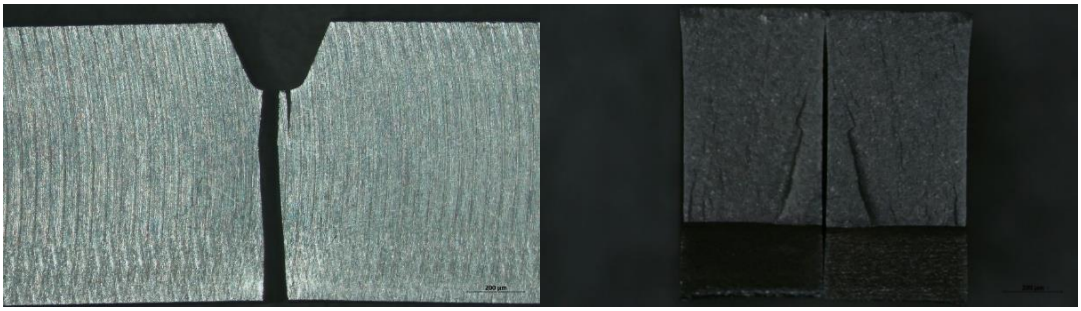


Figure 123 - Group 1 Charpy specimen: lateral view (left) and top view (right).

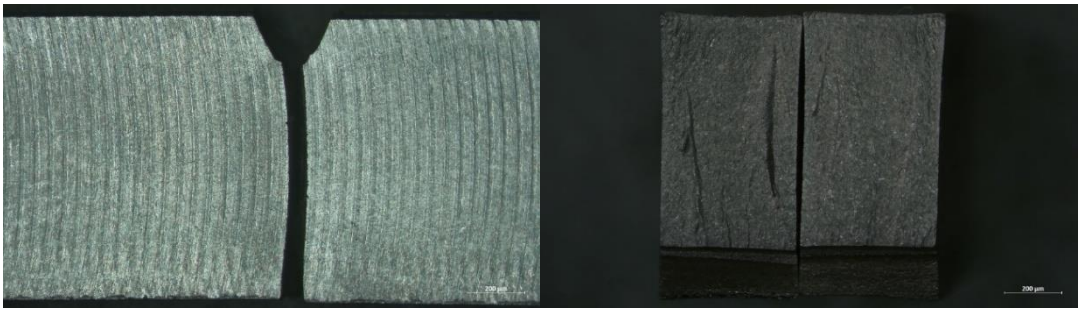


Figure 124 - Group 2 Charpy specimen: lateral view (left) and top view (right).

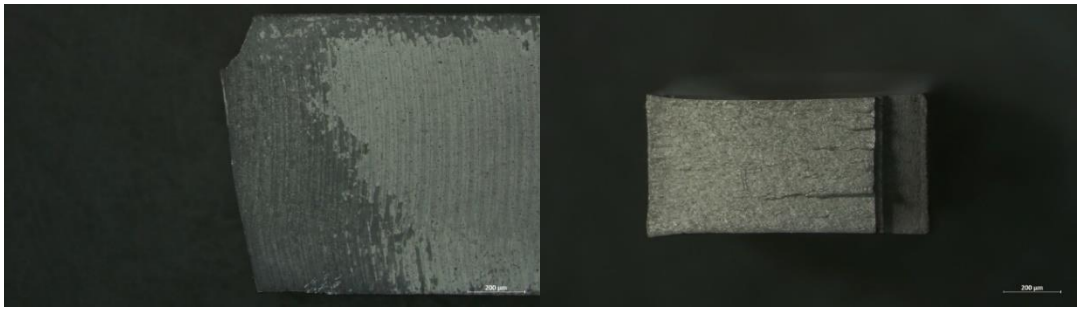


Figure 125 - Group 3 Charpy specimen: lateral view (left) and top view (right).

Charpy toughness tests allowed possible determination of the differences between the toughness of parts when at room temperature phase, at increased temperature, and in an annealed sample at room temperature, respectively.

The test pieces, when compared with different temperatures, revealed some difference regarding toughness characteristics, with the test piece at 20ºC room temperature having 4 joules vs the 2.7 joules at 70ºC – this can be explained by the fact that, the sample at 70ºC, having a fully austenite phase, revealed itself to be harder and more brittle, revealing itself not to be as ductile, despite the difference being of only 1.3 Joules, it effectively meant a decrease of 32.5% in toughness absorption characteristics. Bibliographical

research agrees with that hypothesis of the austenitic phase being more brittle than the martensite phase, which tends to have better energy absorption and increase fracture toughness characteristics.

When comparing annealed vs non-annealed samples at room temperature, it also did not reveal any noticeable differences, with the non-annealed sample having 4 Joules vs the annealed sample having 3.5 Joules – a decrease in 12.5% of the toughness, which is not enough deviation for significant conclusions.

3.2.4. Transformation temperature properties

This procedure is realized through heating and cooling of the specimen at a controlled rate in a controlled environment, with the heat flow between the test material and a reference material due to energy changes continuously monitored, with absorption of energy resulting in an endothermic peak on heating (and where we can see the martensite values) and a release of energy resulting in an exothermic peak on cooling (and where we can see the austenite values), due to the phase transformation mechanism.

The graph can be said to start at the lower left corner and move until the lower right corner (heating), where the peaks are the austenite start and finish values (by order) and continuing at the top right corner and move until the top left corner (cooling), where the peaks are the martensite start and finish values (by order).

The powder material graph results is shown, followed by the non-powder samples DSC analysis with different annealing treatments. There is also visualization of a table and further discussion of the results.

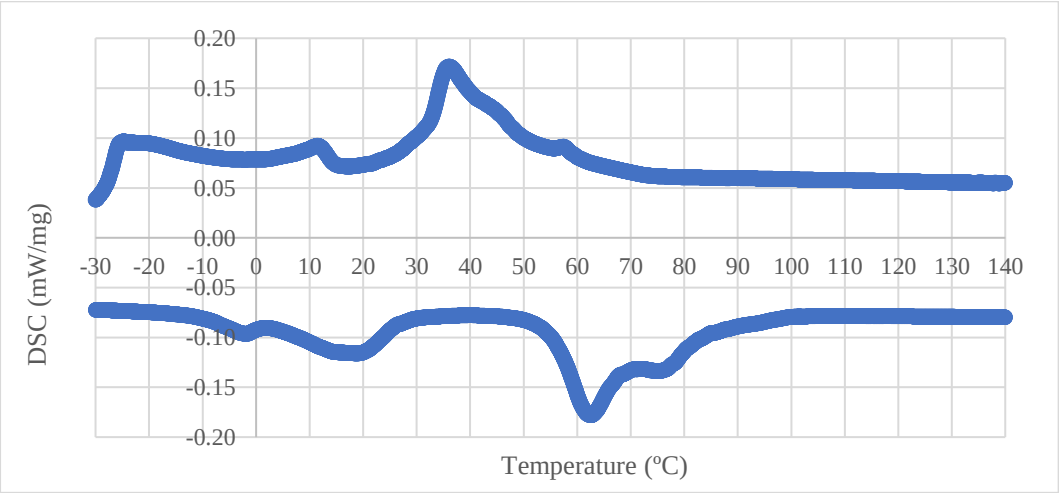


Figure 126 - NI-Ti powder DSC graph.

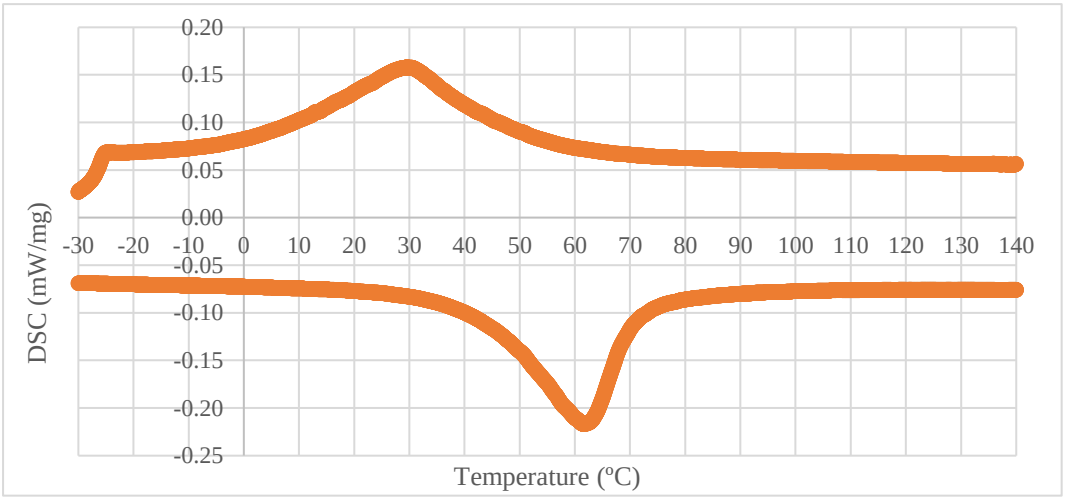


Figure 127 – Non-annealed DSC graph.

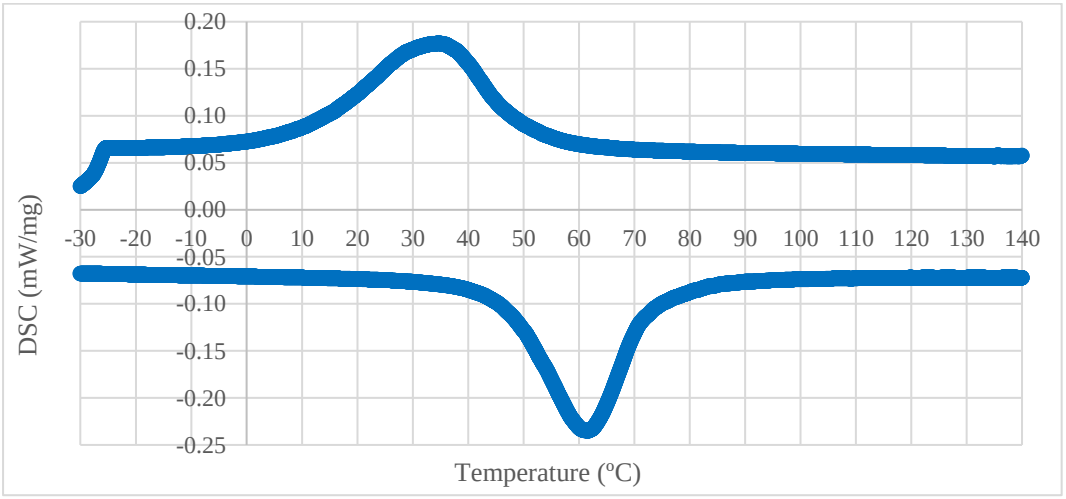


Figure 128 - Annealed at 800ºC DSC graph.

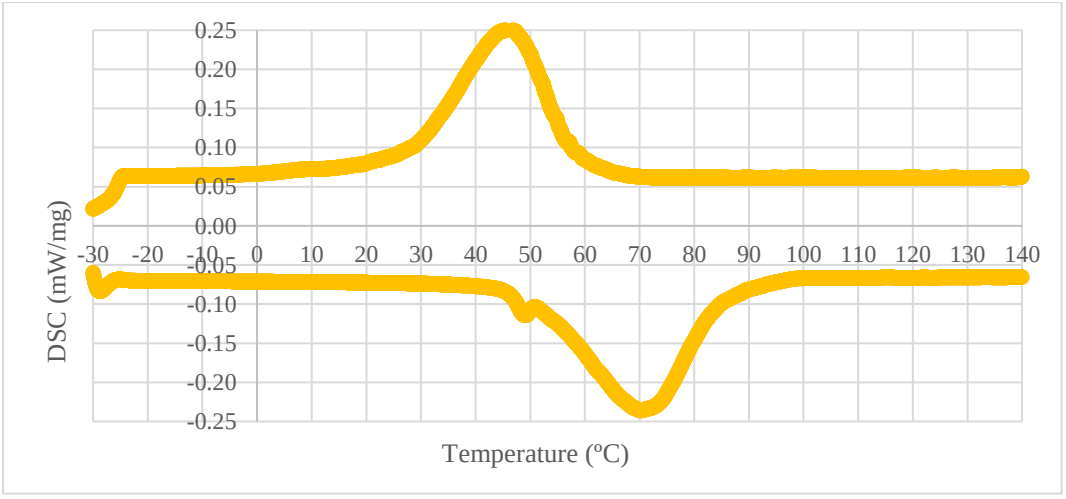


Figure 129 - Annealed at 800ºC and 500ºC DSC graph.

Total results can be seen as follows from the next table, for total comparison.

Table 19 - DSC properties results.

Sample	Ms (ºC)	Mf (ºC)	As (ºC)	Af (ºC)
Powder	65	30	50	85
Non-annealed	50	5	45	70
Annealing 800ºC	50	10	45	75
Double annealing 800ºC/500ºC	60	30	50	85

Firstly, when discussing the powder sample, it is worth noting that this was so that there could be a preliminary report of possible transformation temperatures possible. In general, the DSC of the powder material is inaccurate and presents too much variability due to the irregularity between different grain zones, and the possibility of certain parts being sintered before others, with too much time between follow up thermal changes between parts of the same sample.

When discussing non-powder samples, the results are much more interesting. It is clear that the transformation peaks become more pronounced and displaced to the right of the graph - increased temperature values – as we increase the annealing treatments developed and its intensity. The usage of a double annealing also increases such peaks and movements, in a much more pronounced manner. It is possible to visualize, at the austenite start, the possibility of the R-phase formation, referring to twinned martensite, which might be induced by the treatments done (figures 130 and 131)

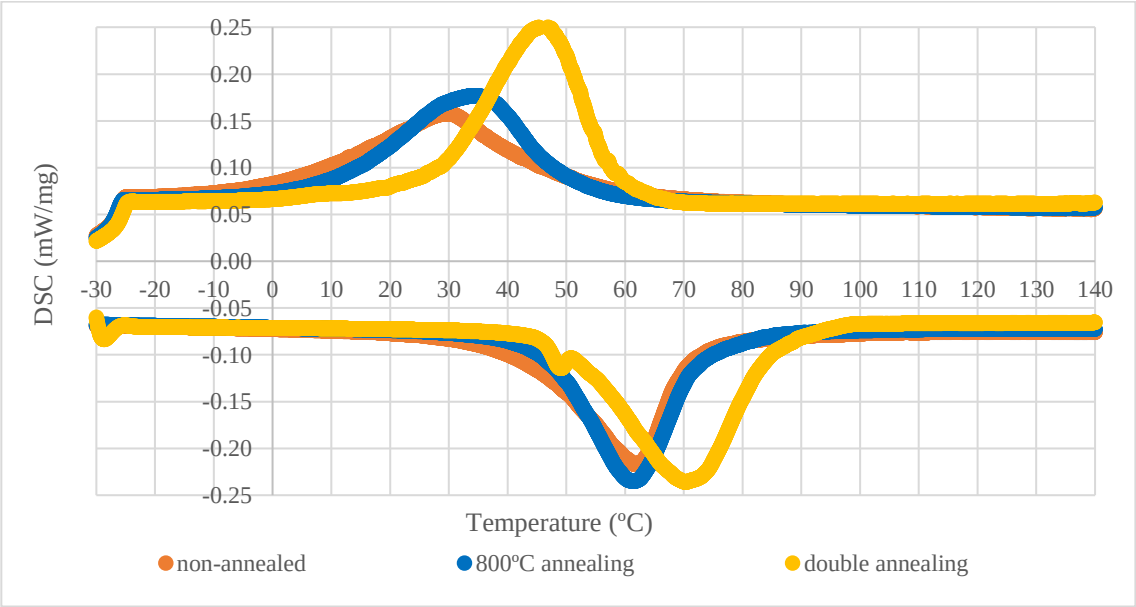


Figure 130 - Comparison between non-powder samples.

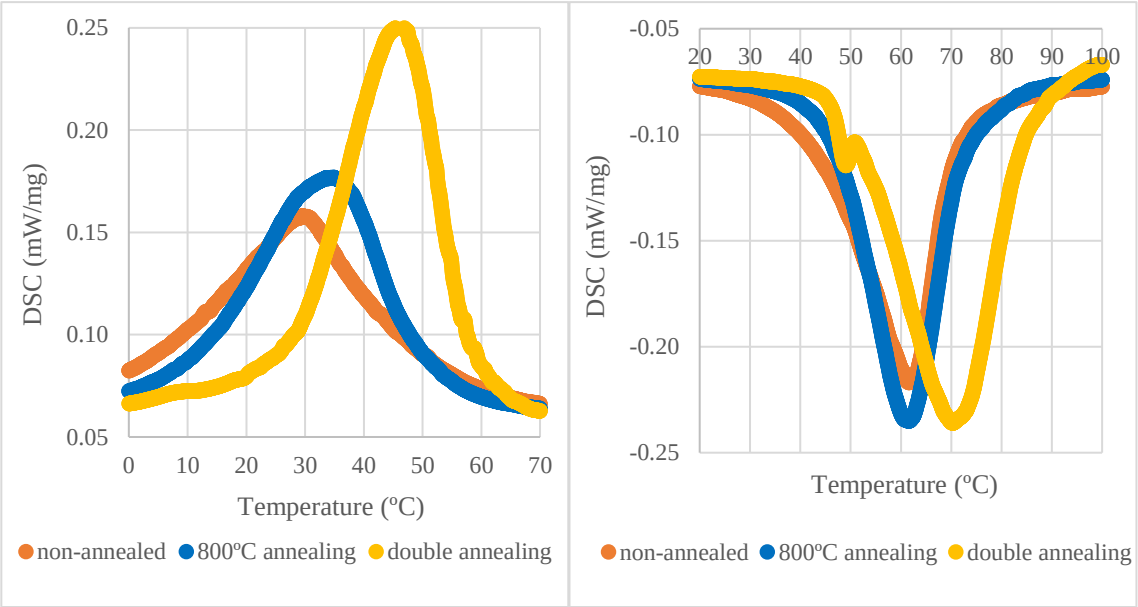


Figure 131 – Martensite (left) and austenite (right) curve comparison between the non-powder samples.

Analysis of transformation temperature through differential scanning calorimetry allowed the visualization of the start and finish temperatures of the austenite and martensite transformations. It is clear that, at room temperature, the specimen will have a partially martensitic, partially austenitic composition. Such procedure might explain why compressive test values at 70ºC were given different results regarding stiffness / Young Modulus.

At the same time, it is clear that, with annealing operations done, there is the existence of an increase in the energy of the peak of transformation temperature, being more defined and pronounced.

Additionally, there is an increase in the necessary transformation temperatures for the total change of the phases in the specimens, with a modification in the martensite finish temperature and in the austenite start temperature accounting for an increase in 10ºC.

3.2.5. Hardness properties

The results of the first procedure of the hardness tests are shown in tables 20 and 21, with distinction between the non-annealed and annealed samples. Additionally, figures 132, 133 and 134 show a more graphical interpretation of the given results.

Table 20 - Non-annealed samples hardness results.

Non-annealed samples	Force (kgf)	Hardness (HV)		
		22ºC	70ºC	100ºC
CR1	40	234	232	232
CR2	20	216	195	210
TR1	20	114	127	201
TR2	20	195	210	210
CH1	20	182	183	201
CH2	20	189	175	232
Average	-	189	187	214

Table 21 - Annealed samples hardness results.

Annealed samples	Force (kgf)	Hardness (HV)		
		22ºC	70ºC	100ºC
CR1	20	228	231	232
CR2	20	209	190	201
TR1	20	175	161	201
TR2	20	210	210	201
CH1	20	183	148	175
CH2	20	182	160	183
Average	-	189	183	199

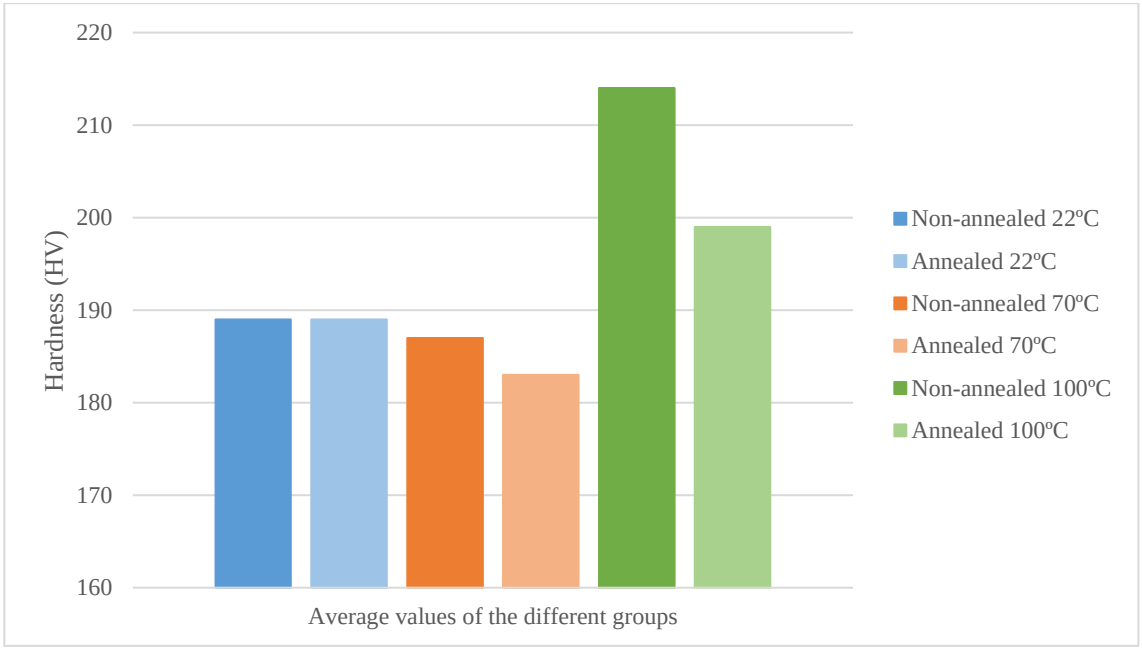


Figure 132 - Graphical average results of the first hardness procedure.

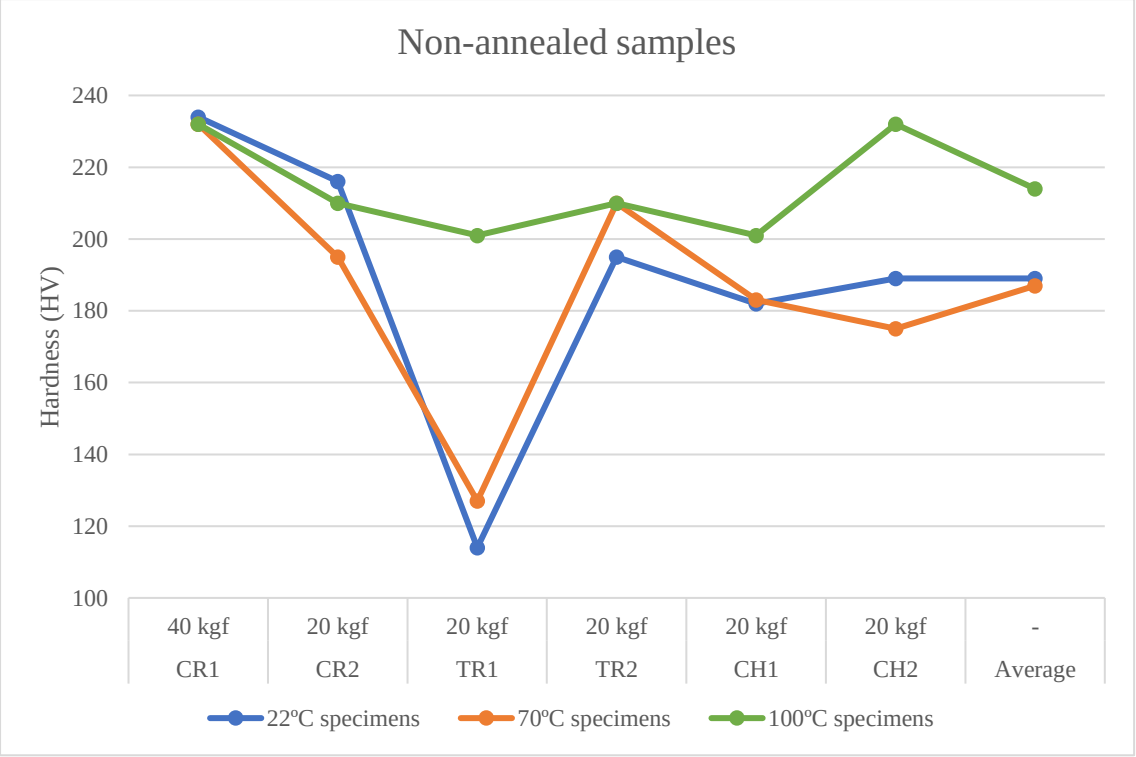


Figure 133 – First procedure non-annealed graphical results.

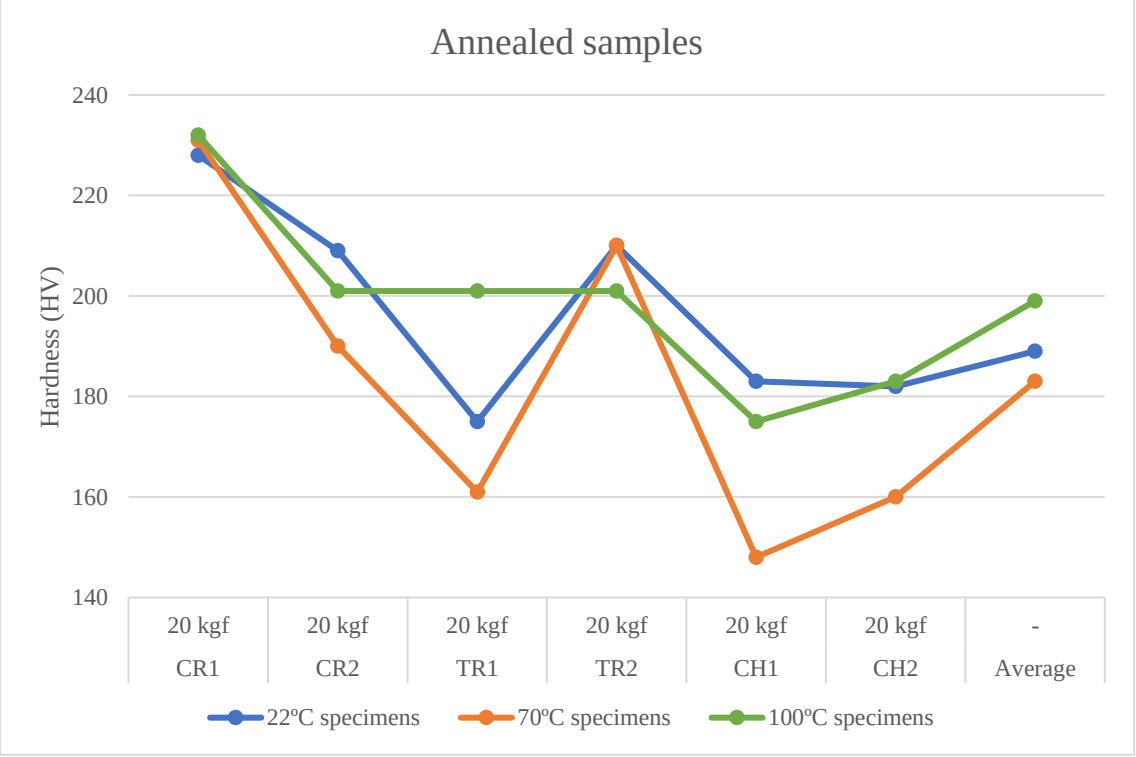


Figure 134 – First procedure annealed graphical results.

The results of the second procedure of the hardness tests are shown in the next table as follows, with distinction between the room temperature (22ºC) and heated (150ºC) groups. Figure 135 shows a more graphical interpretation of the results.

Table 22 - Second procedure 22°C hardness results.

Samples tested at 22ºC		Force (kgf)	Hardness (HV)
Non-annealed	Specimen 1	20	168
	Specimen 2	20	183
Annealed	Specimen 3	20	168
	Specimen 4	20	165
Average		-	171

Table 23 - Second procedure 150°C hardness results.

Samples tested at 150ºC		Force (kgf)	Hardness (HV)
Non-annealed	Specimen 1	20	224
	Specimen 2	20	277
Annealed	Specimen 3	20	243
	Specimen 4	20	236
Average		-	245

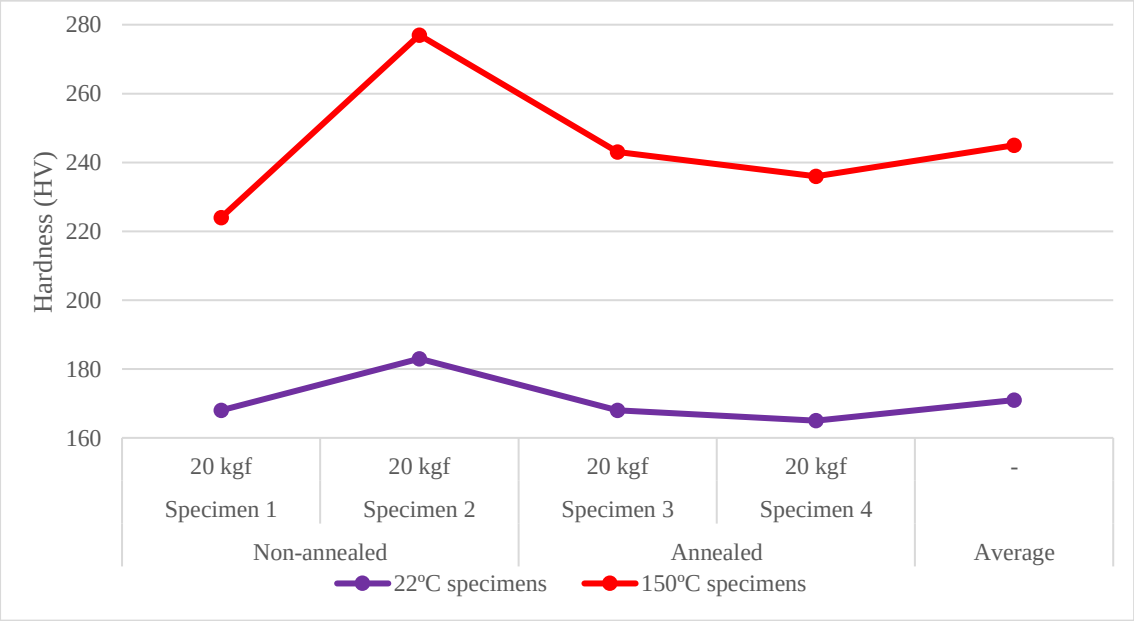


Figure 135 - Second procedure graphical results.

Comparing the first and second procedure by joining all overall data, we can see the following values as shown in figure 136. First procedure contributes with the 22ºC, 70ºC and 100ºC results, while the second procedure contributes with 22ºC (second) and 150ºC results.

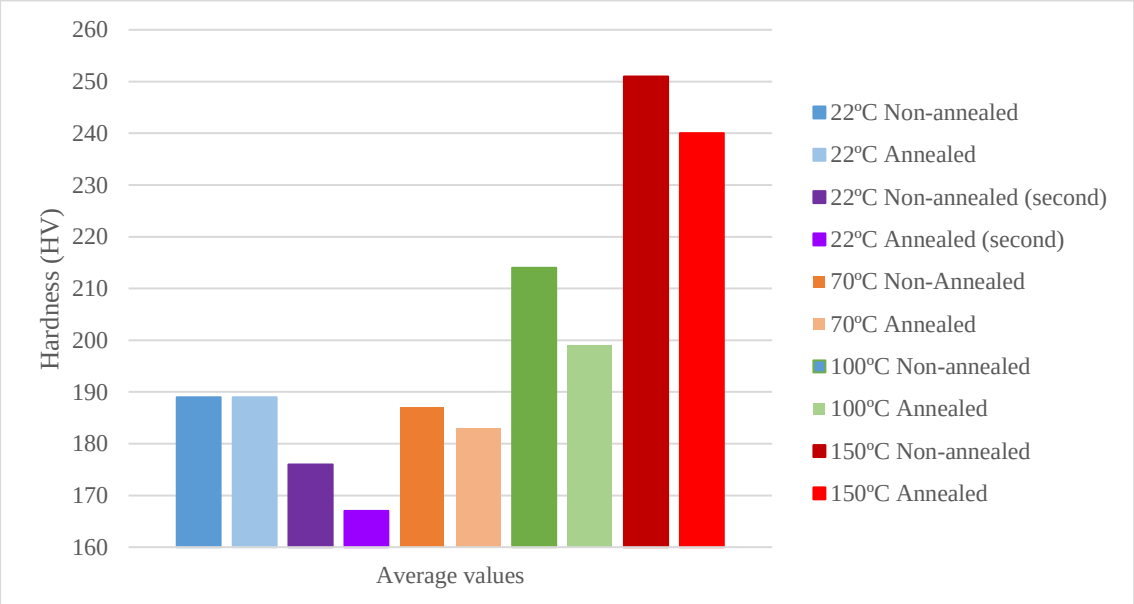


Figure 136 - Graphical average results of global hardness results.

It is clear that, by looking at hardness values, the material starts exhibiting higher hardness values when above 100ºC, additionally increasing throughout the 150ºC, but staying at similar hardness values at 22ºC and 70ºC.

This means that, at 22ºC and 70ºC, the material did not start to harden, meaning it is still in the martensite phase. At 100ºC and 150ºC, it already starts exhibiting transformation into the austenite phase.

It is worth noting that, due to the manual process of taking out the specimens from the oven, positioning them in a hardness testing machine at room temperature, taking 1 to 2 minutes, might affect in a non-light way the actual temperature of the specimens. This mean that, for example, the 70ºC samples, could actually be at 40ºC, not being able therefore, to have reached enough temperature to start the actual austenite transformation.

Another factor to consider is how, with annealing treatments done, there is a clear reduction of hardness in the material – this was expected as it is usual for annealing treatments to reduce hardness so as to increase ductility, as a final stage or for posterior processing of the material. (Huang & Liu, Effect of annealing on the transformation behavior and superelasticity of NiTi shape memory alloy, 2001)

3.2.6. Microstructure

The results of microstructure etching are shown nonetheless, with usage of the 2nd solution (HF + H2O2), since it proved to demonstrate clearer results (although even these proved to be lacklustre). Microstructure was taken from the resin moulds used for hardness testing.

3.2.6.1. Compression microstructure

The compression specimen microstructure is shown as follows.

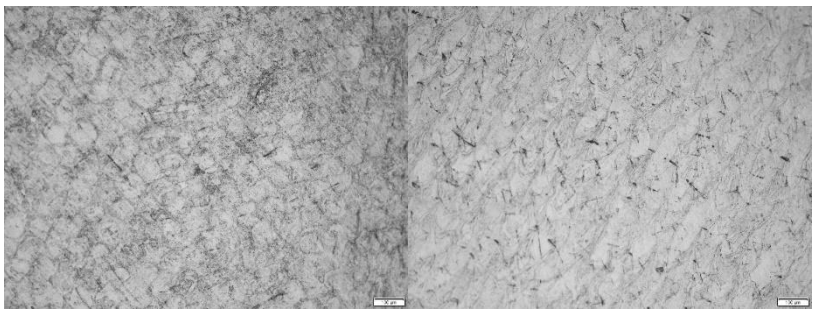


Figure 137 - CR1 and CR2 non-annealed microstructure (HF + H2O2).

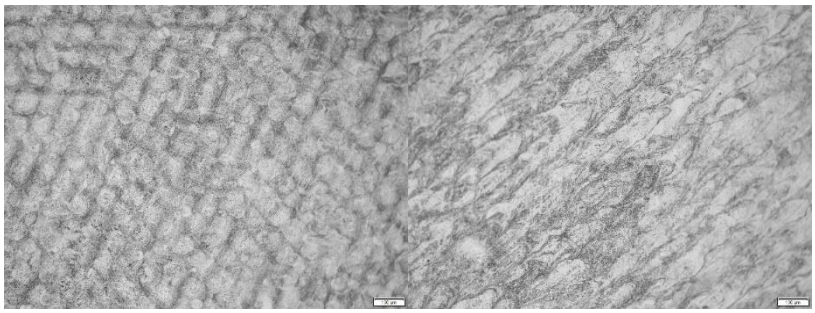


Figure 138 - CR1 and CR2 annealed microstructure (HF + H2O2).

3.2.6.2. Traction microstructure

The traction specimen microstructure is shown as follows.

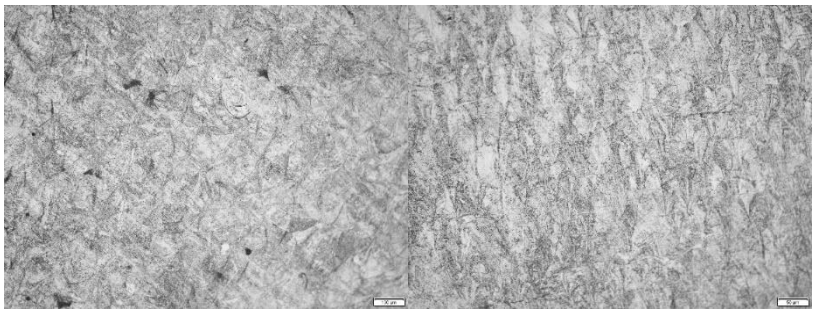


Figure 139 - TR1 and TR2 non-annealed microstructure (HF + H2O2).

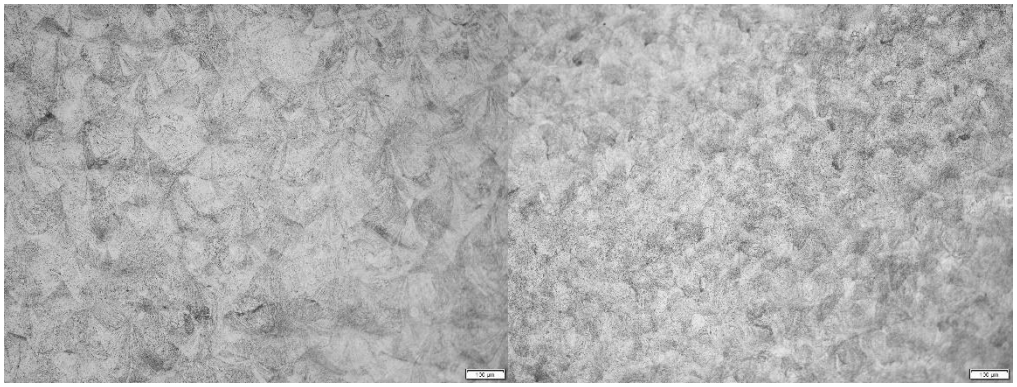


Figure 140 - TR1 and TR2 annealed microstructure (HF + H2O2).

3.2.6.3. Charpy microstructure

The fracture toughness specimen microstructure is shown as follows.

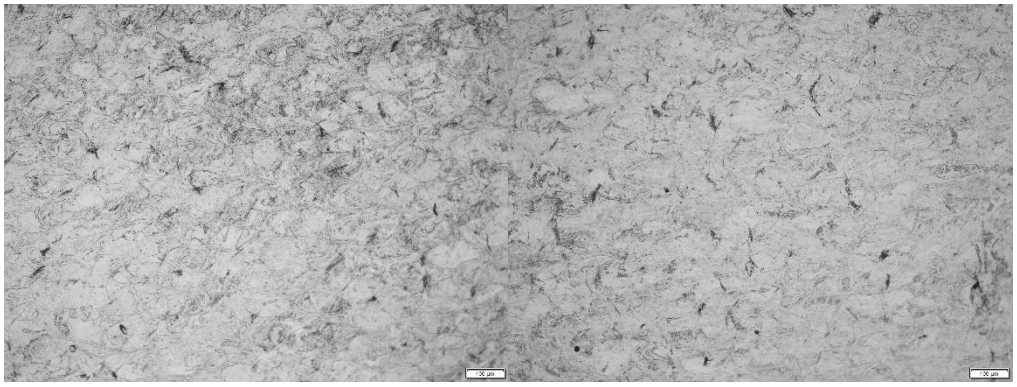


Figure 141 - CH1 and CH2 non-annealed microstructure (HF + H2O2).

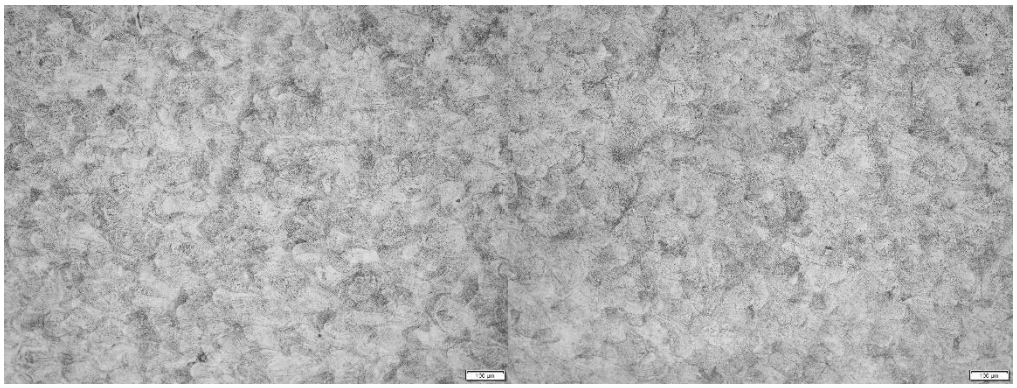


Figure 142 - CH1 and CH2 annealed microstructure (HF + H2O2).

It is clear to see that the build orientation has a significant impact on the disposition of the grains, assuming a direction through the aforementioned build direction. Despite such behaviour, the lack of proper etching makes any sort of analysis mostly ineffective.

3.2.7. Porosity

The results of the porosity analysis are shown as follows in figures 143 and 144 and data is shown in tables 24 and 25.

The red lines show the blackest part which were deemed indication of porosity. Through this, there was subsequent calculus of the proper area, and overall percentage of total area occupied by such parts, translating into a rough estimation of the porosity.

3.2.7.1. Non-annealed sample

The related images for the non-annealed samples are shown as follows.

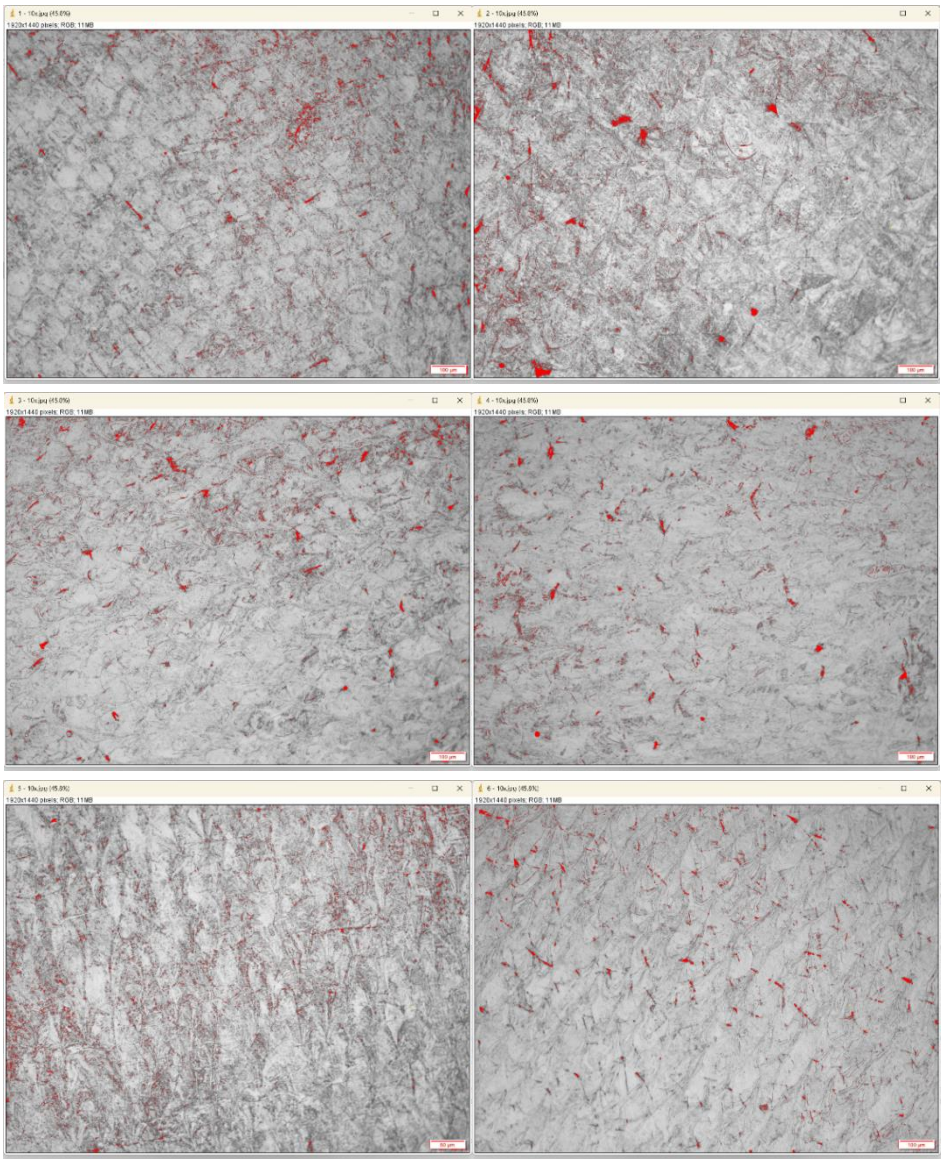


Figure 143 - Non-annealed samples with colour threshold input.

3.2.7.2. Annealed sample

The related images for the non-annealed samples are shown as follows.

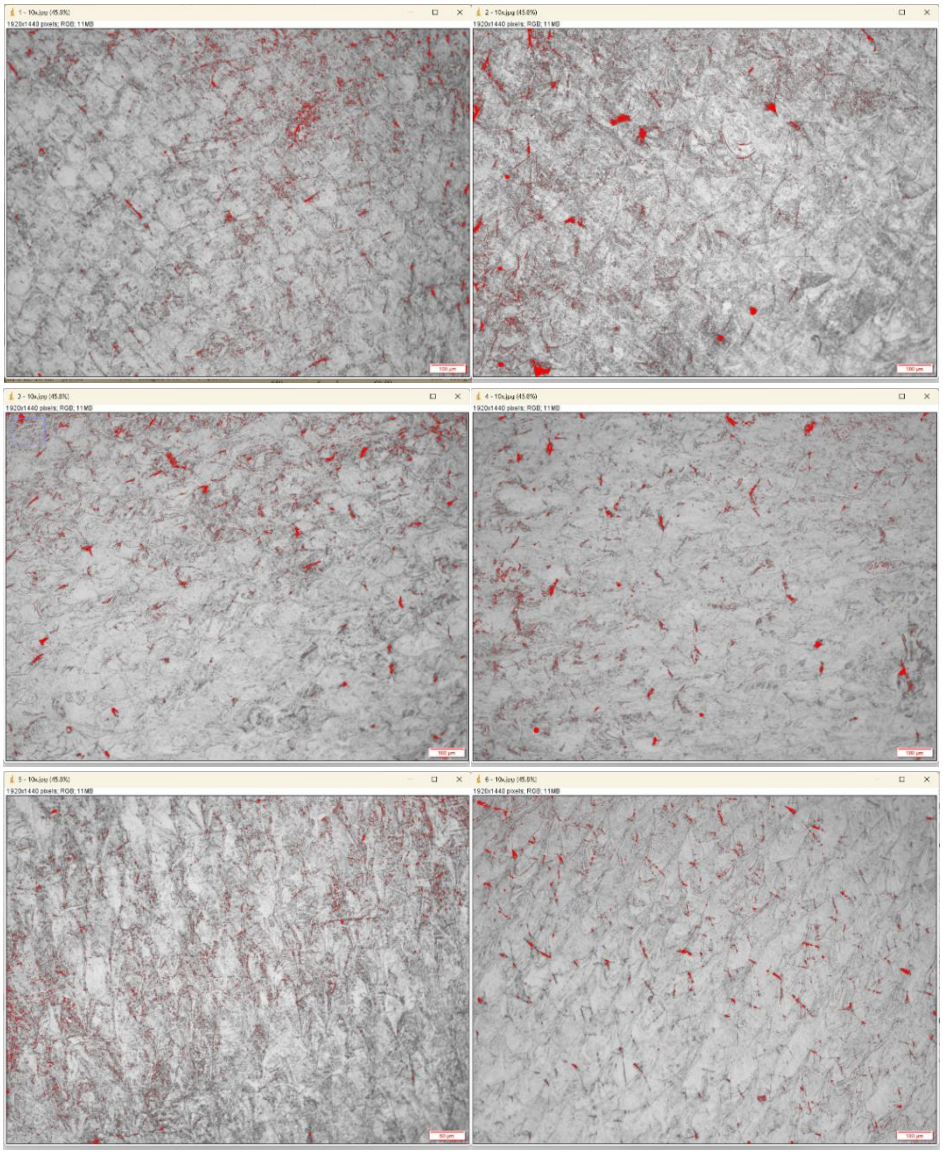


Figure 144 - Annealed samples with colour threshold input.

There was calculation of the area highlighted, and the results are shown as follows. It is clear to see that the porosity is relatively low, having acceptable values of density above 99.5%, and without significant changes between the non-annealed and annealed specimens.

Table 24 - Non-annealed porosity values.

ImageJ Porosity Analysis		Porosity area (µm2)	Porosity (%)	Density (%)
Non-annealed	Specimen 1	2889.599	0.20	99.80
	Specimen 2	5447.334	0.38	99.62
	Specimen 3	4653.573	0.32	99.68
	Specimen 4	6132.111	0.42	99.58
	Specimen 5	1569.016	0.11	99.89
	Specimen 6	5992.424	0.41	99.59
Average		4447.343	0.31	99.69
Total Area of the image (µm2)		1451793.724		100

Table 25 - Annealed porosity values.

ImageJ Porosity Analysis		Porosity area (µm2)	Porosity (%)	Density (%)
Non-annealed	Specimen 1	2891.064	0.20	99.80
	Specimen 2	6824.866	0.47	99.53
	Specimen 3	5545.659	0.38	99.62
	Specimen 4	7181.511	0.50	99.50
	Specimen 5	622.272	0.04	99.96
	Specimen 6	4119.272	0.28	99.72
Average		4530.774	0.31	99.69
Total Area of the image (µm2)		1451793.724		100

3.2.8. Shape memory recovery

Results for the shape memory effect testing can be seen as shown in the next table.

Table 26 - Results of the SME test.

Deformation cycles	Pre-deformation height (mm)	Post-deformation height (mm)	Post-heating cycle height (mm)
1st	24.7	24.2	24.62
2nd	24.62	23.41	24.37
3rd	24.37	23.3	24.25
4th	24.25	23.23	24.19

Of note that pre-deformation and post-heating cycle measurements were similar, when comparing between different deformation cycles (the beginning of one of the deformation cycles was the finish of another one). It can be seen that there is still adequate recovery of the shape memory effect, with the results also shown in figure 145, for optimal visualization of the process.

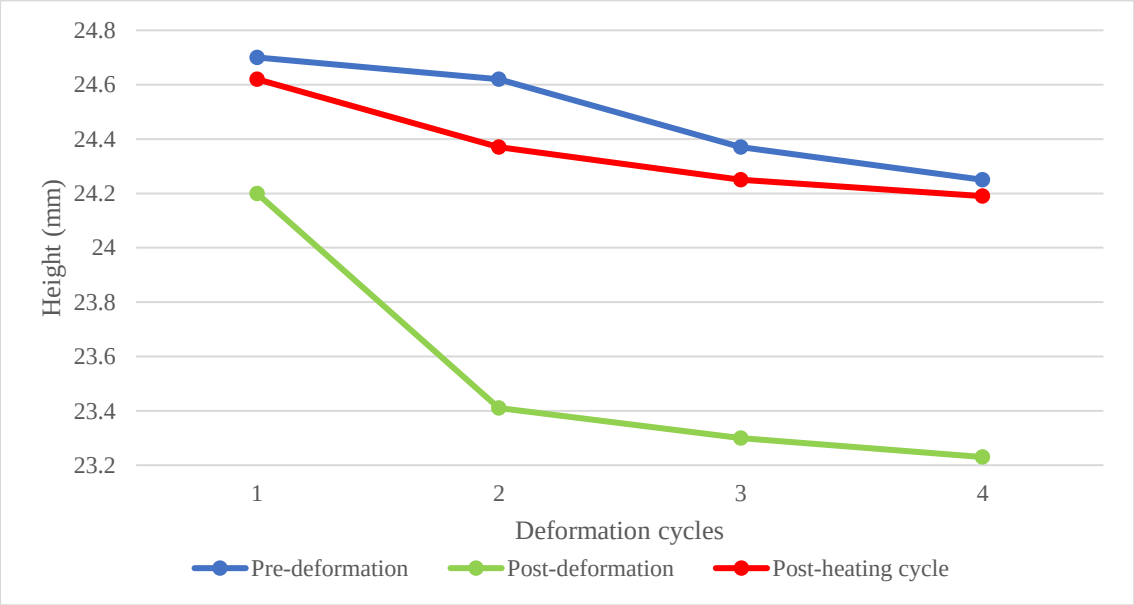


Figure 145 - Graphical results of the SME test.

As said before, the testing machine for the SME effect was similar to the operation regarding the E9 compression testing, with determination of the stress-strain curves between the results, which are shown as follows in figures 146 and 147.

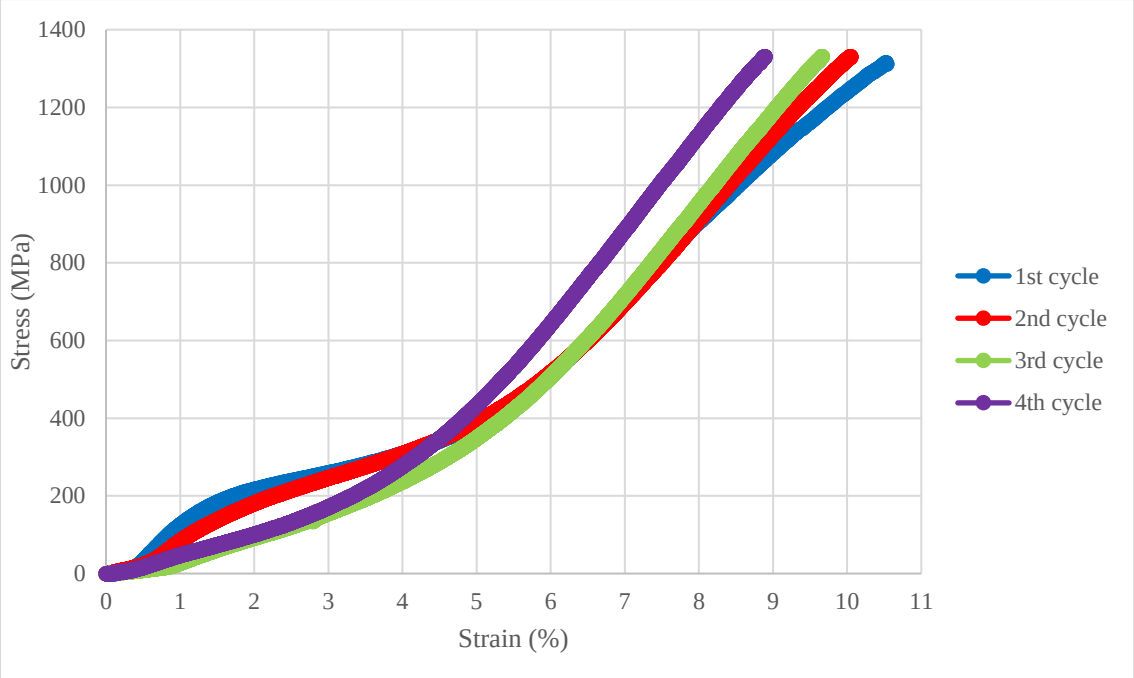


Figure 146 - Stress-strain curves of the compression across several deformation cycles.

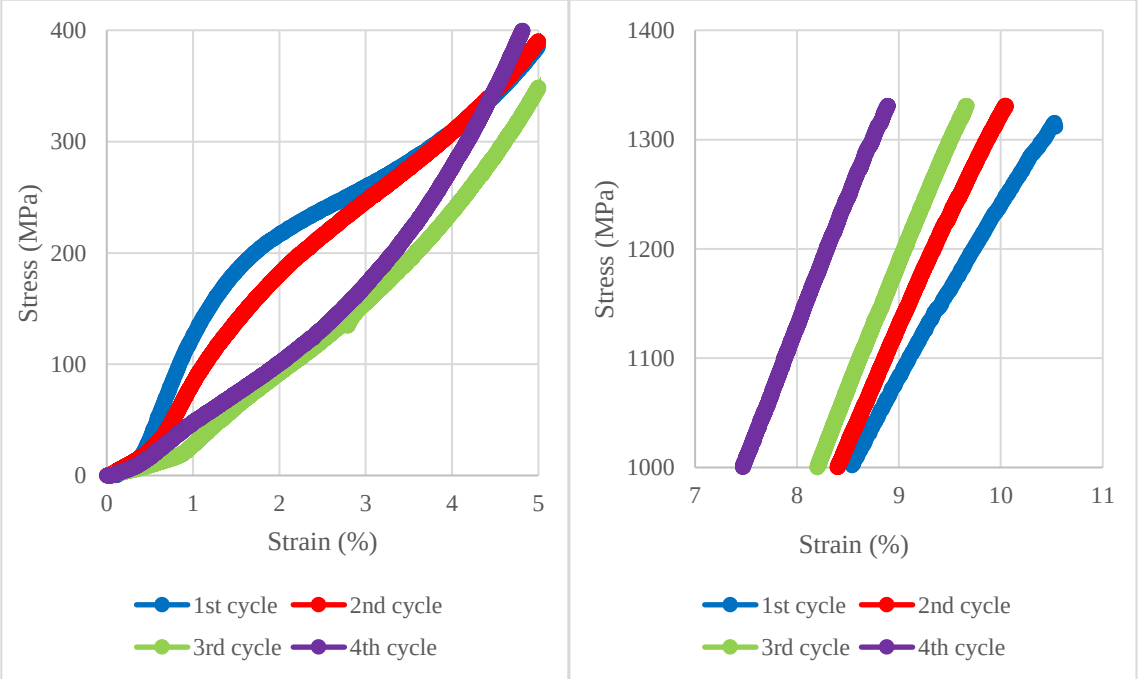


Figure 147 – Start (left) and finish (right) of the stress-strain curves of the compression across the deformation cycles.

There is the creation of table 27, with a myriad of different properties which could be collected from the stress-strain curve. Calculations related to these properties can be seen in annex I.

Table 27 - Deformation cycles overall properties.

Chosen Group	1st cycle	2nd cycle	3rd cycle	4th cycle
Young Modulus (GPa)	15.64	10.94	6.18	5.79
Max Strain (%) (A)	10.5	10	9.7	8.9
Recovered strain (after heating and compared to origin of cycle) (%) (B)	84	79	89	94
Effective recovered strain (%) (A*B)	8.82	7.9	8.63	8.37
Compressive Yield strength (MPa)	200	180	110	90
Ultimate Compressive Strength (MPa)	>1300			

It is clear to see that, with more and more deformation cycles, both the total achieved strain at 150 KN, the Young Modulus of the material, and the compressive yield strength starts decreasing, meaning that the material start behaving in a less stiff and more flexible way, while becoming weaker and less resistant.

Analysing the beginning of the stress-strain curve, the first two deformation cycles have a much more accentuated and conventional stress-strain curve, with the last two offering a much less pronounced and overall weaker profile – this could indicate not as much of a tendency of detwinning martensite, possibly due to the already past of the detwinned status – meaning possible tendency, at the third cycle, of vastly different behaviour with the adaption of the martensite unto the cyclic system, as can be seen in figure 148 (Turner, 2001).

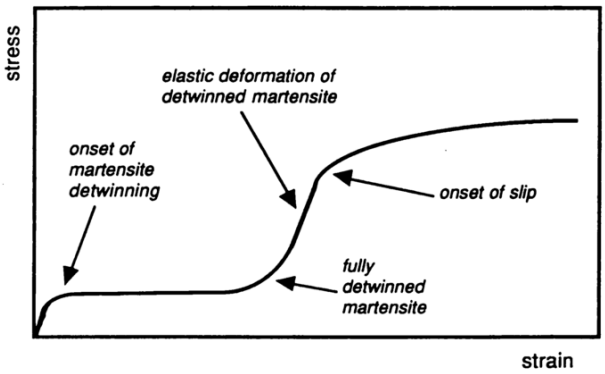


Figure 148 - Stress-strain curve and its relation to detwinned martensite (Turner, 2001).

3.2.9. SEM analysis

So as to analyse the constituents of the specimens and for a better visualization of the overall microstructure, the fracture of the tensile specimens – cut in half so that a part of them could be inserted into resin for the previous mentioned "first procedure" hardness testing – was analysed through scanning electrode microscopy analysis. In particular, there was usage of the 2 interfaces of fracture of a non-annealed sample, and one of the annealed samples. The remaining was already used with the resin embedded configuration for previous hardness testing.

3.2.9.1. Microstructural

There was the collection of images on the non-annealed and annealed samples. Although such imagery doesn't substitute for a properly etched microstructure analysis, it

possible to see parts of microstructure through this method, and it would be an interesting addition.

i) Non-annealed sample

The non-annealed sample images are shown as follows. A total of 4 images were collected of each interface – the base and the neck portions of the specimen.

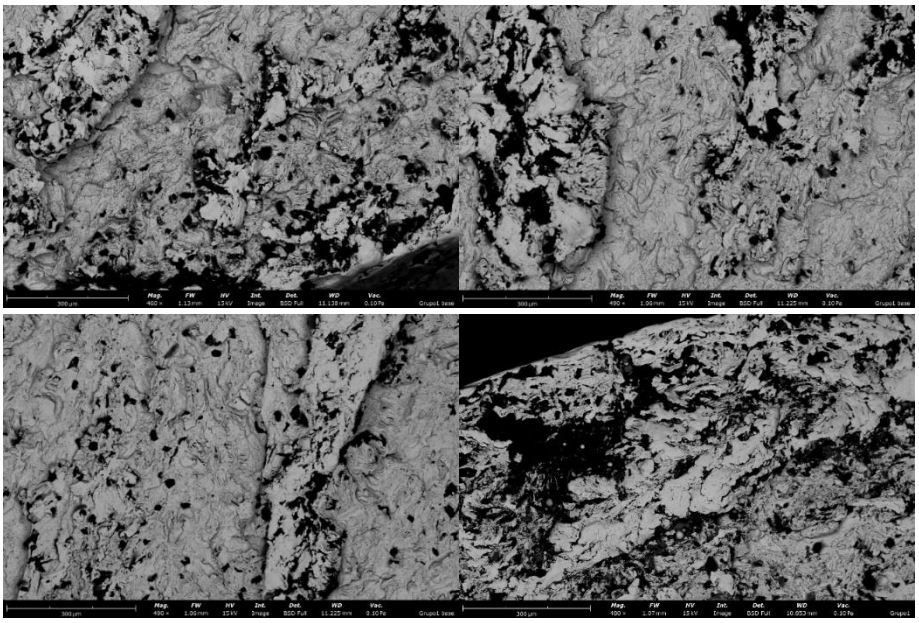


Figure 149 - Base interface images.

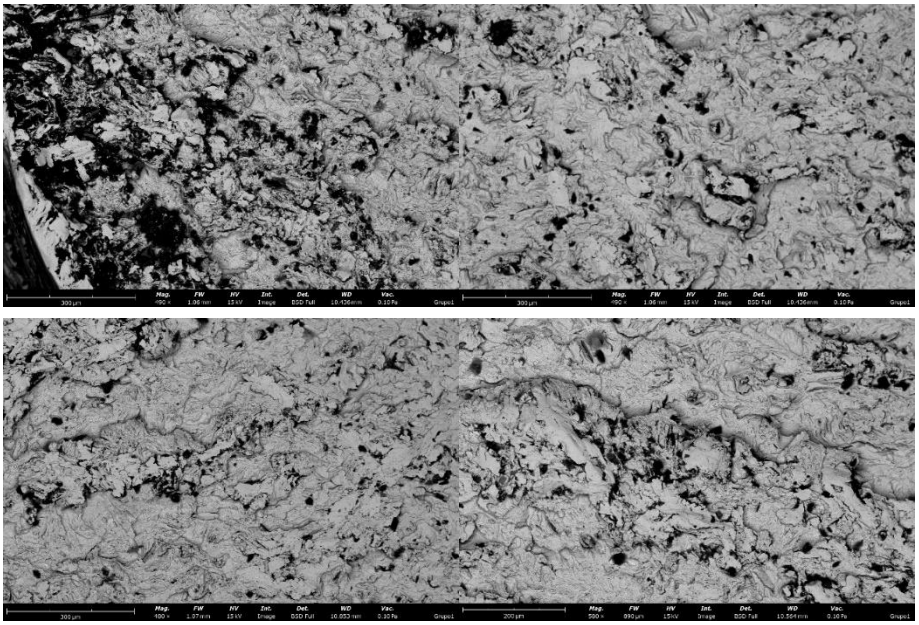


Figure 150 - Neck interface images.

ii) Annealed sample

The annealed sample images are shown as follows. A total of 6 images were collected of the base interface.

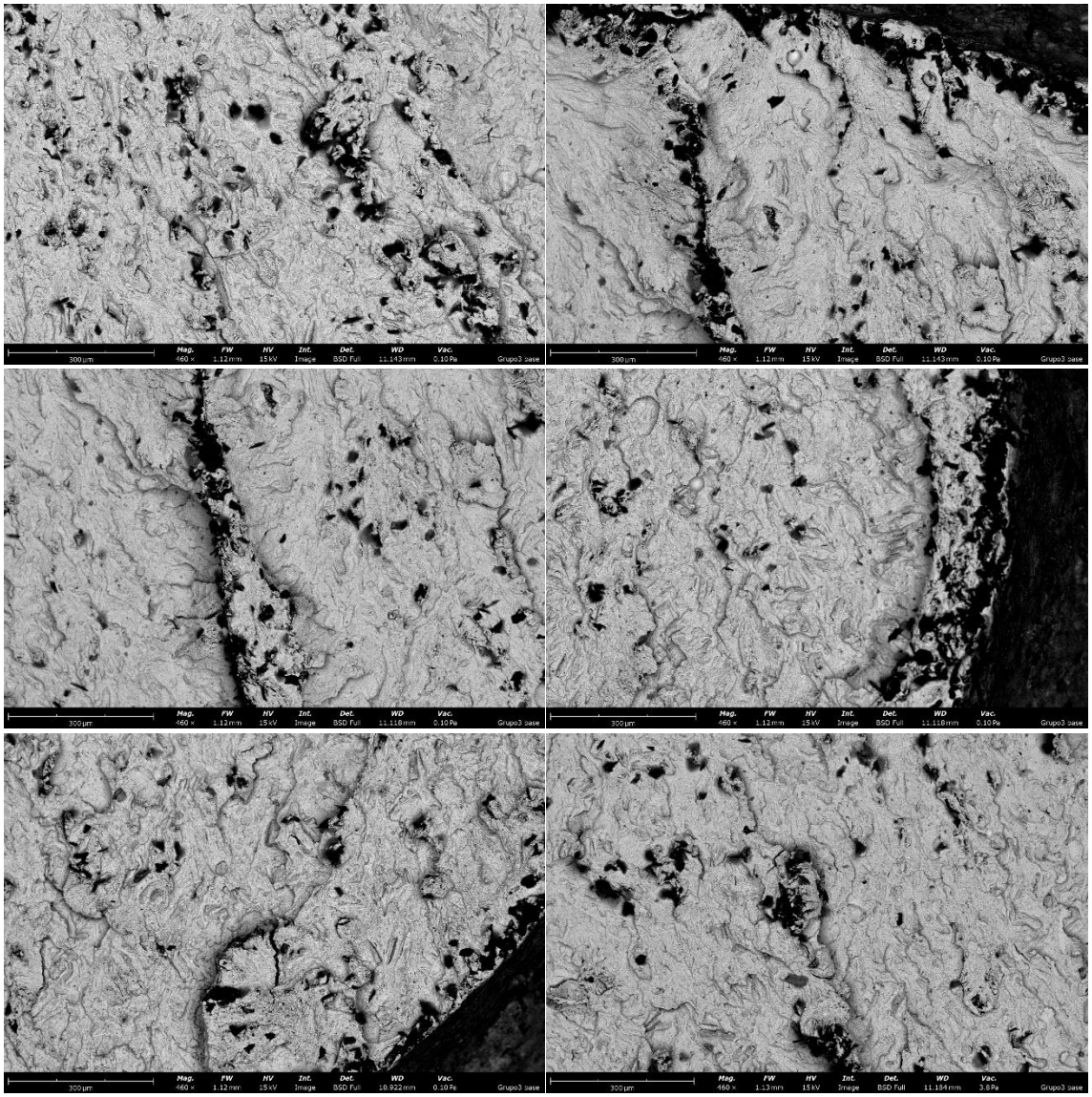


Figure 151 - Base interface images.

3.2.9.2. Composition analysis

There was composition analysis of three overall images – two of the non-annealed sample (first and second image) and one of the annealed samples (third image). Each had software analysis executed so as to visualize its composition, in some points of the image. Overall, the images are closer to the expected values

i) First image – non-annealed sample

There was the choice of 6 points (figure 152), which were analysed, and which results are shown as follows, as well as the original image for analysis. Of note that the variation between points is minimal, except for point 2, which could reflect impurities of the microstructure in its manipulation. The results (figure 153) are very similar to the second and third images, if it wouldn't be for the analysis of the impurities existing in point 2 of the first mage, meaning a high presence of iron carbon and chromium in such impurities, and which drastically alters the final average results of the balance of all samples collected. The first image therefore deviates from expected, with reduced contents of Nickel and Titanium, substituted by the aforementioned components.

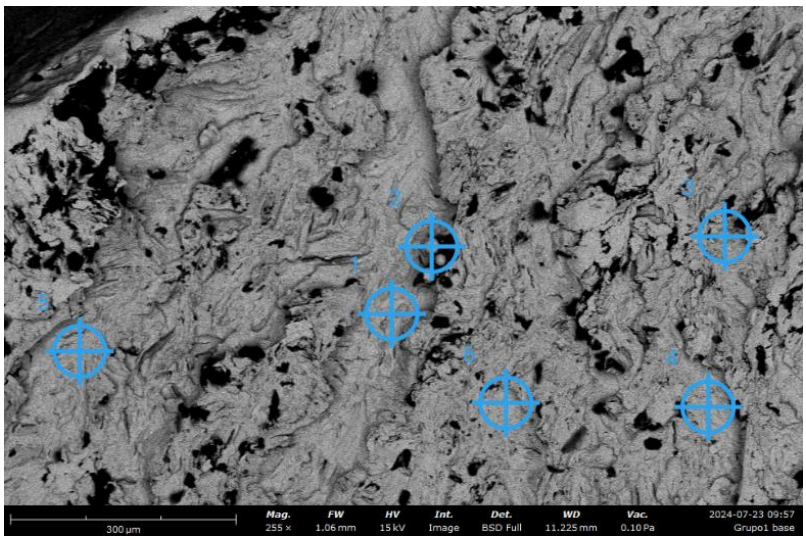
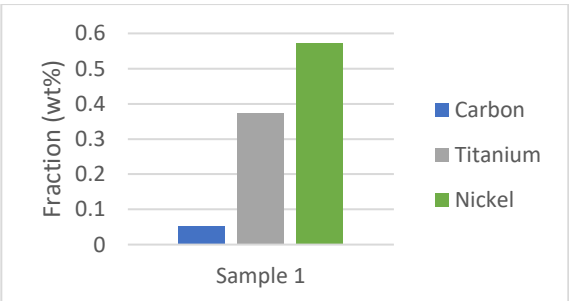
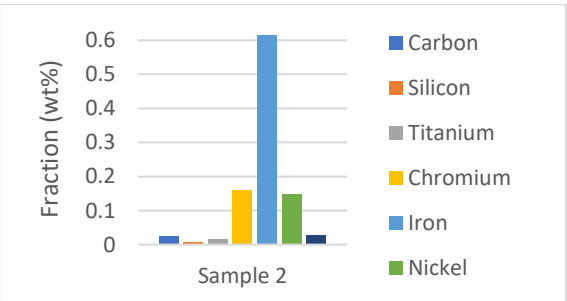


Figure 152 - Image of non-annealed specimen (first image).





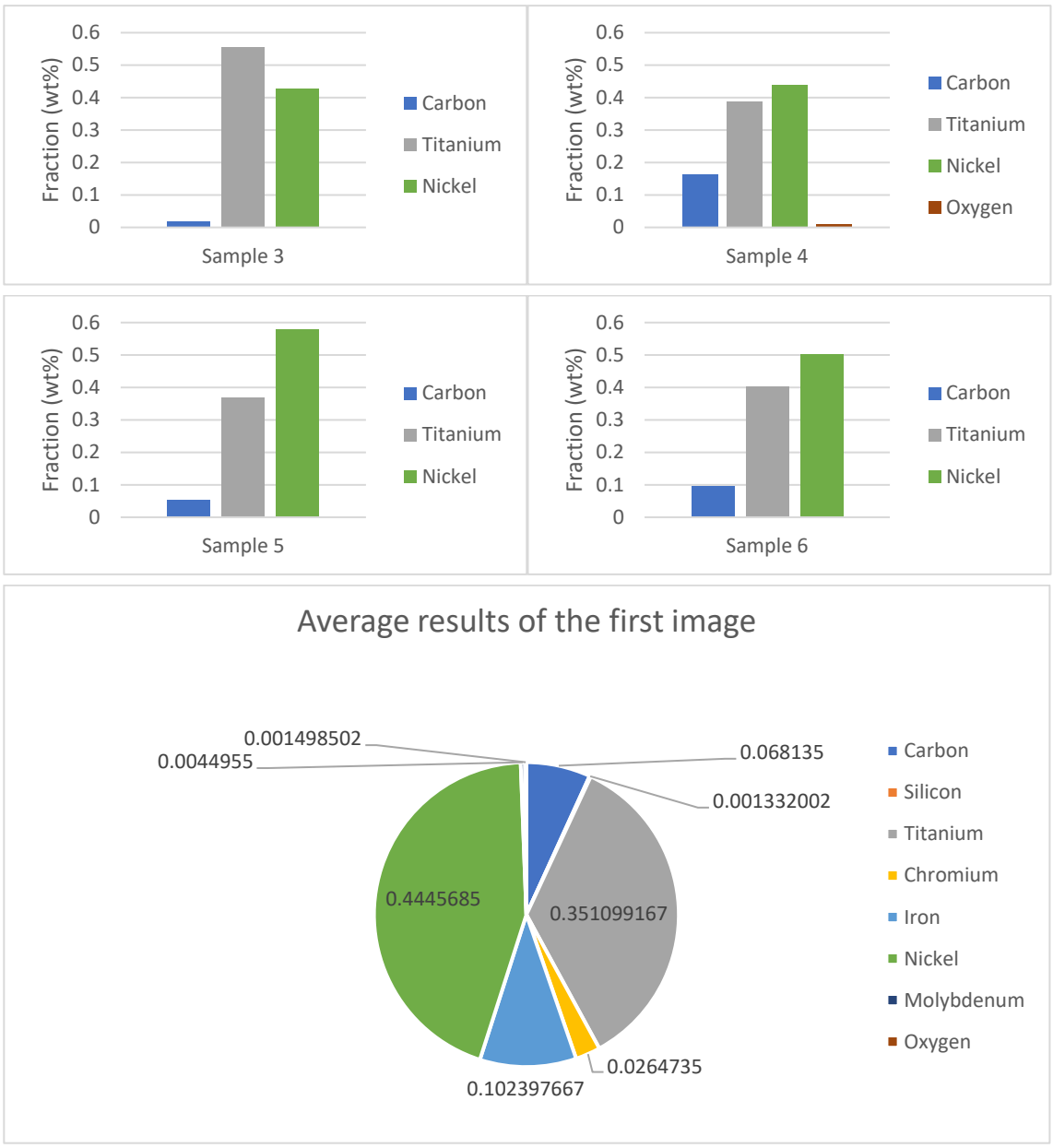


Figure 153 - Composition results of the various samples in the first image.

ii) Second image – non-annealed sample

There was the choice of 2 points (figure 154), which were analysed, and which results are shown(figure 155), as well as the original image for analysis. Of note that the variation between points is minimal, and there is a tendency for Nickel and Titanium ass the main constituents, and a minor group composed of carbon. The second image has compositions similar to expected, with only slight deviation in slightly lower component of Nickel, compensated by slightly superior Titanium content.

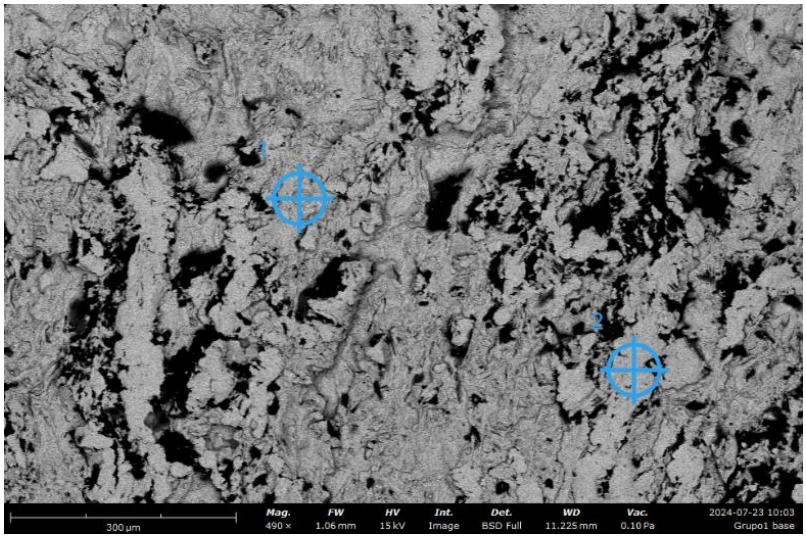


Figure 154 - Image of non-annealed specimen (second image).

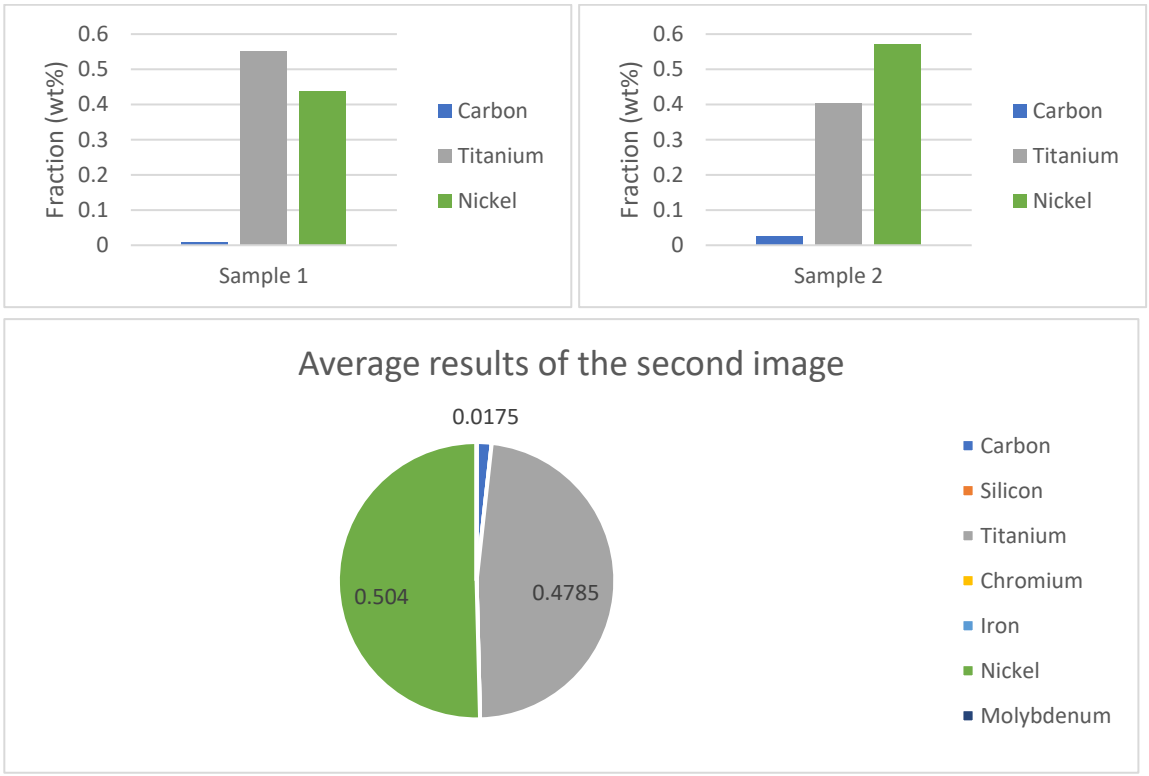


Figure 155 - Composition results of the various samples in the second image.

iii) Third image – annealed sample

There was the choice of 4 points (figure 156), which were analysed, and which results are shown as follows (figure 157), as well as the original image for analysis. Of note that the variation between points is minimal, and there is a clear tendency for Nickel as the main constituent, followed by Titanium, and a minor group composed of carbon. Image 3 as compositions similar to expected.

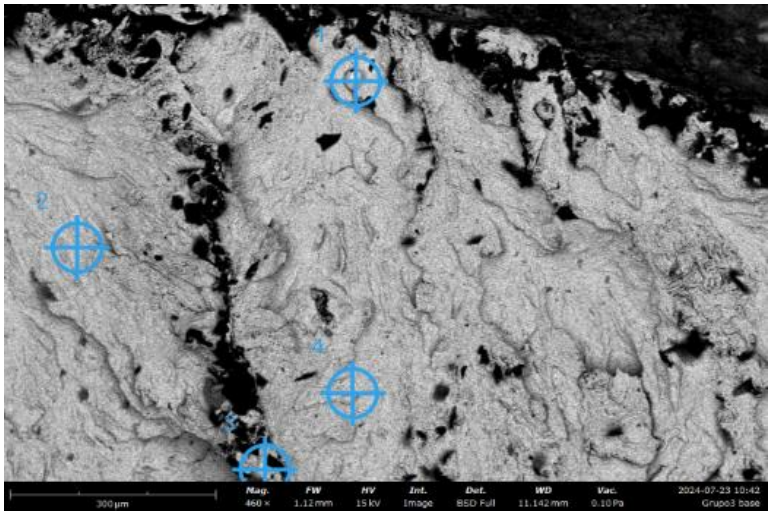


Figure 156 - Image of annealed specimen (third image).

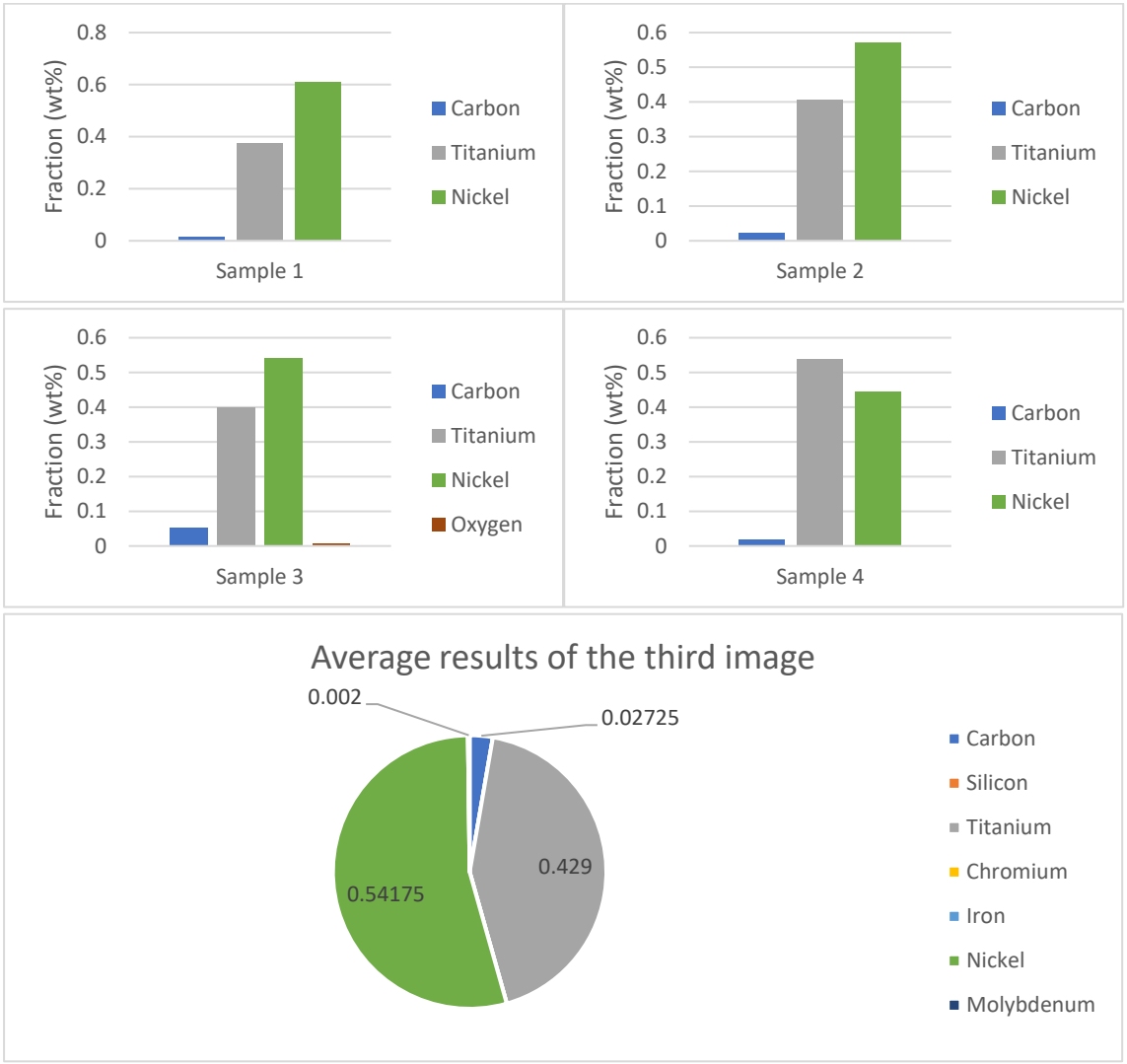


Figure 157 - Composition results of the various samples in the third image.

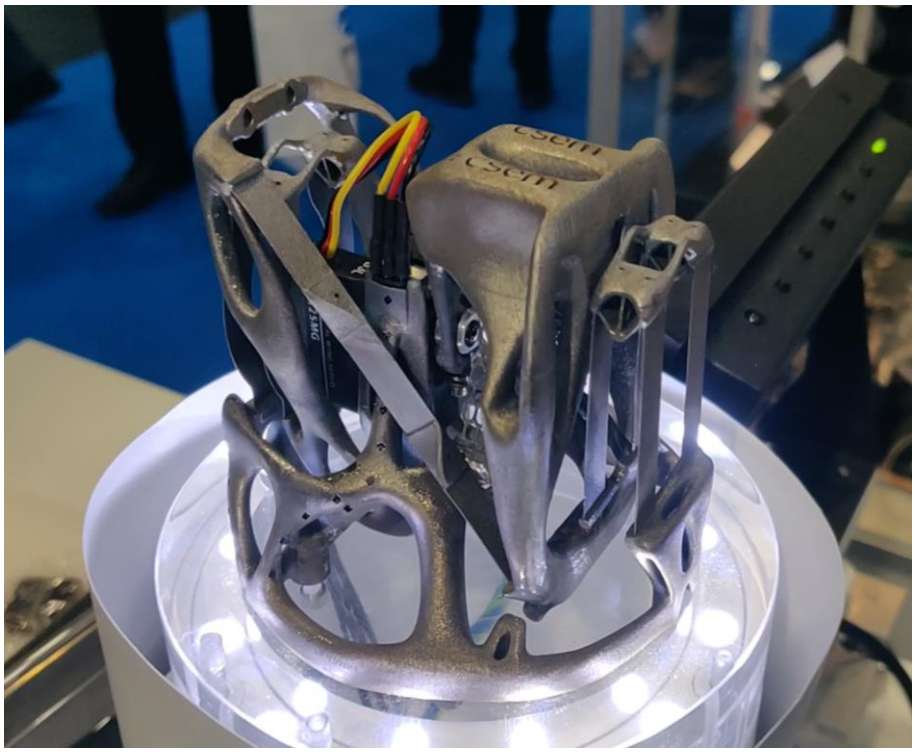


Figure 158 – Another example of a thermomechanical actuator of CSEM with Ni-Ti SMA alloy usage (courtesy of CSEM).

4. Conclusion

It is worth noting that the bibliographical and experimental works were conclusive in a broad range of parameters. There was clear characterization of the state-of-art of Metal Additive Manufacturing, with Laser-Powder Bed Fusion in detail, of Shape Memory Alloys, and its synergetic element through the use of what is known as 4D printing. Additionally, there was clear analysis of important parameters related to traction, compression, hardness, fracture toughness, hardness and the shape memory effect, and its relation both in austenite and martensite phases, and the influence of annealing treatments.

This thesis was elucidative in several parameters, which are explained as follows.

Bibliographic analysis

- Metal Additive Manufacturing is having an exponential growth in industrial development for the last 10 years. Advances in laser technology and optical systems, better material-mechanical interaction understanding, and the expiration of private patents from major corporations have been key factors.
- Laser Powder Bed Fusion has the biggest market share of Metal Additive Manufacturing, being the most utilized. The materials, post-processing and manufacturing parameters are quite varied and allow for high versatility.
- Shape Memory Alloys have been getting a steady increase in the last 30 years.
- The conjunction of both L-PBF and SMAs have been facing an exponential growth in scientific research, with L-PBF being able to circumvent some of the difficulties with the manufacturing of this type of alloys, culminating in the term 4D printing.
- There was a clear understanding of the advantages, disadvantages, mechanisms, applications and challenges of the given fields of research.
- There is a wide range of application possibilities, with the most usage being found in biomedical, aerospace and automotive components, and in turn having the biggest market growth. Overall, it is still, however, a very recent technology.
- Near-future applications show high potential in sectors such as space, non-intrusive biomedical, and adaptive clothing manufacturing.

Experimental analysis

- Tensile and compressive properties have quite different properties altogether, and these are heavily influenced by the build direction of the specimens. The stiffness of a given phase is considerably modified by the mentioned forces.
- There is clear evidence of significant hardness increase when going from low-temperature martensite phase to high-temperature austenite phase. Despite popular myth, the austenite phase is not necessarily stiffer or more resistant than the martensite phase and depends on build orientation and type of force exerted.
- Fully detwinning of the martensite starts accommodating with the material after two full cycles of deformation, heavily changing the beginning part of stress-strain properties – the material no longer has the effect of heavy martensite twinning.
- Significant recovering of strain can be visualized of given test pieces due to proper heating cycles executed on them. This proves the shape memory effect and gives useful information in the time-effect of this material and validation of its dynamics in the 4D printing paradigm.
- There is a clear difficulty in purchasing, supplying and overall management of this Ni-Ti alloys manufactured through L-PBF, both due to its rarity as well as its lack of established presence in the modern industrial world.
- Annealing treatments reduce hardness but allow for increased ductility of the specimens, with possibilities of bigger maximum strains.
- Annealing treatments, and even consecutive ones, have an effect of increasing the transformation temperature, while creating a more pronounced and defined peak in exothermic/endothermic reactions. Double annealing increases such paradigm, contributing for the overall increased effect aforementioned.
- Etching solutions of HCl + HNO3, HF + H2O2 AND Kroll's reagent proved ineffective at the analysis of the microstructure.
- The composition is mostly homogeneous, even in fractures, despite some elements of impurities due to the fracture itself, by utilization of SEM analysis.
- The specimens are hard and difficult to machine, due to possible effects of pseudoelasticity in the material, overall reflecting the useful of MAM and L-PBF for manufacture of this type of alloys.

4.1. Future works

Regarding future research that can be developed on this topic, there is the possibility of several related yet not explored topics that could be of interest:

- More specimens of each type for more accurate and precise results, and for a more rigorous and scientific process of applied research.
- Economical comparison between machined and additive manufactured test pieces, in a more business, economic and financial-related paradigm.
- Change of manufacturing parameters (laser power, scan speed, build direction, etc) related to the test pieces and analyse the effect in its properties, metallurgy, porosity, defects, and others (a key problem would be attempt to circumvent built-in parameters of the manufacturing units).
- Change of chemical composition, regarding the Nickel to Titanium balance and analysis the modifications it would incur in its properties and metallurgy.
- Optimization of machining parameters for products produced through metal additive manufacturing, in its post-processing, and with machinability tests for the material at hand.
- Development of practical prototypes with this technology, such as, for example, thermomechanical linear actuators.
- Evaluation of several post treatments (HIP, different annealing parameters, machining, etc) and their effects on the given test pieces.
- Experimental tests related to the F2082, E3097 and E3098 tests for possible additional characterization of the material.
- Utilization of computed tomography for scanning of defects.
- More tests related to tensile and compressive properties between martensite and austenite phases, and between annealed and non-annealed specimens.
- Adequate etching of specimen, possibly through use of electrolytic etching.

References

1) 16 - AM for automotive industry. (2021). In J. Vasco, *Additive Manufacturing* (pp. 505-530).
2) *3D printing at BMW*. (2020). Retrieved from BMW Group Press: https://www.press.bmwgroup.com/global/article/detail/T0322259EN/industrial-scale-3d-printing-continues-to-advance-at-bmw-group?language=en
3) 3DEO. (2022). *An Introductory Overview of Metal Extrusion 3D Printing*. Retrieved from 3DEO Metal 3D Printing: https://www.3deo.co/featured/metal-3d-printing-processes-metal-extrusion-3d-printing/
4) 3DEO. (2022). *Metal Additive Manufacturing (AM) Processes – Binder Jetting*. Retrieved from Metal 3D Printing: https://www.3deo.co/metal-3d-printing/metal-additive-manufacturing-am-processes-binder-jetting/
5) 3DEO. (2022). *The Advantages & Disadvantages of Material Jetting in Metal 3D Printing*. Retrieved from 3DEO Metal 3D Printing: https://www.3deo.co/manufacturing/intro-to-metal-additive-manufacturing-am-processes-material-jetting/
6) (2023). *4D Printing Market - Global Industry Analysis 2023 – 2032.* Precedence Research.
7) (2024). *4D Printing Market Size & Share Analysis - Growth Trends & Forecasts (2024 - 2029).* Mordor Intelligence.
8) *Additive Manufacturing and the U.S. Army's Improved Turbine Engine*. (2021). Retrieved from https://www.army.mil/article/248519/additive_manufacturing_and_the_u_s_armys_improved_turbine_engine
9) *Additive Manufacturing Research Group - Directed Energy Deposition*. (2023). Retrieved from Loughborough University: https://www.lboro.ac.uk/research/amrg/about/the7categoriesofadditivemanufacturing/directedenergydeposition/
10) Afazov, S., Ceesay, L., Larkin, O., Berglind, L., Denmark, W., & Ozturk, E. (2021). A methodology for precision manufacture of a nozzle using hybrid L-PBF. *Journal of Engineering Manufacture*.
11) Ahmed, A., Arya, S., Gupta, V., Furukawa, H., & Khosla, A. (2021). 4D printing: Fundamentals, materials, applications and challenges. *Polymer 228*.
12) Alagha, Hussain, & Zaki. (2021). Additive manufacturing of shape memory alloys: A review with emphasis on powder bed systems. *materials & Design Vol. 204*.
13) Ali, Sabyrov, & Shehab. (2022). Powder bed fusion–laser melting (PBF–LM) process. *Progress in Additive Manufacturing*.
14) *All You Need to Know About Metal Binder Jetting*. (2019). Retrieved from AMFG: https://amfg.ai/2019/07/03/metal-binder-jetting-all-you-need-to-know/

15) *AM 101: Hybrid Manufacturing*. (2019). Retrieved from Additive Manufacturing Media: https://www.additivemanufacturing.media/kc/what-is-additive-manufacturing/articles/am-101-hybrid-manufacturing

16) *AM at GE Aviation*. (2013). Retrieved from Laser Focus World: https://www.laserfocusworld.com/industrial-laser-solutions/article/14216415/additive-manufacturing-at-ge-aviation

17) *AM in turbines*. (2024). Retrieved from Gas Turbine World: https://gasturbineworld.com/additive-manufacturing/

18) (2024). *AMPOWER Report 2024.* AMPOWER.

19) *Army's Jointless Hull subsection tool*. (2023). Retrieved from Defense Visual Information Distribution Service: https://www.dvidshub.net/image/7702398/armys-jointless-hull-subsection-tool

20) *Army's Jointless Hull 3D metal printer recognized for technical achievement*. (2024). Retrieved from U.S. Army: https://www.army.mil/article/273032/armys_jointless_hull_3d_metal_printer_recognized_for_technical_achievement

21) Asnafi. (2021). Application of Laser-Based Powder Bed Fusion for Direct Metal Tooling. *Metals 2021*.

22) ASTM E-23. (2016). *Standard Test Methods for Notched Bar Impact Testing of Metallic Materials*. ASTM Society.

23) ASTM E-8M. (2022). *Standard Test Methods for Tension Testing of Metallic Materials*. ASTM Society.

24) ASTM E-9. (2000). *Standard Test Methods of Compression Testing of Metallic Materials at Room Temperature*. ASTM Society.

25) ASTM F-2004. (2017). *Standard Test Method for Transformation Temperature of Nickel-Titanium Alloys by Thermal Analysis*. ASTM Society.

26) ASTM F-2005. (2000). *Standard Terminology for Nickel-Titanium Shape Memory Alloys*. ASTM Society.

27) ASTM F-2516. (2022). *Standard Test Method for Tension Testing of Nickel-Titanium Superelastic Materials*. ASTM Society.

28) *Automated AM for car parts*. (2023). Retrieved from Eletrooptics: https://www.electrooptics.com/article/bmw-sets-automated-additive-manufacturing-line-car-parts

29) *Automotive Parts with L-PBF*. (2021). Retrieved from Alloyed official website: https://alloyed.com/alloys-case-study/automotive-headlights/

30) Azarhoushang, Marinescu, Rowe, Dimitrov, & Ohmori. (2022). *Tribology and Fundamentals of Abrasive Machining Processes, Third Edition.* Elsevier.

31) Babaev, Promakhov, Schulz, Semenov, Bakhmat, & Vorozhtsov. (2022). Processes of Physical Treatment of Stainless Steels Obtained by Additive Manufacturing. *Metals 2022*.

32) Barik, & Samal. (2022). 12 - NiTi-based coupling devices. In *Nickel-Titanium Smart Hybrid Materials* (pp. 215-243). Elsevier.

33) Bartolomeu, F., Costa, M., Alves, N., Miranda, G., & Silva, F. (2020). Additive manufacturing of NiTi-Ti6Al4V multi-material cellular structures targeting orthopedic implants. *Optics and Lasers in Engineering 134*.

34) Behera, Sahoo, & Mohapatra. (2022). 14 - Nickel–titanium smart hybrid materials for automotive industry. In *Nickel-Titanium Smart Hybrid Materials* (pp. 271-295).

35) Bibb, Eggbeer, & Williams. (2006). Rapid manufacture of removable partial denture frameworks. *Rapid Prototyping Journal*.

36) *Boeing begins 3D-printing Apache helicopter parts*. (2023). Retrieved from Defense News: https://www.defensenews.com/industry/techwatch/2023/10/18/boeing-begins-3d-printing-apache-helicopter-parts/

37) *Brake Calipper from 3D Printing*. (2018). Retrieved from Newsroom Bugatti: https://newsroom.bugatti.com/press-releases/world-premiere-brake-caliper-from-3-d-printer

38) Bucsek, A. N., Paranjape, H. M., & Stebner, A. P. (2016). Myths and Truths of Nitinol Mechanics: Elasticity and Tension – Compression Asymmetry. *Shap. Mem. Superelasticity (2016) Vol. 2 DOI: 10.1007/s40830-016-0074-z*, 264-271.

39) Buxani. (2018). *Tooling for injection molding using laser-powder bed fusion.* University of Lousiville, EUA.

40) Campbell, I., Diegel, O., Kowen, J., & Wohlers, T. (2017). *Wohlers Report.*

41) Cao, Y., Zhou, X., Cong, D., Zheng, H., Cao, Y., Nie, Z., . . . Wang, Y. (2020). Large tunable elastocaloric effect in additively manufactured Ni-Ti shape memory alloys. *Acta Materiala 194*, 178-189.

42) Carman, Inman, Kudva, & Leo. (2015). Memorial article for Ephrahim Garcia. *Smart Materials and Structures*.

43) Cataldi, Liu, Bissett, & Kinloch. (2022). *A Review on Printing of Responsive Smart and 4D Structures Using 2D Materials.*

44) (2024). *CATEC data regarding Ni-Ti build job manufacturing.* Sevilla: CATEC.

45) Chekotu, J. C., Groarke, R., O'Toole, K., & Brabazon, D. (2019). Advances in Selective Laser Melting of Nitinol Shape Memory Alloy Part Production. *Materials 2019*.

46) *Chemical polishing*. (2024). Retrieved from Inox group: https://inoxgrup.ru/uslugi/chemical-polish-nf-metals/

47) *Chevrolet Corvette SMA*. (2013). Retrieved from General Motors Media: https://media.gm.com/media/us/en/chevrolet/bcportal.html/currentVideoId/2149323982001/pnId/20/typeId/c/currentChannelId/Most%20Recent.html

48) Cobbinah, Nzeukou, Onawale, & Matizamhuka. (2021). *Laser Powder Bed Fusion of Potential Superalloys: A Review.* Department of Metallurgical Engineering, Vaal University of Technology, South Africa.

49) Constanza, & Tata. (2020). Shape Memory Alloys for Aerospace, Recent Developments, and New Applications: A Short Review. *Materials*.

50) Coroado, J., Ganguly, S., Williams, S., Suder, W., Meco, S., & Pardal, G. (2022). Comparison of continuous and pulsed wave lasers in keyhole welding of stainless-steel to aluminium. *The International Journal of Advanced Manufacturing Technology, Volume 119*, 367–387.

51) Dejene, & Lemu. (2023). Current Status and Challenges of Powder Bed Fusion-Based Metal Additive Manufacturing. *Metals 2023*.

52) Deloitte. (2016). *Industry 4.0 and the chemicals industry.*

53) *Digital Alloys' Guide to Metal Additive Manufacturing*. (2020). Retrieved from Metal Additive Manufacturing: https://www.digitalalloys.com/blog/application-criteria-metal-additive-manufacturing/

54) Duerig, T. W., & Bhattacharya, K. (2015). The Influence of the R-Phase on the Superelastic Behavior of NiTi. *Shap. Mem. Superelasticity (2015) 1*, 153-161.

55) Dzogbewu, T., & Beer, D. J. (2023). Additive manufacturing of NiTi shape memory alloy and its industrial applications. *Heliyon Vol. 10 Issue 1*.

56) Fang, C., & Wang, W. (2020). 1- Introduction to Shape-Memory Alloys. In *Shape Memory Alloys for Seismic Resilience* (pp. 1-38). Springer.

57) Farber, E., Zhu, J.-N., Popovich, A., & Popovich, V. (2020). A review of NiTi shape memory alloy as a smart material produced by additive manufacturing. *Materials Today: Proceedings 30*, 761-767.

58) Ferraro, Pirozzi, Annacondia, & Donato. (2019). Powder bed fusion/sintering machines: safety at workplaces. *International Conference on Industry 4.0 and Smart Manufacturing (ISM 2019)*.

59) *Ford Performance 3D-printed inlet*. (2019). Retrieved from https://www.3dnatives.com/en/ford-3d-printed-metal-part-050220195/#!

60) *Fraunhofer ILT spin-off*. (2019). Retrieved from Optics.org: https://optics.org/news/10/10/48

61) Frazier, W. E. (2014). Metal Additive Manufacturing: A Review. *Journal of Materials Engineering and Performance, Volume 23, Issue 6 DOI: 10.1007/s11665-014-0958-z*, 1917-1928.

62) Gangil, Siddiquee, & Maheshwari. (2020). Towards applications, processing and advancements in shape memory alloy and its composites. *Journal of Manufacturing Processes Vol. 59*, 205-220.

63) *GE Additive Print Services selected by General Dynamics Land Systems*. (2019). Retrieved from GE official website: https://www.ge.com/additive/press-releases/ge-additive-print-services-selected-general-dynamics-land-systems-metal-additive

64) *GE and the U.S. Army conduct T901 Preliminary Design Review*. (2018). Retrieved from GE Aerospace: https://www.geaerospace.com/news/articles/product/ahead-curve-ge-and-us-army-conduct-t901-preliminary-design-review

65) Gebisa, & Lemu. (2017). *A case study on topology optimized design for additive manufacturing.* IOP Publishing Ltd.

66) Gibson, I., Rosen, D., Stucker, B., & Khorasani, M. (2021). 10 - Direct Energy Deposition. In *Additive Manufacturing Technologies, Third Edition* (pp. 285 - 317). Springer Nature Switzerland AG.

67) Gibson, I., Rosen, D., Stucker, B., & Khorasani, M. (2021). 16 - Post-Processing. In *Additive Manufacturing Technologies, Third Edition* (pp. 457 - 487). Springer Nature Switzerland AG.

68) Gibson, I., Rosen, D., Stucker, B., & Khorasani, M. (2021). 5 - Powder Bed Fusion. In *Additive Manufacturing Technologies, Third Edition* (pp. 125 - 169). Springer Nature Switzerland AG.

69) (2018). *Global Shape Memory Alloys Market Size, Industry Report, 2019-2025.* Grand View Research.

70) *GM's first use of heat-activated shape memory alloy to replace heavier motorized part*. (2013). Retrieved from Green Car Congress: https://www.greencarcongress.com/2013/02/sma-20130212.html

71) Grossin, D., Montón, A., Navarrete-Segado, P., Özmen, E., Urruth, G., Maury, F., . . . Bertrand, G. (2021). A review of additive manufacturing of ceramics by powder bed selective laser processing (sintering / melting): Calcium phosphate, silicon carbide, zirconia, alumina, and their composites. *Open Ceramics, Volume 5*.

72) Gupta, K., Jain, N. K., & Laubscher, R. F. (2017). Conventional and Advanced Finishing of Gears. *Advanced Gear Manufacturing and Finishing*, 127-165.

73) *Hardness tester WOLPERT, type Dia-Testor 2RC*. (2024). Retrieved from Genten Machines: https://www.genten.be/en/shop/article/9000002785/Hardness_tester_WOLPERT,_type_Dia-Testor_2RC

74) Hartl, & Lagoudas. (2007). Aerospace applications of shape memory alloys. *Proceedings of the Institution of Mechanical Engineers Vol. 221 Part G: Aerospace Engineering*.

75) Hewlett-Packard. (2024). *HP Metal Jet S100 Printing Solution Manual.*

76) *History of Selective Laser Sintering*. (2023). Retrieved from Selective Laser Sintering: https://www.selective-lasersintering.com/history-of-selective-laser-sintering/

77) *Hot Isostatic Pressing: Improving quality and performance in AM parts production*. (2015). Retrieved from Metal AM: https://www.metal-am.com/articles/hot-isostatic-pressing-improving-quality-and-performance-in-3d-printing/

78) Huang, X., & Liu, Y. (2001). Effect of annealing on the transformation behavior and superelasticity of NiTi shape memory alloy. *Scripta Materialia, Volume 45, Issue 2*, 153-160.

79) Huang, X., Nohava, J., Zhang, B., & Ramirez, A. (2016). Nanoindentation of NiTi shape memory thin films at elevated temperatures. *International Journal of Smart and Nano Materials, 2:1, DOI: 10.1080/19475411.2011.558179*, 39-49.

80) Huckstepp, A. (2019). *Powder Bed Fusion (PBF)*. Retrieved from Medium: https://medium.com/@alexhuckstepp/powder-bed-fusion-pbf-what-you-need-to-know-ff4443dce949

81) Hybrid metal additive manufacturing: A state–of–the-art review. (2021). In J. Pragana, R. Sampaio, I. Bragança, C. Silva, & P. Martins, *Advances in Industrial and Manufacturing Engineering.* Lisboa.

82) *Hypermetal website*. (2024). Retrieved from https://hypermetal.eu/en/home/

83) Jani, Leary, Subic, & Gibson. (2014). A review of shape memory alloy research, applications and opportunities. *Materials & Design Vol. 56*.

84) Junior, V. L., Jr, V. A., & Savi, M. A. (2016). Introduction to Smart Materials and Structures. In *Dynamics of SMart SYstems and Strucutres* (pp. 121-134). Elsevier.

85) Katona, Bognár, Berta, Nagy, & Hirschberg. (2013). Chemical etching of nitinol stents. *Acta of Bioengineering and Biomechanics Vol. 15, No. 4; DOI: 10.5277/abb130401*, 3-8.

86) Kerschbaumer, M., & Ernst, G. (2004). *Hybrid manufacturing process for rapid high performance tooling combining high speed milling and laser cladding.*

87) Khidir, Mohammed, Nor, & Mustafa. (2007). A new concept of a linear smart actuator. *Sensors and Actuators A: Physical*, 244-249.

88) Kim, Heo, Rodrigue, Lee, Pané, Han, & Ahn. (2023). Shape Memory Alloy (SMA) Actuators: The Role of Material, Form, and Scaling Effects. *Advanced Materials Vol. 35*.

89) *Kingsbury UK L-PBF Benefits*. (2024). Retrieved from Kingsbury UK: https://kingsburyuk.com/key-advantages-of-powder-bed-fusion/

90) Kitzig-Frank, Tawakoli, & Azarhoushang. (2017). Material removal mechanism in ultrasonic-assisted grinding of Al2O3 by single-grain scratch test. *The International Journal of Advanced Manufacturing Technology*.

91) Kowen, J. (2019). *Powder removal: The Achilles heel of powder bed-based metal Additive Manufacturing*. Retrieved from Metal AM Magazine: https://www.metal-am.com/articles/powder-removal-in-powder-bed-based-metal-3d-printing/

92) Kruth, J.-P., Leu, M., & Nakagawa, T. (1998). Progress in Additive Manufacturing and Rapid Prototyping. *CIRP Annals, Volume 47, Issue 2*, 525-540.

93) Kruth, J.-P., Mercelis, P., Vaerenbergh, J. V., Froyen, L., & Rombouts, M. (2005). Binding mechanisms in selective laser sintering and selective laser melting. *Rapid Prototyping Journal Vol. 11 No. 1*, 26-36.

94) Kuang, Roach, Wu, Hamel, Ding, Wan, . . . Qi. (2018). Advances in 4D Printing: Materials and Applications. *Advanced Functional Materials 29*.

95) *Kurtz Ersa Alpha 140*. (2021). Retrieved from Metal AM Magazine: https://www.metal-am.com/kurtz-ersa-enters-into-metal-am-market-with-launch-of-alpha-140/

96) Lagoudas, D., Ravi-Chandar, K., Sarh, K., & Popov, P. (2003). Dynamic Loading of Polycrystalline Shape. *Mechanics of Materials Vol. 35*, 689-716.

97) *Laser cleaning*. (2020). Retrieved from Finmark Laser: https://finmarklaser.com/services/laser-cleaning/

98) *Laser Powder Bed Fusion*. (2024). Retrieved from ILT Fraunhofer: https://www.ilt.fraunhofer.de/en/media-center/brochures/b-laser-powder-bed-fusion.html

99) Laubach, Hildebrand, Suresh, Wagels, Kobbe, Gilbert, . . . Hutmacher. (2023). The Concept of Scaffold-Guided Bone Regeneration for the Treatment of Long Bone Defects: Current Clinical Application and Future Perspective. *Advanced Functional Biomaterials in Regenerative Medicine*.

100) Leary, Huang, Ataalla, Baxter, & Subic. (2013). Design of shape memory alloy actuators for direct power by an automotive battery. *Materials & Design*, 460-466.

101) Lee, H., Lim, C., Low, M., Tham, N., Murukeshan, V., & Kim, Y. (2017). Lasers in Additive Manufacturing: A Review. *INTERNATIONAL JOURNAL OF PRECISION ENGINEERING AND MANUFACTURING-GREEN TECHNOLOGY*.

102) Li, J., Zhu, Z., Hu, J., Zhou, Z., Zhang, X., & Zhao, W. (2020). Particle collision-based abrasive flow mechanisms in precision machining. *The International Journal of Advanced Manufacturing Technology, Volume 110*, 1819–1831.

103) Liu, J., Wang, Z., & Xu, Z. (2022). Electrochemical Polishing of Ti6Al4V Alloy Assisted by High-Speed Flow of Micro-Abrasive Particles in NaNO3 Electrolyte. *Materials 2022, Volume 15*.

104) Lu, H., Yang, C., Luo, X., Ma, H., Song, B., Li, Y., & Zhang, L. (2019). Ultrahigh-performance TiNi shape memory alloy by 4D printing. *Materials Science & Engineering A 763*.

105) *LUMEX Avance-25*. (2018). Retrieved from Matsuura website: https://www.lumex-matsuura.com/english/lumex-avance-25

106) Ma, J., Huang, H., & Huang, J. (2013). Characteristics Analysis and Testing of SMA Spring Actuator. *Advances in Materials Science and Engineering, Volume 2013, Issue 1*.

107) Mahmood, M. A., Ullah, A., Shah, M., Rehman, A. U., Salamci, M. U., & Khraisheh, M. (2023). Thermal Post-Processing Techniques for Additive Manufacturing. In *Handbook of Post-Processing in Additive Manufacturing* (pp. 87-110). Texas & Qatar.

108) Majumdar, & Manna. (2012). *Laser-Assisted Fabrication of Materials.* Springer.

109) Manik, & Sahu. (2022). 10 - Biocompatibility of NiTi. In *Nickel-Titanium Smart Hybrid Materials* (pp. 173-190). Elsevier.

110) Mátyási, G. (2023). Analysis of STL Files. In *Mathematical and Computer Modelling.* Budapest University of Technology and Economics.

111) McKinsey. (2021). *Technology deep dive: 3-D or 4-D printing.*

112) McKinsey. (2022). *What are Industry 4.0, the Fourth Industrial Revolution, and 4IR?* Retrieved from McKinsey & Company.

113) Mehrpouya, & Bidsorkhi. (2016). MEMS applications of NiTi based shape memory alloys: A review. *Micro and Nanosystems*.

114) *Memory Metal Suspension for Military Vehicles*. (2016). Retrieved from BAE Systems official website: https://www.baesystems.com/en/article/ironclad-beetles-inspire-new--memory--metal-suspension-for-military-vehicles

115) (2024). *Metal Additive Manufacturing Global Market Report.* The Business Research Company.

116) *Metal Additive Manufacturing History*. (2024). Retrieved from Additive Manufacturing Report: https://additive-manufacturing-report.com/technology/metal/metal-additive-manufacturing-history/

117) (2024). *Metal Additive Manufacturing Market Size, Share, Report 2023-2032.* Precedence Research.

118) Metelkova, J., Paggi, U., Marco, I., & Sinico, M. (2023). Mould manufacturing by hybrid laser powder bed fusion of M789 steel on a functional base. *Advancing Precision in Additive Manufacturing.* Leuven, Belgium.

119) Metelkova, J., Paggi, U., Marco, I., Sinico, M., Thijs, L., & Hooreweder, B. V. (2023). *Mould manufacturing by hybrid laser powder bed fusion of M789 steel on a functional base.*

120) MicroChemicals GmbH. (2024). *Basics of Microstructuring.* Ulm, Germany: MicroChemicals GmbH.

121) MIhálcz, I. (2001). Fundamental characteristics and desgn method for nickel-titanium shape memory alloy. *Periodica Polytechnica Mechanical Engineering Vol. 45, No.1*, 75-86.

122) Momeni, Seyed, Medhi, Liu, & Ni. (2017). A review of 4D printing. *Materials and Design 122*, 42-79.

123) Mueller, Riede, Eberle, Reutlinger, Brandão, Pambaguian, . . . Leyen. (2019). *Microstructural, mechanical, and thermo-physical characterization of hypereutectic AlSi40 fabricated by selective laser melting, 2019.*

124) Munir, Biesiekierski, Wen, & Li. (2020). Chapter 7 - Selective laser melting in biomedical manufacturing. In *Metallic Biomaterials Processing and Medical Device Manufacturing* (pp. 235-269).

125) Murr, L. E., Gaytan, S. M., Ramirez, D. A., Martinez, E., Hernandez, J., Amato, K. N., . . . Wicker, R. B. (2012). Metal Fabrication by Additive Manufacturing Using Laser and Electron Beam Melting Technologies. In *Journal of Materials Science and Technology.*

126) Narra, S. P., Mittwede, P. N., Wolf, S. D., & Urish, K. L. (2019). *Additive Manufacturing in Total Joint Arthroplasty.* National Librabry of Medicine.

127) NASA. (1972). *55-Nitinol: The alloy with a memory: its physical metallurgy, properties and applications.*

128) *Ni-Ti SMA*. (2002). Retrieved from Azom Catalogue: https://www.azom.com/article.aspx?ArticleID=1365

129) Olakanmi, Cochrane, & Dalgarno. (2015). *A review on selective laser sintering/melting of aluminium alloy powders: processing, microstructure and properties.* Institute for Materials Research, University of Leeds, United Kingdom.

130) Oliveira, F., Miranda, G., Oliveira, J., & Ferreira, D. (2022). Advances in Mould Making through L-PBF Additive Manufacturing: From Geometric Freedom to New Materials Design. *Materiais 2022*.

131) Oliveira, J. P., LaLonde, A., & Ma, J. (2020). Processing parameters in laser powder bed fusion metal additive manufacturing. In *Materials & Design.*

132) Omori, Ando, Okano, Tanaka, Kainuma, & Ishida. (2011). Superelastic effect in polycrystalline ferrous alloys. *Science*.

133) Orgéas, L., & Favier, D. (1998). STRESS-INDUCED MARTENSITIC TRANSFORMATION OF A NiTi ALLOY IN ISOTHERMAL SHEAR, TENSION AND COMPRESSION. *Acta mater. Vol. 46, No. 15*, 5579-5591.

134) Pandey, Nallagundla, & Dhande. (2003). Slicing procedures in layered manufacturing: A review. *Rapid Prototyping Journal*.

135) Parvizi, Hashemi, & Moein. (2022). 19 - NiTi shape memory alloys: properties. In *Nickel-Titanium Smart Hybrid Materialss* (pp. 399-426).

136) Patel, Dubey, Roshan, & Behera. (2023). Elastic and transformation behaviour of equiatomic NiTi shape memory alloys fabricated at different sintering temperatures. *Materials Today*.

137) Patel, S., Behera, B., Swain, B., Roshan, R., Sahoo, D., & Behera, A. (2020). A review on NiTi alloys for biomedical applications and their biocompatibility. *Materials Today: Proceedings Vol. 33*, 5548-5551.

138) Patil, A., & Sarje, S. (2021). Additive manufacturing with shape changing/memory materials: A review on 4D printing technology. *Materials Today: Proceedings 44*, 1744-1749.

139) Pei, & Loh. (2018). Technological considerations for 4D printing: an overview. *Progress in Additive Manufacturing (2018)*.

140) Pereira. (2009). *Um Estudo Sobre Atuadores Lineares com Molas Helicoidais de Ligas com Memória de Forma.* Rio de Janeiro: CEFET/RJ.

141) Petrini, & Migliavacca. (2011). Biomedical Applications of Shape Memory Alloys. *Jorunal of Metallurgy*.

142) Povoden-Karadeniz, Cirstea, Lang, Wojcik, & Kozeschnik. (2013). Thermodynamics of Ti–Ni shape memory alloys. *CALPHAD Vol. 41*, 128-139.

143) *Powder Bed Fusion*. (2023). Retrieved from Loughborough University: https://www.lboro.ac.uk/research/amrg/about/the7categoriesofadditivemanufacturing/powderbedfusion/

144) Prasad, & Wanhill. (2016). Shape Memory Alloys (SMAs) for Aerospace Applications. In *Aerospace Materials and Material Technologies* (pp. 467-481). Springer.

145) Prathyusha, & Babu. (2022). A review on additive manufacturing and topology optimization process for weight reduction studies in various industrial applications. *Materials Today Proceedings: Vol. 62*, 109-117.

146) *Prima Additive L-PBF Benefits*. (2023). Retrieved from https://www.primaadditive.com/en/news/vision/benefits-designing-powder-bed-fusion

147) Reichman. (2003). *U.S.A. Patent No. US7082868B2.*

148) *Renishaw AM 500Q*. (2024). Retrieved from Renisahw online website: https://www.renishaw.com/media/img/gen/fa905d79e8084356b37f4f9d7a5ef7e4.jpg

149) *Renishaw AM Orthopedic implants*. (2018). Retrieved from Medical Developments: https://www.todaysmedicaldevelopments.com/news/renishaw-additive-manufacturing-orthopedic-implants/

150) *Rheinmetall turns to SLM*. (2017). Retrieved from SME: https://www.sme.org/rheinmetall-turns-slm

151) Rhoades, L. (1991). Abrasive flow machining: a case study. In *Journal of Materials Processing Technology.*

152) Riensche, A., Carriere, P., Smoqi, Z., Menendez, A., Frigola, P., & Kutsaev, S. (2022). Application of hybrid laser powder bed fusion additive manufacturing to microwave radio frequency quarter wave cavity resonators. *he International Journal of Advanced Manufacturing Technology (2023) 124 (1-2) DOI:10.1007/s00170-022-10547-y*, 619-632.

153) Saedi, S., Moghaddam, N. S., Amerinatanzi, A., Elahinia, M., & Karaca, H. E. (2018). On the effects of selective laser melting process parameters on microstructure and thermomechanical response of Ni-rich NiTi. *Acta Materiala 144*, 552-560.

154) Saedi, S., Saghaian, S. E., Jahadakbar, A., Moghaddam, N. S., Andani, M. T., Saghaian, S. M., . . . Karaca, H. E. (2018). Shape memory response of porous NiTi shape memory alloys fabricated by selective laser melting. *Journal of Materials Science: Materials in Medicine (2018)*, 29-40.

155) Sajjad, R., Chauhdary, S., Anwar, M., Zahid, A., Khosa, A., Imran, M., & Sajjad, M. (2024). A review of 4D printing & Technologies, shape shifting, smart polymer based materials, and biomedical applications. *Advanced Industrial and Engineering Polymer Research 7*, 20-36.

156) Samal, Jena, Varshney, & Kumar. (2023). 23 - 4D printing: An experimental case study on processing of shape memory polymer by FDM/FFF for nature inspired structures. In *Advances in Additive Manufacturing* (pp. 361-377). Elsevier.

157) Santos, Shiomi, Osakada, & Laoui. (2005). *Rapid manufacturing of metal components by laser forming.* Osakada Laboratory, Graduate School of Engineering Science, Department of Mechanical Science and Bioengineering, Osaka University,.

158) Saritha, D., & Boyina, D. (2020). A concise review on 4D printing technology. *Materials Today: Proceedings 46*, 692-695.

159) Sathishkumar, Kumar, Ganesh, Venkatesh, Radhika, Vignesh, & Pazhani. (2023). Possibilities, performance and challenges of nitinol alloy fabricated by DED and PBF for biomedical implants. *Journal of Manufacturing Processes 102*, 885-909.

160) Savi, Paiva, Araujo, & Paula. (2016). Shape Memory Alloys. In *Dynamics of Smart Systems and Structures* (pp. 155-188). Springer.

161) Schleifenbaum, J. (2023). *"Additive Manufacturing" class.* RWTH Aachen University - Digital Additive Production DAP.

162) Schneck, M., Horn, M., Schmitt, M., Seidel, C., Schlick, G., & Reinhart, G. (2021). *Review on additive hybrid- and multi-material-manufacturing of metals by powder bed fusion: state of technology and development potential.*

163) Sefene, E. (2022). State-of-the-art of selective laser melting process: A comprehensive review. In *Journal of Manufacturing Systems.* SME.

164) (2018). *Shape Memory Alloys Market Research Report 2018-2030.* Market Research Future.

165) Shiva, S., Palani, I., Mishra, S., Paul, C., & Kukreja, L. (2014). Investigations on the influence of composition in the development of Ni–Ti shape memory alloy using laser based additive manufacturing. *Optics & Laser Technology 69*, 44-51.

166) Siebold. (2019). Additive Manufacturing for Serial Production of High-Performance Metal Parts. *ASME Mech. Eng.*

167) *Siemens Gas Turbines*. (2024). Retrieved from Siemens Energy: https://www.siemens-energy.com/global/en/home/products-services/product-offerings/gas-turbines.html

168) Sittner, P., Landa, M., Lukas, P., & Novak, V. (2006). R-phase transformation phenomena in thermomechanically loaded NiTi polycrystals. *Mechanics of Materials 38*, 475-492.

169) *SLS Inventor of the Year*. (2015). Retrieved from 3Dprint.com: https://3dprint.com/106689/sls-2015-inventor-of-the-year/

170) Squillace, A. (2023). *"Additive Manufacturing" class.* UNINA Napoli University.

171) Stachiv, I., Alarcon, E., & Lamac, M. (2021). *Shape Memory Alloys and Polymers for MEMS/NEMS Applications: Review on Recent Findings and Challenges in Design, Preparation, and Characterization.*

172) *Submarine Components from 3D Printers*. (2020). Retrieved from EDR Magazine: https://www.edrmagazine.eu/submarine-components-from-3d-printers-to-enter-series-production

173) Tanzi, Farè, & Candiani. (2019). 4 - Biomaterials and Applications. In *Foundations of Biomaterials Engineering.* Springer.

174) *Terma A/S F-35 AM reductions*. (n.d.). Retrieved from Force Technology official website: https://forcetechnology.com/en/cases/terma-reduces-material-use-production-time-am

175) Ternik, Zadravec, & Rudolf. (2017). Numerical analysis of the NiTi solidification process influence of thermal conductivity. *Science of SIntering*.

176) *ThyssenKrupp TechCenter AM*. (2024). Retrieved from ThyssenKrupp official website: https://www.thyssenkrupp.com/en/stories/techcenter-additive-manufacturing--new-opportunities-for-industries

177) Torok, Zink, Ageyeva, Hatos, Zobac, Fekete, . . . Kovacs. (2022). Laser powder bed fusion and casting for an advanced hybrid prototype mold. *Journal of Manufacturing Processes*.

178) Turner, T. (2001). *Thermomechanical Response of Shape Memory Alloy Hybrid Composites.* NASA.

179) Vafadar, A. (2021). Advances in Metal Additive Manufacturing: A Review of Common Processes, Industrial Applications, and Current Challenges. Edith Cowan University, Australia.

180) Velu, Kumar, Balan, & Mazumder. (2021). Chapter 14 - Laser aided metal additive manufacturing and postprocessing: a comprehensive review. In *Additive Manfuacturing.*

181) Vemury, C., Corradi, M., Abozaid, F., Charles, A., & Hughes, D. (2021). *The behaviour of Nitinol Wire Bundles for Structural Applications.*

182) Vlamidir, Timko, Holubzak, & Novak. (2023). Roughness surface analysis of samples produced by the additive manufacturing process. In *TRANSCOM 2023: 15th International Scientific Conference on Sustainable, Modern and Safe Transport.* Rome.

183) Wang, Y., Cui, H., Esworthy, T., Mei, D., Wang, Y., & Zhang, L. (2022). Emerging 4D Printing Strategies for Next-Generation Tissue Regeneration and Medical Devices. *Advanced Materials 34*.

184) Wei, S., Zhang, J., Zhang, L., Zhang, Y., Song, B., Wang, X., . . . Shi, Y. (2023). Laser powder bed fusion additive manufacturing of NiTi shape memory alloys: a review. *International Journal of Extreme Manufacturing 5*.

185) Welfen, E. (2020). *A hybrid additive and subtractive manufacturing approach for multi-material components.* Iowa State University.

186) *WFL Millturn*. (2024). Retrieved from WFL: https://www.wfl.at/pt/solucoes/millturn/m80-m80-g-m80x-m80x-g-m85-m85-g

187) *What is Selective Laser Sintering*. (2024). Retrieved from Markforged 3D Printing Basics: https://markforged.com/resources/learn/3d-printing-basics/3d-printing-processes/what-is-selective-laser-sintering-sls

188) (2024). *Wohlers Report.* Wohlers.

189) Yadroitsev, Yadroitsava, I., MacDonald, & Plessis. (2021). Chapter 21 - Industrial Applications. In *Fundamentals of Laser Powder Bed Fusion of Metals.*

190) Yan, J., Battiato, I., & Fadel, G. (2016). *Planning the process parameters during Direct Metal Deposition of functionally graded thin-walled parts based on a 2D model.* University of Texas at Austin.

191) Yang, M., & Qiao, P. (2010). 4 - High energy absorbing materials for blast resistant design. *Blast Protection of Civil Infrastructures and Vehicles Using Composites*, 88-119.

192) Yang, Y., Zhan, J., Li, B., Lin, J., Gao, J., Zhang, Z., . . . Gloriant, T. (2019). Laser beam energy dependence of martensitic transformation in SLM fabricated NiTi shape memory alloy. *Materiala 6*.

193) Zaki, W., Moumni, Z., & Morin, C. (2011). Modeling Tensile-Compressive Asymmetry for Superelastic Shape Memory Alloys. *Mechanics of Advanced Materials and Structures, 18*, 559-564.

194) Zang, K. (2015). *Optimization of support structures for selective laser melting.*

195) Zhang, & Liu. (2015). Effect of sequential turning and burnishing on the surface integrity of Cr–Ni-based stainless steel formed by laser cladding process. In *Surface and Coatings Technology* (pp. 327-335). Elsevier.

196) Zhang, X.-L., Wang, S., Jiang, Y., Huang, J., Wang, S.-P., Zhang, Q.-Q., . . . Zhang, Z.-H. (2024). Influence of building directions on the impact properties of NiTi fabricated via laser powder bed fusion . *Journal of Materials Research and Technology 28*, 3186-3195.

197) Zhao, Y., Taya, M., Kang, Y., & Kawasaki, A. (2005). Compression behavior of porous NiTi shape memory alloy. *Acta Materialia 53*.

198) Zhu, J., Zhou, H., Wang, C., Zhou, L., Yuan, S., & Zhang, W. (2021). A review of topology optimization for additive manufacturing: Status and challenges. In *Chinese Journal of Aeronautics* (pp. 91-110). Elsevier.

Annexes

Annex A – Different types of MAM technologies

This annex relates to MAM technologies apart from L-PBF, with its usage in industrial development in both its basic and hybrid forms.

a) Direct Energy Deposition

Direct Energy Deposition is a type of technology that utilizes a nozzle mounted on a multi axis arm, depositing melted material onto a specified surface, where there is posterior solidification. Fundamentally, it is similar to material extrusion, however, the nozzle is less restricted in the axis and directions it can move, not being fixed to a specific axis of movement. After L-PBF, this technology is currently the one with the most usage in the metal AM market. A schematic is shown in figures 159 and 160.

The material, which has the possibility of being deposited from any angle due to the 4 and 5 axis machines, is melted upon deposition with a laser or electron beam.

Such process is ideal for repairing and maintaining of structural parts, being very used in industries requiring extensive and frequent maintenance procedures (Additive Manufacturing Research Group - Directed Energy Deposition, 2023).

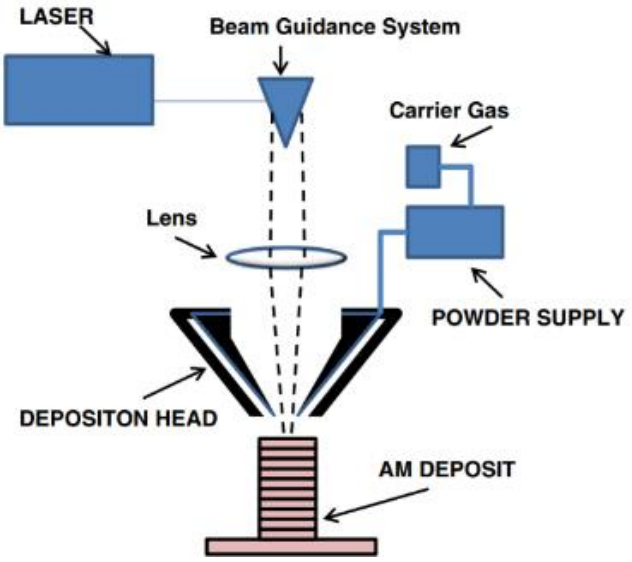


Figure 159 - DED schematic 1 (Frazier, 2014).

While less accurate than L-PBF, DED is more material efficient when compared to powder bed systems, due to the virtually zero waste created. It allows a very interesting freedom of movement and manipulation, through use of 4 or 5 axis machines. In such manufacturing, it is the arm that normally moves while the object remains fixed, although this can be reversed or even both can be moving. Normally there is the utilization of reduced oxygen levels in the process atmosphere for better process control. Of note that this process is only possible due to the very fast cooling times, which are typically between 1000 – 5000 ºC / s. Typical layer thicknesses are between 0.25mm and 0.5mm (Gibson, Rosen, Stucker, & Khorasani, 10 - Direct Energy Deposition, 2021).

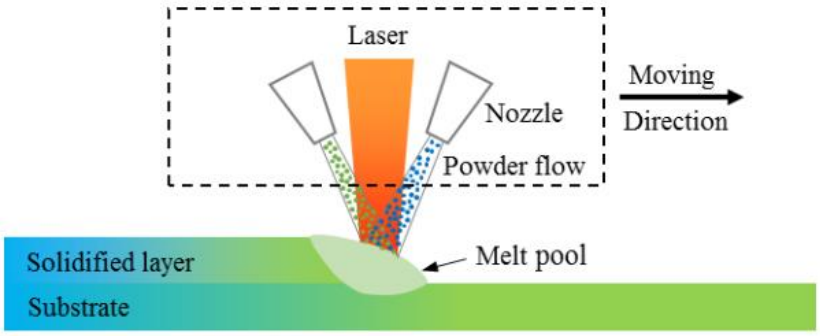


Figure 160 - DED schematic 2 (Yan, Battiato, & Fadel, 2016).

The process of DED generally goes as follows: a 4-5 axis arm moves around the fixed or movable object, with the material being deposited onto the existing surfaces of such object, the material is either in wire or powder form. There is the usage of a laser, electron beam or plasma arc, upon deposition. Further material is added layer by layer until solidification, creating or repairing exiting features into the existing object (Gibson, Rosen, Stucker, & Khorasani, 10 - Direct Energy Deposition, 2021).

b) Material / Binder Jetting

Binder Jetting is a powder bed process that utilizes inkjet technology and a binding agent. The liquid binder is used to "glue" the metal powder together within and between layers. A layer of metal powder is first rolled onto the build tray, and then an inkjet print head moves along the x and y axes and deposits binder in the shape of the part for each respective layer. After each layer is created, the build platform is lowered incrementally to make room for the next layer. The part being printed is supported within the powder bed by the unbound powder, which is then removed to complete the process. The result is a "green part" which then needs to be placed in a sintering furnace to achieve final part density. (3DEO, Metal Additive Manufacturing (AM) Processes – Binder Jetting, 2022). Schematic can be seen in figure 161.

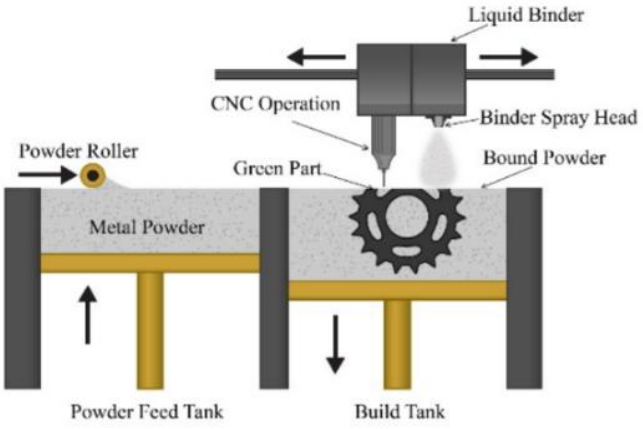


Figure 161 - Binder Jetting schematic (All You Need to Know About Metal Binder Jetting, 2019).

Material Jetting is relatively similar to binder jetting, with one key difference — instead of a binder being jetted through the printhead, a metallic material is jetted. This material is jetted onto the build tray directly using either a continuous jetting or Drop on Demand (DOD) process. The jetted metal is deposited on the build tray in the cross section of the part for that layer. This process continues as it builds up layer after layer. The resulting part still needs to be sintered in a furnace to achieve final part density. Previously, material jetting was limited to plastics and polymers, but recent advances have seen new companies attempting to commercialize the process for metals (3DEO, The Advantages & Disadvantages of Material Jetting in Metal 3D Printing, 2022). Schematic can be seen in figure 162.

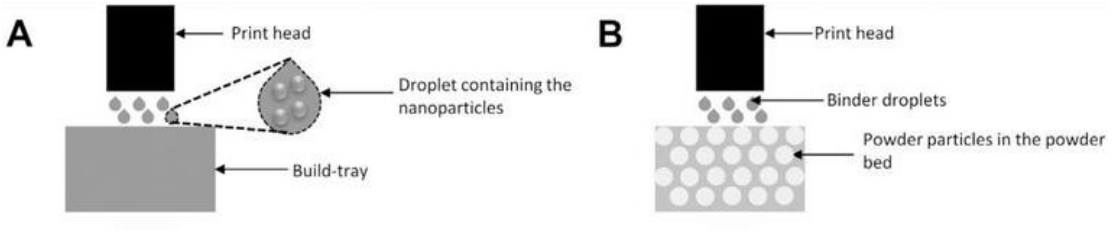


Figure 162 - Schematic of the metal AM processes: (A) nanoparticle material jetting and (B) binder jetting (Narra, Mittwede, Wolf, & Urish, 2019).

An example of state-of-art metal jet is the HP Metal Jet S100 Printing Solution, which allows for unprecedent speed of manufacture of components, especially when compared with L-PBF technologies, since it can instantly build all the layer with each mechanical action (instead of point-by-point laser sintering), achieving much faster manufacturing and at a mass volume, however at much smaller geometrical dimensions (maximum effective build volume is 430x309x170 mm). (Hewlett-Packard, 2024). Schematic can be seen in figure 163.

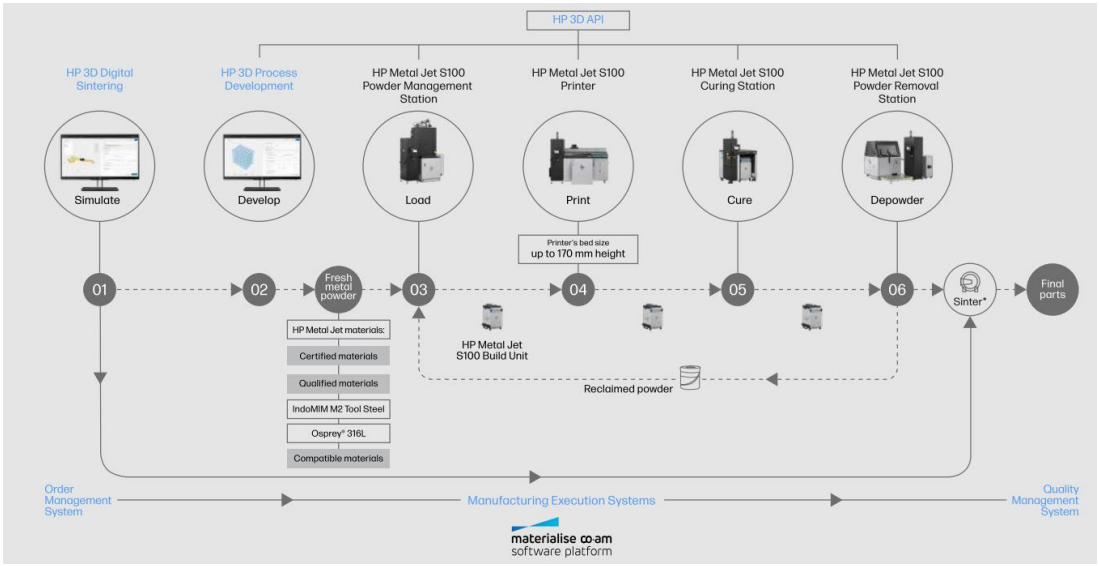


Figure 163 - Hewlett-Packard Metal Jet S100 process workflow (Hewlett-Packard, 2024).

c) Material Extrusion

Metal extrusion in additive manufacturing is a fairly new process. Similar to the wildly popular plastic-based FDM process, the filament is heated and drawn through a nozzle and then deposited layer-by-layer. This filament is a combination of thermoplastic material and metallic particles. The nozzle moves in the X and Y axes across the part for a given layer. The build platform then lowers to make room for new layers (3DEO, An Introductory Overview of Metal Extrusion 3D Printing, 2022). A schematic can be seen in figure 164.

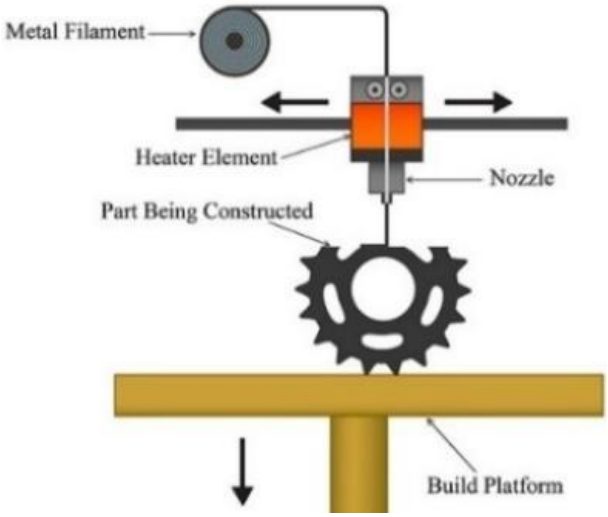


Figure 164 - Material Extrusion schematic (3DEO, An Introductory Overview of Metal Extrusion 3D Printing, 2022).

After the part is complete, it is placed into a sintering furnace to burn out the remaining plastic and sinter the metal particles together. Extrusion-based additive manufacturing has been widely used for plastics and polymers but was only recently developed to create metal parts (3DEO, An Introductory Overview of Metal Extrusion 3D Printing, 2022).

d) Hybrid possibilities

There are a myriad of ways to combine the versatility of metal AM with the precision or capabilities of other developed manufactured methods. The most common method is the usage of metal additive manufacturing techniques with some subtractive process, such as, for example, a 3D print of a near-net shape, instead of a simple forging or casting process, with subtractive CNC milling capabilities being deployed thereafter to finish the part, and for better precision. An example can be seen in figure 165 and 166.



Figure 165 - Turbine casing manufactured with Lasertec 65, with Inconel and bronze, and machined thereafter (AM 101: Hybrid Manufacturing, 2019).

This allows a myriad of advantages to be used, with the possibility of build-up and repair of damaged parts, the reduction of machining work, and the minimization of cycle times by eliminating or, at least, severely reducing, the time it takes to change the manufacturing process, and reducing error because the printed part does not have to leave the build envelope and be reset on a separate machine. It also allows a very interchangeable process which means creating features that would be inaccessible with other processes, and the better creation of internal features such as cooling channels or runners.

Kerschnbauer and Ernst integrated a DED nozzle into a 5-axis CNC machining system in 2004. In such a process, the built component is machined after a specified quantity of layers created through DED, with the study concluding that, in this particular case, alternating DED and machining did not allow the usage of cooling lubrication. It also concluded that materials for the machining part needed to resist machining of advanced alloys at very high temperatures. Several manufacturers have been developing this technology, with the most famous example being the Lasertec 65 model, created by DMG MORI in 2014. (Kerschbaumer & Ernst, 2004) (AM 101: Hybrid Manufacturing, 2019)

In 2015, WFL Millturn GmbH created the M80 Millturn, combining DED technology, with a drill chunk that allows turning, increasing therefore the versatility and usefulness of the first process. (WFL Millturn, 2024).



Figure 166 - For this rotor manufacturing, hybrid manufacturing allows the usage of Inconel 625 to the portions that require wear and heat resistance, and the usage of steel for the rest (AM 101: Hybrid Manufacturing, 2019).

The US's Department of Defense Joint Hull program (figure 167) tried to create a hybrid MAM machine that would use metal additive manufacturing techniques for creation and repair of, in this case, the rotor blades of a Boeing AH-64 Apache attack helicopter. This is as a preliminary experiment to test the viability of more parts of this helicopter being manufactured through additive processes, as part of Boeing's research

and technology unit. The system in question used additive friction stir deposition (an experimental solid-state deposition manufacturing process, based on the ideas of friction-stir welding technology) and CNC machining, for synthesis of both systems. (Metelkova J. , et al., 2023).

In other example, the US Army Jointless Hull subsection is a hybrid MAM used for engineering and the development of a full size jointless hull, which “will be capable of producing large metal parts such as monolithic hulls for military ground vehicles”. (Army's Jointless Hull 3D metal printer recognized for technical achievement, 2024)



Figure 167 - Joint Hull Program, experimental program trying to converge various MAM techniques (Army’s Jointless Hull subsection tool, 2023).

These are some of the examples of the endless possibilities that such hybridization and symbiosis between various technologies can achieve in the current era, with advances in R&D, machine learning, material technology, and maturity of the MAM technology increasingly using this hybrid AM processes.

Annex B – Laser - Powder Mechanisms

In this annex, there is presentation of a more in-depth analysis of the differences between the various laser-powder interaction mechanisms.

a) Solid-state sintering

Sintering describes the fusion of particles without achieving complete melting at elevated temperatures, normally occurring at temperatures between 50% and 100% of the designated melting temperature, with the minimization of total free energy being the main driving force for solid-state sintering. The mechanism of sintering occurs mainly through diffusion between powder particles. We can say that surface energy is therefore given by the equation as follows (Gibson, Rosen, Stucker, & Khorasani, 5 - Powder Bed Fusion, 2021).

$$E_s = \gamma_s \times S_A$$

Where:

γ_S is the surface energy per area for a particular temperature, material and atmosphere

S_A is the total particle surface area

When particles fuse at elevated temperatures, there is a decrease of the total surface area, so surface energy also decreases. With the decrease of the total surface area, there is also a decrease of the rate of sintering, with either high sintering temperatures or high sintering times being necessary in order to achieve low porosity levels.

As the surface area is a function of particle size, one can conclude that the surface area to volume ratio has a direct correlation with sintering capabilities, with larger ratios translating into greater free energy driving force, meaning that smaller particles experience greater tendency for consolidation and necking, meaning sinterization at a faster ratio and beginning at lower temperatures. As the diffusion rates increase exponentially with temperature, there is quicker sinterization as there is an approach to the melting temperature (figure 168 illustrates the process).

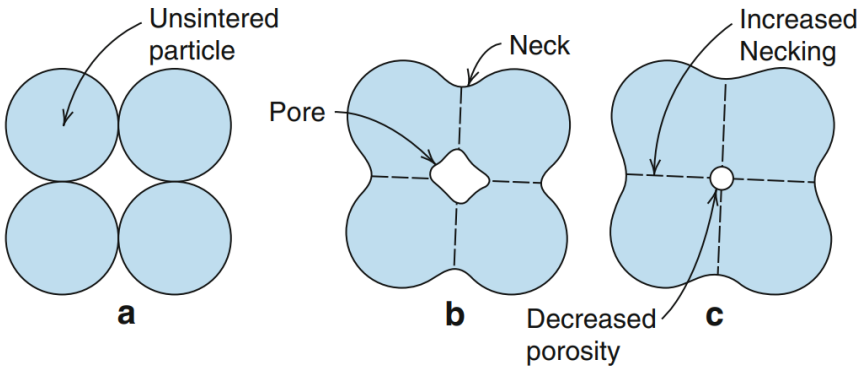


Figure 168 - Solid-State Sintering. (a) – before sintering; (b) - beginning stages of sintering process, with agglomeration of particles when temperatures are above half of the melting temperature; (c) - developing stages of sintering process, with increased necking and decreased porosity (Gibson, Rosen, Stucker, & Khorasani, 5 - Powder Bed Fusion, 2021).

Despite this, it is worth noting that, even with this exponential function, diffusion induced sintering, also known as solid-state sintering, is the slowest fusion mechanism for PBF.

This ends up being a great disadvantage since a shorter time to fusion means a more economically competitive process, therefore attempts must be made to increase fusion rate so as to increase build rate. Since the time for fusion by sintering is much longer than for melting, few AM processes use sintering as a primary fusion mechanism.

Despite this, sintering is important due to various phenomenon's that may happen in the manufacturing procedure of this the AM process.

One of these is the effect of loose powder sintering when heating up the powder bed, which can have positive (gain a degree of tensile and compressive strength, minimizing part curling) and negative feedback (agglomeration of powder particles means that the average particle size will increase each time it is recycled, limiting therefore the usefulness of the recycling process). There is also the case of secondary fusion process happening in powder adjacent to the part being built, meaning the phenomenon of "part growth," where the originally scanned part starts growing a "skin" of increasing thickness, increasing as the powder bed is kept at an elevated temperature.

Another case is the rare result of 100% porosity free results, being very hard to achieve, with various techniques having been developed to try to reduce this characteristic, one of them being holding the scanned part at an elevated temperature, where there is the combination of solid-state sintering with other high-temperature phenomena such as metal grain growth, causing the porosity to effectively decrease, however at the cost of irregularity of thickness between layers of the powder bed, which can be minimized with very careful controlling of the cooling rate and bed temperature (Kruth, Mercelis, Vaerenbergh, Froyen, & Rombouts, 2005) (Gibson, Rosen, Stucker, & Khorasani, 5 - Powder Bed Fusion, 2021) (Squillace, 2023).

b) Chemical-induced sintering

This sintering process investigated by the Fraunhofer Institute IPT involves the use of thermally activated chemical reactions between through powder-powder or powder-atmosphere interactions, so as to form a by-product that binds the particles together, reducing heavily the time needed for sintering.

This process is mostly used in ceramic materials, however, not being worthy of particular note in MAM procedures, therefore it will not be developed further. A simple example of this process being used nowadays is the laser processing of SiC in presence of oxygen, where SiO2 forms and binds together a composite of SiC and SiO2 (Kruth, Mercelis, Vaerenbergh, Froyen, & Rombouts, 2005) (Gibson, Rosen, Stucker, & Khorasani, 5 - Powder Bed Fusion, 2021) (Squillace, 2023).

c) Liquid-phase sintering

This is by far the most versatile mechanism for PBF manufacturing, with liquid-phase sintering (LPS) (figure 169) being used to refer to the fusion of powder particles where a part of them remain molten whilst another part maintains the solid state, with the molten part acting as a binder for the solid particles. Through this process, particles at elevated temperatures can be bound together without the necessity for direct melting or sintering, which vastly expediates the manufacturing process.

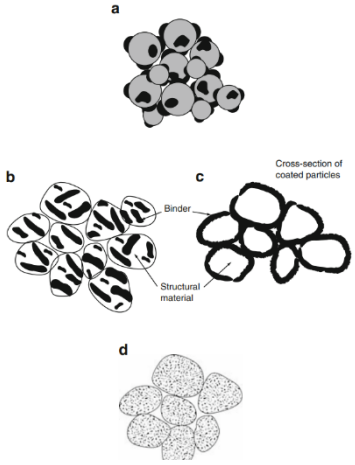


Figure 169 - Variations of the liquid-phase sintering process. These are: (a) separate particles; (b) composite particles; (c) coated particles; (d) indistinct mixtures (Kruth, Leu, & Nakagawa, 1998).

Liquid phase-sintering can be divided on its mechanism, depending on what type of materials will be used, more exactly whether there is distinction between the aforementioned binder and the structural materials.

I. Distinct Binder and Structural Materials

There are three main ways that distinct binder and structural materials can be combined. These are as separate particles, as composite particles, and as coated particles.

The first case, separate particles, is the most common and is sufficient for most cases, with a simple well mixed combination of binder and structural powder particles. When the structural material has the dominant properties desired in the final structure, it is advantageous for the binder to be smaller than the structural material, when discussing particles sizes, since it allows efficient packing of the powder, better binding (since the smaller binder particles can better adjust into the gaps between the structural particles) and lower post-binding porosity and shrinkage.

In the case, the heat source passes by quickly, with the molten binder having not enough time to flow through, and for surface tensions to draw the particle together before there is solidification of the binder, which can result in parts with very high porosity, which can be averted through required post processing procedures. These pieces are termed as “green” parts before the necessary post-processing procedure in a furnace to achieve the final part properties.

Of note that some materials are economically manufactured at particles sizes too small for an effective powder dispensing and levelling necessary in this procedure separate particle procedure. This can result in increased benefits in the structural and

binder materials to be bound together into larger particles altogether, creating therefore composite particles.

Composite particles are the second case and contain both the binder and structural material in powder particle. This can be achieved through mechanical alloying of binder particles with structural ones, or through grinding of cast, moulded and extruded mixtures into a powder, with the advantage of this type of particles being the higher density green parts and the better surface finish that can be achieved, when compared with separate particles. Composite particles can be constituted of metal binders with higher melting point metal structure materials and can be clearly distinguished from each other, when under microscopic analysis.

There are cases where a composite can be formed through coating of structural particles with the usage of a binder material, which can end up being more effective than random agglomerations of binder and structural materials. These particles are named coated particles and are the third case, offering a myriad of advantages, such as, better absorption of laser energy, a superior, more effective binding process of structural particles and better flow properties.

The random distribution of the constituents in the processing of separate or composite particles can translate into suboptimal heat energy absorption dynamics, with the material with higher absorptivity properties assimilating the most energy of the process. This, when allied with cases where the conduction rate from one particle type to another is inferior to the absorption rate, may mean the possibility of higher-meting-temperature material being melted prior to the lower-melting-temperature one, meaning the anticipated microstructure can vary greatly from the practical results. Although this possibility of manipulation of the material that can melt first can be beneficial in some cases, it is, in most applications, completely unnecessary and not the intent when formulating the binder/structural material combination.

So as to better minimize this possibilities, coated particles allow the overcoming of this phenomenon of possible structural melting material heating problem associated with the random constituent mixtures and agglomerates. If the structural particle is coated with a binder material, the laser radiation must necessarily pass through the binder before reaching the structural particle, ensuring therefore that the correct constituent is the one being melted. Therea are other benefits to such a process, such as increased build rate due to the binder being positioned at the most effective location for the gluing of adjacent particles altogether, since there is a more efficient utilization of the material, translating in the proportion of binder material to structural material in coated particles being usually less than its proportion in separate and composite particles. Another benefit is related to the spherically geometry of the coated particles. Coated particles retain the spherical nature of the underlying particle shape, which, in structural metal powder is spherical, which are easier to deposit and to smooth using powder spreading techniques, being

therefore easier to handle, alleviating the procedures of the manufacturing process (Kruth, Mercelis, Vaerenbergh, Froyen, & Rombouts, 2005) (Gibson, Rosen, Stucker, & Khorasani, 5 - Powder Bed Fusion, 2021) (Squillace, 2023).

II. Indistinct Binder and Structural Materials

In metals, LPS can occur when no distinct binder and structural materials are present in the powder particle, during the partial melting of a single particle type or when an alloy has lower-melting-temperature components.

In non-eutectic alloys, this melting occurs between the liquidus and solidus temperature of the alloy in question, where there will only be partial melting when the temperature is maintained in this region, with regions of the alloy with higher concentrations of the lower-melting-temperature being melted first.

It was this discovery, that many metal alloys can be partially melted only, if we exercise careful application of thermal energy, that allowed the creation of the first EOS DMLS machines, in the beginning stages of PBF technology. Of note that subsequent processes that were commercialized with the refinement of the technology did not pursue this avenue of approach, instead focusing in fully melting the metal alloys subjected for processing (Kruth, Mercelis, Vaerenbergh, Froyen, & Rombouts, 2005) (Gibson, Rosen, Stucker, & Khorasani, 5 - Powder Bed Fusion, 2021) (Squillace, 2023).

d) Full Melting

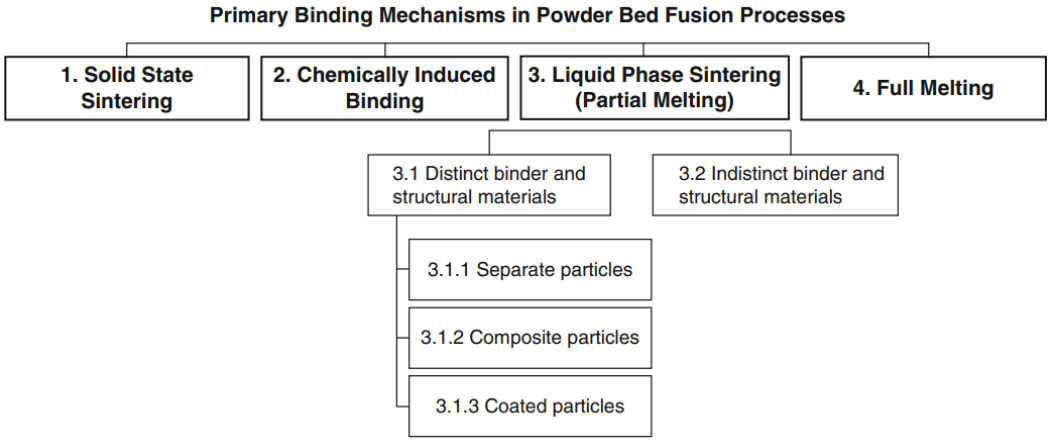
The mechanism of full melting is the most commonly associated with PBF processing of metal alloys for modern industrial use. In such materials, the entire region of the material is subjected to an amount of heat energy that allows melting surpassing the depth of the powder bed layer, with the thermal energy of subsequent scanning procedures (which can be deployed through either laser or electron beam, as mentioned earlier in Section L-PBF vs EB-PBF) being sufficient for a remelting of the previously deposited powder bed layer, which means this process has great effectiveness in the creation of well-bonded, structurally sound, high density structures, obtained through engineering metals.

The engineering alloys mostly utilized in the machines (such as Titanium, Stainless Steel, Cobalt-Cromium, etc) are typically fully melted, with the rapid melting and solidification that this process allows resulting in unique properties that can be quite distinct from identical alloys created through other manufacturing processes such as casting or metal forming.

Regardless of the technology at hand being known as SLM, DMLS, LaserCUSING, EBM, or other variations, they all use these specific binding mechanisms that were talked

about, with the possibility of varying between them, and in fact, normally more than one is present in its manufacturing process, depending as such in the powder material compositions and the thermal energy parameters. (Kruth, Mercelis, Vaerenbergh, Froyen, & Rombouts, 2005) (Gibson, Rosen, Stucker, & Khorasani, 5 - Powder Bed Fusion, 2021) (Squillace, 2023). Overall schematic of binding mechanisms is shown in table 28.

Table 28 - The binding mechanism in L-PBF (Gibson, Rosen, Stucker, & Khorasani, 5 - Powder Bed Fusion, 2021).



Annex C – Processing Parameters

A typical L-PBF machine includes two galvanometers, with one being for the X-axis and another for the Y-axis motion, with scanning occurring in two modes: contour mode and fill mode. In contour mode, the outline for a particular section is scanned, mainly for better accuracy reasons and for surface finishing around the perimeter of the piece. Contour is normally the last for better definition of the part.

The remaining cross-section is scanned through use of a fill pattern, with a common one being unidirectional. Bidirectional (also known as zig-zag), interlayers - where there is division of the surface unto different subsections, with different directions or strategies applied unto it - and interlayer rotations, where there is only rotation of the laser beam in the surface itself. Examples of patterns are shown in figure 170.

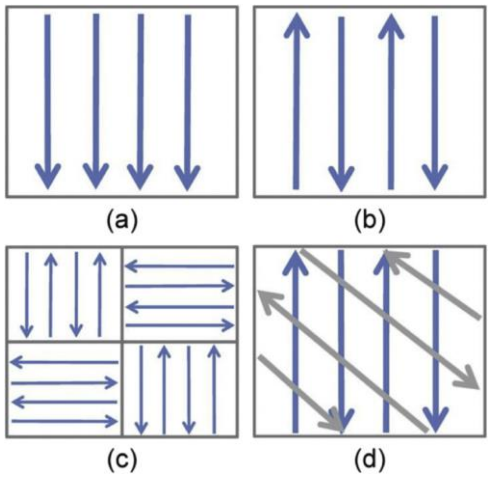


Figure 170 - Different possible scanning patterns: (a) unidirectional (b) bidirectional (zigzag) (c) interlayer (d) interlayer rotation.

In metal alloys processing, the fill section being usually subdivided into stripes (each being scanned sequentially, and with stripe angle rotation every layer), and squares (with each square being processed separately), with randomized scanning being often used so that

there is no preference regarding the direction of the residual stresses that the scanning will induce. An example is shown in figure 171.

In addition to the melt pool characteristics, scan pattern and strategy can have a quite profound impact on residual stress accumulation within a part. A notable example is, for example, the changing of laser paths when the part is moved from one place to another, causing the part to distort more in one location than the other.

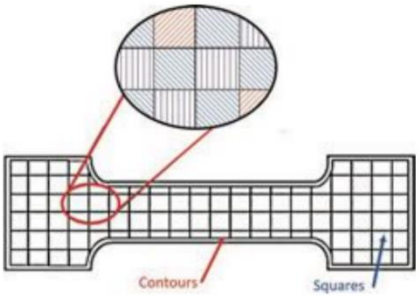


Figure 171 - Scan strategies in L-PBF (Squillace, 2023).

Powder size, size distribution and shape can also influence powder bed density, laser absorption characteristics, thermal conductivity and spreading. Finer particles absorb laser energy more efficiently due to a bigger surface area. Therefore, powder bed temperature, laser power, scan speed and spacing need to be balanced for an optimal synthesis between the melt pool size, dimensional accuracy, surface finish, build rate, and the mechanical properties. As a general rule, powder bed temperature should be kept uniform and constant so as to achieve repeatable results.

There are several possibilities for the thermal combinations between the laser power and the powder bed temperature. High laser power and high bed temperature combinations produce dense parts but will result in part growth, poor recyclability and in increased difficulty for cleaning of parts. Meanwhile, the opposite, low laser power and low bed temperature combinations produce better dimensional accuracy but will result in lower density parts and a higher tendency for layer delamination. High laser power and low bed temperature result in an increased tendency for non-uniform shrinkage and the build-up of residual stresses, which leads to curling of parts.

The input of energy required for fusion of the powder into a solid part that can be usable is determined by laser power, the spot size, the scan speed and the bed temperature, with a deeper fusion depth and therefore larger melt pool diameter being able to be achieved as long as the laser dwells in a particular location.

Operating at lower laser powers requires a decrease in scan speed so as to ensure proper particle fusion, with melt pool size dependent on the before mentioned settings of laser power, scan speed, spot size, and the bed temperature. Scan spacing therefore must be selected so as to ensure sufficient degree of melt pool overlap between the lines of material being fused to ensure a good quality and consistency of the part.

It is worth mentioning that the powder bed density can strongly influence the part quality, being governed by powder shape, size, distribution and spreading mechanism. Generally, for metal additive manufacturing, powder vary between 50 to 60% density,

with the higher the powder packing density, the higher the bed thermal conductivity and the better the mechanical properties of the part.

In modern times, most L-PBF machinery for industrial usage uses continuous wave lasers, however there is significant research being developed for pulsed lasers, which have a range of potential benefits such as the elimination of molten metal behaviour to form disconnected balls. Despite this, there is still more tendency to use continuous wave (CW) lasers due to faster processing when compared to pulsed ones (PW), translating into increased machine productivity (Gibson, Rosen, Stucker, & Khorasani, 5 - Powder Bed Fusion, 2021) (Squillace, 2023). Figure 172 illustrates the differences.

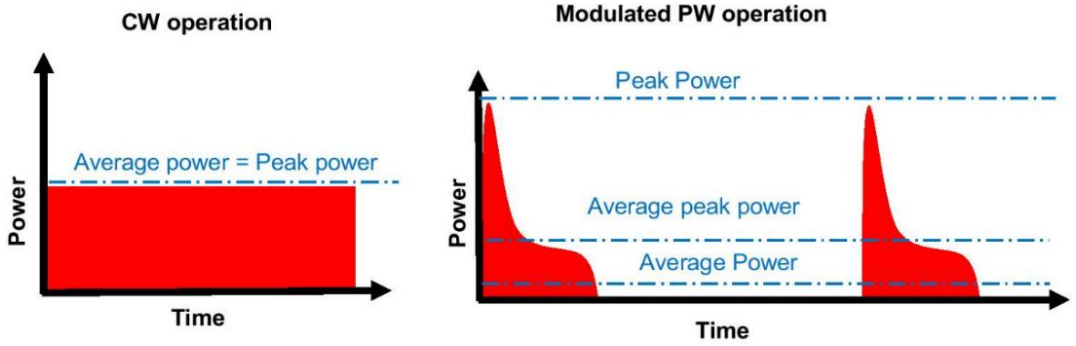


Figure 172 - CW vs PW (Coroado, et al., 2022).

In practical terms, overlapping scan lines will create different melt pool dynamics than single scan tracks. If the laser returns to a spot on a return pass prior to solidification of the material, it will have a similar effect to longer dwell time (or lower scan speed).

Figure 173 illustrates the dynamics. Therefore, more rapid scan speeds can be used for multiple pass scanning than when in single line scanning, as long as the beam returns before solidification.

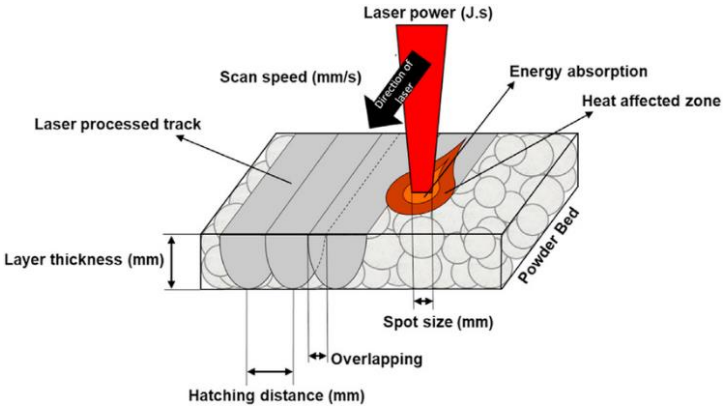


Figure 173 - Laser process parameters (Grossin, et al., 2021).

Defects such as balling can be avoided while still utilizing high scan rates, by simply splitting the cross section into small squares that are scanned individually, effectively creating the same as a line-shaped/elliptical shaped laser spot size the width of a square, with multiple passes created due to the overlapping generated from the smaller cross section.

Studies have also shown that residual stresses and corresponding part deflection will increase with a bigger track length, therefore dividing the scan area into small squares

(known as island scanning) and subsequently scanning each segment with short tracks is highly beneficial, giving an additional reason for subdividing the layer cross-section into small squares for metals. An example of a scan pattern is shown in figure 174.

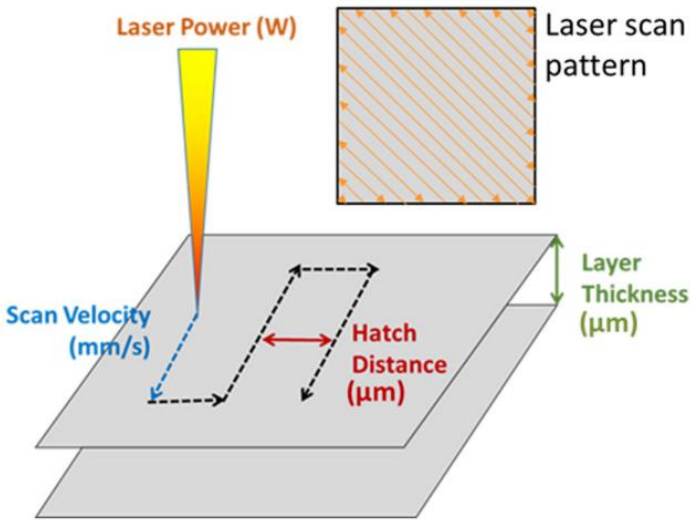


Figure 174 - Example of scan pattern (Oliveira, LaLonde, & Ma, 2020).

Randomization of square scanning and changing of the primary scan direction between the squares is also recommended and preferential since it helps alleviating preferential build-up of residual stresses. Additionally, scanning of the stripes where the angle of the stripe changes with each different layer also has a positive effect on the residual stress minimization. Due to all these reasons, stripes and square scan patterns are extensively used in metal L-PBF processes (Gibson, Rosen, Stucker, & Khorasani, 5 - Powder Bed Fusion, 2021) (Squillace, 2023) (Sefene, 2022)

Annex D – Thermal Interactions

It is important to clearly define which type of energy interaction we are interacting with in L-PBF systems.

The melt pool size and depth are dependent on absorbed energy density, with a simplified energy density equation used for correlation of the input process parameters to the density and strength of produced parts (Gibson, Rosen, Stucker, & Khorasani, 5 - Powder Bed Fusion, 2021), which goes as follows:

$$E_A = \frac{P}{SS \times HS}$$

With:

E – applied energy density (Andrews number)
P – laser power
SS – scan speed
HS – scan spacing / hatch spacing between parallel lines

In such a simplified model, applied energy increases proportionally with laser power and inversely with velocity and scan spacing. Although this does not include powder absorptivity, heat of fusion, laser spot size, machine configuration, between others, it provides a simplified approach for desired optimization of machine configuration. Through such simplified equation, and with a given material, laser spot size, and machine configuration, we can determine the minimum applied energy necessary for adequate fusion of the process, with build speed being maximized by utilization of the best combination of laser power, scan rate, and scan spacing, for a particular machine (Gibson, Rosen, Stucker, & Khorasani, 5 - Powder Bed Fusion, 2021).

In figure 175, we can see types of tracks formed through various combinations of Laser power, and scan speed combinations.

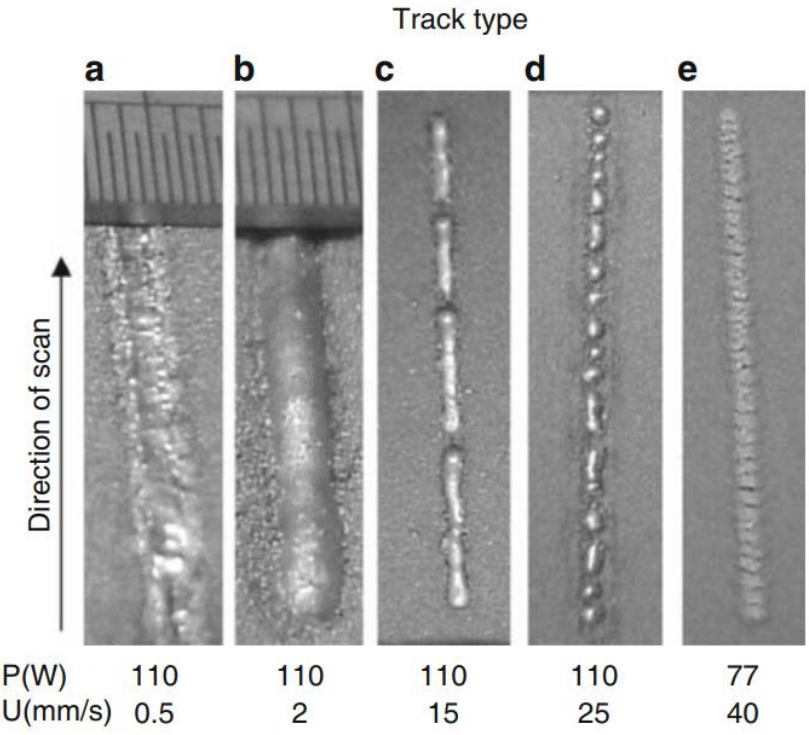


Figure 175 - Types of tracks (Gibson, Rosen, Stucker, & Khorasani, 5 - Powder Bed Fusion, 2021).

For better visualization, there is shown a process map with the aforementioned combinations, as can be seen in figure 176.

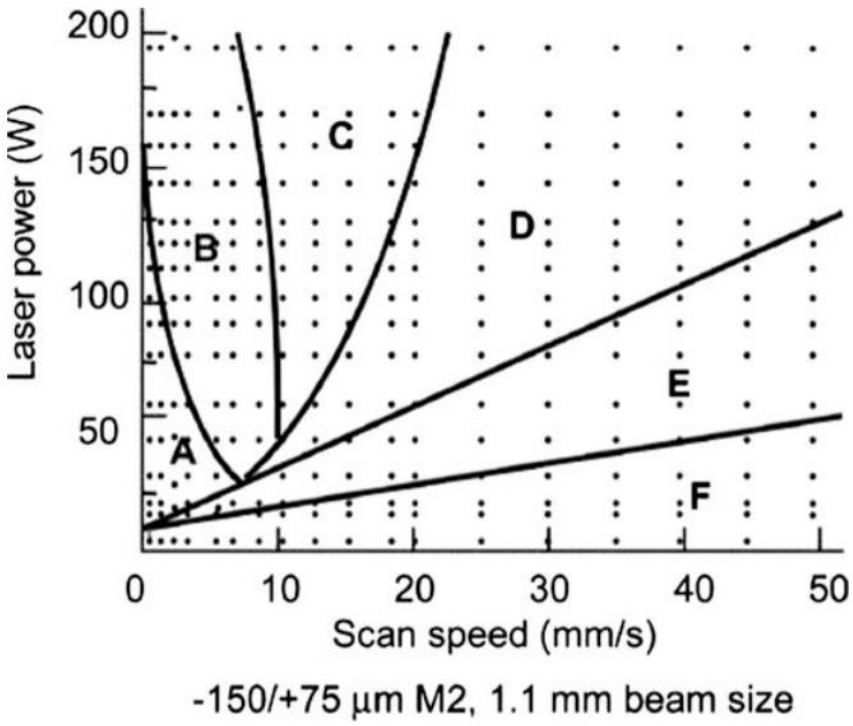


Figure 176 - Process parameters of track types (Gibson, Rosen, Stucker, & Khorasani, 5 - Powder Bed Fusion, 2021).

As described by Childs et al., the tracks of type A were continuous and flat topped/ slightly concave. Meanwhile, at higher speeds, tracks became rounded and sank into the bed. As the speed increases, type C tracks, the tracks became occasionally broken, but not with the regularity that can be seen in track types D, with the regularity and frequence of broken tracks causing an effect designated as balling effect (see section defects). At even higher speeds, fragile tracks, type E, were formed, where the maximum temperature exceeds solidus but does not reach liquidus temperature (meaning: partially melted or liquid phase sintered tracks). In region F, at the highest speed, with the lowest power combinations, no melting occurred.

When visualizing and reflecting on these results and types of tracks, it is obvious that build speed optimization is a complex subject, and that a simple maximization of scan speed for a particular power and scan spacing is not possible. Despite this, tracks type A and B can be seen as a guide for process optimization.

The equation seen 2 pages before solves for energy density per surface area, however, since the applied energy from a heat source is absorbed by a volume of the material, it is also worth calculating volumetric energy density (Gibson, Rosen, Stucker, & Khorasani, 5 - Powder Bed Fusion, 2021) (Squillace, 2023) (Sefene, 2022).

$$ED_v = \frac{P \times \eta_p}{SS \times HS \times LT}$$

$$ED_v = \frac{P}{\frac{PD}{ET} \times HS \times LT}$$

With:

E – applied energy density (Andrews number)
P – laser power
Np – powder absorptivity
SS – scan speed
PD – point distance (distance travelled between spot centers during pulsed heating)
ET – exposure time per pulse
HS – scan spacing / hatch spacing between parallel lines
LT – layer thickness

First equation is for continuous wave, while the second equation is for pulsed wave. This is when we say that the melt pool is in the liquid phase. For situations where the melt pool is solidified before the fusion of the next laser pass, the equation is as follows:

$$ED_v = \frac{P \times \eta_p}{SS \times BD \times LT}$$

With

BD – beam diameter

When we calculate volumetric energy density as a function of the melt pool depth, we can use the following equation.

$$ED_v = \frac{P \times \eta_p}{SS \times BD \times MD}$$

With:

MD – melt pool depth, which normally varies between 50% and 80% of heat penetration depth, which in turn, can be calculated through the following equation.

$$\delta_{\mathrm{h}} = 2\sqrt{\kappa t_{\mathrm{i}}} = 2\sqrt{\frac{K}{\rho C_{\mathrm{p}}} t_{\mathrm{i}}}$$

If there is the situation of pulsed lasers, ti is pulsed time, while for CW, it is as follows.

$$t_{\mathrm{i}} = \frac{\mathrm{BD}}{\mathrm{SS}}$$

Generally, input volumetric energy density is independent of the layer thickness and hatch spacing, which can be obtained through:

$$\mathrm{ED}_{\mathrm{v}} = \frac{P}{\mathrm{SS} \times \mathrm{BD} \times \mathrm{MD}}$$

All these equations are under the assumption that we are simplifying by neglecting heat of fusion, bed temperature, preheat condition, and others.

Another important phenomenon that was not aborded was heat dispersion, following gaussian beam rules, with energy density calculations increasing in complexity, for example, as follows:

$$\mathrm{ED}_{\mathrm{vG}} = \frac{2P \times \eta_{\mathrm{p}}}{\pi \times \mathrm{BD}^2 \times \mathrm{MD}} \exp\left(\frac{-2\left(\left(x - (\mathrm{SS} \times t) \right)^2 + y^2 \right)}{\mathrm{BR}^2} \right)$$

With:

BR – beam radius

Gaussian distribution of the laser beam and overall related dynamics are shown in figure 177.

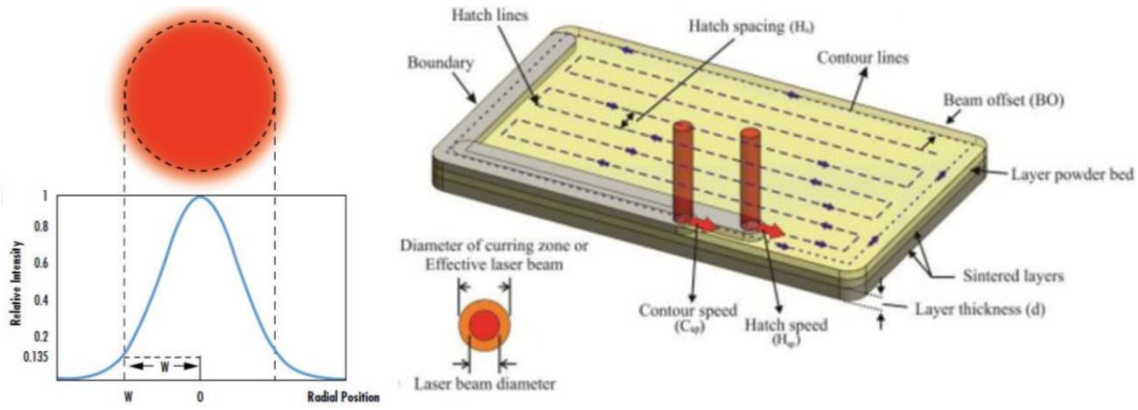


Figure 177 - Gaussian distribution of laser beam
(Gibson, Rosen, Stucker, & Khorasani, 5 - Powder Bed Fusion, 2021) (Zang, 2015).

And where we can see that the highest energy density is applied normally at the centre of the laser beam, due to increased energy concentration there, due to the gaussian distribution of the laser beam existing. Of note that this is a simplified view of the process involved, with relative explanation of the most significant parameters. The real-life conditions are more complex, requiring computer assisted calculations in areas such as thermodynamics, material interaction, and applied physics (Gibson, Rosen, Stucker, & Khorasani, 5 - Powder Bed Fusion, 2021) (Squillace, 2023).

Annex E – Accuracy Improvements

There are several ways to improve the accuracy of manufacturing, through visualization and understanding of the sources, of error, model pre-processing, and machining strategies, among others.

i) Sources of error

Process-dependent errors affect the accuracy of the X-Y plane differently from the Z-axis accuracy. These errors come from the positioning and indexing limitations of specific machine architectures, the lack of closed-loop process monitoring and control strategies (using sensors to monitor the process, autonomously identifying the necessary process modifications, and adjusting accordingly), and from issues fundamental to volumetric rates of material addiction (such as melt pool).

Additionally, for many processes, accuracy improvements will require fully automatic real-time control strategies to monitor and control the process, rather than the need to rely on expert operator feedback. The integration of synergetic elements between additive and subtractive technologies is another method for process accuracy improvement, being subject of extensive research grants of both private corporations and public R&D institutes (Gibson, Rosen, Stucker, & Khorasani, 5 - Powder Bed Fusion, 2021) (Squillace, 2023).

Phenomena which are material-dependent can also play a role in accuracy and residual stress-induced distortions, being quite difficult to counteract due to modern lack of knowledge regarding predictive capabilities understanding of various shrinkage and residual stresses variations. For enhancing of these predictive capabilities, quantitative understanding of the effects of process parameters, build style, part orientation, support structures and other factors on the magnitude of shrinkage, residual stresses and distortions is paramount to advancing on this field. In the meantime, a common solution for components with high degree of accuracy requirements is adding extra material and achieving the final desired accuracy via subtractive technologies, by, as an example, pre-processing of the specific .STL file to compensate for inaccuracies, followed by finish machining of the final part (Gibson, Rosen, Stucker, & Khorasani, 5 - Powder Bed Fusion, 2021) (Squillace, 2023).

ii) Model pre-processing

The position of the part within the L-PBF manufacturing unit and its orientation will influence accuracy of the built part, as well as surface finish and the total build time. Therefore, translation and rotation of the part for manufacturing are applied for optimization of the mentioned parameters.

Shrinkage often occurs both during and after manufacturing and being of particular note the post-process furnace operations for indirect processing of the metal AM built part. So as to combat such phenomena, there is the usage of a scale factor, so as to compensate for the average shrinkage of the process chain. However, even taking this into account, one must be wary of shrinkage variations.

In order to compensate for such variation, we can use the highest theoretical shrinkage value, meaning ribs and similar structures will always be at least, as big as the desired geometry. The problem is that channels and holes will be too large, thus simply using the largest shrink value is not an acceptable solution.

In order to be certain of enough material left in the built part, for machining post-processing, there is the necessity of adding an outer material shell to the model. This shell will allow the presence of material everywhere in the part, with many studies shown that shrinkage variations are geometry dependent, even when using same furnace process parameter setting and same L-PBF manufacturing characteristics.

Therefore, compensating for shrinkage variation uncertainties requires an offset of the original model, so as to allow a surplus of material that can be machined in post-processing, so as to allow the desired accuracy of the designed part. (Gibson, Rosen, Stucker, & Khorasani, 5 - Powder Bed Fusion, 2021) (Squillace, 2023)

iii) Machining strategy

Machining strategy can also have a role in the final manufacturing of the procedure, with the post-processing through CNC operations being quite usual for finishing operations, and for a better accuracy and precision requirements. The synergy possible between additive and subtractive technologies has been cause of extensive research, with possibilities of integrating AM and CNC operations in hybrid machines, as seen in the relevant section of Hybrid AM-CNC. Such combination allows the complexity of MAM allied with the finishing and precision of CNC so as to create products with more quality (Squillace, 2023).

Annex F – Surface Finishing Technologies

a) Mechanical

Regarding mechanical surface finishing technologies, the main ones are vibratory polishing, sand blasting, shot peening (also known as shot blasting), hybrid AM-CNC, and abrasive flow machining.

Vibratory polishing or finishing is the most used mass finishing process in industry, mainly because of its automation capabilities and superior parts handling, with a vibratory finishing machine being usually composed of a spring-mounted open-top container attached to an oscillation/vibration generator (figure 178).

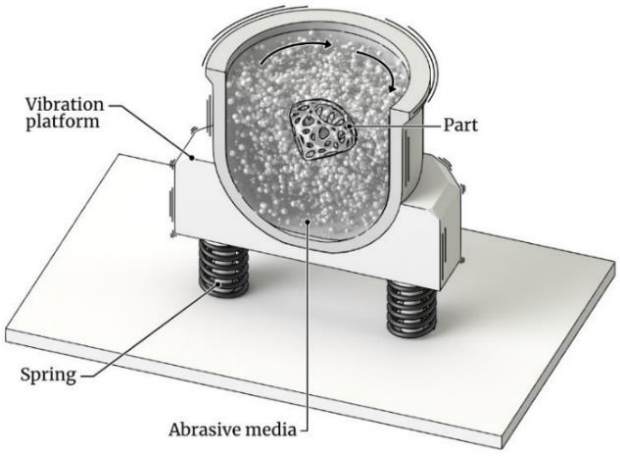


Figure 178 – Schematic diagram of the implementation of the vibratory tumbling process in a free abrasive (Babaev, et al., 2022).

In such process, abrasives with high dimensions and density are typically used in a vibrating machine, with the friction between the abrasives and the parts providing the smoothing process. The vibrations are induced by an excenter (a shaft with an offset mass connected to an electric motor), and there is the possibility of electromagnetic vibration generators. This process is cost-effective, does not require clamping of the part, is feasible

for all materials, is environmentally friendly, and has the possibility of multiple parts being treated simultaneously. Unfortunately, there is high wear of the abrasive particles, it struggles to smooth small features, and is almost impossible regarding inner ones, being unsuitable for high precision manufacturing.

Meanwhile, sand blasting and shot peening are the two most common variants of abrasive blasting, an abrasive machining process where the abrasives is propelled with compressed air or centrifugal force against the workpiece at high speeds. Sandblasting and shotblasting processes are quite similar, with the main differences being that shotblasting is much more aggressive than sandblasting - since it uses denser materials and higher velocities – and centrifugal force used commonly in shotblasting while in sandblasting compressed air is the most employed means (figure 179).

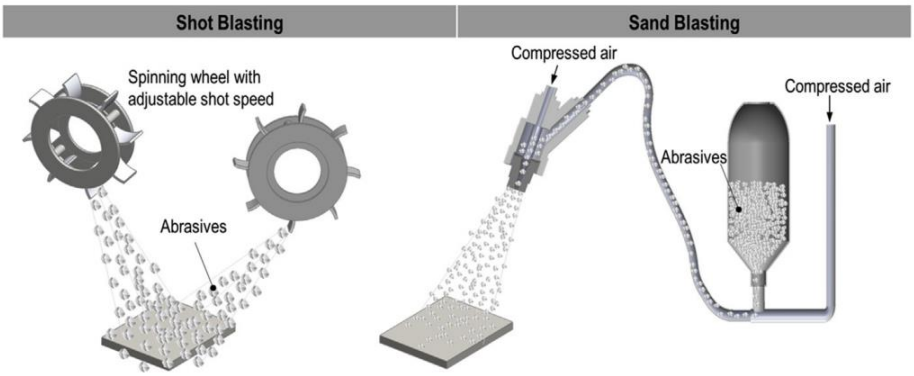


Figure 179 - Abrasive blasting processes (Kitzig-Frank, Tawakoli, & Azarhoushang, 2017).

In such abrasive blasting systems, the media (i.e. the abrasives stream) enters the compressed air stream from a reservoir or container in air blast systems. Valves direct the media, with abrasive particles accelerated through a nozzle. Finally, the blasted or shot media return to the container through a recycling system. Of note that a mechanical feeding unit can be used in centrifugal blast systems, pushing media into a spinning wheel mechanism, with abrasives accelerated through centrifugal force, and propelled against the workpiece surface. (Kitzig-Frank, Tawakoli, & Azarhoushang, 2017) (Azarhoushang, Marinescu, Rowe, Dimitrov, & Ohmori, 2022)

In sand blasting, the smoothing effect is achieved by means of high friction of the sand particles against the workpiece, while, in the shot peening post-processing technique, it is a cold working process which is used to generate compressive residual stresses, which will, in turn, supress tensile residual stresses, decreasing the chance of crack propagation and increase the part's life cycle.

In shot peening (figure 180), the shot is made so as to impact the built part at high velocities, with plastic deformation occurring at the surface level, and the material below this deformed area resisting deformation. In general, the creation of compressive residual stresses through this process enhances the roughness, the hardness, the compressive yield strength, and the wear resistance of the part. Shot peening post-processing operations can refine the grain size of the built part material.

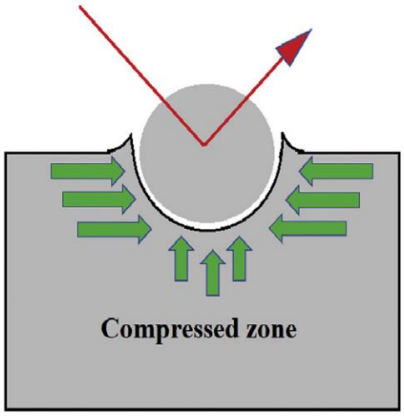


Figure 180 - Shot peening mechanism (Velu, Kumar, Balan, & Mazumder, 2021).

Both sand blasting and shot peening have similar benefits of being cost-effective, not requiring clamping of parts, being environmentally friendly, and having good surface quality achievable, with the differences of sand blasting being feasible for all materials and shot peening increasing the superficial mechanical properties. The main drawbacks in both processes are not being very suitable for very high precision surface quality, with sand blasting being typically a manual and directional process and shot peening being used only for metal parts. (Zhang & Liu, 2015) (Velu, Kumar, Balan, & Mazumder, 2021).

Hybrid AM-CNC operations can also be used for upgrading of the built part through implementation of high technological post processing. These operations are not exclusive to PBF processes, with various combinations possible and considerable R&D efforts being made into practical and cost-efficient implementation of subtractive technologies synergistically allied with additive technology.

Hybrid CNC-AM has the benefits of being fully automated, having very high surface quality (due to machining) and has increased productivity due to the deep integration possible in MAM, while coming with the drawbacks of being suitable only for metal parts, has higher waste production, increased investment costs, and the conditional of physical access into the parts being dictated by tool dimensions.

Abrasive flow machining (figure 181), meanwhile, works in the principle of forcing a flowable abrasive media through the workpiece, being able to process many selected passages on the workpiece

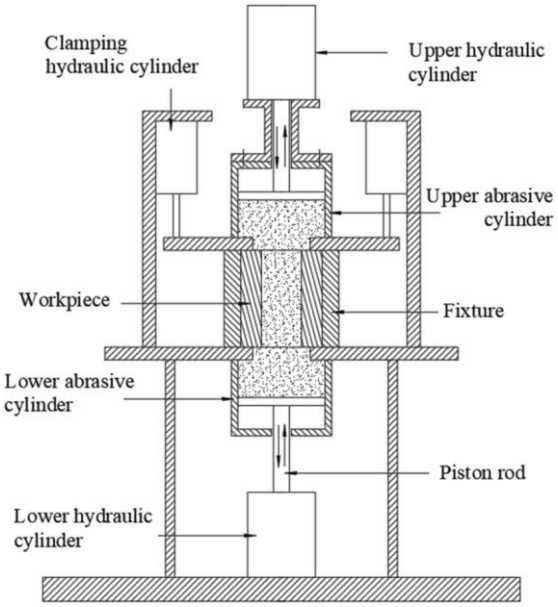


Figure 181 - Schematic diagram of Abrasive flow machining mechanism (Li, et al., 2020).

simultaneously, through restriction of the media through the part. Several parts can be worked on simultaneously in one fixture, with production rates of hundreds of parts per hour. The AFM process can yield typical 90% improvements in surface finishes with stock removal controllable to less than 10% of stock removed.

This post-processing operation is able to create repeatable, predictable results in the delivery of finishing operations, which offer flexibility and automation in final machining operations as integral parts of the overall manufacturing cycle, being synergistically allied to automation technology, for reduced cycle times maintaining overall quality of manufacturing (Rhoades, 1991).

b) Chemical

Regarding chemical interaction-based surface treatments, the main treatments used for MAM operations are chemical polishing and electrochemical polishing.

When chemical polishing (figure 182) is utilized, the parts are immersed into purposely made chemical solutions that are kept under temperature and stirring controlled conditions. The smoothing process takes place by means of surface corrosion interactions. It creates high surface quality and is a time-effective process, while being feasible for complex parts with inner features. However, this comes at the cost of high environmental impact, (a significant concern in Western Industrial policies), high costs related to operation infrastructure and waste removal, and the necessity of different solutions for different materials, with necessary constant supervision in the operation itself for prevention of damage to the inner surfaces (over etched), hampering the parts functionality and operating safety (Gibson, Rosen, Stucker, & Khorasani, 5 - Powder Bed Fusion, 2021) (Squillace, 2023).

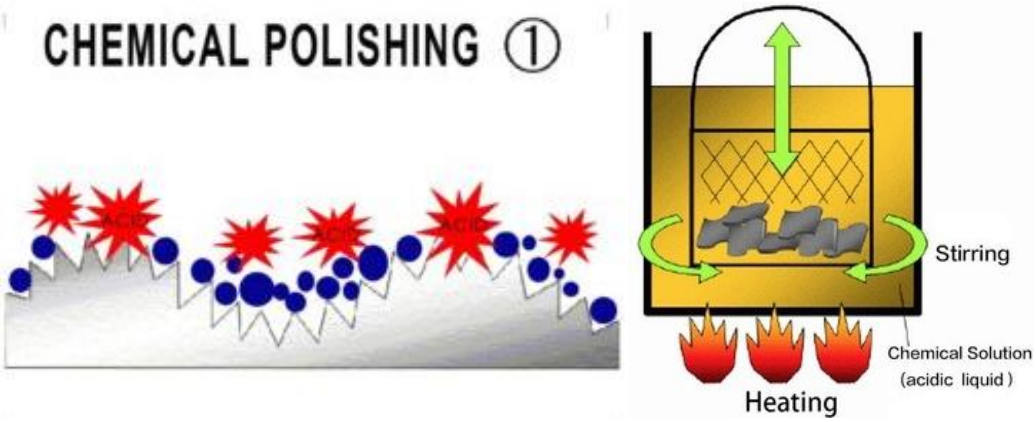


Figure 182 - Chemical polishing operations (Chemical polishing, 2024).

Regarding electrochemical polishing (figure 183), it is quite similar to chemical polishing, with the distinctions of being controlled through application of an electric potential in an electrolytic cell, and only being possible in metals (as opposed to metals

and polymers in chemical polishing) (Gibson, Rosen, Stucker, & Khorasani, 5 - Powder Bed Fusion, 2021) (Squillace, 2023).

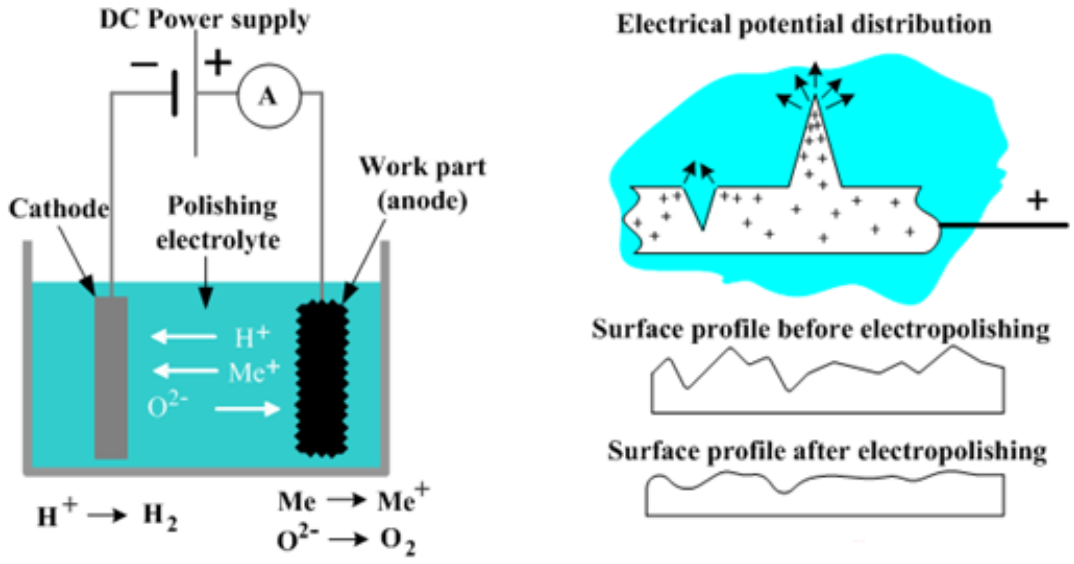


Figure 183 - Electrochemical polishing operation (Liu, Wang, & Xu, 2022).

Similarly to chemical polishing, electrochemical polishing creates high surface quality and is a time-effective process and is more feasible for complex parts with inner features, whilst being more selective on surface asperities overall. It comes with the drawbacks of, similarly to chemical polishing, of high environmental impact, high costs related to operation infrastructure and waste removal, and the necessity of different solutions for different materials, with the added caveat of process efficiency being dependant on current electric field distribution. (Gibson, Rosen, Stucker, & Khorasani, 5 - Powder Bed Fusion, 2021) (Squillace, 2023)

c) Thermal

In thermal post-processing interactions, the main ones used in the industry are laser polishing and thermal deburring technology.

In laser polishing (figure 184), through utilization of a laser source, the parent surface asperities can be removed through either material vaporisation (known as ablation) or through re-melting. This allows for very high surface quality, and high degrees of control and automation possibilities, while being environmentally friendly, at the cost of being greatly affected by the geometry of parts and laser absorption characteristics of a material, having very low access into complex and/or inner part features and high costs of labour (when not automated). (Gibson, Rosen, Stucker, & Khorasani, 5 - Powder Bed Fusion, 2021) (Squillace, 2023)

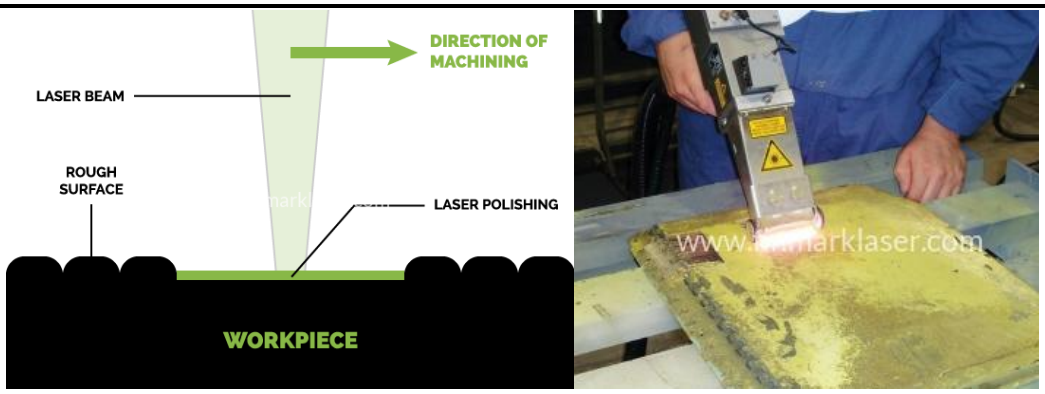


Figure 184 - Laser polishing process: schematic (left) and application example (right) (Laser cleaning, 2020).

Thermal deburring (figure 185), also known as thermal energy method (TEM), is a process that deburrs components by igniting a volatile gas mixture within a pressurized chamber containing the work piece gear, creating a combustion heat wave that reaches more than 3000°C in milliseconds, burning off the burrs and flashing, by taking advantage of the high surface-to-volume ratios of these parts when compared to the part itself.

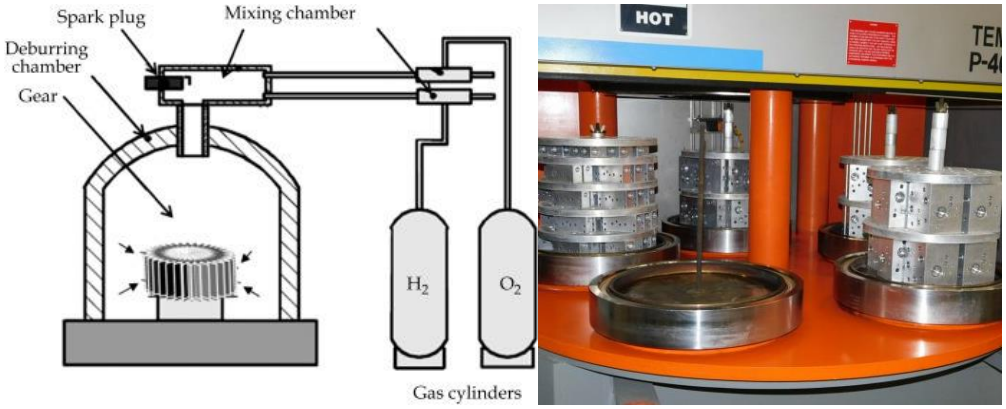


Figure 185 – Thermal deburring process: schematic (left) and application example (right) (Gupta, Jain, & Laubscher, 2017).

It is very suitable for build supports removal and complex inner features, has high degrees of automation and control, and is a tool-less process, coming at the cost of high investment costs and not being very useful for surface roughness reductions. (Gupta, Jain, & Laubscher, 2017)

There is additionally the possibility of hot isostatic pressing (HIP), which is the applications of temperature and pressure to as-built components, for a specified time of operation. HIP processes use isostatic force on a material at high temperatures, therefore, in this type of post-processing, temperature and pressure are the two critical parameters, and there is usage of an inert argon environment so as to minimize oxidation – the pressure acts on all surfaces of the component through all directions.

HIP (figure 186) assumes a significant role for eliminating defects such as lack-of-fusion, keyhole, residual stresses and gas pores, while reducing porosity, alleviating anisotropy and overall obtaining the best mechanical properties for the mentioned parts – managing to densify the material to almost 100% porosity

It is worth noting that the synergy between MAM and HIP allows for metal parts that required different assemblies to be produced as one part, resulting in significant cost savings. (Hot Isostatic Pressing: Improving quality and performance in AM parts production, 2015) (Mahmood, et al., 2023)

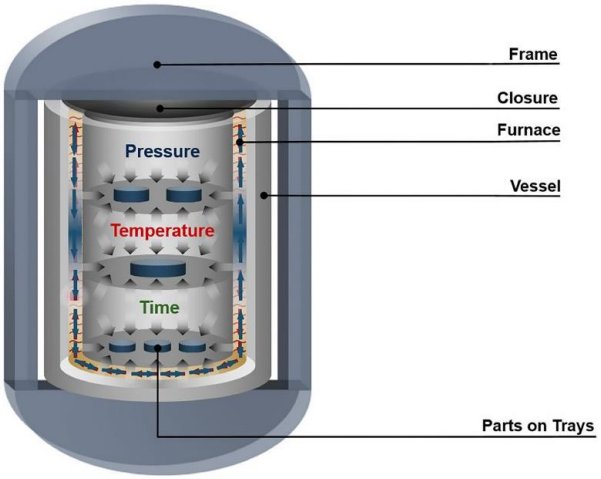


Figure 186 - HIP schematic of the equipment and process
(Hot Isostatic Pressing: Improving quality and performance in AM parts production, 2015).

Annex G – Tension calculus

There was determination of the yield point, by offset of the linear portion of the stress-strain curve by +0.2% along the strain axis, for calculus of the yield strength (figures 186, 187 and 188)

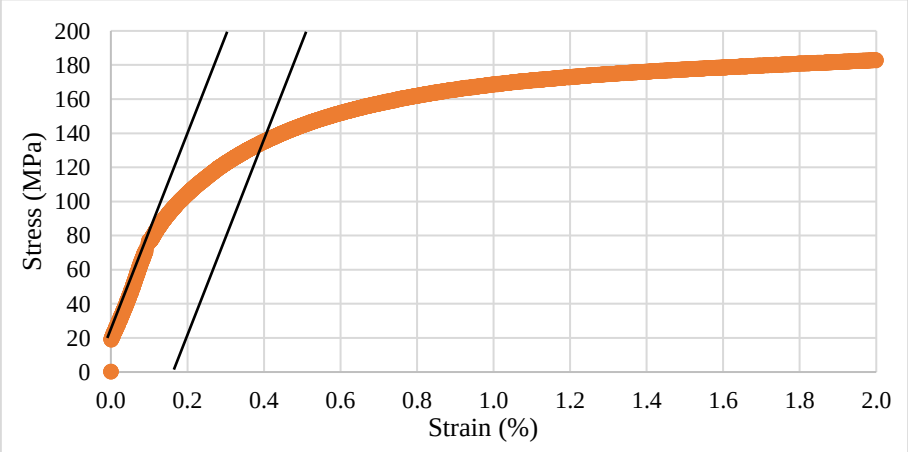


Figure 187 - Group 1 0.2% offset.

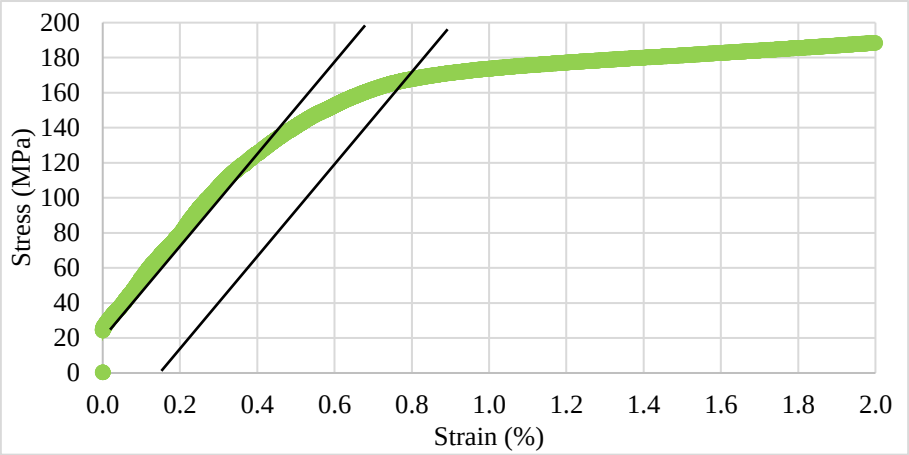


Figure 188 - Group 2 0.2% offset.

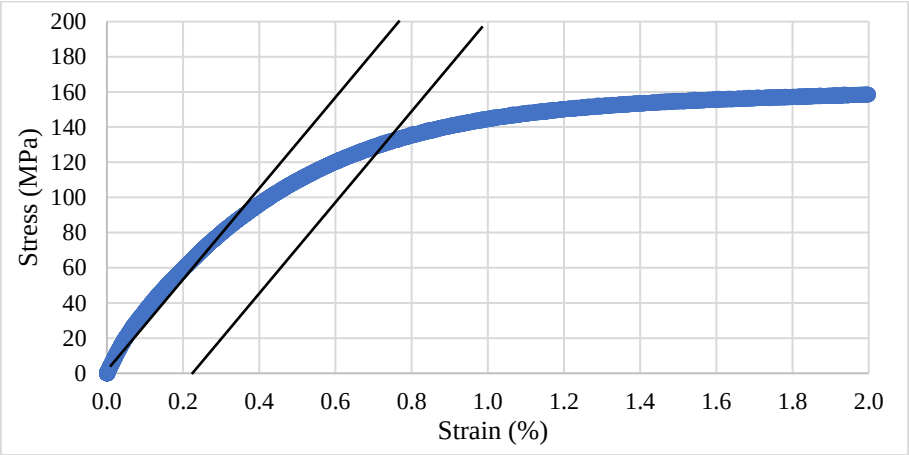


Figure 189 - Group 3 0.2% offset.

There was additional determination of the Young Modulus, by calculations referring to the elastic region line progression (figures 189, 190 and 191).

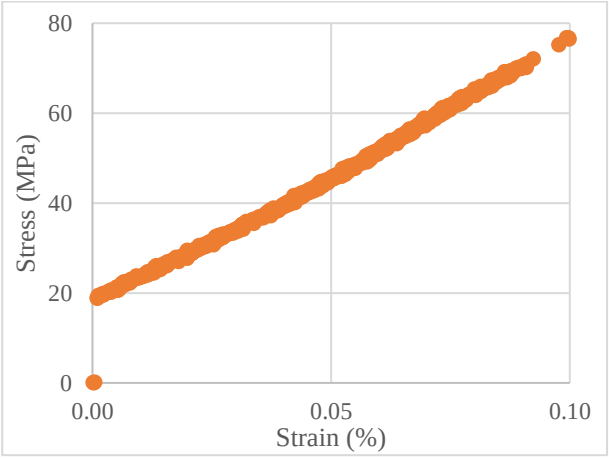


Figure 190 - Group 1 (tensile) elastic region

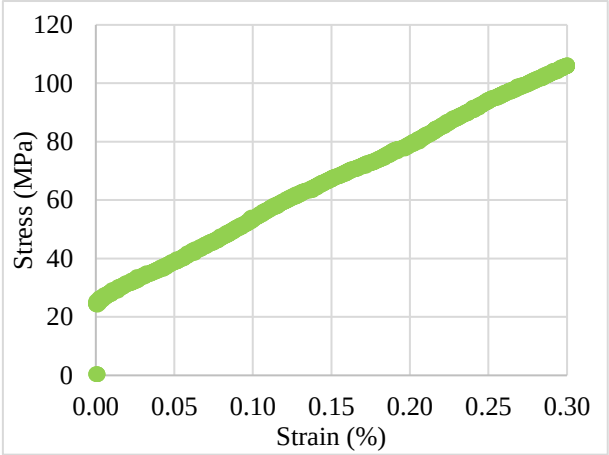


Figure 191 - Group 2 (tensile) elastic region.

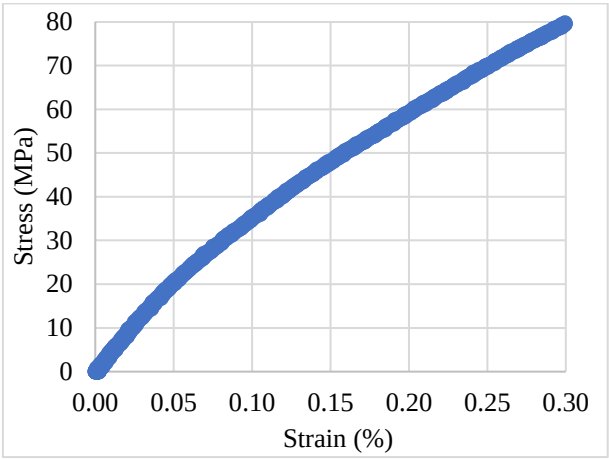


Figure 192 - Group 3 (tensile) elastic region.

$$E1 = \sigma/\epsilon = \frac{76 - 18.8\ (Mpa)}{0.10\%} = \frac{57.2 * 10^6\ (Pa)}{0.001} = 57.2 * 10^9 Pa = 57.2\ GPa$$

$$E2 = \sigma/\epsilon = \frac{106.2 - 24.8\ (Mpa)}{0.30\%} = \frac{81.4 * 10^6\ (Pa)}{0.003} = 27.1 * 10^9 Pa = 27.1\ GPa$$

$$E3 = \sigma/\epsilon = \frac{79.9 - 0\ (Mpa)}{0.30\%} = \frac{79.9 * 10^6\ (Pa)}{0.003} = 26.6 * 10^9 Pa = 26.6\ GPa$$

Annex H – Compression calculus

There was determination of the yield point, by offset of the linear portion of the stress-strain curve by +0.2% along the strain axis, for calculus of the yield strength (figures 192, 193 and 194).

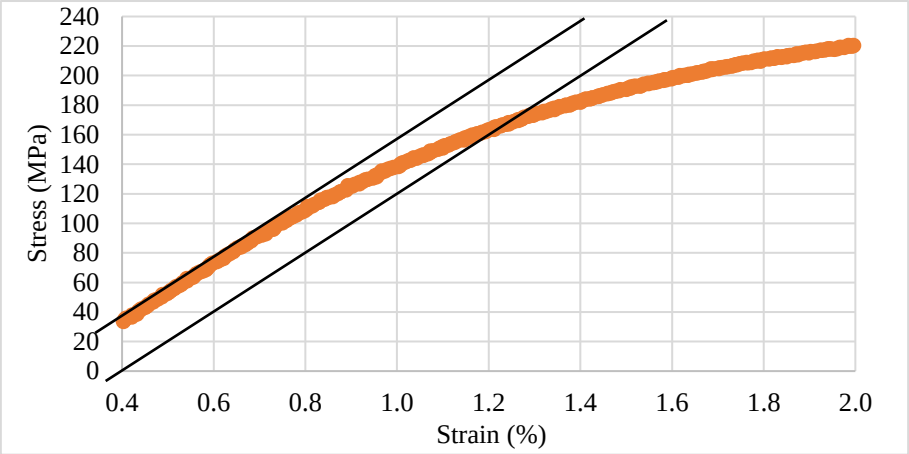


Figure 193 - Group 1 compressive yield strength at 0.2% elongation visualization.

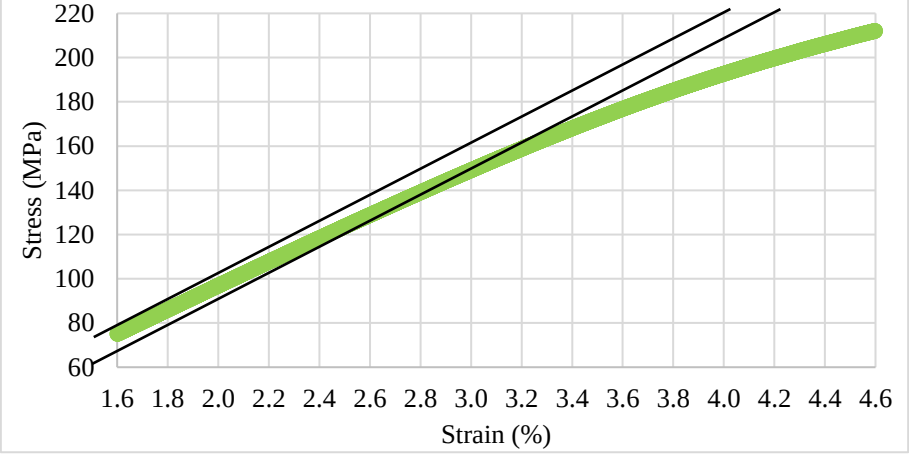


Figure 194 - Group 2 compressive yield strength at 0.2% elongation visualization.

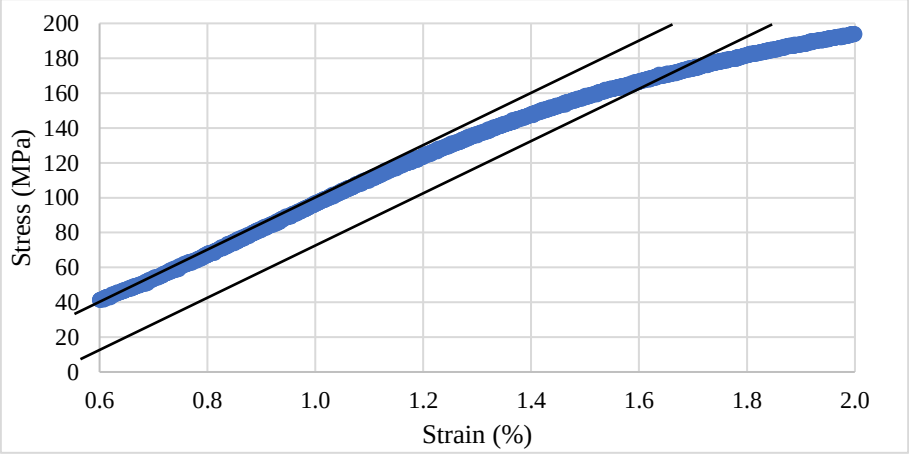


Figure 195 - Group 3 compressive yield strength at 0.2% elongation visualization.

There was additional determination of the Young Modulus, by calculations referring to the elastic region line progression (figures 195, 196 and 197).

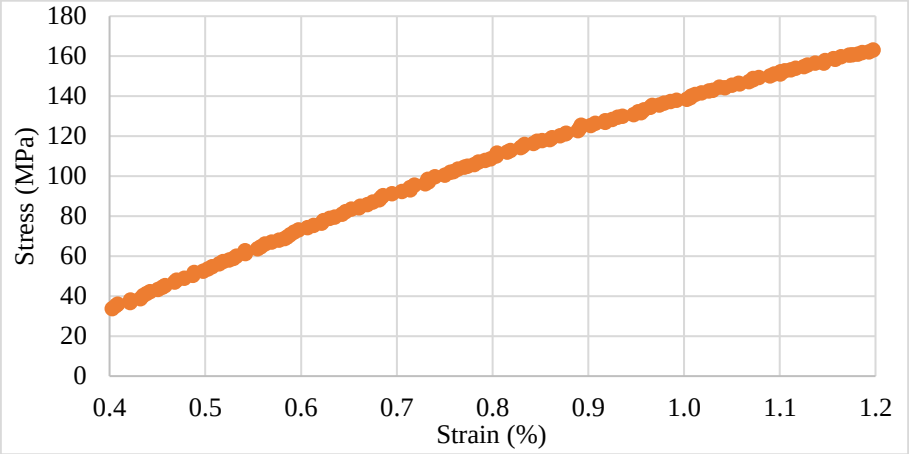


Figure 196 - Group 1 (compressive) elastic region.

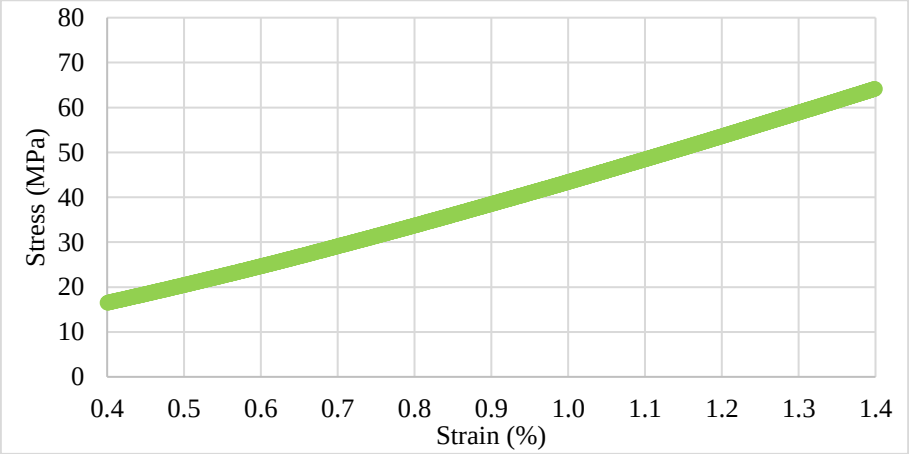


Figure 197 - Group 2 (compressive) elastic region.

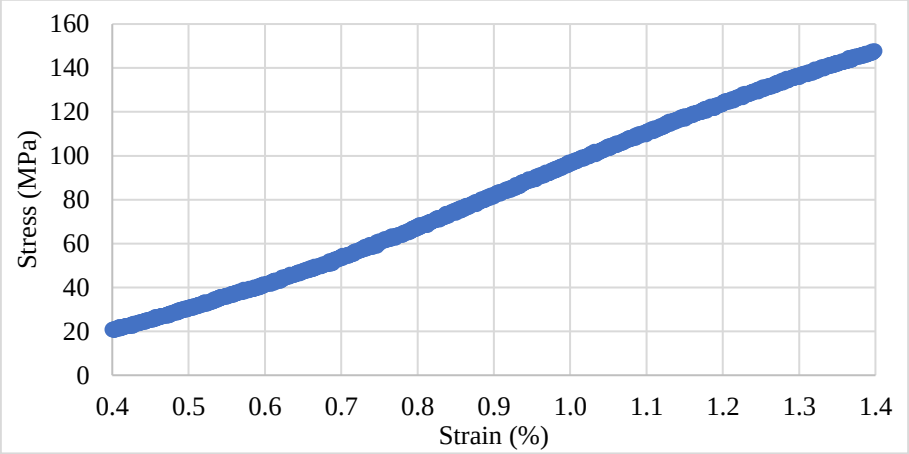


Figure 198 - Group 3 (compressive) elastic region.

$$E1 = \sigma/\epsilon = \frac{163.4 - 33.7\ (Mpa)}{1.20\%} = \frac{129.7 * 10^6\ (Pa)}{0.012} = 10.8 * 10^9 Pa = 10.8\ GPa$$

$$E2 = \sigma/\epsilon = \frac{63.7 - 16.4\ (Mpa)}{1.00\%} = \frac{47.3 * 10^6\ (Pa)}{0.01} = 4.7 * 10^9 Pa = 4.7\ GPa$$

$$E3 = \sigma/\epsilon = \frac{148.3 - 20.9\ (Mpa)}{1.0\%} = \frac{127.4 * 10^6\ (Pa)}{0.01} = 12.7 * 10^9 Pa = 12.7\ GPa$$

Annex I – SME calculus

There was determination of the yield point, by offset of the linear portion of the stress-strain curve by +0.2% along the strain axis, for calculus of the yield strength (figures 198, 199, 200 and 201).

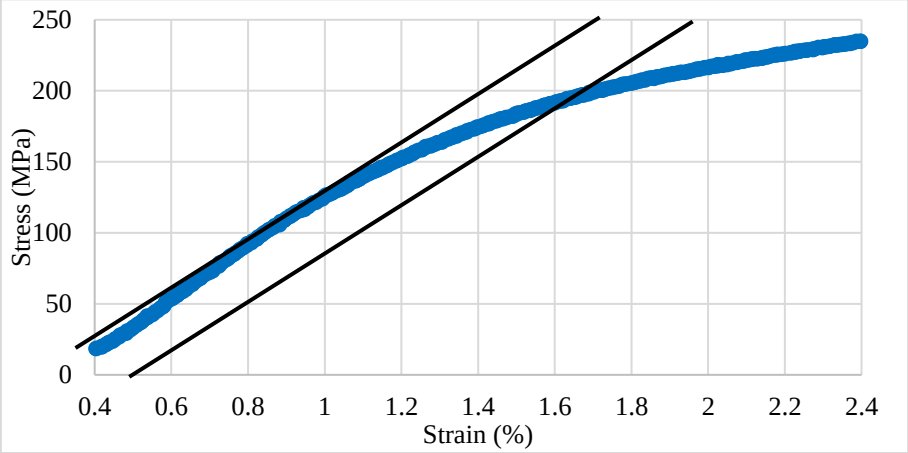


Figure 199 – 1st cycle compressive yield strength at 0.2% elongation visualization.

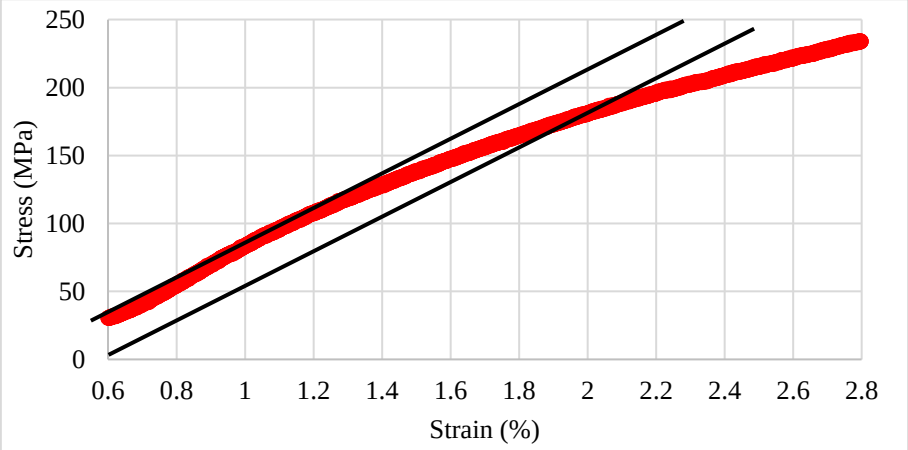


Figure 200 - 2nd cycle compressive yield strength at 0.2% elongation visualization.

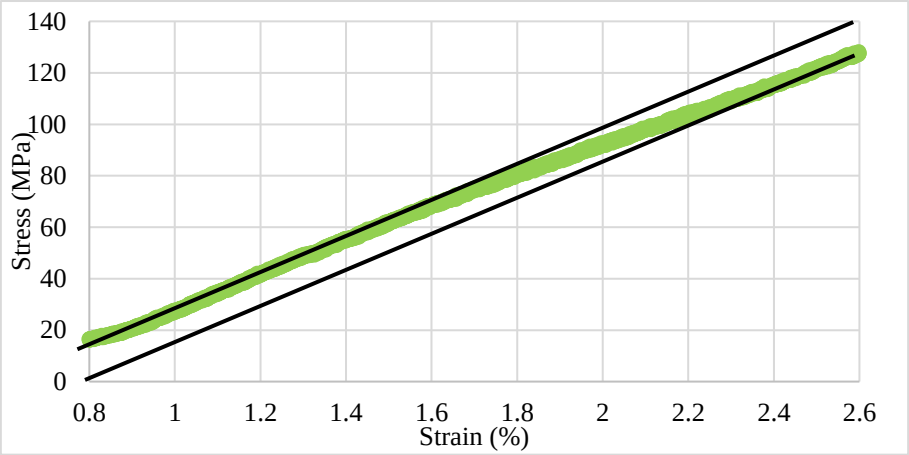


Figure 201 – 3rd cycle compressive yield strength at 0.2% elongation visualization.

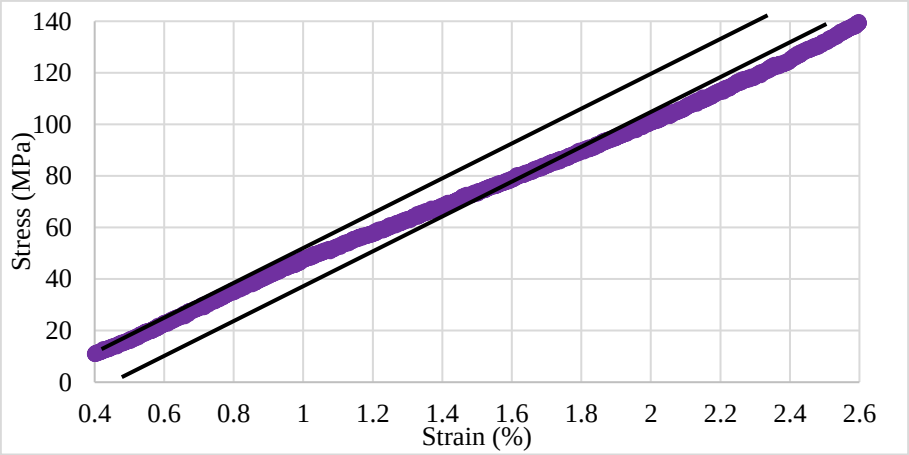


Figure 202 - 4th cycle compressive yield strength at 0.2% elongation visualization.

There was additional determination of the Young Modulus, by calculations referring to the elastic region line progression (figures 202, 203, 204 and 205).

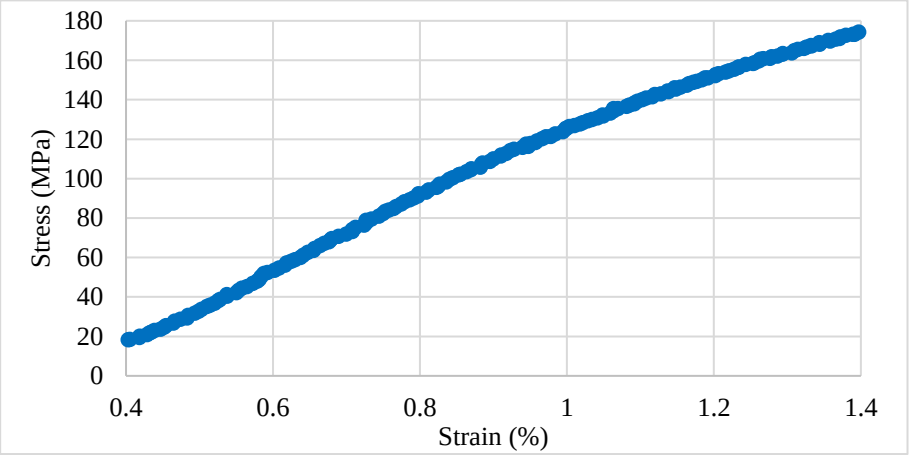


Figure 203 - 1st cycle (compressive) elastic region.

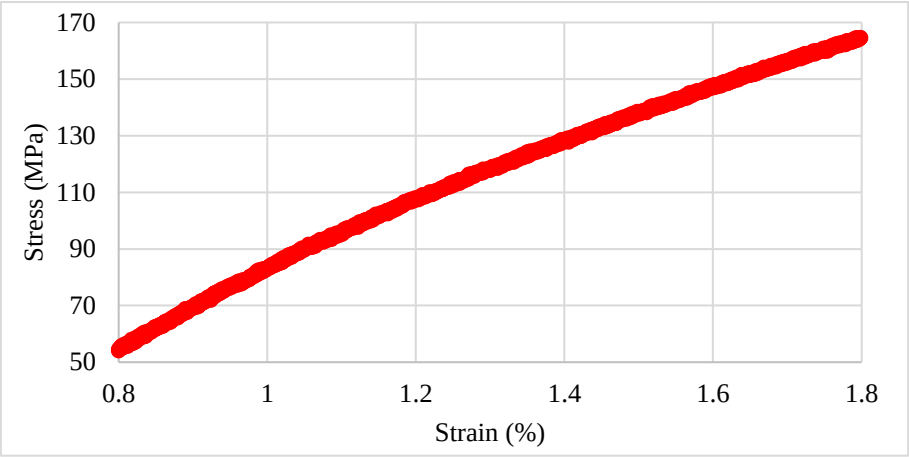


Figure 204 - 2nd cycle (compressive) elastic region.

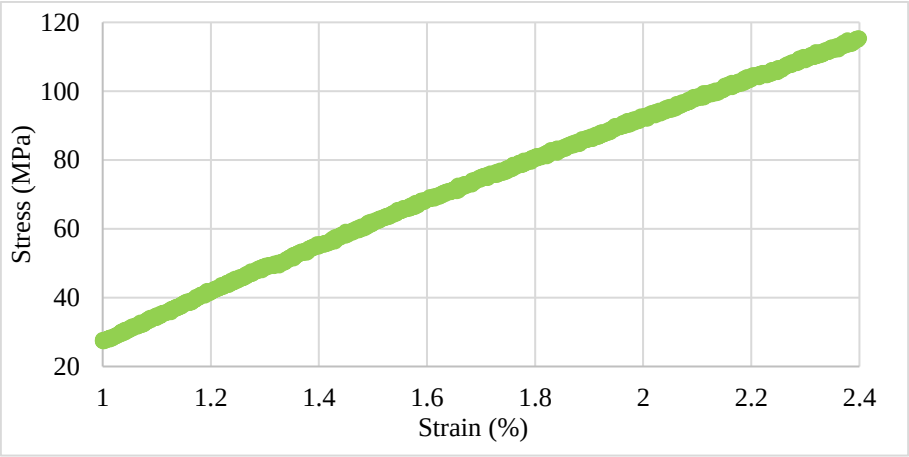


Figure 205 - 3rd cycle (compressive) elastic region.

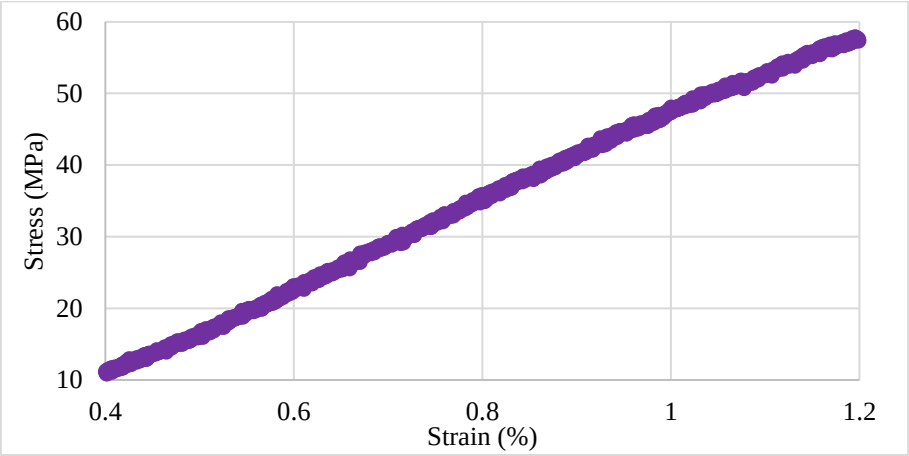


Figure 206 - 4th cycle (compressive) elastic region.

$$E1 = \sigma/\epsilon = \frac{175.0 - 18.6\ (Mpa)}{1.00\%} = \frac{156.4 * 10^6\ (Pa)}{0.01} = 15.64 * 10^9 Pa = 15.64\ GPa$$

$$E2 = \sigma/\epsilon = \frac{165 - 55.6\ (Mpa)}{1.00\%} = \frac{109.4 * 10^6\ (Pa)}{0.01} = 10.94 * 10^9 Pa = 10.94\ GPa$$

$$E3 = \sigma/\epsilon = \frac{115.2 - 28.7\ (Mpa)}{1.40\%} = \frac{86.5 * 10^6\ (Pa)}{0.014} = 6.18 * 10^9 Pa = 6.18\ GPa$$

$$E4 = \sigma/\epsilon = \frac{57.3 - 11\ (Mpa)}{0.8\%} = \frac{46.3 * 10^6\ (Pa)}{0.008} = 5.79 * 10^9 Pa = 5.79\ GPa$$

The recovered strain (after heating and compared to origin of cycle) relevant calculations are show as follows.

$$Recovered\ strain = 1 - \frac{pre - def\ height - post - heat\ height}{pre - def\ height - post - def\ height}$$

$$1st\ cycle\ recovered\ strain = 1 - \frac{24.7 - 24.62}{24.7 - 24.2} = 84\%$$

$$2nd\ cycle\ recovered\ strain = 1 - \frac{24.62 - 24.37}{24.62 - 23.41} = 79\%$$

$$3rd\ cycle\ recovered\ strain = 1 - \frac{24.37 - 24.25}{24.37 - 23.3} = 89\%$$

$$4th\ cycle\ recovered\ strain = 1 - \frac{24.25 - 24.19}{24.25 - 23.23} = 94\%$$